(1.) EXPERIMENTAL INVESTIGATION OF HYDROUS MELTING OF THE EARTH'S UPPER MANTLE, AND

(2.) OLIVINE ABUNDANCES AND COMPOSITIONS IN HAWAIIAN LAVAS.

Thesis by

Joseph Brian Balta

In Partial Fulfillment of the Requirements for the

degree of

Doctorate of Philosophy

CALIFORNIA INSTITUTE OF TECHNOLOGY

Pasadena, California

2010

(Defended November 20th, 2009)

ACKNOWLEDGEMENTS

First and foremost, I need to acknowledge my advisor, Dr. Paul Asimow, for more things than I know how to adequately put into words. I can't begin to fathom how much I've learned thanks to Paul, and I've always been amazed at his willingness to try to actually make sure we got through everything, even when I went down a wrong path or when things went wrong.

Secondly, I need to thank practically everyone on the 3rd floor of the Arms building. In particular, I must thank Jed Mosenfelder for teaching me how to run everything in our lab and for constantly having an open door when I needed to talk to someone about why the last experiment didn't work. I also need to recognize Mike Baker and John Beckett, for never actually installing a trap door in their office for use when I came by to ask them something (and they had plenty of opportunities should they have chosen to do so).

There are many other names beyond those few who I would feel remiss if I did not acknowledge as well, for a number of contributions to my research and learning here. These include: Sally Newman, Ma Chi, George Rossman, Liz Muira, Paula Antoshechkina, John Eiler, Ed Stolper, and Magnus Eek for a variety of contributions. I also would like to acknowledge Joe Kirschvink, Jason Saleeby, Joann Stock, and Jean-Philippe Avouac for the many field trips they've organized over my years here.

I also feel like I should acknowledge the entire graduate student population, since I'm not sure there's anyone I want to leave out. Specifically, I need to note contributions from Andrew Matzen, Laura Hebert, Sarah Miller, June Wicks, Ryan Petterson, Kevin Lewis, Ravi Kanda, Bob Kopp, and Charlie Verdel from that population for their help and friendship over the years. I also should acknowledge the administrative support staff in the department, who have been helpful in countless ways. I would also like to acknowledge the 2005 Chicago White Sox, and my family.

Finally, I need to acknowledge and thank my wife, Jennifer Balta, for putting up with years of me coming home in a foul mood late at night after an experiment failed or after a long test, for always being there for me, for always listening even when I didn’t want to talk, for being my best friend, and for being everything I could ever ask for in a partner.

ABSTRACT

(1)

The presence of small amounts of water dissolved within nominally-anhydrous minerals in the earth has significant effects on the chemistry of melting in the mantle. Upwelling rock containing water will melt at greater depths than the same rock would if it were volatile-free, and the chemistry of these hydrous melts is expected to be quite different from that of anhydrous melts. We have developed new experimental techniques and applied them to melting under pressures where hydrous melting is of the greatest natural importance. We have also controlled the content of carbon, another volatile element, to produce melts from a range of compositions not previously sampled experimentally.

The liquid composition shows a number of interesting properties. Compared to anhydrous melts from the same pressure, it shows decreased modal olivine and increased silica content. Compared to carbon-containing experiments, it suggests that carbon interacts with water when both volatiles are present, and may act to oppose the effects of water. The presence of a hydrous liquid also has an important effect on the coexisting solid chemistry. High-aluminum clinopyroxenes are commonly observed at this pressure in anhydrous systems. However, in all of our volatile-containing experiments, the clinopyroxenes show a substantial decrease in aluminum content and an increase in calcium content. Many elements, including water, enter into the clinopyroxene structure by coupled substitution with aluminum, and thus reduced clinopyroxene aluminum content during natural melting will decrease the partitioning of these elements during melting.

(2)

Variations in the modal abundance of olivine are the main mineralogical differences amongst typical Hawaiian lavas. A large quantity of olivine must crystallize from the Hawaiian parental liquids prior to eruption to produce the erupted lavas. The chemistry and abundance of these olivines reflects the behavior of the magmatic system in a number of

ways. We have used the chemistry of these olivines and lavas to estimate the parental liquid compositions in Hawaiian volcanoes, to infer the relationship between the olivines and the lavas that host them, and to probe the evolution of Hawaiian volcanoes over time.

TABLE OF CONTENTS

Chapter V:

LIST OF TABLES AND FIGURES

INTRODUCTION

By

J. Brian Balta

Part 1: Experimental investigation of hydrous melting of the Earth's upper mantle

It is now well established that volatile elements including carbon and water strongly influence the melting of rocks on Earth. The presence of either component in an upwelling rock will cause it to begin melting at greater pressures and lower temperatures than it would if it were volatile-free. A number of experiments and analyses of natural rocks have built a basic understanding of how these components interact with natural minerals. In the mantle, a small amount of water can be hosted within the structure of most nominally anhydrous minerals (e.g., Bell and Rossman, 1992; Mosenfelder et al., 2006). Beneath a mid-ocean ridge, mantle peridotite upwells to fill the space created as the oceanic plates spread apart. When it crosses its solidus pressure and temperature, this material begins to melt, producing the liquids that eventually are erupted as mid-ocean ridge basalts. As a volatile component, water partitions strongly into the liquid phase during melting (e.g., Michael, 1995; Hirth and Kohlstedt, 1996; Danyushevsky et al., 2000). Consequently, the presence of water is also able to suppress the solidus of peridotite, such that peridotites with higher water contents will melt at greater depths (Hirth and Kohlstedt, 1996). Anhydrous peridotites would typically be expected to begin melting at ~60 km depth (Hirschmann et al., 2009), and the presence of water could increase this depth by several 10's of km depending on the exact amount of water present and its relationship to the solids.

Understanding the effects of water on melting under mid-ocean ridges therefore requires experiments equilibrating solids and liquids with compositions that are representative of the upper mantle, conducted under pressure and temperature conditions that approximate those that are found on Earth. However, a number of experimental difficulties have thus far prevented a full analysis of hydrous melting under these

conditions. These issues include: the difficulty in quenching liquids from high pressure to unaltered glass that can be analyzed at low pressure, interaction of samples with the capsule materials encasing them, and contamination of experiments by carbon during heating (Liu et al., 2006).

We have performed experiments that have successfully equilibrated hydrous liquids with natural solids at the pressures and temperatures of interest after overcoming these difficulties. The results of these experiments make up Part 1 of this thesis. We were able to successfully quench hydrous liquids to analyzable glasses from 3 GPa pressure and 1375°C. To quench these liquids, we adapted the technique of Putirka et al. (1996) which was effective at producing a glass in our piston-cylinder. Preventing significant interaction of the samples with the capsules was more complicated. To contain water during the experiments, we chose to use capsules composed of an alloy of $Au_{75}Pd_{25}$, which is commonly used as a capsule material for water-bearing experiments (e.g., Kawamoto and Hirose, 1994). However, capsules composed of Au/Pd alloys will take up small amounts of several elements at high temperature, including Fe, which is a major element in natural rocks. Avoiding significant Fe loss to our capsules motivated the work in Chapter 4 of this thesis. We performed experiments to calibrate the equilibrium iron concentration in this alloy as a function of iron activity, such that we gained the ability to pre-saturate capsules with an appropriate amount of iron before use in high-pressure experiments. Thus, we were able to precondition our capsules with enough iron to avoid significant iron loss or gain to the capsules during the run. Finally, to control carbon contamination during experiments, we applied a version of the double-capsule design of Kägi et al. (2005), which was originally designed to control oxygen fugacity during

hydrous experiments. By creating a large outer capsule filled with the same contents as the inner capsule, the concentration of carbon in the final liquids only increased slightly during the experiments, allowing us to examine low-carbon, hydrous melts that have not previously been sampled.

The liquids we produced and the solids that they have equilibrated with appear to have significant implications for the understanding of natural peridotite melting on earth. The basic effect of water on the composition of silicate liquids has been understood as increasing the silica content of the liquid at the expense of other oxides such as magnesium and iron (e.g., Kushiro, 1968; Gaetani and Grove, 1998; Liu et al., 2006). Because these oxides are the main components of olivine, the ratio of silica to iron and magnesium can be understood as reflecting increasing or decreasing amounts of olivine in the melt. However, a number of variables other than simply water content affect this ratio by affecting the stability of olivine. For example, increasing carbon content appears to oppose the effect of increasing water. Compared to hydrous melting at lower temperatures and lower pressures (e.g., Gaetani and Grove, 1998), our liquid shows higher magnesium and iron contents and lower silica, while compared to anhydrous melts from the same pressure and higher temperature (e.g., Walter, 1998) our liquid shows higher silica and lower magnesium and iron. Our experiments show the magnitude of this effect under plausible conditions for the production of natural hydrous melts and likely closely reflect the actual composition of natural liquids.

The hydrous melting experiments also show important changes in the composition of the co-existing clinopyroxenes. Previously, virtually every experiment produced at 3 GPa pressure shows clinopyroxenes with a substantial amount of aluminum in their

structure (e.g. Walter, 1998; Longhi, 2002). Indeed, our starting solid material was synthesized without water present and also shows high aluminum contents in the clinopyroxenes. However, when these clinopyroxenes are exposed to a hydrous melt, there is a substantial shift in their composition to lower aluminum contents. These experiments show clinopyroxenes with lower aluminum contents than any previous set of experiments at this pressure, including our own synthesis work, suggesting that the presence of water must be responsible for the change in clinopyroxene composition. Clinopyroxene aluminum contents have been proposed to be particularly important for the partitioning of a number of elements during melting due to coupled substitutions between trace elements and aluminum in the clinopyroxene structure (e.g., Blundy et al., 1998). Most notably, water itself has been proposed to enter the pyroxene structure by this mechanism (e.g., Aubaud et al., 2004; Hirschmann et al., 2009). Our experiments suggest that the presence of water in fact causes a decrease in the partition coefficient (= concentration in solid/concentration in liquid) for water during melting and therefore can produce hydrous melts with higher water contents than were previously expected.

A final set of results from these experiments is presented in Chapter 3, which discusses the measured partition coefficients between garnet and hydrous melts for iron and manganese. Anhydrous melting would only be expected to produce melts in the presence of significant quantities of garnet if the melting happened at particularly high temperatures (Robinson and Wood, 1998). Hydrous melts however are produced at greater pressures and lower temperatures than anhydrous melts, and thus could be produced in the garnet field. Manganese contents and the iron/manganese ratio of magmatic rocks have recently assumed a key role in a number of petrologic debates, as

new high-precision measurements of manganese contents have allowed for the quantification of small variations (e.g., Sobolev et al., 2007; Qin and Humayun, 2008). Our experiments show manganese to have a surprisingly large partition coefficient in garnet during hydrous melting, such that changing the modal abundance of garnet in a melting source by changes in composition or pressure could produce measurable changes in the iron/manganese ratio of the resulting melt. We explore the resulting liquid compositions for the partition coefficients we measure and compare them with the liquids produced via natural melting.

Part 2: Olivine abundances and compositions in Hawaiian lavas

The final chapter of this thesis moves from examination of the melting process to examining the details of the processes of crystallization and mixing within Hawaiian magma chambers. The main compositional difference seen in basalts produced from the main stage of activity at a Hawaiian volcano reflects the addition of significant quantities of olivine to a basaltic liquid (e.g., Wright, 1971). This olivine is formed by crystallization of liquids after they enter the volcano's plumbing system. The compositional variation between different Hawaiian units is caused by the entrainment of varying amounts of this olivine during eruption. Using data collected from a number of sources including the recent Hawaiian drill cores (e.g., Garcia et al., 2007; Haskins and Garcia, 2004; Quane et al., 2000) we have analyzed the amounts and compositions of olivines through time at the different volcanoes. Several trends seem apparent. Overall, Mauna Kea appears to erupt substantially more olivine than other volcanoes, while Kilauea appears to erupt less. Mauna Kea shows an increase in olivine output with time, which suggests changing eruptive conditions with time, possibly due to an elevated

overall magma flux compared with other Hawaiian volcanoes. Mauna Kea's olivines also show a surprising enrichment in calcium compared with other Hawaiian volcanoes, likely expressing the same phenomenon. Using calibrations developed in recent years (e.g., Toplis, 2005; Wang and Gaetani, 2008) for the composition of olivine produced by crystallizing a liquid of known composition, we have also mathematically reversed the process of olivine crystallization to calculate average parental liquids feeding the best-sampled Hawaiian volcanoes.

REFERENCES

Aubaud, C., Hauri, E. H., and Hirschmann, M. M. (2004) Hydrogen partition coefficients between nominally anhydrous minerals and basaltic melts. *Geophys. Res. Lett.* ***31***, *L20611*.

Blundy, J. D., Robinson, J. A. C., and Wood, B. J. (1998) Heavy REE are compatible in clinopyroxene on the spinel lherzolite solidus. *Earth Planet Sc. Lett.* **160**, 493-504.

Gaetani, G. A. and Grove, T. L. (1998) The influence of water on melting of mantle peridotite. *Contrib. Mineral. Petr.* **131**, 323-346.

Garcia, M. O., Haskins, E. H., Stolper, E. M., and Baker, M. (2007) Stratigraphy of the Hawai'i Scientific Drilling Project core (HSDP2): anatomy of a Hawaiian shield volcano. *Geochem. Geophys. Geosyst.* **8**.

Haskins, E. H. and Garcia, M. O. (2004) Scientific drilling reveals geochemical heterogeneity within the Ko'olau shield, Hawai'i. *Contrib. Mineral. Petr.*, 162-188.

Hirschmann, M. M., Tenner, T., Aubaud, C., and Withers, A. C. (2009) Dehydration melting of nominally anhydrous mantle: the primacy of partitioning. *Phys. Earth Planet In.* **176**, 54-68.

Kägi, R., Muntener, O., Ulmer, P., and Ottolini, L. (2005) Piston-cylinder experiments on H_2O undersaturated Fe-bearing systems: An experimental setup approaching $f(O_2)$ conditions of natural calc-alkaline magmas. *Am. Mineral.* **90**, 708-717.

Kawamoto, T. and Hirose, K. (1994) Au-Pd sample containers for melting experiments on iron and water bearing systems. *Eur. J. Mineral.* **6**, 381-385.

Kushiro, I. (1968) Compositions of magmas formed by partial melting of the Earth's upper mantle. *J. Geophys. Res.* **73**, 619-634.

Liu, X., O'Neill, H. S. C., and Berry, A. J. (2006) The effects of small amounts of H_2O, CO_2 and Na_2O on the partial melting of spinel lherzolite in the system CaO-MgO-Al_2O_3-SiO_2 +/- H_2O +/- CO_2 +/- Na_2O at 1.1 GPa. *J. Petrol.* **47**, 409-434.

Longhi, J. (2002) Some phase equilibrium systematics of lherzolite melting: I. *Geochem. Geophys. Geosyst.* **3**, 1020.

Putirka, K., Johnson, M., Kinzler, R., Longhi, J., and Walker, D. (1996) Thermobarometry of mafic igneous rocks based on clinopyroxene-liquid equilibria, 0–30 kbar. *Contrib. Mineral. Petr.* **123**, 92-108.

Qin, L. and Humayun, M. (2008) The Fe/Mn ratio in MORB and OIB determined by ICP-MS. *Geochim. Cosmochim. Ac.* **72**, 1660-1677.

Quane, S. L., Garcia, M. O., Guillou, H., and Hulsebosch, T. P. (2000) Magmatic history of the east rift zone of Kilauea Volcano, Hawai'i, based on drill core SOH-1. *J. Volcanol. Geoth. Res.* **102**, 319-388.

Robinson, J. A. C. and Wood, B. J. (1998) The depth of the spinel to garnet transition at the peridotite solidus. *Earth Planet Sc. Lett.* **164**, 277-284.

Sobolev, A. V., Hofmann, A. W., Kuzmin, D. V., Yaxley, G. M., Arndt, N. T., Chung, S.-L., Danyushevsky, L. V., Elliott, T., Frey, F. A., Garcia, M. O., Gurenko, A. A., Kamenetsky, V. S., Kerr, A. C., Krivolutskaya, N. A., Matvienkov, V. V., Nikogosian, I. K., Rocholl, A., Sigurdsson, I. A., Sushchevskaya, N. M., and Teklay, M. (2007) The amount of recycled crust in sources of mantle-derived melts. *Science* **316**, 412-417.

Toplis, M. J. (2005) The thermodynamics of iron and magnesium partitioning between olivine and liquid: criteria for assessing and predicting equilibrium in natural and experimental systems. *Contrib. Mineral. Petr.* **149**, 22-39.

Walter, M. J. (1998) Melting of garnet peridotite and the origin of komatiite and depleted lithosphere. *J. Petrol.* **39**, 29-60.

Wang, Z. and Gaetani, G. A. (2008) Partitioning of Ni between olivine and siliceous eclogite partial melt: experimental constraints on the mantle source of Hawaiian basalts. *Contrib. Mineral. Petr.* **156**, 661-678.

Wright, T. L. (1971) Chemistry of Kilauea and Mauna Loa lava in space and time. *U.S. Geological Survey Professional Paper* **735**, 1-40.

HYDROUS, LOW-CARBON MELTING OF GARNET PERIDOTITE

By

J. Brian Balta

Paul D. Asimow

Jed L. Mosenfelder

ABSTRACT

The presence of volatile species in Earth's upper mantle drives the formation of low-degree melts at pressures and temperatures where volatile-free mantle rocks would be subsolidus. The two most abundant volatile species, given the oxidation state of the Earth's upper mantle, are carbon dioxide and water. Understanding the influence of these species, separately and together, on melting processes requires well-controlled data on pure volatile systems as well as mixed-volatile experiments at the conditions of interest where these species have the most influence. We present experimental melting results from 3 GPa and 1375°C on hydrous systems with controlled water contents and rigorously minimized carbon contamination in order to analyze the effect of water on the melting of fertile peridotite KLB-1 in the garnet field. Compared to anhydrous experiments at this pressure, the addition of water to the peridotite produces a melt with an increased SiO_2 content relative to MgO and FeO. This effect is tantamount to an increase in the stability of olivine at the solidus relative to the other crystalline phases. There is also a substantial change in the composition of clinopyroxene in equilibrium with the melt; the clinopyroxene field contracts when water is added to the system, producing clinopyroxenes with higher CaO than typically found at these pressures. The contraction of the clinopyroxene field decreases the bulk partition coefficients of TiO_2 and Na_2O, which are less compatible in a hydrous system than an anhydrous system. We present an analysis of the remaining oxides and their behavior during hydrous melting, and compare our liquid composition to anhydrous experiments and modeled liquid compositions at similar pressures. The contraction of the clinopyroxene field during hydrous melting has important implications for melting of the mantle, including possibly

decreasing the bulk partition coefficient for water during melting and pushing the initiation of hydrous melting deeper into the garnet field.

1. INTRODUCTION

Water plays a fundamental role in the melting of Earth's mantle. Water strongly interacts with other components in non-ideal silicate melt solutions and therefore has direct effects on melt chemistry in equilibrium with residual solids. Furthermore, the presence of a volatile species, such as water, in upwelling mantle will allow a source rock to melt at higher pressures and lower temperatures than the same rock would if it were volatile-free, implying an indirect effect due to melting under different conditions and in the presence of different mineral assemblages and compositions. The direct and indirect effects together can significantly modify the composition of liquids generated in the mantle, and understanding the effects of water on the melting of the Earth's mantle therefore requires experiments on natural compositions (or close analogs) across the substantial range of temperatures, pressures, and compositions accessible to modern melting regimes.

Pioneering early work on hydrous melting of mantle-like compositions was conducted by Kushiro and co-workers, on simplified systems such as enstatite-H_2O (Kushiro et al., 1968), forsterite-enstatite-diopside-H_2O (Kushiro, 1969), and forsterite-diopsite-silica-H_2O (Kushiro, 1972). One important result of these simplified melting experiments is that the presence of dissolved water in a silicate melt in equilibrium with solids tends to drive the melt to higher silica contents. This is explained by the reaction between water and bridging oxygens in the tetrahedral silicate network, which depolymerizes the liquid and lowers the activity coefficient of silica (Mysen et al., 1980).

Moving past simple systems, a full accounting for the effect of water on the melting column must involve hydrous experiments on more complex systems, including

those without a free vapor phase where the activity of water is not fixed (as occurs in the mantle). Liu et al. (2006) produced experiments on hydrous liquid compositions in equilibrium with a simplified spinel lherzolite at 1.2 GPa pressure. Gaetani and Grove (1998) produced experiments on hydrous basaltic liquids in equilibrium with synthetic lherzolite and harzburgite lithologies at pressures from 1.2 to 2 GPa. Falloon and Danyushevsky (2000) and Parman and Grove (2004) also produced hydrous melts in equilibrium with harzburgite lithologies from 1.5 to 2.5 and 1.5 to 2.2 GPa, respectively.

While these experiments provide valuable information about the effect of water on melting, there are several differences between them and the style of hydrous melting likely to occur under mid-ocean ridges. First, under a mid-ocean ridge, water is expected to flux a low-degree melt at greater depths than are sampled by these experiments (Asimow and Langmuir, 2003) if the peridotite contains a few hundred ppm water by weight. These depths are typically expected to be in the garnet field (Asimow et al., 2004), and thus the solid mineralogy and likely the partitioning of a number of elements will be significantly different from that measured at lower pressures. Second, experiments conducted on analogue systems or in equilibrium with harzburgitic lithologies may also show compositions and partitioning significantly different from those in equilibrium with more fertile lherzolites. As hydrous melting is likely to produce only low degree melts, it is unlikely that their production would be able to deplete the solid residue enough to produce a harzburgite; higher degrees of melting at lower pressures would be required (e.g., Asimow, 1999; Kelemen et al., 1992). Finally, as noted by Liu et al. (2006), a common concern with hydrous melting experiments at any condition has been infiltration of carbon into experimental charges. As carbonate and

water can have a strong mutual interaction in a silicate melt phase, the presence of variable amounts of carbon entering a hydrous melt will affect the activity of water and potentially that of other reactive species in the liquid.

The production of melt within the garnet field under mid-ocean ridges in particular has been a longstanding issue. Trace element and isotopic characteristics of mid-ocean ridge basalt (MORB) have been interpreted to suggest that garnet is necessary as a residual phase in the melting zone (e.g., Salters and Hart, 1989; Shen and Forsyth 1995). However, this constraint is at odds with a number of other indicators which suggest that high temperatures and very high degrees of melting would be required to melt peridotite in the garnet field (Iwamori et al., 1995; Robinson and Wood, 1998), and measurements that suggest that the garnet signature is strongest in MORB representing lower total degrees of melting. Other solutions have been proposed to resolve this controversy, such as melting of distinct pyroxenites in the MORB source (Hirschmann and Stolper, 1996), elevated pressures of melting (Shen and Forsyth, 1995), or increased compatibility of rare earth elements in aluminous clinopyroxene (cpx) at high pressures (Blundy et al., 1998). Each of these proposed explanations for the garnet signature has potential complications. Pertermann and Hirschmann (2003b) examined experimental melting of pyroxenite bodies and found that they could not make up more than 2% of the MORB source region based on the differences in chemistry. The Shen and Forsyth model requires melting to stop at depths much greater than would be expected by melting models (e.g., Asimow et al., 1999), implies a correlation between crustal thickness and spreading rate which is not observed (White et al., 1992), and is inconsistent with other aspects of the major element chemistry (Kinzler, 1997). The partition coefficients (D =

concentration of species in solid/concentration of species in liquid) of Blundy et al. (1998) differ from those of other authors (e.g., Salters and Longhi, 1999) and require highly aluminous cpx that may not exist under certain circumstances (see below). As hydrous melting likely takes place in the garnet field and is expected to produce low degree melts, experiments on the chemistry of hydrous melting under typical mid-ocean ridge conditions may provide an alternative explanation for the garnet signature, and therefore investigation of melting under these conditions is necessary.

We have designed and conducted experiments with these issues in mind to illustrate the effects of limited quantities of water on the melting of fertile peridotite under low-carbon, garnet facies conditions. These experiments show first that the effect of water on the overall liquid composition is similar to that found by Gaetani and Grove (1998) on carbon-containing, lower pressure samples; the presence of water serves to decrease the ratio of (MgO + FeO)/SiO_2 and thus increases the SiO_2 content of the liquid if considered on a volatile-free basis. Second, we show that the presence of carbon, even at low concentrations, interacts with water in the liquid and may serve to counteract some of the effect of the presence of water. Third, we find that the interaction of hydrous melts with the fertile peridotite mineralogy has significant and unexpected effects on the modal abundance and composition of cpx during melting, and these effects are potentially very important for the partitioning of a large number of components of silicate melts. One specific consequence of the presence of garnet on the minor element makeup of silicate melts is detailed in Chapter 3 of this thesis.

2. METHODS

2.1 General approach

Producing equilibrium, low-degree melts has historically been a difficult problem for experimental petrology, as it is much easier to sample and analyze high-degree melts. Two general categories of methods have been explored that should be noted here: extraction methods and so-called sandwich methods. A number of authors have employed techniques based on the maintenance of open pore space or highly wetting surfaces towards which low-degree melts can segregate during experiments. Kushiro and Hirose (1992), Johnson and Kushiro (1992), Hirose and Kushiro (1993), Baker and Stolper (1994), and Baker et al. (1995) employed a diamond-aggregate technique, where pore space between diamond crystals was used to trap the initial melts extracted during melting. The intent of these experiments is for the rapidly extracted melt to diffusively equilibrate with interstitial melt in the solid pile and then to form an unmodified glass upon quenching because of its distance from nucleation sites for quench crystals. Later extraction techniques include crimped capsule or foil layers (Holloway and Kawamoto, 1997) or vitreous carbon spheres (Schwab and Johnston, 2001, Wasylenki et al., 2003, and Pertermann and Hirschmann, 2003a). For our experiments, the diamond aggregate technique would be inappropriate, as the presence of diamond or vitreous carbon would provide an immediate potential source of carbon if there were any reaction with oxygen in the sample, and vitreous carbon spheres are known to take up water on their own (Wasylenki et al., 2003). The presence of carbon-rich phases would also make accurate determinations of dissolved carbon contents difficult (Pertermann and Hirschmann, 2003a).

"Sandwich" experiments, as a general class, attempt to produce large, analyzable pools of low-degree melts that escape quench modification by reacting a melt of a

composition close to the predicted low-degree melt composition with solids until the liquid becomes multiply-saturated with the solids (Stolper, 1980, Takahashi and Kushiro 1983). Several ideas have been proposed to attempt to improve upon this technique. One difficulty is that the solid compositions tend to change as they react with the liquids, producing solids and liquids that are in equilibrium with each other, but which are not necessarily representative of the mantle. Wallace and Green (1988) and Robinson et al. (1998) proposed one solution: adding an iterative procedure, where each successive liquid is synthesized based on the composition measured in the previous experiment until the liquid and solid compositions no longer evolve during the run. This improves on the multiple-saturation technique by making the solid compositions more representative of the mantle. But, as our experiments will demonstrate, the high variance of natural peridotite equilibria imply non-uniqueness, namely that a range of solid and liquid compositions can be in equilibrium at the same conditions, all of which may satisfy a mass balance constraint and thus appear to be plausible equilibrium states of a given source composition. Furthermore, in the case of highly compatible or highly incompatible elements, it is possible that the liquid and solid compositions can be trapped in metastable local minima or in situations where many, many iterations are required to approach equilibrium. Hirschmann and Dasgupta (2006) proposed an approach to converge on the liquid composition at the solidus: measuring the solid/melt partition coefficients and calculating the next iterative liquid using the batch melting equation evaluated in the limit of zero melt fraction. This technique also has potential complications. First, highly-incompatible or highly-compatible elements may have partition coefficients that cannot be accurately measured due to low concentration in one phase. Second, calculating the

bulk partition coefficients requires accurate knowledge of the modal abundance of the solid phases, which may be difficult to estimate. Finally, this technique does not guarantee that the oxides will sum to 100% after its application, and therefore requires a choice to either exclude a closure component from the calculation or to renormalize the calculated solidus liquid composition, neither of which is an optimal approach.

For our experiments, we use a hybrid of the regular and modified iterative sandwich techniques. We set up the experiments in the conventional iterative sandwich format, reacting a hydrous liquid with solid garnet peridotite. At each step, we measure mineral/melt partition coefficients, calculate bulk partition coefficients, and use the modified iterative sandwich technique to calculate the concentrations of most of the oxides in the next candidate liquid. For very incompatible or very compatible elements and for elements such as SiO_2, where the forecasting method is unstable or compromised by closure, we will simply use the conventional sandwich technique and adopt the measured concentration in the melt as the concentration for the next candidate liquid. We use modal abundances calculated by least-squares solution of the mass balance constraint whereby the bulk peridotite composition must be a linear combination of the measured mineral compositions. We also consider the effect that shifts in the modal abundance of the solid phases would have on the bulk partition coefficients to estimate a reasonable range of possible natural compositions that could represent solidus melt compositions.

Assessing convergence of the iterative process is a difficult task, because the Gibbs phase rule suggests that the liquid in equilibrium with three solid phases at fixed temperature and pressure will still have multiple degrees of freedom in a natural system of >10 components, including the volatiles and the minor elements. Furthermore, the

partitioning of several elements may be determined by the particular liquid composition, especially if they interact strongly with the volatiles. Our approach is therefore to synthesize a liquid that is within the range of compositions that will be multiply saturated with the KLB-1 assemblage under these pressure and temperature conditions. Then, we will perform repeat experiments varying parameters such as the ratio of solid to liquid and the total water content to define the range of accessible liquid compositions and to attempt to constrain how the liquid composition changes with the parameters that we can adjust.

2.1.1 Solid preparation

A major concern for these experiments was the initial state of the solids added during each run. The equilibrium we want to observe is hydrous liquid with fertile garnet peridotite. Most of the commonly available natural fertile peridotites, however, are spinel or plagioclase peridotites due to reaction at low pressures during their ascent. If a spinel peridotite were mixed with a hydrous liquid under pressures where garnet is the stable aluminous phase, the sample could easily move away from the true equilibrium due to multiple ongoing reactions. For example, the melt might rapidly equilibrate with a slowly evolving population of pyroxenes as their modes and composition change due to the spinel to garnet reaction. It was therefore judged to be important to begin these experiments with a peridotite that was already stably equilibrated within the garnet field. This step will also be useful in providing a peridotite produced under the same pressure and similar temperature to our melting experiments for comparison of solid compositions.

To produce this peridotite, we took a sample of natural KLB-1 peridotite powder of variable grain size (kindly supplied by C. Herzberg, from the same powder as the

original KLB-1 of E. Takahashi) and ground it along with less than 1% by weight of a magnesian garnet from Arizona (supplied by G.R. Rossman, composition given in table 1). This garnet was added to give seed grains, reducing the needed reaction time by avoiding nucleation problems. The mixture was ground for several hours in an alumina mortar and pestle to reduce the maximum grain size from ~100 μm to ~1 μm or below. This grain size was required to allow for sub-solidus recrystallization on the timescales of these experiments. The powder was dried and loaded into a combined molybdenum/gold/palladium/iron capsule. The capsule was prepared by submersing a 3 mm outer diameter (o.d.) Au_{75}/Pd_{25} capsule in Kilauea 1919 basalt at 1190 °C for 48 hours under a controlled H_2-CO_2 gas stream with an fO_2 set at 1.6 log units below the QFM buffer, following the technique outlined in Chapter 4. This produced a capsule with ~4% dissolved Fe. The presence of Fe tended to make the capsule more brittle and likely to tear when compressed, so this capsule was hammered into a molybdenum sheath to prevent tearing. The sheath was made by drilling a 3 mm. hole into a 4 mm o.d. molybdenum rod, with a 1 mm thick lid cut from the same stock and used to cover the capsule during the high-pressure experiment. The powder was packed into the capsule, and the full capsule was heated to 1000 °C under a H_2-CO_2 gas stream with an fO_2 set 2 log units below the QFM buffer, within the range of predicted mantle values. This step was necessary to devolatilize the peridotite, and the gas stream was used to prevent oxidation of the sample during heating. The capsule was then removed from the furnace and kept at 300 °C until the gold-palladium capsule was welded shut. The molybdenum lid was placed on top of the capsule loosely during loading and welded itself to the remainder of the capsule upon compression.

All of our experiments were conducted at a nominal pressure of 3 GPa in a ½" piston-cylinder device. The cell was composed of an outer sheath of calcium fluoride as pressure medium, a straight-walled graphite heating element, and crushable MgO spacers to center the capsule in the hot spot. Temperature was monitored during the run using a $W_5Re_{95}/W_{26}Re_{74}$ thermocouple (type C), with no pressure correction on the E.M.F., and recorded temperature fluctuations were typically 2 °C or less. Experiments were first placed at pressure and allowed to sit for a period of at least an hour to allow for compaction before heating; this technique seems to help provide a seal against volatile loss or gain during heating of the run. No correction was applied to the pressure to account for friction. Previous calibration work on this press suggests that the nominal 3 GPa pressure may require a negative correction of up to 0.2 GPa (Mosenfelder et al., 2006). However, the calibration work was done at much lower temperatures and this misfit may decrease with increased temperature due to decreasing friction. Consequently, we estimate that all experiments here were performed at an identical pressure in the range of 2.8-3.0 GPa, pending refinement by further calibration work. The recrystallization runs were held at a measured temperature of 1350 °C and (nominally) 3 GPa for a period of at least 336 hours. The experimental temperature should be below the dry solidus of KLB-1 (Herzberg et al., 2000) and samples did not melt unless the capsule failed. The run times were long enough to homogenize the sample to the level measured by electron microprobe in all major and measured trace elements (Figure 1) except for NiO, which declines significantly near the edge of the sample due to Ni loss to the capsule. Temperature gradients within the capsule are possible and have not been calibrated, but

the homogeneity of the final samples suggests that they are limited to <20°C in both the sub-solidus and the melting experiments.

2.1.2. Liquid preparation

The hydrous liquid in these experiments was synthesized from laboratory grade oxides and carbonates. The initial seed liquid for the iteration was the calculated solidus liquid with 1 wt. % H_2O from KLB-1 peridotite at 3 GPa according to the pHMELTS algorithm (Smith and Asimow, 2005). Further liquids were synthesized based on the resulting liquid compositions. The mix was initially made with a deficit of Al_2O_3 since H_2O would be later added in the form of gibbsite ($Al(OH)_3$). Oxides and carbonate reagents were first dried individually, mixed by weight, ground under ethanol for >8 hours, and step-heated to 800 °C in air to decarbonate the mixture. The mixture was then placed at 1000 °C for ~12 hours at fO_2 10^{-13} bars to convert most of the iron into Fe^{2+}. The mixture was then heated in a platinum crucible above 1450°C in an H_2-CO_2 gas stream with fO_2 2 log units below the QFM buffer, for 1 hour. The crucible was previously iron-preconditioned using the technique of Kessel et al. (2001) to avoid iron-loss to it. Na_2O is expected to be the most volatile element during this procedure (e.g., Tsuchiyama et al., 1981) and no significant Na_2O loss was observed during sample preparation. The liquid was quenched to a glass by immersing the crucible in water. The glass was then broken apart and re-ground for 4 hours along with powdered gibbsite as a water source, with the amount calculated to make up for the missing Al_2O_3 and to give several wt. % H_2O. Gibbsite was used because we were able to verify by mass spectrometry that the gibbsite was carbon-free; other water-containing minerals, such as

brucite, were found to be carbon-contaminated and could not be used for controlled-carbon experiments.

2.1.3. Capsule design

Our capsule design was key to meeting our experimental goals of maintaining hydrous samples while avoiding carbon infiltration or other changes in parameters such as fO_2 that could affect the equilibrium liquid composition. We adapted the double-capsule design proposed by Kägi et al. (2005), which was originally used as a means of controlling fO_2 in hydrous experiments. The capsule was constructed by loading a 1.6 mm. o.d. iron-preconditioned $Au_{75}Pd_{25}$ inner capsule with a mixture of roughly equal proportions of the recrystallized garnet peridotite (see above) and a powdered hydrous glass (see above). After welding (see below), this inner capsule was loaded along with more of the same powdered hydrous glass and extra liquid water into an outer capsule made from a larger iron-preconditioned 3.8 mm o.d. Pt tube (Figure 2). The extra water was loaded by microsyringe because the diffusion of hydrogen through platinum is faster than through $Au_{75}Pd_{25}$ (Chou, 1986). Both the outer and inner capsule were arc welded shut with the cold end immersed in a bath of liquid nitrogen to avoid excessive dehydration during welding, which was a major issue for the smaller capsules. The inner capsule was Fe-preconditioned using the calibration of Chapter 4 of this thesis, and the outer capsule was Fe-preconditioned using the calibration of Kessel et al. (2001). The outer capsule contained up to 20 times more glass than the inner capsule and was intended to serve as a large reservoir to slow the diffusion of carbon into the sample from the exterior. The likely source of carbon contamination is the graphite heating element

used in the cell. In addition to buffering the water content and oxygen fugacity, this technique was found to effectively slow diffusion of carbon into the inner capsule.

2.1.4. Melting experiments

Melting experiments were run using the same piston-cylinder protocol as described above for the subsolidus recrystallization experiments except for temperature and time. Melting was conducted at 1375 °C for periods from 6 to 20 hours. Quenching hydrous basaltic glasses from 3GPa has historically been a challenge. Our experiments were quenched by shutting off the power; this achieved quench from the run temperature to < 200 °C in under 10 seconds. Coincident with the time of quenching, we dropped the pressure by releasing the oil pressure in the master ram cylinder. This technique was similar to that employed by Putirka et al. **(**1996), but we did not drop the pressure as aggressively prior to quenching because the melting point of $Au_{75}Pd_{25}$ alloys is close to the experimental temperature and too large a pressure drop could have caused the capsules to cross their melting point by decompression. Obvious vesiculation on quench was not observed.

2.2. Analytical techniques

Capsules were sectioned using a K.D. Unipress type WS-22 wire saw, with a cut down the centerline to hopefully cross the inner capsule. One half of the capsule was mounted in and vacuum-impregnated with epoxy, polished using alumina and diamond grits, and carbon coated for analysis by electron microprobe and scanning electron microscope. Quantitative analyses were conducted using the JEOL JXA-8200 electron microprobe at the California Institute of Technology in wavelength dispersive mode. Liquid compositions were measured using a current of 10 nA and a spot size of 15-20

μm, with 20 seconds counted on-peak and 10 seconds counted off-peak. Sodium and potassium were counted first to minimize loss of volatile elements. Lower current analyses were also performed to confirm that sodium and potassium were not being lost. Solids were analyzed using a focused beam, a current of 30-40 nA, and identical counting times.

Volatile contents in the glasses were measured using a Nicolet Magna 860 FTIR spectrometer coupled to a Spectra-Tech Continuum microscope. Spectra were obtained on doubly-polished sections of the experiments from 1000 to 6000 cm^{-1} using unpolarized light, a KBr beamsplitter, and an MCT-A detector. Sample thickness and flatness were checked using a digital micrometer close to the analyzed spots, and wedging was typically limited to a few micrometers. We used rectangular apertures greater than 30 μm in the short direction and attempted to avoid contamination by solid phases, cracks, and edges. Multiple spots were checked on several samples to establish homogeneity of volatile contents (typically better than 10% across single runs). Water contents were calculated from absorbances based on the composition-dependent calibration of Ohlhorst et al. (2001) and electron probe analyses of the major-element glass composition. Slight extrapolation was required, as the lowest SiO_2 content used in the calibration was 50%, while our liquids have slightly lower total SiO_2. Carbonate contents were calculated using the calibration of Fine and Stolper (1986). Glass densities were calculated using the iterative technique of Aubaud et al. (2007), although their calibration does not include carbonate. Linear background corrections and a manual subtraction procedure were used, potentially giving small additional errors on each analysis.

Overall, we estimate the relative error on the volatile content calculations to be ~10% based on the repeat analyses of individual samples (1σ), which is sufficient for the purposes of this study. The largest sources of error are measurement of the sample thickness at the site of analysis and the exact absorbance calibration. Typically, for the measured water contents, the absolute error is about ± 0.5% H_2O. This error is of similar magnitude to the error on the calibration for the absorbance peaks used. Reduced errors on similar analyses are likely possible in the future, but would require a more detailed understanding of the relationship between the multiple peaks near 4500 cm^{-1} (see below) and the total water content, and calibration of absorption coefficients across a wider range of silicate liquid compositions including picritic basalts and basalts with variable amounts of carbonate.

To confirm the calibration, we analyzed several samples at different thicknesses, allowing us to calculate water contents based on the OH^- vibration peak at ~3600 cm^{-1} and by a combination of the H_2O and OH^- vibration peaks at ~5200 and ~4500 cm^{-1}. The errors on the 3600 cm^{-1} peak are estimated to be much smaller and do not require significant recalibration for the liquid composition; for this peak, we used the absorption coefficient of Dixon et al. (1995). For the overtone peaks, sample thicknesses of >100 μm were commonly used, while sample thicknesses <50 μm were necessary to bring the 3600 cm^{-1} peak on scale. These repeat measurements at different thicknesses and typically on different spots produced total water contents on individual samples that were within 2% of each other, significantly less than the estimated analytical error.

2.2.1. MELTS Calculations:

For comparison with our experimental liquid composition, we produced several calculated hydrous, low-degree silicate melt compositions using pHMELTS (Smith and Asimow, 2005). The calculations were done two ways (a sort of numerical reversal experiment), to ensure that the algorithm was not being caught in local minima. We used the solid KLB-1 composition, edited to improve the calculation by avoiding elements that the algorithm does not treat well (no potassium or manganese) and calculated the equilibrium melt composition at 3GPa and 1375°C, beginning with excess water. We then decreased the available water content towards zero until the melt composition did not change significantly at each step. Next we started the calculation subsolidus and found the initial melt composition during heating, varying the water content until the solidus was reached at 1375°C. These two calculations produced similar liquid compositions, although they required slightly different bulk water contents.

3. RESULTS

3.1. Recrystallization experiments

We have reproduced several nearly-identical sub-solidus peridotites from our KLB-1 starting mix showing no obvious evidence for zonation other than in NiO (Figure 1), which can be interpreted as evidence for close approach to equilibrium (Parman and Grove, 2004). The texture appeared to show additional evidence of equilibrium, with subhedral to euhedral grain shapes and developed triple grain junctions. The peridotites consisted of mixtures of olivine, cpx, and garnet. No orthopyroxene (opx) was observed in any experiment, as was predicted for the KLB-1 composition by Longhi (2002). Final mineral grain sizes were between 5 and 20 μm for all minerals. Average mineral compositions are reported in Table 1. Olivine Mg#'s (= 100 * molar MgO/[MgO+FeO])

averaged 89.8, consistent with fertile upper mantle and suggesting limited iron loss to the capsule. Using the bulk KLB-1 composition given by Davis et al. (2009) and our measured mineral compositions, we estimated modal abundances by least-squares mass balance; there was typically a slight residual on CaO (which could reflect contamination of the sample by natural caliche). Mineral compositions and calculated modal abundances are given in Table 1.

3.2. Hydrous melting experiments.

All reported experiments produced a hydrous, low-carbon basaltic glass in equilibrium with solid garnet, cpx, and olivine (Figure 3). Opx was only observed in the initial experimental step which started with a higher silica liquid composition; none was observed in equilibrium with the final estimated solidus liquid composition, consistent with the lack of opx in the solid KLB-1. A single opx composition from an early iteration is reported in Table 1 for comparison to opx measured by others in anhydrous experiments. The double-capsule technique was successful at limiting carbon diffusion when the inner capsule remained intact. A number of times, however, the inner capsule was either partially dehydrated or failed during the run and contained limited hydrous silicate glass that was typically highly quench-modified due to the abundance of surfaces for nucleation. However, in such experiments, the volume of the outer capsule was often still sufficient to produce a low-carbon, hydrous, silicate glass that had reacted and equilibrated with the solid assemblage; in these runs the large volume was sufficient to accomplish the major experimental goals of hydrated liquids with limited carbon contamination. Hence, they were sometimes used as iteration steps to predict subsequent

liquid compositions. Measured carbon contents were a factor of 5-10 lower than those reported by Gaetani and Grove (1998) (Figure 4).

Experiments contained large amounts of measurable silicate glass (Figure 3), in pools up to ~500 μm in diameter. Basalts wetted most crystal surfaces, giving opportunity for full reaction of the liquid with the solids. Solids always sank to the bottom of each capsule regardless of loading configuration. Samples did show substantial modification on quench. Virtually all solid grains showed an iron-rich quench rim 1-3 μm thick that was avoided during probe analysis except in a few samples where the cpx grains were too small to analyze without contamination; no other zonation was commonly observed in the crystals. Interstitial liquid occasionally formed quench needles, and was always depleted in MgO and FeO compared to the large melt pool. Elongate quench needles were common at the boundary between solids and liquids. The boundary between the capsule walls and the liquid pool commonly showed quench crystallization of 10 to 100 μm of pargasitic amphibole of a composition close to the unmodified glass. In all cases, these quench features were avoided for analyses. Large pools of homogeneous glass were still available despite these quench features. In some samples, 100 nm-scale phases were observed visually within the glass pools, presumably also occurring on quench. However, these phases were much smaller than the activation volume of the electron probe or the wavelength of the infrared radiation, and no obvious change was observed in compositions between areas with and without those phases, although the quench phases may have slightly affected the Fe/Mg ratio and thus the calculated K_D for some experiments. Still, the assumption of homogeneous glass is very likely adequate even in those cases.

Establishment of equilibrium in this variety of experiment is difficult, as an appropriate reversal experiment test has not been devised. Several techniques suggest that these experiments either achieved liquid/solid equilibrium or were very close. First, measured values of the olivine liquid K_D parameter were between 0.32 and 0.40 and most consistently near 0.35-0.36. The calibration of Toplis (2005) predicts a K_D value of ~0.36 at these liquid compositions, with K_D increasing as H_2O content decreases. Our measured K_D values are consistent with the K_D values reported by Gaetani and Grove (1998) on their hydrous experiments from lower temperatures and pressures, and are generally within the range deemed acceptable by Toplis (2005). Two samples have high K_D values (0.38 and 0.40), potentially reflecting either disequilibrium between the liquid and the solids due to Fe loss to the capsules or slight changes in the Fe-Mg distribution on quench. However, the overall difference in liquid composition appears small and confined to the Fe-Mg system, which will be treated together, and therefore the data for these experiments are still included here. These two samples would require a loss of less than 10% of the available Fe in the liquid to the capsule to be consistent with the other measured K_D values.

Iron contents were variable between successive experiments due to the initial condition of the liquid and the capsule. The initial guess composition was higher in Fe than the final composition, and therefore the initial capsules were prepared with higher Fe than necessary. For the initial experiments, the capsules buffered the iron content at a higher level than predicted; this produced olivines with Mg# 86-87 and liquids with lower MgO contents than would be expected in actual mantle liquids. Capsules were then resynthesized with less Fe to equilibrate with a lower-iron liquid composition; these

liquids equilibrated with Mg# 88-90 olivine, close to the expected mantle value. Measured liquid and solid compositions are given in Table 2.

Additional evidence that these samples either represent equilibrium assemblages or at least close approaches to equilibrium comes from a number of sources. Typically, Fe-Mg zoning, which would be commonly expected in the case of significant Fe loss or gain, is easily seen in electron microprobe transects across single grains or visually, using back-scattered electron imagery (BSE). In our experiments, zoning is typically only barely visible in BSE imaging (Figure 3), and measurements of solid compositions from cores and rims of grains are typically indistinguishable if obvious quench features are avoided. A lack of clear zoning has been taken previously as evidence for close approach to equilibrium (Parman and Grove, 2004). If these experiments were far from equilibrium, significant zoning would be expected as the solid compositions shift substantially during the run (see below). Additionally, experiments were run for different durations from 6-20 hours, and there was no correlation between zoning and experiment duration, suggesting that much of the reaction is rapid relative to the timescales of the experiment. Finally, as nickel was found to be compatible in our capsules, measuring grains with significant nickel contents would suggest a lack of equilibrium, and this was not observed at the level of the errors on the electron microprobe analyses (Table 2). While these experimental timescales are short compared to those run by others (e.g., Parman and Grove, 2004, Walter, 1998) the small grain sizes and high water contents likely allowed fast reaction between the solid and liquid assemblages, allowing for a close approach to equilibrium on the timescale of these experiments.

Volatile compositions were measured on the glasses via FTIR. Measured volatile compositions combined with electron probe totals typically gave totals that were 98% or better. Mismatch decreased in the samples with lower measured water contents. Typical water-containing glass spectra are displayed in Figure 5. Significant and unexpected structure was observed in the IR spectra. We report the first analyses of water-containing glasses that show the 4500 cm^{-1} peak split into multiple peaks, typically a triplet, rather than a single peak. In more evolved basaltic liquids, a single peak near 4500 cm^{-1} is common, and a small shoulder is occasionally observed (Sally Newman, personal communication, 2009). In our experiments, observation of multiple peaks near 4500 cm^{-1} was common. In many minerals, this region of the IR spectrum shows complexity due to bonding between the OH^- groups and other structural elements in the mineral (e.g., Bishop et al., 2002). Our composition differs from previously analyzed basalts in several ways that could be related to the peak-splitting. Typical basalts that have been measured before were often lower in total MgO than these basalts (Dixon et al., 1995); our liquids have much higher total MgO and FeO than fractionated MORB, for example. It is also possible that the strong interaction of carbonate and water at high pressures could produce changes in the IR spectra. We hypothesize that the normal 4500 cm^{-1} peak splits into multiple peaks in our experiments because of interactions between the Si-O-H groups and other components in the melt. Specifically, our experiments have much higher MgO contents and possibly CO_3^{2-} contents than most natural erupted basalts due to the fractional crystallization and degassing processes that affect natural liquids prior to eruption, and these interactions may be the cause of these additional peaks.

Interaction was possibly observed between the water and carbonate groups in the liquid. At low carbon contents, the 4500 cm^{-1} peak was a similar thickness-normalized height in multiple experiments. At higher carbonate concentrations, the 4500 cm^{-1} peak was observed to increase in size (Figure 6). This interaction suggests that the carbonate is serving to create additional bridging oxygens that can be separated by reaction with water to give additional hydroxyl groups, and this carbonate interaction is a potential explanation for the splitting of the IR peaks. The lowest water-content sample, R380, falls off this trend. This sample could fall away from the trend if it is not fully saturated in OH^- because of its lower water content. Dixon and Stolper (1995) showed that it took significant total water contents, typically ~4% H_2O, to fully saturate a basaltic liquid in OH^-. The remaining liquids have higher water contents, may thus be much closer to saturated in OH^-, and may better demonstrate the interaction between the water and carbonate species.

4. DISCUSSION

Previous experimental and theoretical work allows for the evaluation of our liquid and solid compositions via comparison with anhydrous liquids from these pressures, hydrous liquids from lower pressures, and calculated liquid compositions. Anhydrous experiments from 3-7 GPa on fertile peridotites were conducted by Walter (1998) and have served as the basis for analysis of melting at these pressures by a number of workers (e.g., Humayun et al., 2004; Herzberg, 2006). Longhi (2002) produced anhydrous melting experiments from 2.4-3.4 GPa with similar compositions to those reported by Walter (1998), used those experiments as the basis for creating the empirical BATCH calculator, and applied the calculation to anhydrous peridotite melting under similar conditions.

Gaetani and Grove (1998) produced hydrous, carbon-containing liquids at lower pressures, from 1.2 to 2 GPa. All these experiments and the calculated liquid composition from pHMELTS will be used to place our results in context. Following the approach of Gaetani and Grove (1998), we will analyze these liquids both on a renormalized volatile-free basis, to allow for direct comparison with volatile-free melting experiments, and on a hydrous basis to attempt to better constrain the underlying thermodynamics, and partitioning. An average composition, based on our experiments, that should be in equilibrium with Mg#~89 olivine is given in Table 3, presented both on a hydrous, low-carbon basis and on a volatile-free basis, normalized to 100% total. Also given are liquids from the closest temperature and pressure conditions available from the other four studies mentioned above. The pHMELTS algorithm calculates a liquid that is vastly over-enriched in Na_2O, as discussed later. This necessitates care when using individual oxide compositions from those calculations to make inferences; ratios of one oxide to another and normative mineral components will be considered as, in many cases, these quantities are more robust (except those involving Na_2O). Volatile-free liquid compositions are displayed graphically in Figure 7 for comparison.

4.1. MgO, FeO, SiO_2

The effect of the addition of H_2O on the MgO + FeO and SiO_2 contents of silicate melts has been a major source of controversy since it was originally proposed that direct hydrous melting of peridotite was a method of producing high-silica, andesitic melts from the mantle (e.g., Kushiro, 1972). In their peridotite melting experiments, Gaetani and Grove (1998) proposed that the major effect of the addition of water during melting was to move the liquid from olivine-normative to quartz-normative by increasing the SiO_2

content of the liquid when considered on an anhydrous basis, which led to a similar decrease in the (MgO + FeO)/SiO_2 ratio. When considering the hydrous components, however, those authors found that the SiO_2 content of the liquid actually decreased slightly with additional water. Based on a more simplified system, Liu et al. (2006) agreed that the MgO/SiO_2 ratio decreases in hydrous liquids, but noted that the SiO_2 content of the liquid did not appreciably change as H_2O was added. Therefore, the change in MgO/SiO_2 in their experiments was due entirely to the decreasing MgO content of the liquid with increasing water. While their system used only MgO, our liquids contain both MgO and FeO — both major components of olivine — and thus we will consider these oxides jointly. The pHMELTS algorithm calculates a hydrous liquid with a much lower SiO_2 content than our liquid and the highest (MgO + FeO)/SiO_2 ratio of any near-solidus liquid considered here.

Comparison of the results of our melting experiments with the anhydrous liquids from 3 GPa of Walter (1998) and Longhi (2002) shows that our experiments typically have less SiO_2 than either of the predicted liquid compositions when our results are considered on a hydrous basis (Figure 8). When renormalized to volatile-free conditions however, the SiO_2 content of our liquids becomes higher than the SiO_2 content of the anhydrous liquids. This result is consistent with the effect of water on peridotite melts observed at lower pressures by Gaetani and Grove (1998). However, our liquids show SiO_2 contents when considered either on hydrous or volatile-free bases that are similar to or higher than the liquids measured by Gaetani and Grove (1998) at lower pressure. This behavior is somewhat surprising, as their experiments typically contain opx, and the silica activity fixed by the opx-olivine equilibrium is known to shift to lower values with

increasing pressure. Our experiments lack opx, and so should lie at still lower SiO_2 activity than the opx-olivine buffer. Both higher pressure and opx-undersaturation suggest that our experiments must have lower SiO_2 activity than those of Gaetani and Grove (1998) and yet the SiO_2 content of our liquids is not lower. There are several possible explanations. Liu et al. (2006) noted that there was a correlation between increasing Na_2O in their liquids and increasing silica content. Our liquids do show higher Na_2O than the liquids considered by Gaetani and Grove (1998), which could have a corresponding effect on the silica activity coefficient and silica content. Liu et al. (2006) also noted that the presence of CO_2 can serve to counteract some of the effect of the addition of water to liquids. While Liu et al. (2006) did not note any significant change in SiO_2 due to the addition of water, our experiments and those of Gaetani and Grove (1998) both show increasing liquid SiO_2 contents with increasing water (Figure 8). The high carbon contents in the experiments of Gaetani and Grove (1998) could drive the liquid to lower SiO_2 values because of the interaction between CO_3^{2-} and the hydrous liquids. Another possibility involves the cpx composition and the effects of CaO in the pyroxene quadrilateral, which may destabilize opx in our runs in a way that is not obvious from the dynamics of the MgO-FeO-SiO_2 ternary (see below).

The MgO content of our liquid can be understood in a similar fashion, in particular when both the MgO and FeO content of the liquid are combined into normative olivine. As described above, the FeO content of our liquids is fixed by the composition of the capsule material containing it. In the higher FeO experiments, the MgO content of the liquid adjusted to a lower value by solid crystallization. When compared to the liquids of Walter (1998), Longhi (2002), and that calculated by pHMELTS, our hydrous liquids are

measurably lower in (MgO + FeO)/SiO_2 (Figure 8). Compared to the hydrous compositions from lower pressure, our experiments show higher MgO + FeO contents. This is likely due to the well-established increase of total liquid MgO + FeO in equilibrium with the solid lherzolite assemblage with increasing pressure and temperature (Longhi, 2002). Our experiments are at higher pressure and higher temperature than the hydrous experiments of Gaetani and Grove (1998) and thus have higher MgO + FeO contents, while the MgO + FeO contents are lower than those from the hotter, anhydrous experiments of Longhi (2002) and Walter (1998). Liu et al. (2006) showed that an increase in water content of a liquid was associated with a decrease in MgO content, similar to these experiments.

An alternative and equivalent description for this set of changes is that the addition of water to the liquid expands the stability field of solid olivine relative to the other phases present (Figure 9). Longhi (2002) showed that as the pressure increases on a solid peridotite assemblage, the melt in equilibrium with the full peridotite assemblage increases in olivine component. As the pressure and temperature of melting increases, the olivine liquidus field contracts and the liquid composition moves towards olivine on a phase diagram. The addition of water decreases the (MgO + FeO)/SiO_2 ratio, as shown earlier, and moves the liquid composition away from olivine (Figure 9). Adding water to a silicate liquid has the effect of depolymerizing the liquid; bridging oxygens are separated by the reaction of water that produces OH^- groups. This effect on the liquid qualitatively makes the liquid more “olivine-like”, in the sense that the olivine structure contains no bridging oxygen atoms and would be considered fully depolymerized. During crystallization of liquids at low pressure during cooling, the effect of water is well

established: increased water content causes additional crystallization of olivine relative to the other phases (e.g., Asimow et al., 2004). The addition of water at pressure during melting appears to have a similar effect. Although a rigorous explanation of these relationships would require detailed understanding of the relationship between liquid speciation and component activities, it is frequently true that, just as making a liquid compositionally more like some solid tends to move the liquid towards the liquidus field of that mineral, so making a liquid structurally more like olivine has a similar effect.

The liquid calculated by the pHMELTS algorithm misses the effect of water on the $(MgO + FeO)/SiO_2$ ratio by the largest amount. The program likely has only a limited knowledge of the effects of water on the phase relations at high pressure and was previously not calibrated with any knowledge of the effect of CO_3^{2-} on the melting relations, which could further obscure this trend in the calibration of that model. In addition, the effect of H_2O in that model may be overwhelmed by the effect of the large Na_2O content of the calculated liquid.

4.2. Al_2O_3

When considered on a volatile-free basis, the Al_2O_3 content of our liquid appears to be controlled by the presence of garnet in the equilibrium solids. While not all of the experiments of Walter (1998) contained garnet, and no single experiment at 3 GPa reported analyses of both garnet and liquid compositions, one can estimate a liquid composition in equilibrium with garnet at 3GPa by extrapolation from Walter's data. Our liquid has a similar renormalized Al_2O_3 content to that estimate. Compared to the experiments of Gaetani and Grove (1998), which were all at least partially within the spinel field or were much closer to the spinel to garnet transition, our liquid is

substantially lower in Al_2O_3 content than any of their liquids. This comparison suggests that the increasing stability of garnet with pressure causes a significant decrease in liquid Al_2O_3 content, while the presence of water may have little effect on the stability field of garnet at these conditions compared to the effects of temperature and pressure.

Longhi (2002) presented several calculations of liquid compositions using his BATCH program that show interesting behavior in Al_2O_3. The model recovers the high-melt fraction experimental result of Walter (1998) closely. The calculated liquid composition from a 1% melt of primitive upper mantle (PUM) had notably lower liquid Al_2O_3 than the higher melt fraction calculation. As our volatile-free aluminum contents are close to those of Walter (1998) this could suggest that our experiments are slightly higher-degree melts than hoped. However, since our experiments are saturated with garnet, the presence of this abundant, high-aluminum phase may impose a practical limit on liquid Al_2O_3 contents. An alternative explanation could be that the PUM composition used by Longhi (2002) is richer in opx than KLB-1. Longhi (2002) acknowledges that the BATCH program does not recover very well the compositions of the pyroxenes in the calibration experiments, in particular their Al_2O_3 contents. Our pyroxenes are also very different from the pyroxenes in anhydrous experiments due to the effect of water on the phase equilibria for cpx (see below). The lack of opx combined with the decreased concentration of Al_2O_3 in cpx may make Al_2O_3 slightly more incompatible even in the presence of garnet, and thus could push Al_2O_3 slightly higher even in low-degree melts.

The pHMELTS algorithm shows Al_2O_3 to be much more compatible relative to the other oxides than seen in our experiments. The model predicts a negative correlation between liquid Al_2O_3 contents and water contents during melting (Asimow et al., 2004),

which is not observed in these experiments. The algorithm appears to overestimate the stability of garnet during melting, including too little garnet in the melting reaction relative to the pyroxenes.

4.3 CaO

CaO is perhaps the most interesting oxide in our experiments, in that its behavior cannot be understood by a simple relationship between a constant solid and liquid composition. Consequently, varying CaO abundances was the main reason why the MISE procedure of Hirschmann and Dasgupta (2007) could not be applied fully to all phases.

At low pressures, a large miscibility gap exists between cpx and opx. As pressure increases on solid peridotite, the stability field of cpx expands significantly, and eventually the cpx field expands enough that opx is no longer stable in most common peridotites (Longhi and Bertka, 1996). In our sub-solidus equilibration experiments on a KLB-1 composition, this behavior is clearly seen. The peridotite begins as a mixture of olivine, opx, cpx, and spinel. The initial cpx was measured to contain ~19.5% CaO by weight (Davis et al., 2009). After recrystallization at 3 GPa, the spinel and opx have both reacted out, producing garnet and a cpx with a much lower CaO content, typically ~12%. This behavior is consistent with the compositions of the cpx grains measured in the anhydrous melting experiments discussed here. The CaO content of the cpx in the study of Walter (1998) decreased with increasing temperature or pressure, 10.65% at 3 GPa. Our peridotite was recrystallized at a temperature 150°C below the lowest temperature experiment from Walter (1998) and thus shows a slightly higher CaO content, but overall the behavior is very consistent. The cpx measured by Longhi (2002) show even lower CaO contents at similar pressures and temperatures. The cpx from our sub-solidus

experiments plot very close to the predicted edge of the 2.8 GPA cpx field from Longhi (2002) (Figure 10).

Gaetani and Grove (1998) conducted lower-pressure experiments that were both hydrous and anhydrous, and noted that there was a slight increase in the CaO content of their cpx in their hydrous experiments at 1.6 GPa. However, because the expansion in the cpx field occurs mostly at pressures higher than sampled by their experiments, the effect was minimal.

When the cpx in our recrystallized peridotites is exposed to a hydrous silicate melt, there is a significant shift in the equilibrium cpx composition. The cpx emerged from every hydrous experiment with ~17% CaO. Graphically, this composition plots well inside the anhydrous field boundary for cpx from these pressures, suggesting that there has been substantial contraction of the cpx field due to the presence of the hydrous melt (Figure 10). There is only slight variation in the pyroxene composition between successive runs, and these variations potentially correlate with the alkali and water contents of the liquid, although these relationships could be complicated by the presence of small amounts of carbonate. This change in solid composition violates one of the precepts for the iterative sandwich experiment, that the solid composition introduced at each step should be the same as the solid composition at the end of the experiment, and thus prevented completion of a full iterative sandwich procedure.

The change in the equilibrium cpx composition in hydrous samples has potentially significant implications for melting of variably enriched sources. The increasing CaO content of a cpx will have two competing effects on the bulk partitioning; CaO would be expected to be more compatible with this change, as the CaO content of

the solids has increased. However, this contraction in the cpx field could also have the effect of decreasing the modal abundance of cpx, perhaps by stabilizing opx to higher pressure. As experiments at higher pressure typically show a gradual decrease in the liquid CaO content (Walter, 1998), we believe that the contrary effect of re-contracting the cpx field will be to slightly increase the expected CaO content of the liquid in equilibrium with peridotite, but this will depend strongly on the overall bulk composition.

Compared to the other available experiments, this conclusion appears to be supported by our data. At all conditions, the liquids of Longhi (2002) are significantly lower in CaO content than our liquid. This is also true of our liquid compared to the calculated low-degree melt of PUM from the BATCH program. More useful than CaO concentration itself is the CaO/Al_2O_3 ratio, as Al_2O_3 shows little change once buffered by garnet, but may be useful as an indicator of degree of melting. The experiments of Longhi (2002) have significantly lower CaO/Al_2O_3 ratios than our experiments, again suggesting that CaO is more incompatible in the case of hydrous melting.

Compared to the 3 GPa experiments of Walter (1998), our liquid has a slightly lower CaO content. The CaO/Al_2O_3 ratio of our liquid is also lower than that of Walter (1998), although the difference is smaller. This potentially relates to the presence of opx in those experiments, which would make CaO more incompatible in the solids than in our experiments that are lacking opx.

The hydrous experiments of Gaetani and Grove (1998) show CaO contents that are slightly higher than our liquid. This is not unexpected, as the CaO content of a liquid in equilibrium with a full lherzolite assemblage should decrease with increasing pressure as discussed above. The cpx in our experiments has slightly lower total CaO than the

experiments of Gaetani and Grove, suggesting that the cpx composition field has expanded slightly, causing the change in liquid CaO content (Figure 10). Our liquid however is higher in CaO/Al_2O_3 than the liquids of Gaetani and Grove (1998) due to the lower Al_2O_3 in our experiments as discussed above.

Comparison with the pHMELTS model-calculated liquid perhaps best illustrates the effect of the contraction of the cpx field on the melt composition. The pHMELTS-calculated liquid has the lowest CaO content and lowest CaO/Al_2O_3 ratio of any liquid given here. Thus, the algorithm believes that under these conditions, CaO is substantially more compatible than actually seen in our experiments. The pHMELTS algorithm calculates a higher fraction of pyroxenes and garnet in the KLB-1 mix than we see at any step, and consequently it predicts CaO significantly more compatible than is seen in any of the available experiments.

It is more difficult to postulate a mechanism for this cpx behavior than it was for olivine, as the interaction of olivine with hydrous melts has been much more thoroughly studied. The pyroxene structure involves some sharing of oxygen atoms between silica tetrahedral, and so is more polymerized than olivine. Adding water to a silicate liquid therefore is qualitatively making the liquid less pyroxene-like and therefore should reduce the stability of cpx relative to the anhydrous case. One possible explanation is that the presence of water decreases the stability of cpx enough that high-Al_2O_3 cpx becomes particularly unstable and only a higher calcium cpx similar to those seen at lower pressures can remain stable. Alternatively, the chemistry could be viewed as water destabilizing the opx component in the solid. Longhi (2002) and others suggest that in anhydrous systems, opx should be a product of the melting reaction at 3 GPa. If the

presence of water instead moved opx back to being a reactant, the melting reaction could proceed by drawing the opx component out of the cpx and into the liquid. This mechanism could be illustrated qualitatively in Figure 10 by the motion of our measured liquid compositions away from olivine and the liquid composition from Longhi (2002) and towards opx with increasing water contents.

4.4. Na_2O

The Na_2O content of low-degree silicate melts from pressure has long been an open question due to experiments that produced liquids with very high Na_2O contents at low melt fractions (e.g., Robinson et al., 1998). These experiments suggest that Na_2O behaves as a highly incompatible element, partitioning strongly into the liquid phase. The pHMELTS algorithm also calculates a liquid with Na_2O contents that appear unreasonably high. Longhi (2002) proposed an alternative: that as pressure increased, the partition coefficient of Na_2O in cpx would increase, and this compatibility would serve as a barrier to the generation of high Na_2O contents in liquids from pressures above 2 GPa. Specifically, from pressures of 3 GPa higher, Longhi (2002) proposed that the liquids would be limited to about 2.5% Na_2O at the lowest melt fractions and in enriched sources. Our experiments are able to produce liquids that have measurably higher Na_2O contents than this limit; although variations in solid modal abundances cause some variation in Na_2O, our experimental values ranged from 2.6% up to 3.42% Na_2O. In context with the other elements, this behavior is unsurprising. The expansion of the olivine field and contraction of the cpx field due to the presence of water would be expected to decrease the bulk partition coefficient of Na_2O. Indeed, the cpx data in the experiments of Longhi (2002) typically show higher Na_2O contents and higher values of

D_{Na2O} than seen in our hydrous experiments. While our liquid Na_2O concentrations only mildly exceed the Longhi limit, these experiments suggest that hydrous melting and its effects on the solid relations can be expected to increase the Na_2O content of silicate liquids from depth.

Because Na_2O only makes up a small portion of the melt, it is the first element that we can analyze using the MISE procedure of Hirschmann and Dasgupta (2007) without having to worry about a large correction for closure (bringing the glass totals to 100%). When we use the measured partition coefficients for these experiments, the solid composition for KLB-1 given by Davis et al. (2009), and modal abundances calculated by mass balance, the predicted liquid should have 2.5% Na_2O, close to the range of measured compositions. However, this calculation is made more difficult by the change in cpx stability in the hydrous system; as the cpx field contracts, the modal abundance of cpx should decrease. Any attempt to take into account this decrease in cpx abundance in the MISE procedure leads to a liquid with higher Na_2O. Using the modal abundances calculated by pHMELTS which includes some opx, we calculate a liquid with over 4.0% Na_2O. This effort suggests that our Na_2O contents are not unreasonable and that a range of 2.5%-4% Na_2O likely spans much of the accessible range in Na_2O contents at these pressures, but also illustrates the difficulty of applying the MISE procedure with variable solid modal abundances and compositions.

4.5. K_2O

K_2O is the only measured oxide other than the volatiles that is perfectly incompatible at the level of the measurements applied here. K_2O varies from 0.25% to 0.5% in our liquids, but even in the most potassic experiment and with solid compositions

measured at high currents and long counting times, K_2O cannot be statistically distinguished from zero in any solid phase. Including this element in any MISE calculation produces a calculated liquid with very high K_2O contents, and therefore this calculation was not performed on this element. K_2O contents in natural liquids formed from peridotite could potentially cover a large range in compositions, with potentially corresponding effects on the other oxides in the liquid, as illustrated by the arrows in figure 9.

4.6. Cr_2O_3

Compared to the measured liquid composition in every other study from 3 GPa considered here, the Cr_2O_3 content of our liquid is lower by a significant amount. In our samples, Cr_2O_3 is incompatible in olivine, but is strongly compatible in garnet and only slightly less compatible in cpx. Despite the fact that our experiments are conducted outside the stability field of spinel, compatibility in these two phases pushes the Cr_2O_3 content of our liquid very low. We measure only 0.1-0.15% Cr_2O_3 in our liquids. The experiments of Gaetani and Grove (1998) typically also show low Cr_2O_3 contents, but many of them contain spinel, a phase in which Cr_2O_3 is compatible. None of the experiments of Walter (1998) or the calculated compositions from the BATCH algorithm of Longhi (2002) show Cr_2O_3 contents as low as our experiments. The solids measured in Walter (1998) do show Cr_2O_3 contents similar to or greater than those measured in our garnets and cpx, but overall would have slightly lower partition coefficients because of the higher liquid contents. The pHMELTS calculation also gives liquids with much higher Cr_2O_3 contents than we measured, because the algorithm does not yet include Cr_2O_3-bearing components in any solid other than spinel.

The MISE procedure suggests that our liquid compositions are consistent with the partition coefficients that we measure. Application of the MISE procedure predicts liquid compositions of 0.10 to 0.12% Cr_2O_3, very similar to the amounts measured in our experiments. Hydrous melting at high pressure therefore appears to produce liquids with very low Cr_2O_3 contents.

4.7. TiO_2

Longhi (2002) spent significant effort attempting to understand the partitioning of TiO_2 during high-pressure melting. He proposed that two major effects could explain the TiO_2 contents of low-degree melts, both related to the partitioning of TiO_2 between cpx and melt. As the cpx field expanded with increasing pressure, D_{TiO2} decreased and consequently liquid TiO_2 contents increased. Similarly, as the liquid alkali content decreased (which also correlates with increasing pressure), D_{TiO2} decreased. Because our experiments show significant changes in cpx composition and liquid sodium content associated with the presence of water, it follows that the partitioning of TiO_2 may be significantly different in our experiments from those conducted either at lower pressures or without water.

A starting point for analyzing the partitioning of TiO_2 during hydrous melting is our sub-solidus experiments, with low CaO cpx. Based on the analysis of Longhi (2002), we should expect that as CaO increases in cpx, D_{TiO2} should increase. Below the solidus temperature, we see that TiO_2 contents in the garnet and cpx are roughly similar. Garnet typically shows slightly higher TiO_2 contents than the cpx, 0.265% compared to 0.237%, but this difference is barely resolvable above the error in the analyses (~0.015%, 1σ). These values are a factor of two lower than the TiO_2 contents reported in garnet by

Walter (1998) but are similar to the TiO_2 contents reported in some of his cpx, although those measurements show considerable variability from run to run.

When the solid peridotite reacts with the liquid, the cpx field contracts as described above, and the CaO content of the cpx increases. According to the presentation of Longhi (2002), this transition should be associated with an increase in D_{TiO2} for cpx. However, our experiments consistently show the opposite behavior: D_{TiO2} decreases for cpx when the minerals are reacted with hydrous liquids. At either a constant TiO_2 content in the garnet or a constant solid TiO_2 content, D_{TiO2} is lower in the hydrous case. Our measured values of D_{TiO2} cluster between 0.15 and 0.20 (with one outlier at 0.28 in R385, the experiment with the highest liquid Na_2O and K_2O).

Longhi (2002) proposes that another key variable for determing D_{TiO2} is the alkali content of the liquid. Our liquids show higher Na_2O content than those of Longhi (2002) which, based on his work, we expect to be associated with increased D_{TiO2}. As noted, the D_{TiO2} we measure falls below the calculated value predicted by the BATCH algorithm for a cpx with the CaO content measured in our experiments. However, the measured values of D_{TiO2} fall within the range of experimental results given by Longhi (2002) at these alkali contents; it seems BATCH predicts a lower value of D_{TiO2} than shown by most of the experiments at low alkali contents. Overall, our experiments produce liquids with higher alkali contents and lower TiO_2 contents than predicted by BATCH, requiring that the bulk D_{TiO2} in our experiments is greater than predicted by the BATCH algorithm despite the decrease in D_{TiO2} for cpx. This result is due to a combination of the effect of alkalis on D_{TiO2} for cpx and the compatibility of TiO_2 in garnet, which appears to be the main host for TiO_2 during our experiments.

When the MISE procedure is used, the predicted TiO_2 content of our liquid is higher than that measured in any liquid; from 1.0 to 1.5% TiO_2 depending on the solid assemblage. This result suggests that our liquids may not have sufficient TiO_2 to equilibrate with solid KLB-1. However, if this were the case, then our solids should consistently show a decrease in TiO_2 content, a behavior that is not always true for the garnets (Table 2). The measured partition coefficients can only be reconciled with the MISE procedure if the solids have a higher proportion of garnet or if our starting material has slightly less TiO_2 than the measured KLB-1 composition given by Davis et al. (2009). It is possible that the liquid TiO_2 content is reduced slightly because the additional garnet added to the solid assemblage may have increased the bulk D_{TiO2}. For our final hydrous liquid composition we estimate a TiO_2 concentration of 0.9%, but this number is sensitive to small changes in source mineralogy.

Overall, TiO_2 partitioning appears to be a complicated function of the mineral modes, liquid composition, and solid compositions. Garnet appears to be the main host phase for TiO_2, and thus its abundance may control the initial liquid TiO_2 contents. Because of the high garnet content, our liquids have lower TiO_2 contents than the low-degree, high-pressure melt of Longhi (2002). If the correlation suggested by Longhi (2002) between liquid alkali contents and bulk D_{TiO2} is correct, it may require a correlation between D_{TiO2} for garnet and liquid alkali contents. This should be investigated in future experiments.

While attempting to model fractional crystallization and source trends for the Azores, Asimow et al. (2004) noted that the MELTS algorithm shows an increase in partition coefficient for TiO_2 in low-degree liquids, but possibly overestimates the effect.

pHMELTS calculates a higher TiO_2 content than seen in our liquids, but also includes opx in the solids, which would further decrease the D_{TiO2} and increase the TiO_2 content in the liquid. pHMELTS calculates a TiO_2 content that is not substantially different from what would be predicted using the MISE technique of Hirschmann and Dasgupta (2006). The diamond aggregate experiments of Baker et al. (1995) showed TiO_2 concentrations that are at or below the lowest values given here. The higher TiO_2 concentrations measured here are therefore consistent with the proposal of Asimow et al. (2004) that the pHMELTS model and the experiments of Baker et al. (1995) overestimate the compatibility of TiO_2 at low melt fractions.

4.8. H_2O contents and implications for mantle melting and partitioning

Our experiments are typically more hydrous than the liquids that might be expected at these temperatures from estimates of the dry solidus temperature and the magnitude of solidus depression due to water. The pHMELTS algorithm, for example, predicts liquid compositions with half as much water as we see in our average experimental liquid when the solidus is adjusted to 1375 °C. If the partition coefficient for H_2O remained near 0.01, as is expected based on some calibrations (e.g., Aubaud et al., 2004; Hirschmann et al., 2009), then the source for a liquid with 5% water would be required to have ~500 ppm H_2O. This is much higher than estimated for normal MORB source (Michael, 1988; Hirth and Kohlstedt, 1996; Gose et al., 2009) and may only be applicable to enriched, hotspot-affected, or subduction-related environments.

However, the behavior seen in our series of melting experiments is more complex than this simple partitioning model. Our experiments sample a wide variety of water contents, from 2.7% to 6.0% H_2O in the melt. Furthermore, the composition of the liquid

appears to vary with water content (Figures 8, 9, and 10). These experiments suggest that melts of varying composition can be produced in equilibrium with the solid peridotite assemblage across a variety of total water contents, and no single water content can be fully representative of the liquid in equilibrium with KLB-1 under these pressure and temperature conditions.

The contraction of the cpx field described above has very important implications for the partitioning of water during mantle melting. Based in part on measurements from the experiments of Gaetani and Grove (1998), Aubaud et al. (2004) and Hauri et al. (2006) proposed that the partitioning of water between melt and olivine or pyroxene was a strong function of the Al_2O_3 content of the solid phase due to charge-coupled substitution of H^+-Al^{3+} for Si^{4+}. Despite increased pressure, the cpx in our experiments show aluminum contents that are equal to or in many cases less than those in the experiments of Gaetani and Grove (1998). This low Al_2O_3 content appears to be caused by a combination of the contraction of the cpx field described above and the high abundance of garnet in the solids. This behavior is also consistent with the lower Al_2O_3 content of our liquid than those from lower pressures.

As our pyroxenes have lower Al_2O_3 content, the calibrations of Hauri et al. (2006) and Aubaud et al. (2004) predict that D_{H2O} in our experiments should be less than in the experiments of Gaetani and Grove (1998). While our final liquid did not equilibrate with opx, we did see opx in a previous iteration in equilibrium with a hydrous liquid, and thus we can also estimate its Al_2O_3 content based on those measurements. Both pyroxenes in our experiments showed Al_2O_3 contents between 5-6%, which in the Hauri or Aubaud calibrations would give a $D_{H2O} \sim 0.015$ for both pyroxenes (Tables 1 and 2). These values

are significantly below those used by Aubaud et al. (2004), Hauri et al. (2006), or Hirshmann et al. (2009) to estimate the storage capacity of the upper mantle and the water content of low-degree melts. Using these partition coefficients, the mineral modes calculated here, and estimates of the partition coefficient between olivine and garnet and liquid, we calculate a bulk D_{H2O} ~ 0.006, 50% lower than the value calculated by Aubaud et al. (2004) or Hirschmann et al. (2009) at pressures close to 3 GPa.

The decreasing Al_2O_3 content of pyroxenes in the garnet field seen here therefore has a number of implications for the behavior of water in the mantle. Previously the water storage capacity of the upper mantle was expected to increase with increasing depth due to the increasing Al_2O_3 content of the pyroxenes until reversing at pressures greater than 3 GPa as the modal abundance of garnet increased (Hirschmann et al., 2005; Hirschmann et al., 2009). Our experiments show lower pyroxene Al_2O_3 contents than previously measured at this pressure. If the partition coefficient D_{H2O} estimated here is accurate, it also suggests that in the upper mantle, water would be less compatible than estimated by Aubaud et al. (2004) or Hirschmann et al. (2009). Because the available pyroxenes from 2.8-3.0 GPa all contained significantly more Al_2O_3 than seen in our experiments, those authors predicted that mantle with low total water contents would only melt at depths close to the dry peridotite solidus. Our experiments show that the decreased partition coefficient for water could persist to lower pressures than previously seen, close to the spinel to garnet transition. The liquid water contents seen here could therefore still be produced by melting of a mantle with more typical water contents, possibly down to 100-200 ppm. These water contents could still provide substantial solidus depression, contrary to the suggestion of Hirschmann et al. (2009) that peridotites with ~100 ppm water would

only melt close to the dry solidus. We caution that the partition coefficient D_{H2O} could not be measured directly in our experiments because of the small grain size; the partition coefficient could only be estimated by measurement of the pyroxene Al_2O_3 content. Our experimental technique could potentially be modified using coarser-grained starting materials to allow for measurement of the actual D_{H2O} and we suggest that completing such experiments in the presence of substantial garnet is particularly important.

Several authors have attempted to estimate the bulk partition coefficient for H_2O during production of natural basalts by comparing the partitioning of water to various rare earth elements that may have similar *D* values. Michael (1995) suggested that in samples from the mid-Atlantic ridge, the partition coefficient for water was close to that of cerium. Danyushevsky et al. (2000) measured rocks from the East Pacific Rise and the Southeast Indian Ridge and made a similar comparison to Ce, but also analyzed rocks from the Lamont Seamounts west of the East Pacific Rise and found instead that the partition coefficient of water was closer to that of La, a more incompatible element. In back-arc basins, H_2O acts most like Nd, a more compatible element than Ce (Stolper and Newman, 1994). This data suggests a mechanism for this variation that was not previously known. Coupled substitution mechanisms with aluminum in pyroxenes have been proposed not just as a method for entry of water into minerals but also for a number of other elements including La and Ce (Blundy et al., 1998, and below). Since the size and charge of water (or hydrogen) is substantially different from either of those rare earth elements, it follows that the relative partitioning of these elements could change substantially over the pressure range covered by a single melting column. The change in relative partition coefficients could be due to a change in the partitioning for La, Ce, or

H_2O and may give information about the modal abundance of pyroxenes in the source, the average depth of melting, or even the temperature profile (if a substantial amount of melting occurred in the anhydrous melting regions). Thus, the decreased D_{H2O} observed in the Lamont Seamounts could be evidence for the production of those liquids at a greater average pressure than those sampled on-axis at ridges, from zones where the stability of garnet was reducing the Al_2O_3 content of any pyroxenes.

Dasgupta et al. (2007) noted that there was likely a strong interaction between carbonate-driven melting at mantle pressures up to 10 GPa and any water present in the upwelling rocks. Our hydrous melting experiments also suggest a strong interaction between water and carbonate during melting (e.g., Figure 6, Figure 8). Dasgupta et al., (2007) suggested that the presence of carbonate-rich melts deeper in an upwelling system may dehydrate the mantle source prior to reaching its hydrous solidus. If that is true, then carbonated peridotite may be expected to produce melts of a very different composition than would hydrated peridotite. Our data suggests tentatively that adding carbonate to a hydrous silicate melt may counteract some of the effect of water on the change in liquid composition by increasing the $(MgO + FeO)/SiO_2$ ratio. The strongest signature of hydrous melting, therefore, might be found in areas that have sources with either high water contents or low carbon contents, whereas high carbon contents and low water contents may be required to produce the signatures of carbonatite melting (Dasgupta and Hirschmann**,** 2007). Further experiments are required on silicate melts with a variety of ratios of carbonate to water contents to better constrain this behavior.

4.9. Additional implications of these experiments for natural melting

Our results suggest that the production of hydrated silicate liquids under mid-ocean ridges from depths several tens of kilometers greater than the dry solidus intersection along an anhydrous adiabat remains plausible. The behavior demonstrated here, including melting in the presence of garnet and the effects of the presence of water on the olivine and cpx fields can potentially have important implications for the chemistry and location of melt generation under mid-ocean ridges.

4.9.1. Presence of garnet during melting.

As discussed above in the introduction, the presence of a garnet signature in the trace element budget of mid-ocean ridge basalts presents a problem for models based on anhydrous peridotite sources. We show here that hydrous melting continues to be a possible resolution for this issue.

The proposal that hydrous melting relates to the garnet signature appears to be consistent with the major element characteristics of our liquids. Kinzler (1997) and previous workers, including Klein and Langmuir (1989), have demonstrated that the major element signatures of MORB show trends where lower melt fractions correlate with higher Na_2O contents and often higher SiO_2 contents. This chemistry is qualitatively consistent with the patterns observed here in hydrous melting; the addition of water during melting both decreases the partition coefficient D_{Na2O} and also produces a liquid with elevated SiO_2. The melts that have the highest Na_2O contents are also those which typically show the strongest garnet signature as well (Shen and Forsyth, 1995). Longhi (2002) shows that at pressures above the spinel-to-garnet transition, Na_2O should become significantly more compatible in cpx during anhydrous melting. In the case of anhydrous melting, therefore, it could be particularly difficult to reconcile the high liquid Na_2O

contents with the presence of garnet, as the liquids produced in the garnet field would be expected to have lower Na_2O contents.

The presence of water during melting offers a possible explanation for the garnet signature and the associated correlations in a number of ways. First, hydrous melts are typically expected to be only low-degree melts which sample a large portion of the available water but do not produce large melt volumes. In this way, a hydrous melt can potentially explain the correlation between the increasing garnet signature and decreasing degree of melting (Shen and Forsyth, 1995). Asimow and Langmuir (2003) calculated that for a constant total amount of melt production represented by a constant crustal thickness, increasing the water content of the source led to a decrease in the average degree of melting represented by the final accumulated liquid, because the additional water led to a larger amount of low-degree hydrous melts being sampled. If these low degree melts were generated in the garnet field, they would carry the garnet signature, and therefore the wettest and coldest sources would produce melts of the lowest average melt fraction and could also carry the strongest garnet signatures.

Based on anhydrous experiments, Robinson and Wood (1998) argued that the spinel-to-garnet transition occurs in the range of 2.5-3.0 GPa in most peridotites, and that production of significant quantities of melt from the garnet field would require melting to begin at even greater pressures, up to 3.5 GPa, with potential temperatures that would generate an implausibly large amount of melt. However, they also conducted sub-solidus experiments and showed that the temperature of the spinel to garnet transition was strongly pressure dependent, with a slope of ~400 °C per GPa. For the temperature used in our experiments, ~1375 °C, extrapolation of their given phase boundary predicts a

spinel to garnet transition of ~2.5 GPa. As melting proceeds, the temperature of the assemblage would decrease as energy is converted to latent heat, and thus the beginning of melting could push the spinel-to-garnet transition to even lower pressures. The experiments of Gaetani and Grove (1998) produced measureable garnet at pressures as low as 1.6 GPa and temperatures as low as 1255 °C. As noted by Gaetani and Grove (1998), water fluxes peridotite melting at lower temperatures than would otherwise occur, and therefore water-driven melting is much more likely to occur within the garnet field and could maintain garnet in the source to much shallower pressures than could be sampled by anhydrous melts.

The partitioning of the rare earth elements and radioactive isotopes has been a key part of the debate over the presence or absence of the garnet signature. Garnet is believed to be the main phase able to retain the heavy rare earth elements (HREE) during melting, and therefore a depleted HREE signature is typically interpreted as a major sign of garnet in the source (e.g., Stolper and Hirschmann, 1996). Compatibility of radioactive elements such as Lu or U can also yield garnet signatures in isotope ratios by fractionating parent and daughter isotopes (e.g., Salters and Hart, 1989). The attribution of such signatures to garnet requires that garnet is the only common phase in the melting zone able to fractionate these elements in the correct sense during melting. Wood et al. (1999) and Blundy et al. (1998) argued that this was not the case by measuring partition coefficients for the key elements, including the HREE and U in aluminous cpx that were significantly greater than those measured elsewhere. The increased compatibility of those elements in cpx at pressure could therefore explain the presence of a so-called garnet signature in liquids produced without the presence of garnet.

Our cpx compositions have important implications for this issue. In the experiments of Wood et al. (1999) and Blundy et al. (1998) where increased partitioning of these elements into cpx was observed, the cpx compositions were highly aluminous, and the substitution mechanism proposed for these elements was a coupled-substitution involving Na^{+} and Al^{3+}. Our hydrous experiments show cpx with much lower Na and Al contents due to the presence of garnet and the contraction of the cpx field in the presence of a hydrous melt. The experiments of Gaetani and Grove (1998) were conducted at similar pressures to the experiment of Blundy et al. (1998) and also produced cpx with lower Al_2O_3 contents than Blundy et al. (1998), suggesting that the highly aluminous cpx required to explain the production of a garnet signature may only occur in anhydrous systems. These hydrous experiments suggest that if significant water is present during melting, the garnet signature cannot be produced by the presence of cpx under these conditions because of the reduced aluminum content of the cpx.

An illustrative example can be found in TiO_2 concentrations. As discussed previously, the contraction of the cpx field seen here led to decreasing TiO_2 contents in the cpx compared to the sub-solidus cpx with higher Al_2O_3 content. Blundy et al. (1998) reported a cpx with 10.47% Al_2O_3 and 0.74% TiO_2 in equilibrium with a melt from lower pressures containing 1.15% TiO_2. While their liquid TiO_2 content is only slightly higher than our predicted liquid, the TiO_2 content of their cpx is a factor of 3-5 greater than we measure and consequently our experiments show a D_{TiO2} for cpx that is also a factor of 3-5 lower than the experiment of Blundy et al. (1998). Although we did not measure trace elements in our experiments, a similar effect on the remaining incompatible elements such as the HREE would mean that during hydrous melting, garnet would be the only

phase capable of creating the trace element and isotopic signatures typically referred to as the garnet signature.

Hirschmann and Stolper (1996) and Pertermann and Hirschmann (2003b) hypothesized that an alternate explanation for the presence of the garnet signature could be the presence of small amounts of pyroxenite in the melting source. Pertermann and Hirschmann (2003b) estimated the magnitude of the typical garnet signature could be explained by ~2% pyroxenite in the MORB source. This suggestion remains a plausible alternate mechanism for generation of the garnet signature that cannot be ruled out by this work, although the observed effect of water-rich melts on the stability field of cpx could have important implications for melting of pyroxenites. We will consider some of the major element implications here and a specific example of minor element signatures in Chapter 3.

4.9.2. Pyroxenitic sources

If the contraction of the cpx field during hydrous melting were a general phenomenon, it potentially has important implications for the melting of variable source lithologies.

Melts of variable calcium contents have been observed from many systems, from very low values up to the very high concentrations in those melts termed ultra-calcic (Kogiso and Hirschmann, 2001). An increasingly fertile source would be expected to have higher cpx abundances than a depleted source, and would also be expected to be more hydrous. Thus, the cpx in an enriched source may be expected to show a stronger contraction of the cpx field alongside a greater modal abundance of cpx. Melting of a hydrous, enriched source may be a method of producing particularly low CaO contents in

liquids that maintain a garnet signature in the trace elements, as the calcium may be more compatible if the source material contains a large quantity of high-CaO cpx. Conversely, it appears extremely difficult to produce liquids with a high CaO content if water is present, forcing the cpx to high CaO contents. Other processes, such as high temperature, carbon-fluxed melting, or high-degree melting of non-peridotite sources may be necessary to produce ultra-calcic liquids. Wet melting could produce moderately elevated CaO contents by reducing the modal abundance of cpx, as seen in our experiments, but the presence of highly calcic cpx could impose an upper limit on the liquid CaO content.

As shown above, the TiO_2 content of liquids can be a particularly strong function of the abundance and composition of the cpx in the solid. The extreme of this behavior is found in the case of melting of a pyroxenite. Pertermann and Hirschmann (2003a) produced very high TiO_2 (up to 6.7%) coexisting with a high-Al_2O_3 cpx If these melts were hydrous and the D_{TiO2} for cpx decreased further, the resulting liquid could be even richer in TiO_2. High liquid TiO_2 concentrations may therefore be a method of identifying contributions from hydrous melting of pyroxenite sources.

4.9.3. Liquid alkali contents

Previously, melting experiments on both peridotite and pyroxenite-rich lithologies produced liquids that tend to decrease in Na_2O content with increasing pressure (Longhi, 2002; Yaxley et al., 2007). Ideally, this would create a situation where the ratio of K_2O/Na_2O in MORB could be interpreted as an indicator of the initial pressure of melting. However, this method has not been particularly effective at predicting pressures (Yaxley et al., 2007). Our experiments suggest that a major complication to any simple explanation of the alkali ratios of a liquid may be the presence of water in its source. If

hydrous melting contracts the stability field of cpx, then it is expected to have the opposite effect of increasing pressure on the partition coefficient for Na_2O; increasing pressure would increase D_{Na2O} while increasing water content would decrease D_{Na2O}. Since hydrous melts are expected to be produced at higher pressures than anhydrous melts, these two effects would interact and potentially create very complicated relationships between the liquid and solid Na_2O contents, pressure, and composition. Hydrous melting of pyroxenite lithologies in particular could be expected to show elevated Na_2O if the effects of water on cpx are similar to those seen in peridotite, in the opposite direction of the simple relationship between K_2O/Na_2O and pressure.

As noted above, K_2O is essentially perfectly incompatible in our experiments. Based on these experiments, K_2O can then be treated either as a tracer of source enrichment or of the volume of source sampled. Asimow and Langmuir (2003) showed that hydrous melting under a mid-ocean ridge could increase the volume of mantle sampled by producing a low-degree melt at greater depths and in rocks that typically would remain sub-solidus had water not been present. Therefore, the presence of water might be expected to increase the potassium content of erupted liquids at mid-ocean ridges by increasing the volume of peridotite that melts. Alternatively, K_2O and water contents in enriched sources would be expected to increase together (Asimow et al., 2004). Increased potassium in liquids may be expected to show interesting correlations with other indicators of source enrichment, and isolating either of these effects in natural MORB may require detailed modeling.

5. CONCLUSION

The presence of water during melting at 3GPa produces liquids with an increased SiO_2 content and a decreased $(MgO+FeO)/SiO_2$ ratio compared to anhydrous melts from the same pressure, consistent with the results from hydrous melting experiments at lower pressures. This effect is tantamount to increasing the stability field of olivine relative to the other phases present. The presence of a hydrous melt also has a strong effect on the composition of the equilibrium clinopyroxene. Anhydrous clinopyroxenes from this pressure show high Al_2O_3 contents, while our hydrous clinopyroxenes show elevated CaO contents and lower Al_2O_3 contents than seen in any anhydrous experiment from this pressure. The clinopyroxene composition field therefore contracts substantially due to the presence of water. Trace elements which may be hosted in the mantle by clinopyroxene through coupled substitutions involving Al_2O_3, including water, will therefore have lower partition coefficients during hydrous melting than during anhydrous melting, and these reduced partition coefficients will strongly affect the water content and the trace element characteristics of any melt produced at this pressure.

6. ACKNOWLEDGEMENTS

This work benefited from many enlightening discussions with Sally Newman, George Rossman, Mark Hirschmann, Liz Muira, Ma Chi, and Mike Baker. The authors would like to thank Alex Sessions and Magnus Eek for the use of their Elemental Analyzer and Ed Stolper and John Beckett for the use of their 1-atmosphere furnaces. This work was supported by the NSF Ocean Sciences Marine Geology and Geophysics program, grant numbers OCE-0241716 and OCE-0550216.

References

Asimow, P. D., Hirschmann, M. M., Ghiorso, M. S., and Stolper, E. M. (1999) Calculation of peridotite partial melting from thermodynamic models of minerals and melts. III. Controls on isobaric melt production and the effect of water on melt production. *J. Petrol.* **40**, 831-851.

Asimow, P. D. and Langmuir, C. H. (2003) The importance of water to oceanic mantle melting regimes. *Nature* **421**, 815-820.

Asimow, P. D., Dixon, J. E., and Langmuir, C. H. (2004) A hydrous melting and fractionation model for mid-ocean ridge basalts: application to the Mid-Atlantic Ridge near the Azores. *Geochem. Geophys. Geosyst.* **5**, Q01E16.

Aubaud, C., Hauri, E. H., and Hirschmann, M. M. (2004) Hydrogen partition coefficients between nominally anhydrous minerals and basaltic melts. *Geophys. Res. Lett.* **31**, L20611.

Aubaud, C., Withers, A. C., Hirschmann, M. M., Guan, Y., Leshin, L. A., Mackwell, S. J., and Bell, D. R. (2007) Intercalibration of FTIR and SIMS for hydrogen measurement in glasses and nominally anhydrous minerals. *Am. Mineral.* **92**, 811-828.

Baker, M. B. and Stolper, E. M. (1994) Determining the composition of high-pressure mantle melts using diamond aggregates. *Geochim. Cosmochim. Ac.* **58**, 2811-2827.

Baker, M. B., Hirschmann, M. M., Ghiorso, M. S., and Stolper, E. M. (1995) Compositions of near-solidus peridotite melts from experiments and thermodynamic calculations. *Nature* **375**, 308-311.

Bishop, J., Madejová, J., Komadel, P., and Fröschl, H. (2002) The influence of structural Fe, Al and Mg on the infrared OH bands in spectra of dioctahedral smectites. *Clay Minerals* **37**, 607-616.

Blundy, J. D., Robinson, J. A. C., and Wood, B. J. (1998) Heavy REE are compatible in clinopyroxene on the spinel lherzolite solidus. *Earth Planet Sc. Lett.* **160**, 493-504.

Chou, I. (1986) Permeability of precious metals to hydrogen at 2 kb total pressure and elevated temperatures. *Am. J. Sci.* **286**, 638-658.

Danyushevsky, L. V., Eggins, S. M., Falloon, T. J., and Christie, D. M. (2000) H_2O abundance in depleted to moderately enriched mid-ocean ridge magmas; part I: incompatible behaviour, implications for mantle storage, and origin of regional variations. *J. Petrology* **41**, 1329-1364.

Dasgupta, R. and Hirschmann, M. (2007) A modified iterative sandwich method for determination of near-solidus partial melt compositions. II. Application to determination of near-solidus melt compositions of carbonated peridotite. *Contrib. Mineral. Petr.* **154**, 647-661.

Dasgupta, R., Hirschmann, M. M., and Smith, N. D. (2007) Water follows carbon: CO_2 incites deep silicate melting and dehydration beneath mid-ocean ridges. *Geology* **35**, 135-138.

Davis, F. A., Tangeman, J. A., Tenner, T. J., and Hirschmann, M. M. (2009) The composition of KLB-1 peridotite. *Am. Mineral.* **94**, 176-180.

Dixon, J. E., Stolper, E. M., and Holloway, J. R. (1995) An experimental study of water and carbon dioxide solubilities in mid ocean ridge basaltic liquids.1. Calibration and solubility models. *J. Petrol.* **36**, 1607-1631.

Falloon, T. J. and Danyushevsky, L. V. (2000) Melting of refractory mantle at 1.5, 2, and 2.5 GPa under anhydrous and H_2O-undersaturated conditions: implications for the petrogenesis of high-Ca boninites and the influence of subduction components on mantle melting. *J. Petrol.* **41**, 257-283.

Fine, G. and Stolper, E. M. (1986) Dissolved carbon dioxide in basaltic glasses: concentrations and speciation. *Earth Planet Sc. Lett.* **76**, 263-278.

Gaetani, G. A. and Grove, T. L. (1998) The influence of water on melting of mantle peridotite. *Contrib. Mineral. Petr.* **131**, 323-346.

Gose, J., Schmadicke, E., and Beran, A. (2009) Water in enstatite from Mid-Atlantic Ridge peridotite: evidence for the water content of suboceanic mantle? *Geology* **37**, 543-546.

Hauri, E. H., Gaetani, G. A., and Green, T. H. (2006) Partitioning of water during melting of the Earth's upper mantle at H_2O-undersaturated conditions. *Earth Planet Sc. Lett.* **248**, 715-734.

Herzberg, C. (2000) New experimental observations on the anhydrous solidus for peridotite KLB-1. *Geochem. Geophys. Geosyst.* **1**, 1051.

Herzberg, C. (2006) Petrology and thermal structure of the Hawaiian plume from Mauna Kea volcano. *Nature* **444**, 605-609.

Hirose, K. and Kushiro, I. (1993) Partial melting of dry peridotites at high pressures - determination of compositions of melts segregated from peridotite assemblage using aggregates of diamond. *Earth Planet Sc. Lett.* **114**, 477-489.

Hirschmann, M. M. and Stolper, E. M. (1996) A possible role for garnet pyroxenite in the origin of the "garnet signature" in MORB. *Contrib. Mineral. Petr.* **124**, 185-208.

Hirschmann, M. M., Aubaud, C., and Withers, A. C. (2005) Storage capacity of H_2O in nominally anhydrous minerals in the upper mantle. *Earth Planet Sc. Lett.* **236**, 167-181.

Hirschmann, M. M. and Dasgupta, R. (2007) A modified iterative sandwich method for determination of near-solidus partial melt compositions. I. Theoretical considerations. *Contrib. Mineral. Petr.* **154**, 635-645.

Hirschmann, M. M., Tenner, T., Aubaud, C., and Withers, A. C. (2009) Dehydration melting of nominally anhydrous mantle: the primacy of partitioning. *Phys. Earth Planet In.* **176**, 54-68.

Hirth, G. and Kohlstedt, D. L. (1996) Water in the oceanic upper mantle: implications for rheology, melt extraction and the evolution of the lithosphere. *Earth Planet Sc. Lett.* **144**, 93-108.

Holloway, J. and Kawamoto, T. (1997) Melting temperature and partial melt chemistry of H_2O-saturated mantle peridotite to 11 gigapascals. *Science* **276**, 240-243.

Humayun, M., Qin, L., and Norman, M. D. (2004) Geochemical evidence for excess iron in the mantle beneath Hawaii. *Science* **306**, 91-94.

Iwamori, H., McKenzie, D., and Takahashi, E. (1995) Melt generation by isentropic mantle upwelling. *Earth Planet Sc. Lett.* **134**, 253-266.

Johnson, K. T. M. and Kushiro, I. (1992) Segregation of high-pressure partial melts from peridotite using aggregates of diamond - a new experimental approach. *Geophys. Res. Lett.* **19**, 1703-1706.

Kägi, R., Muntener, O., Ulmer, P., and Ottolini, L. (2005) Piston-cylinder experiments on H_2O undersaturated Fe-bearing systems: an experimental setup approaching $f(O_2)$ conditions of natural calc-alkaline magmas. *Am. Mineral.* **90**, 708-717.

Kelemen, P. B., Dick, H. J. B., and Quick, J. E. (1992) Formation of harzburgite by pervasive melt/rock reaction in the upper mantle. *Nature* **358**, 635-641.

Kessel, R., Beckett, J. R., and Stolper, E. M. (2001) Thermodynamic properties of the Pt-Fe system. *Am. Mineral.* **86**, 1003-1014.

Kinzler, R. J. (1997) Melting of mantle peridotite at pressures approaching the spinel to garnet transition: application to mid-ocean ridge basalt petrogenesis. *J. Geophys. Res.* **102**, 853-874.

Klein, E. M. and Langmuir, C. H. (1989) Local versus global variations in ocean ridge basalt composition: A Reply. *J. Geophys. Res.* **94**, 4241–4252.

Kogiso, T. and Hirschmann, M. M. (2001) Experimental study of clinopyroxenite partial melting and the origin of ultra-calcic melt inclusions. *Contrib. Mineral. Petr.* **142**, 347-360.

Kushiro, I. (1968) Compositions of magmas formed by partial melting of the Earth's upper mantle. *J. Geophys. Res.* **73**, 619-634.

Kushiro, I. (1969) System forsterite-diopside-silica with and without water at high pressures. *Am. J. Sci.* **267A**, 269-294.

Kushiro, I. (1972) Effect of water on the composition of magmas formed at high pressures. *J. Petrol.* **13**, 311-334.

Kushiro, I. and Hirose, K. (1992) Experimental-determination of composition of melt formed by equilibrium partial melting of peridotite at high-pressures using aggregates of diamond grains. *Proceedings of the Japan Academy Series B-Physical and Biological Sciences* **68**, 63-68.

Liu, X., O'Neill, H. S. C., and Berry, A. J. (2006) The effects of small amounts of H_2O, CO_2 and Na_2O on the partial melting of spinel lherzolite in the system CaO-MgO-Al_2O_3-SiO_2 +/- H_2O +/- CO_2 +/- Na_2O at 1.1 GPa. *J. Petrol.* **47**, 409-434.

Longhi, J. and Bertka, C. M. (1996) Graphical analysis of pigeonite-augite liquidus equilibria. *Am. Mineral.* **81**, 685-695.

Longhi, J. (2002) Some phase equilibrium systematics of lherzolite melting: I. *Geochem. Geophys. Geosyst.* **3**, 1020.

Michael, P. J. (1988) The concentration, behavior and storage of H_2O in the suboceanic upper mantle: implications for mantle metasomatism. *Geochim. Cosmochim. Ac.* **52**, 555-566.

Michael, P. J. (1995) Regionally distinctive sources of depleted MORB - evidence from trace-elements and H_2O. *Earth Planet Sc. Lett.* **131**, 301-320.

Mosenfelder, J. L., Deligne, N. I., Asimow, P. D., and Rossman, G. R. (2006) Hydrogen incorporation in olivine from 2-12 GPa. *Am. Mineral.* **91**, 285-294.

Mysen, B. O., Virgo, D., Harrison, W. J., and Scarfe, C. M. (1980) Solubility mechanism of H_2O in silicate melts at high pressures and temperatures: a Raman spectroscopic study. *Am. Mineral.* **65**, 900-914.

Ohlhorst, S., Behrens, H., and Holtz, F. (2001). Compositional dependence of molar absorptivities of near-infrared OH^- and H_2O bands in rhyolitic to basaltic glasses. *Chem. Geol.* **174**, 5-20.

Parman, S. W. and Grove, T. L. (2004) Harzburgite melting with and without H_2O: experimental data and predictive modeling. *J. Geophys. Res.* **109**, B02201.

Pertermann, M. and Hirschmann, M. M. (2003a) Anhydrous partial melting experiments on MORB-like eclogite: phase relations, phase compositions and mineral-melt partitioning of major elements at 2-3 GPa. *J. Petrol.* **44**, 2173-2201.

Pertermann, M. and Hirschmann, M. M. (2003b) Partial melting experiments on a MORB-like pyroxenite between 2 and 3 GPa: constraints on the presence of pyroxenite in basalt source regions from solidus location and melting rate. *J. Geophys. Res.* **108**, 2125.

Putirka, K., Johnson, M., Kinzler, R., Longhi, J., and Walker, D. (1996) Thermobarometry of mafic igneous rocks based on clinopyroxene-liquid equilibria, 0–30 kbar. *Contrib. Mineral. Petr.* **123**, 92-108.

Robinson, J. A. C. and Wood, B. J. (1998) The depth of the spinel to garnet transition at the peridotite solidus. *Earth Planet Sc. Lett.* **164**, 277-284.

Robinson, J. A. C., Wood, B. J., and Blundy, J. D. (1998) The beginning of melting of fertile and depleted peridotite at 1.5 GPa. *Earth Planet Sc. Lett.* **155**, 97-111.

Salters, V. J. M. and Hart, S. R. (1989) The hafnium paradox and the role of garnet in the source of mid-ocean-ridge basalts. *Nature* **342**, 420-422.

Salters, V. J. M. and Longhi, J. (1999) Trace element partitioning during the initial stages of melting beneath mid-ocean ridges. *Earth Planet Sc. Lett.* **166**, 15-30.

Schwab, B. E. and Johnston, A. D. (2001) Melting systematics of modally variable, compositionally intermediate peridotites and the effects of mineral fertility. *J. Petrology* **42**, 1789-1811.

Shen, Y. and Forsyth, D. W. (1995) Geochemical constraints on initial and final depths of melting beneath mid-ocean ridges. *J. Geophys. Res.* **100**, 2211–2237.

Smith, P. M. and Asimow, P. D. (2005) Adiabat_1ph: A new front end to the MELTS, pMELTS, and pHMELTS models. *Geochem. Geophys. Geosyst.* **6**, Q02004.

Stolper, E. (1980) A phase diagram for mid-ocean ridge basalts: preliminary results and implications for petrogenesis. *Contrib. Mineral. Petr.* **74**, 13-27.

Stolper, E. and Newman, S. (1994) The role of water in the petrogenesis of Mariana Trough magmas. *Earth Planet Sc. Lett.* **121**, 293-325.

Takahashi, E. and Kushiro, I. (1983) Melting of a dry peridotite at high pressures and basalt magma genesis. *Am. Mineral.* **69**, 859-879.

Toplis, M. J. (2005) The thermodynamics of iron and magnesium partitioning between olivine and liquid: criteria for assessing and predicting equilibrium in natural and experimental systems. *Contrib. Mineral. Petr.* **149**, 22-39.

Tsuchiyama, A., Nagahara, H., and Kushiro, I. (1981) Volatilization of sodium from silicate melt spheres and its application to the formation of chondrules. *Geochim. Cosmochim. Ac.* **45**, 1357-1367.

Wallace, M. E. and Green, D. H. (1988) An experimental determination of primary carbonatite magma composition. *Nature* **335**, 343-346.

Walter, M. J. (1998) Melting of garnet peridotite and the origin of komatiite and depleted lithosphere. *J. Petrology* **39**, 29-60.

Wasylenki, L., Baker, M., Kent, A., and Stolper, E. (2003) Near-solidus melting of the shallow upper mantle: partial melting experiments on depleted peridotite. *J. Petrol.* **44**, 1163-1191.

White, R. S., McKenzie, D., and O'Nions, R. K. (1992) Oceanic crustal thickness from seismic measurements and rare earth element inversions. *J. Geophys. Res.* **97**, 19683-19715.

Wood, B. J., Blundy, J. D., and Robinson, J. A. C. (1999) The role of clinopyroxene in generating U-series disequilibrium during mantle melting. *Geochim. Cosmochim. Ac.* **63**, 1613-1620.

Yaxley, G. and Sobolev, A. (2007) High-pressure partial melting of gabbro and its role in the Hawaiian magma source. *Contrib. Mineral. Petr.* **154**, 371-383.

TABLES

Table 1:	Na_2O	MgO	Al_2O_3	SiO_2	K_2O	CaO	TiO_2	NiO	MnO
CPX	1.98(9.1)	19.79(88)	6.85(35)	53.54(73)	0.00(0.5)	12.82(53)	0.26(1.6)	0.07(2.4)	0.10(1.4)
Olivine	0.03(1.1)	49.07(83)	0.13(14)	40.91(76)	0.00(0.4)	0.18(6.8)	0.007(0.6)	0.32(8.6)	0.10(1.7)
Garnet	0.03(2.2)	22.46(25)	22.29(28)	42.64(44)	0.00(0.7)	4.75(13)	0.23(1.5)	0.02(1.6)	0.19(1.7)
Az Gt	0.03(1.1)	20.67(66)	23.30(35)	41.83(68)	0.0(0.6)	4.22(9.2)	0.076(1.8)	0(2.3)	0.32(2.5)
R377 OPX	0.33(3.4)	31.30(21)	5.642(27)	55.60(28)	0.00(0.3)	1.90(9.1)	0.063(0.6)	0.01(1.7)	0.10(1.9)

Continued:	FeO	Cr_2O_3	Totals	Mg#	Modal Abundance
CPX	4.19(19)	0.54(3.2)	100.20(71)	0.893	0.30(2)
Olivine	9.87(61)	0.05(1.9)	100.74(64)	0.898	0.62(4)
Garnet	6.66(11)	0.87(4.6)	100.21(66)	0.857	0.08(4)
Az Gt	8.86(37)	0.30(2.5)	99.66(128)	0.805	
R377 OPX	6.06(23)	0.45(5.4)	101.51(26)	0.901	

Table 1: Measured compositions of solid phases from sub-solidus recrystallized peridotites. Modal Abundance calculated by least squares fit to the bulk composition of KLB-1 given by Davis et al. (2009). The AZ garnet shows the composition of the garnet seed

that was added in small amounts to the peridotite mixture before recrystallization to overcome any nucleation issues. Modal abundances were calculated via least squares fit to the measured compositions. The opx from R377 comes from an earlier step in the iteration and is given to show the composition of opx seen with these hydrous melts. Values in parentheses are 100 * the standard deviation of the electron microprobe analyses, except in the modal abundance column, which is calculated. The variation in modal abundance was calculated by Monte Carlo simulation carrying through the variance in the electron probe measurements and in the bulk composition as given by Davis et al. (2009).

Table 2: experimental results

R385	Na_2O	P_2O_5	MgO	Al_2O_3	SiO_2	K_2O	CaO	TiO_2	NiO	MnO
Liq	3.23(10)	0.00(0.7)	13.40(7.9)	12.71(10)	45.38(29)	0.49(2.7)	9.05(6.2)	0.80(2.4)	0.00(1.8)	0.15(0.6)
Ol	0.02(0.3)	0.00(0.6)	47.71(59)	0.05(1.8)	40.86(12)	0.00(0.3)	0.23(2.4)	0.00(0.5)	0.02(0.8)	0.13(0.5)
Gt	0.04(1.1)	0.00(0.8)	18.76(70)	22.91(22)	42.09(18)	0.00(0.2)	6.13(38)	0.28(6.6)	0.00(0.6)	0.24(0.9)
CPX	1.87(14)	0.01(0.7)	17.24(70)	5.79(43)	53.09(53)	0.00(0.6)	17.44(76)	0.23(9.5)	0.00(0.7)	0.10(0.7)
R390										
Liq	2.78(14)	0.01(1.2)	13.43(6.8)	12.52(12)	43.77(19)	0.44(1.6)	9.85(6.7)	0.72(2.1)	0.02(2.1)	0.16(0.5)
Ol	0.01(0.4)	0.00(0.1)	47.07(19)	0.04(1.8)	40.81(13)	0.00(0)	0.17(1.9)	0.00(0)	0.03(1.2)	0.13(0.7)
Gt	0.02(0.3)	0.01(0.9)	17.21(48)	22.44(19)	41.84(29)	0.00(0.3)	6.99(34)	0.21(3.1)	0.00(0.4)	0.23(0.9)
CPX	1.43(2.4)	0.01(0.6)	17.56(13)	5.35(17)	53.36(37)	0.00(0.3)	17.95(54)	0.12(1.1)	0.00(0.3)	0.10(0.7)
R395										
Liq	2.69(12)	0.01(1.1)	14.47(13)	12.57(13)	45.47(33)	0.37(1.9)	9.49(9.1)	0.69(1.1)	0.00(0.9)	0.14(0.5)
Ol	0.01(3.9)	0.00(0.5)	48.84(12)	0.26(10)	41.36(13)	0.00(0.2)	0.31(30)	0.00(0.4)	0.04(0.9)	0.12(0.3)
Gt	0.02(0.3)	0.00(0.9)	19.57(17)	22.92(31)	42.55(28)	0.00(0)	6.28(14)	0.23(0.0)	0.00(1.2)	0.22(0.5)
CPX	1.39(0.7)	0.01(0.7)	19.03(39)	5.08(19)	53.58(21)	0.00(0.1)	16.05(26)	0.10(8.3)	0.00(0.6)	0.10(0.9)
R389										
Liq	2.46(10)	0.00(1.1)	14.09(24)	13.0(10)	45.29(26)	0.38(3.1)	9.70(6.3)	0.68(1.8)	0.01(1.8)	0.15(0.7)
Ol	0.00(3.7)	0.00(0.6)	47.80(96)	0.03(35)	40.73(42)	0.00(0.2)	0.17(46)	0.00(3.1)	0.01(0.9)	0.13(0.8)
Gt	0.03(6.7)	0.00(0.1)	19.28(43)	22.24(46)	42.12(15)	0.00(0.5)	6.47(81)	0.16(0.9)	0.00(0.2)	0.24(0.3)
CPX	1.10(0.2)	0.00(0.1)	18.04(18)	5.19(1.0)	53.08(7.2)	0.00(0.2)	17.03(0.8)	0.13(0)	0.00(0.7)	0.11(0.2)
R398										
Liq	2.76(1.1)	0.01(0.9)	14.81(34)	12.47(11)	44.69(53)	0.43(0.3)	9.52(23)	0.67(6.2)	0.00(1.8)	0.15(1.8)
Ol	0.00(4.8)	0.00(0.7)	50.14(21)	0.03(6.3)	40.42(25)	0.00(0.3)	0.20(51)	0.00(1.1)	0.01(1.4)	0.12(0.7)
Gt	0.02(0.6)	0.01(0.7)	20.51(54)	22.75(1.8)	41.63(58)	0.00(0)	6.55(3.3)	0.20(0.0)	0.01(1.4)	0.22(0.9)
CPX	1.25(20)	0.02(1.3)	18.74(29)	5.07(14)	53.01(40)	0.00(4.4)	17.27(9.0)	0.10(1.8)	0.01(1.5)	0.09(0.7)
R396										

Liq	2.86(1.1)	0.01(0.5)	13.95(33)	13.01(13)	43.69(27)	0.34(0.2)	9.52(20)	0.74(2.5)	0.00(1.7)	0.14(0.8)
Ol	0.01(0.6)	0.00(1.1)	48.22(53)	0.07(6.4)	40.41(23)	0.00(0.1)	0.27(16)	0.00(0.5)	0.05(1.4)	0.12(1.0)
Gt	0.01(2.3)	0.00(1.1)	20.43(26)	23.01(16)	41.91(21)	0.00(0.3)	6.26(34)	0.17(1.1)	0.00(0.8)	0.23(1.9)
CPX	1.21(6.6)	0.01(2.0)	18.16(15)	5.81(8.7)	52.96(40)	0.00(1.4)	16.93(7.5)	0.12(1.8)	0.00(1.3)	0.09(0.8)
R380IC										
IC Liq	2.47(0.8)	0.01(0.7)	15.15(56)	11.61(24)	44.11(26)	0.23(0.2)	8.11(3.2)	0.54(0.3)	0.01(2.0)	0.12(1.3)
IC OL	0.01(1.1)	0.00(0.9)	46.35(78)	0.11(40)	40.51(35)	0.00(0.3)	0.18(59)	0.00(5.4)	0.05(1.6)	0.10(1.7)
IC GT	0.02(9.9)	0.00(1.5)	19.18(16)	22.60(12)	41.60(27)	0.00(1.9)	5.68(12)	0.22(2.2)	0.01(1.6)	0.20(1.4)
R380OC										
Liq	2.83(1.0)	0.00(1.0)	14.56(22)	12.41(2.4)	44.64(19)	0.32(0.3)	9.30(1.7)	0.64(0.3)	0.00(1.3)	0.14(0.8)
Ol	0.01(3.8)	0.00(0.9)	48.18(54)	0.06(62)	40.73(45)	0.00(0.2)	0.20(41)	0.00(9.3)	0.03(1.2)	0.11(1.4)
Gt	0.04(3.9)	0.01(1.2)	20.30(19)	21.96(23)	42.11(43)	0.00(0.4)	6.17(25)	0.20(2.1)	0.00(0.8)	0.21(1.6)
CPX	1.17(11)	0.01(3.2)	18.79(39)	5.52(9.9)	52.91(10)	0.00(1.4)	15.96(12)	0.10(2.7)	0.00(0.5)	0.10(2.2)
R393 IC										
Liq	2.47(0.8)	0.01(1.0)	13.26(54)	11.91(8.6)	43.67(30)	0.26(0.4)	8.83(3.9)	0.59(0.6)	0.02(2.3)	0.15(1.5)
Ol	0.01(1.2)	0.00(1.1)	46.62(53)	0.08(25)	40.52(24)	0.00(0.3)	0.20(40)	0.00(3.3)	0.04(0.9)	0.11(1.7)
Gt	0.01(10.0)	0.01(1.6)	20.06(61)	22.60(20)	42.15(22)	0.00(2.2)	5.27(34)	0.14(4.2)	0.00(2.7)	0.20(2.2)
R393OC										
Liq	2.87(7.7)	0.01(1.8)	14.06(8.6)	12.75(11)	44.37(18)	0.38(1.3)	9.34(6.5)	0.72(1.1)	0.02(1.6)	0.15(0.6)
Ol	0.01(0.6)	0.01(0.2)	48.63(23)	0.05(0.8)	40.76(10)	0.00(0.2)	0.21(4.2)	0.00(0.2)	0.03(1.0)	0.12(0.1)
Gt	0.01(0.8)	0.01(0.7)	19.89(43)	22.91(7.4)	42.11(13)	0.00(0.2)	6.13(21)	0.21(5.0)	0.00(0.6)	0.22(0.8)
CPX	1.26(3.9)	0.01(0.9)	18.58(19)	5.57(8.1)	52.96(7.0)	0.00(0.3)	16.64(14)	0.13(1.0)	0.01(1.0)	0.10(0.6)

Table 2 continued:

R385	FeO	Cr_2O_3	Oxide Totals	Mg#	K_D	H_2O	CO_3	Liquid totals
Liq	9.12(12)	0.08(2.7)	95.38(45)	0.72		5.53	0.24	101.16

Ol	11.35(28)	0.02(1.9)	100.44(26)	0.88	0.35			
Gt	9.25(59)	0.33(18)	100.08(27)	0.78				
CPX	4.34(29)	0.22(21)	100.40(43)	0.87				
R390								
Liq	10.36(11)	0.10(1.9)	94.28(22)	0.70		5.37	0.28	99.94
Ol	12.30(36)	0.03(0.7)	100.64(8)	0.87	0.34			
Gt	10.71(68)	0.87(12)	100.58(23)	0.74				
CPX	4.39(33)	0.36(7.8)	100.68(16)	0.88				
R395								
Liq	7.24(12)	0.12(1.1)	93.31(57)	0.78		5.31	0.32	98.95
Ol	9.66(42)	0.04(7.3)	100.67(49)	0.90	0.38			
Gt	8.21(82)	0.68(1.5)	100.74(22)	0.81				
CPX	4.11(38)	0.51(10)	100.01(23)	0.89				
R389								
Liq	8.05(12)	0.14(3.7)	94.02(25)	0.76		6	0.15	100.18
Ol	10.91(82)	0.06(31)	99.88(31)	0.89	0.40			
Gt	8.01(59)	1.23(1.6)	99.84(18)	0.81				
CPX	4.41(32)	0.49(0.9)	99.63(14)	0.88				
R398								
Liq	8.56(12)	0.12(12)	94.23(83)	0.75		5.41	0.38	100.03
Ol	9.51(26)	0.06(11)	100.54(45)	0.90	0.33			
Gt	8.24(23)	0.64(0.9)	100.83(107)	0.82				
CPX	4.31(12)	0.34(1.5)	100.27(59)	0.89				
R396								
Liq	8.66(16)	0.09(10)	93.07(34)	0.74		4.78	0.33	98.18
Ol	10.78(52)	0.03(0.8)	100.02(10)	0.89	0.36			
Gt	8.13(17)	0.80(15)	101.00(22)	0.82				
CPX	4.60(11)	0.43(1.3)	100.38(60)	0.88				

R380IC								
IC Liq	11.5(32)	0.15(1.6)	94.13(54)	0.71		2.7	0.24	97.08
IC OL	12.76(81)	0.06(20)	100.17(37)	0.87	0.36			
IC GT	9.48(22)	0.60(1.8)	99.64(41)	0.78				
R380OC								
Liq	9.44(27)	0.11(0.7)	94.46(52)	0.73		4	0.61	99.07
Ol	10.40(48)	0.04(23)	99.82(31)	0.89	0.33			
Gt	7.69(21)	0.67(9.7)	99.41(45)	0.82				
CPX	4.37(18)	0.49(1.4)	99.48(52)	0.88				
R393 IC								
Liq	11.30(17)	0.15(2.1)	92.68(47)	0.68		4.1	0.08	96.86
Ol	12.95(48)	0.07(24)	100.66(37)	0.87	0.33			
Gt	8.70(34)	1.05(3.2)	100.25(56)	0.80				
R393OC								
Liq	8.58(13)	0.10(2.8)	93.39(22)	0.74		4.1	0.105	97.60
Ol	10.76(14)	0.03(0.6)	100.65(24)	0.89	0.36			
Gt	7.85(38)	0.60(14)	100.00(16)	0.82				
CPX	4.18(15)	0.31(8.1)	99.82(18)	0.89				

Table 2: Full experimental results, concentrations given in weight percent. 2 samples do not have cpx analyses presented; the cpx grains available were small and we were unable to obtain electron probe analyses that were not contaminated by the exterior quench layer. An average of these liquid compositions was used to calculate the final representative liquid given in Table 3, with edits to the TiO_2 concentration as discussed in the text. Values in parentheses are 100 * the standard deviation of the electron microprobe measurements. Errors on volatile contents are ~10% relative, as discussed in the text.

Table 3

	This work					
	Hydrous	Volatile-free	pHMELTS	Longhi	Walter	Gaetani and Grove
SiO_2	44.56	47.42	42.44	45.60	46.17	43.88
Al_2O_3	12.60	13.41	8.97	15.10	13.32	15.41
CaO	9.40	10.01	3.00	6.91	10.69	10.2
MgO	14.01	14.91	15.58	15.30	16.90	13.36
FeO	9.04	9.62	9.59	9.60	9.55	8.21
Na_2O	2.78	2.96	15.03	2.68	0.96	2.2
K_2O	0.38	0.41	0.00	2.13	0.56	0.1
MnO	0.15	0.12	0.00	0.21	0.18	0.12
TiO_2	0.90	0.96	1.16	1.43	0.91	0.64
Cr_2O_3	0.12	0.12	1.61	0.22	0.31	0.15
H_2O	4.95		2.56			5.3
CO_3	0.10					1.25

Table 3: Our given liquid composition estimated to be an average hydrous liquid that could be produced by melting KLB-1 under the pressure and temperature conditions used here. The composition is presented on a hydrous basis and renormalized to a volatile-free basis to allow for comparison between studies. The pHMelts liquid was calculated as described in the text. The liquid from Longhi (2002) is their calculated 1% melt of PUM. The liquid from Walter (1998) is experiment 30.12, which is the lowest temperature liquid

composition given from 3 GPa, although the solid assemblage for this sample did not include garnet. The liquid from Gaetani and Grove (1998) is sample B365. These liquids (all normalized to volatile-free conditions) are plotted in figure 7.

FIGURE CAPTIONS

Figure 1: Backscattered electron image of a section of a typical recrystallized peridotite. High relief, bright grains are garnet, lower relief or small grains are cpx, and the darker matrix is composed of olivine grains. Typical grain size is ~20 μm for the garnets and the olivines and ~10 μm for the cpx. Voids are formed where grains were plucked during polishing. Bright spot is a surface contaminant.

Figure 2: Schematic capsule design. Outer capsule and inner capsule are loaded with identical glass starting material, with additional solid peridotite added to inner capsule. Inner capsule is an Fe-preconditioned Au_{75}-Pd_{25} metal, outer capsule is made of Fe-preconditioned Pt.

Figure 3: Backscattered Electron Images of experimental run products. (a) The melt pool at the top of R380. Some quench needles can be seen at the bottom of the image, along with several spots showing polishing or probe-beam damage. AuPd capsule is pure white in this image. (b) The solid pile from the bottom of the same run. Dark crystals are olivine grains, lighter crystals are garnet and cpx. Bright rims around most grains are quench features. Dark, interstitial material is composed of glass or partially crystalline groundmass that has lost much of its MgO, FeO, and often CaO to the quench boundaries on the grains. Horizontal elongate features are cracks formed on quench; occasionally they appear to have bright spots due to polishing material or epoxy being trapped within them. Circular features in Figure 3a also appear to be related to polishing damage or

plucking; they were polished to variable depths and confirmed not to be vesicles optically.

Figure 4: Measured volatile contents for these experiments compared with the volatile contents of Gaetani and Grove (1998) (red point) and the field of volatile contents (blue ellipse) from the experiments of Liu et al. (2006). Our experiments are not only at higher pressure than previously conducted experiments, but they also sample a range of volatile contents that has not been sampled previously.

Figure 5: Example FTIR spectra of glasses. (a) 3600 cm^{-1} water peak from sample R393, thinned down to ~45 μm to bring this peak on scale. (b) The characteristic structure seen in our OH^- peak spectra. The peak near 4000 cm^{-1} is typical of water-bearing glasses, but the peak at 4500 cm^{-1} is split into multiple peaks. Calculating a total OH^- content using the most intense of these peaks in this range, an H_2O content using the 5200 cm^{-1} peak, and using the calibration of Ohlhorst et al. (2000), gives water contents that are indistinguishable from those measured using the 3600 cm^{-1} peak and the calibration of Dixon et al. (1995).

Figure 6: Correlation between OH^- contents and carbonate contents as measured by FTIR. Error bars are as discussed in the text. R380 (red point) falls off the trend as it is the lowest total water content sample and likely has not saturated fully in OH^-.

Figure 7: Concentration in given liquids normalized to concentration in N-MORB of Hofmann (1988). K_2O, MnO, and Cr_2O_3 were compared to a value of 0.1, as they are either not given or are impractically low in that work. pHMelts cannot include MnO or K_2O effectively, so those two oxides were not included in the calculation and their values are not plotted.

Figure 8: Molar (MgO + FeO)/SiO_2 ratios, as described in the text. Also shown in addition to our data are all data points from 3-4 GPa from Walter (1998), the two points from 2 GPa from Gaetani and Grove (1998), and the 1% melt of primitive upper mantle (PUM) at 3 GPa from Longhi (2002). Increasing water in our samples and those of Gaetani and Grove (1998) is associated with increasing X_{SiO2} and a decrease in the ratio $(X_{FeO} + X_{MgO})/X_{SiO2}$, and thus moves towards the lower right in this diagram. Increasing temperature and increasing degree of melting has the opposite effect and moves liquids towards the upper left. Increasing carbon content may counteract some of the effect of water, and thus the samples from Gaetani and Grove plot closer to our field from higher temperature and pressure than might be expected at lower carbon contents. The calculated melt from pHMELTS is also shown. Figure 8b shows the correlation in our samples between increasing water content and decreasing $(X_{FeO} + X_{MgO})/X_{SiO2}$.

Figure 9: Solid and liquid compositions from the experiments presented here plotted in the model system olivine/nepheline-calcium aluminate/larnite/quartz, as described by Longhi (2002). Abbreviations: Jd/CaTS (jadeite/calcium-tschermakite), AnAb

(anorthite/albite), Gt (garnet), OPX (orthopyroxene), Di (diopside), Qtz (quartz), Ol (olivine), NeCa (nepheline-calcium aluminate), Wo (wollastonite) and CPX (clinopyroxene). Here the compositions are projected from wollastonite onto the Ol-Qtz-NeCA plane. Also shown are: the compositions of garnet and cpx from our anhydrous recrystallization experiments (black diamonds, labeled with arrows) and the composition of an anhydrous 1% melt of PUM calculated by Longhi (2002). Each experiment that produced measurements of a liquid, cpx, and garnet composition gives three composition points, shown connected by a triangle. In general, the points move away from the point PUM and away from olivine with increasing total H_2O plus alkali contents, as represented by the arrow. R390 (green triangles) is a notable outlier to this trend. Inset shows the full compositional triangle with the red box delimiting the area seen in the larger image.

Figure 10: Solid and liquid compositions plotted in the same normative component space as Figure 9, but here projected from olivine into the plane OPX-Wo-Jd/CaTS. Also shown are: the composition of our dry cpx and garnet (black diamonds, labeled) the composition of KLB-1 as measured by Davis et al. (2009), the fields of cpx (green ellipse) and garnet (red circle) compositions from the 2.8 GPa experiments of Longhi (2002), the edge of the cpx field at 2.8 GPa from Longhi (2002) (solid green line) the boundary of the cpx field at 0.1 MPa from Longhi (2002) (dashed green line), and the approximate position of the garnet-cpx-olivine cotectic from 2.8 GPa from Longhi (2002) (dashed orange line). Our hydrous experiments produced garnets with slightly more aluminous compositions but still within the field sampled by Longhi (2002). Our

subsolidus cpx composition falls within error on the line forming the edge of the 2.8 GPa cpx field. All of the cpx from our wet experiments shift significantly in composition towards diopside and away from albite-anorthite. This shift consists of a change in composition towards lower Al_2O_3 and higher CaO contents in the hydrous experiments. In general, increasing liquid contents of alkalis + H_2O tends to shift the liquid and cpx composition as shown by the arrows; the cpx moves away from OPX while the liquid moves towards it. Our liquids project within error on the 2.8 GPa olivine-cpx-garnet cotectic from Longhi (2002).

FIGURES

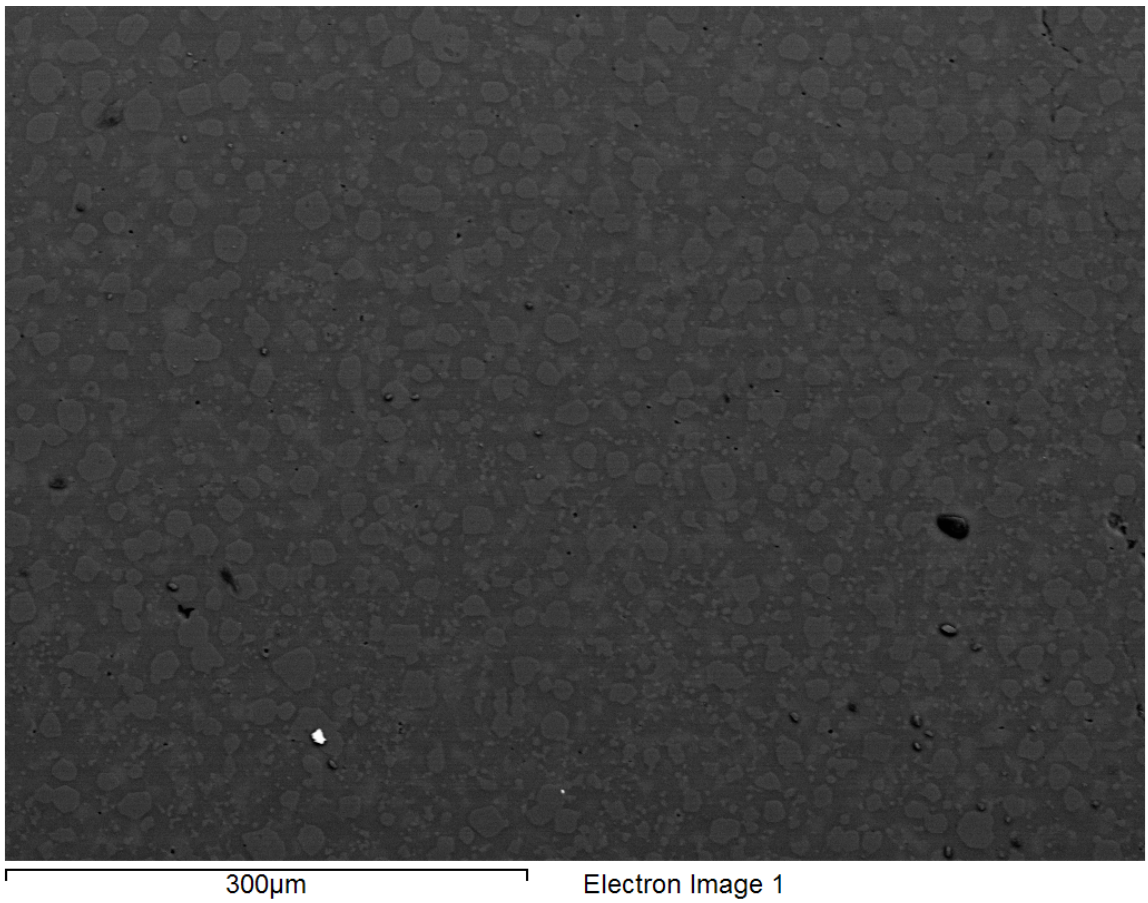

Figure 1

Figure 2

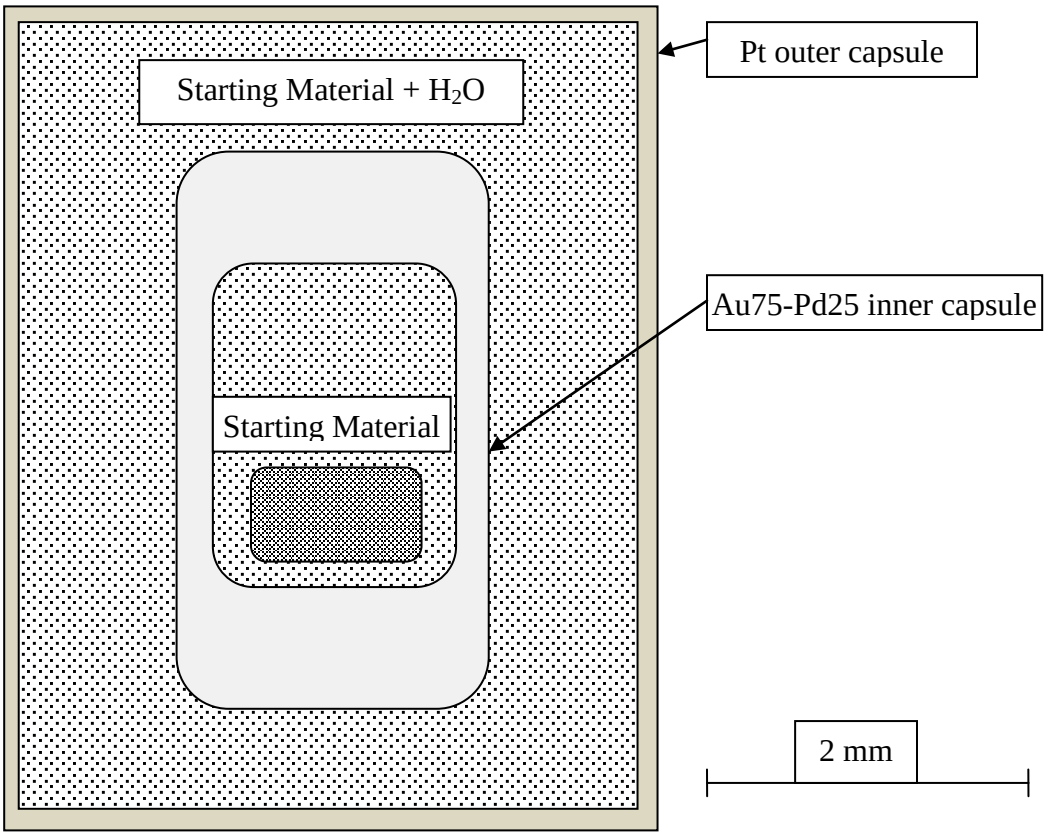
Pt outer capsule
Starting Material + H_2O
Au75-Pd25 inner capsule
Starting Material
2 mm

Figure 3

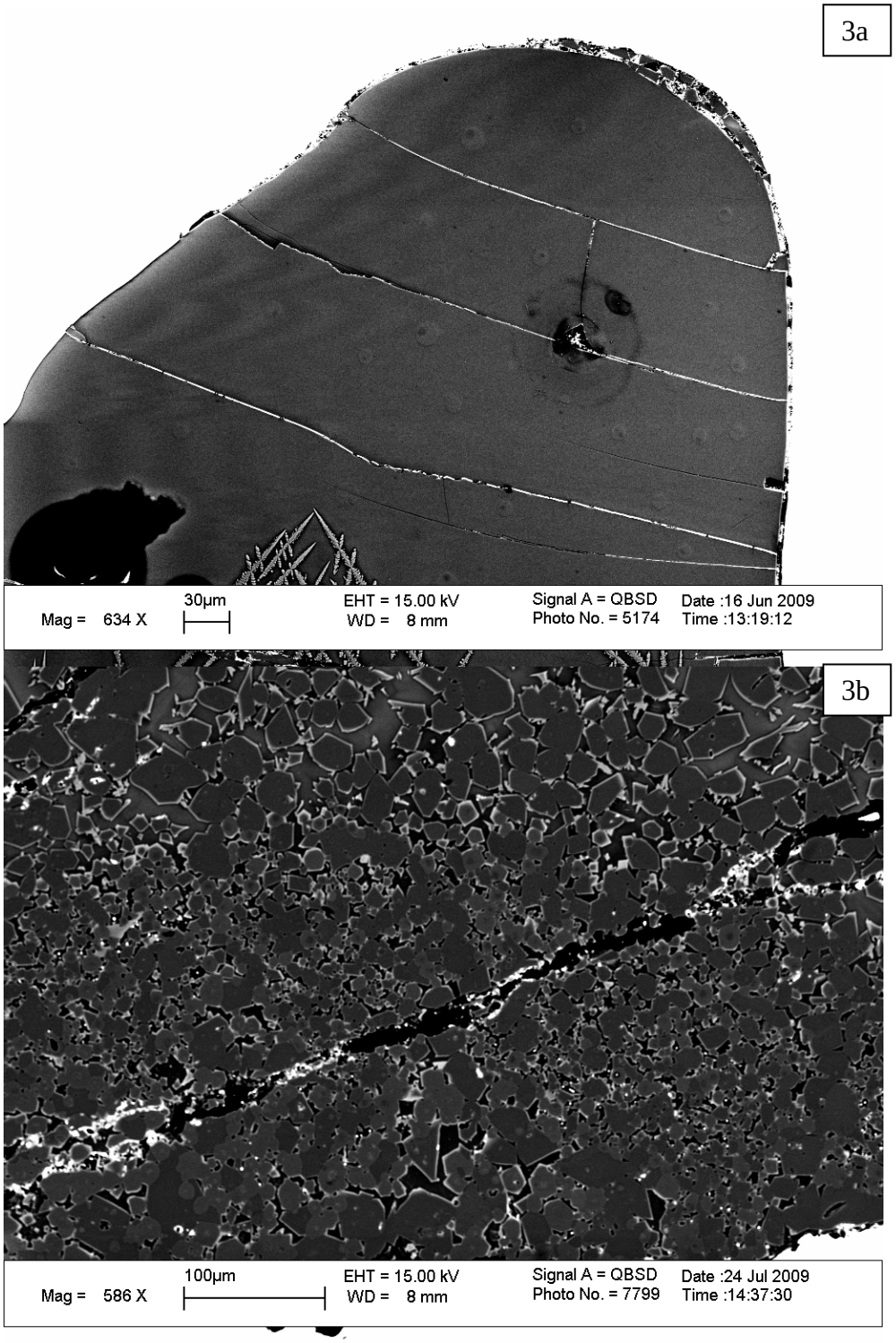
3a
Mag = 634 X
30µm
EHT = 15.00 kV
WD = 8 mm
Signal A = QBSD
Photo No. = 5174
Date :16 Jun 2009
Time :13:19:12
3b
Mag = 586 X
100µm
EHT = 15.00 kV
WD = 8 mm
Signal A = QBSD
Photo No. = 7799
Date :24 Jul 2009
Time :14:37:30

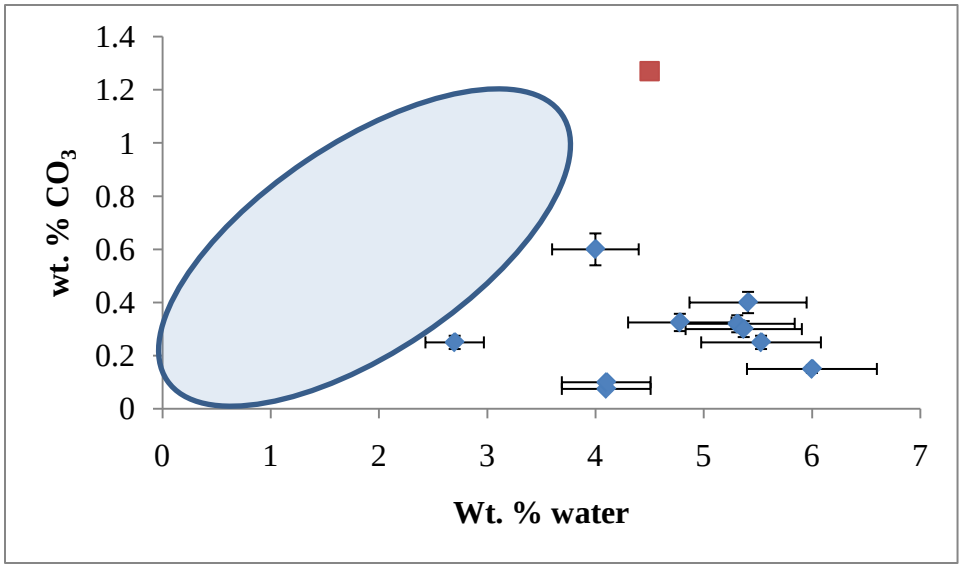

Figure 4

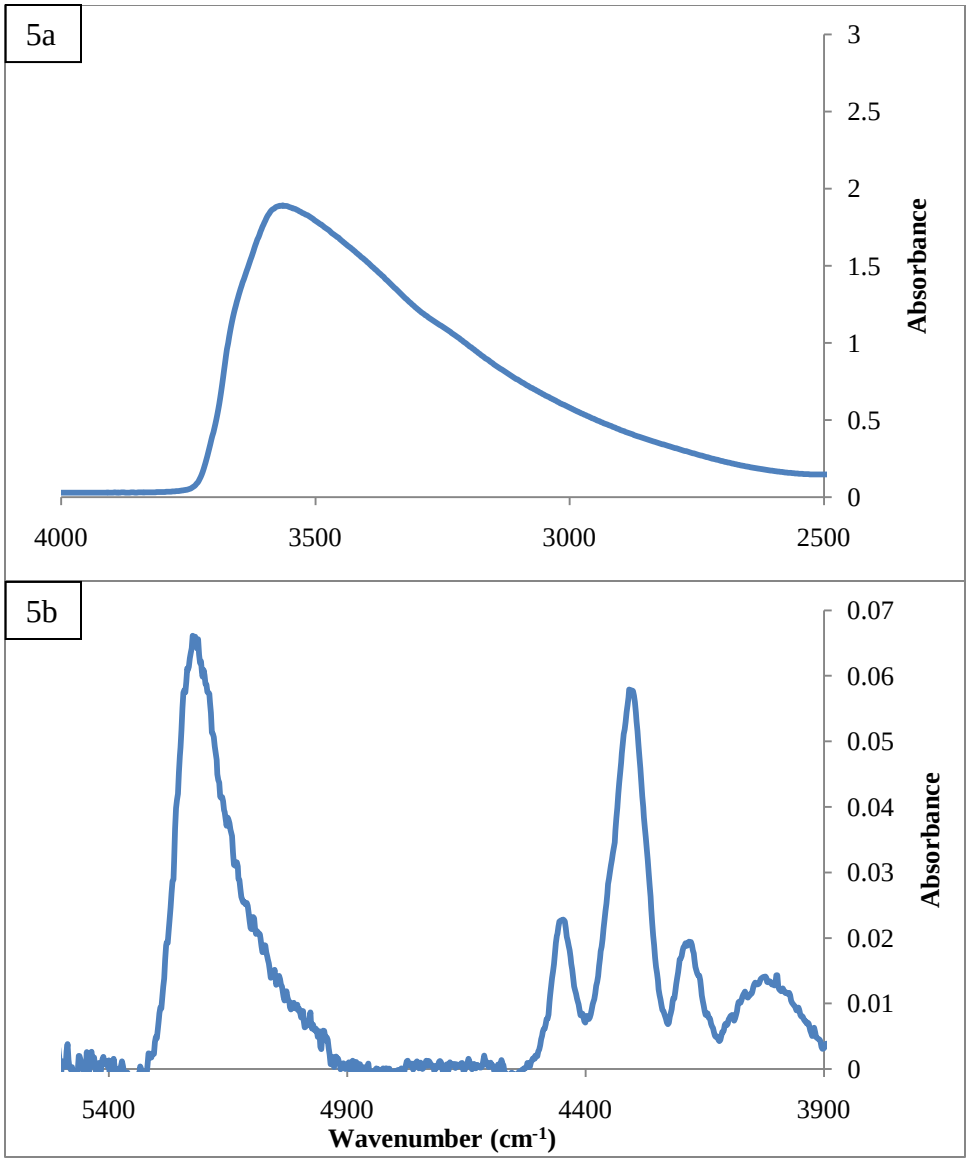
5a
3
2.5
2
1.5
1
0.5
0
Absorbance
4000
3500
3000
2500
5b
0.07
0.06
0.05
0.04
0.03
0.02
0.01
0
Absorbance
5400
4900
4400
3900
Wavenumber (cm-1)

Figure 5

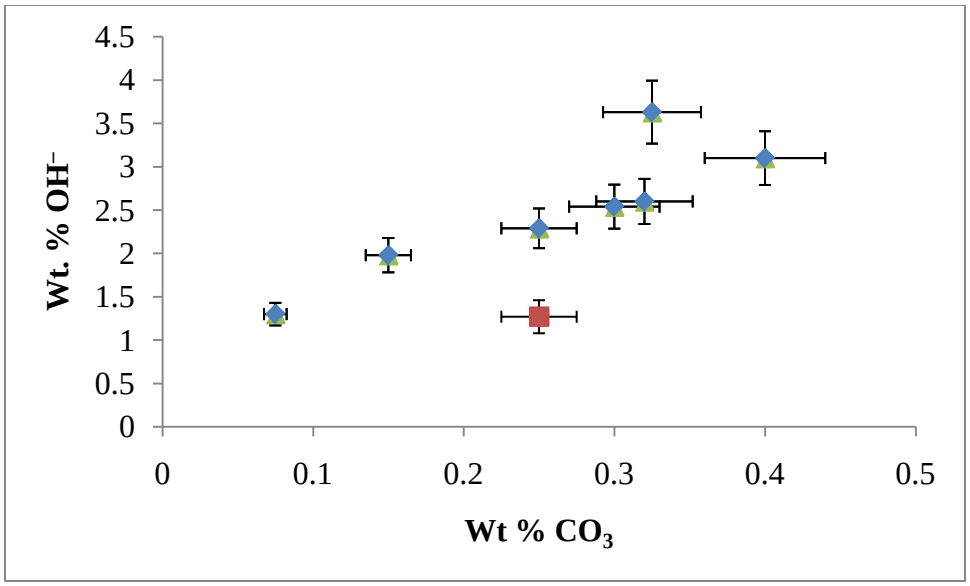

Figure 6

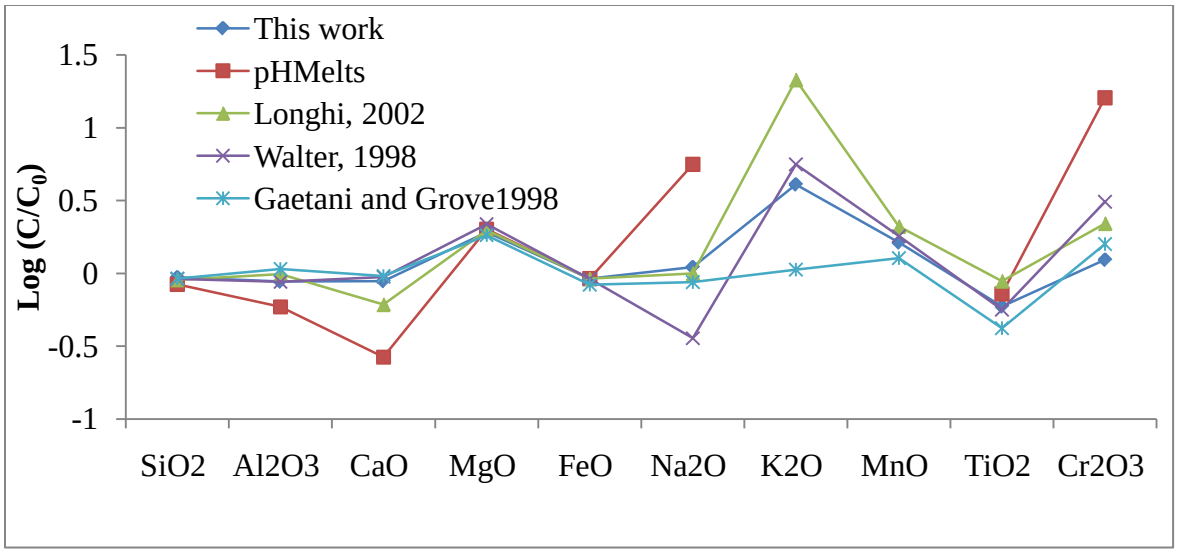
This work
pHMelts
Longhi, 2002
Walter, 1998
Gaetani and Grove1998
1.5
1
0.5
0
-0.5
-1
Log (C/C0)
SiO2
Al2O3
CaO
MgO
FeO
Na2O
K2O
MnO
TiO2
Cr2O3

Figure 7

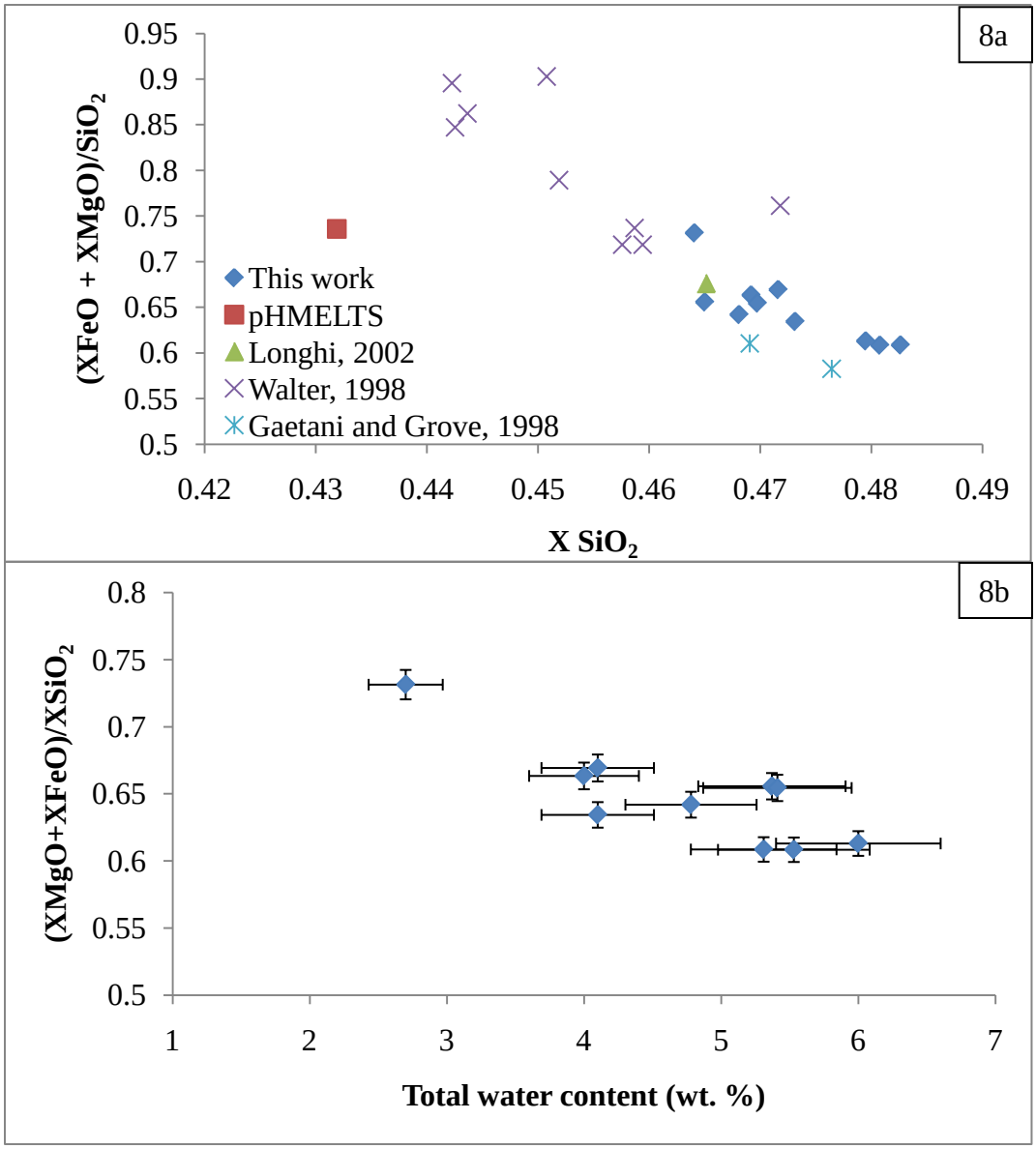
8a
0.95
0.9
0.85
0.8
0.75
0.7
0.65
0.6
0.55
0.5
(XFeO + XMgO)/SiO2
This work
pHMELTS
Longhi, 2002
Walter, 1998
Gaetani and Grove, 1998
0.42
0.43
0.44
0.45
0.46
0.47
0.48
0.49
X SiO2
8b
0.8
0.75
0.7
0.65
0.6
0.55
0.5
(XMgO+XFeO)/XSiO2
1
2
3
4
5
6
7
Total water content (wt. %)

Figure 8

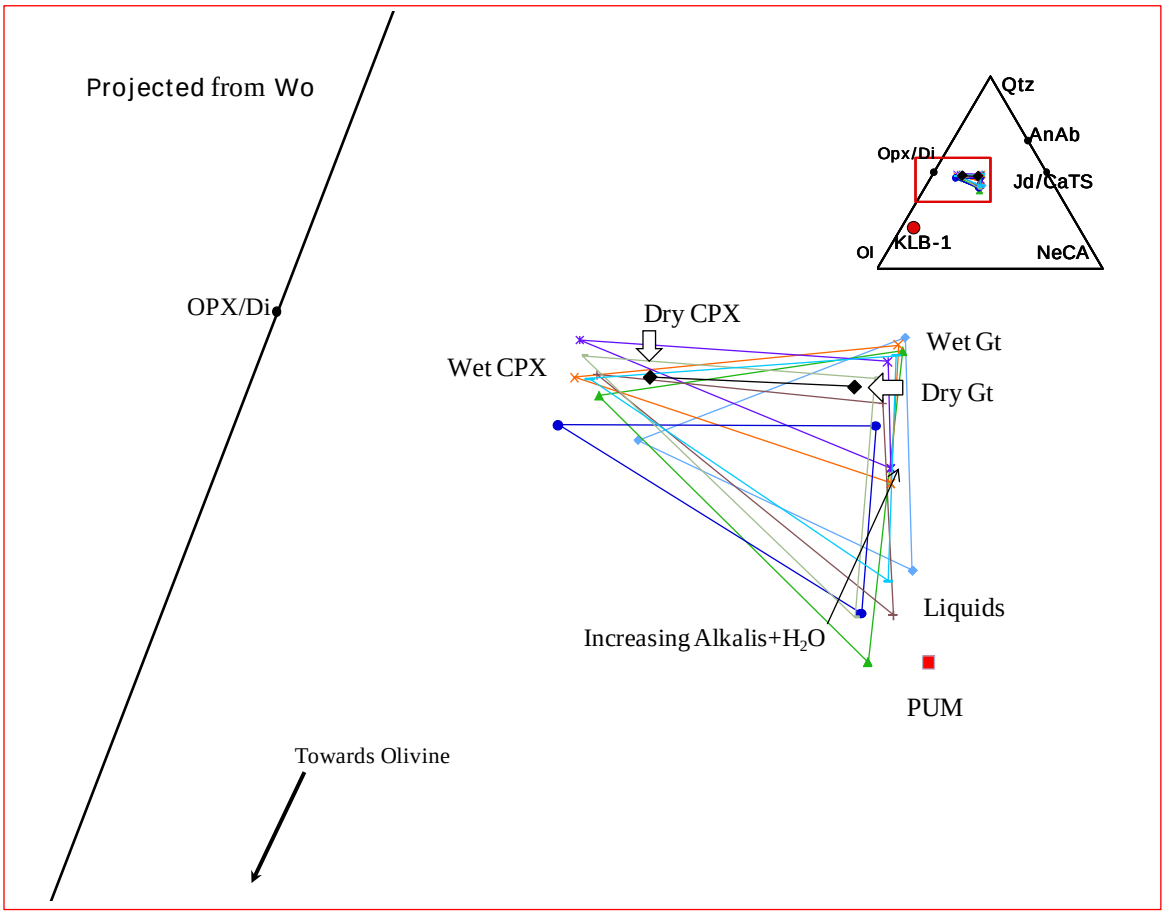
Projected from Wo
OPX/Di
Towards Olivine
Qtz
AnAb
Opx/Di
Jd/CaTS
Ol
KLB-1
NeCA
Dry CPX
Wet CPX
Wet Gt
Dry Gt
Liquids
Increasing Alkalis+H2O
PUM

Figure 9

Figure 10

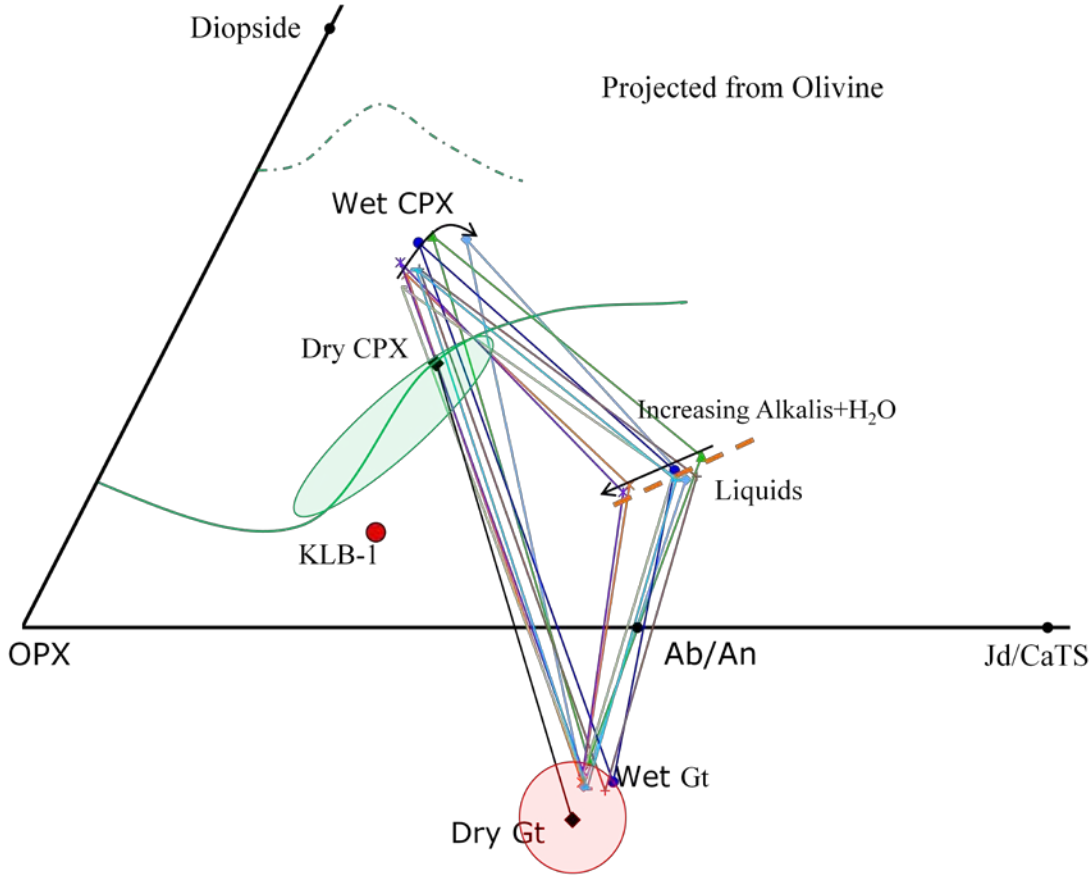
Diopside
Projected from Olivine
Wet CPX
Dry CPX
Increasing Alkalis+H_2O
Liquids
KLB-1
OPX
Ab/An
Jd/CaTS
Wet Gt
Dry Gt

MANGANESE PARTITIONING DURING HYDROUS MELTING OF PERIDOTITE

By

J. Brian Balta

Paul D. Asimow

Jed L. Mosenfelder

ABSTRACT

Manganese contents and the iron/manganese ratio of igneous rocks have been used as a method of probing the heterogeneity in the Earth's mantle during melting of peridotite and pyroxenite lithologies. Most previous work has assumed that changes in these parameters require changes in either source lithology or composition based on experiments that suggest manganese is slightly incompatible during melting and that the iron/manganese ratio is fixed by the presence of olivine. However, the presence of volatiles in the mantle drives melting at lower temperatures and with different compositions than is seen in volatile-free systems, and thus the partitioning behavior of Fe and Mn may in fact vary. We have produced silicate liquids in equilibrium with a peridotite assemblage under hydrous conditions at 3 GPa pressure which show that manganese can also be unexpectedly compatible in garnet at 1375 °C and Mn partitioning between solids and liquids can be strongly affected by temperature and liquid composition. The compatibility of Mn in garnet provides a mechanism for large variations of Mn contents and the Fe/Mn ratio in silicate melts solely involving melting of mantle peridotite with fairly small compositional changes. Correlations between Mn variations and other indices indicative of melting in the presence of garnet may provide a means of more completely understanding the role of garnet at high pressures in peridotite melting.

1. INTRODUCTION

Interpretation of the sources of silicate melting based on the chemical composition of the final products of the melting process is a key goal of modern geochemistry. A common method of interpreting heterogeneity in the mantle source is to identify changes in chemical tracers that are typically associated with variations in lithology or mineral content. A caveat to this technique, however, is that proper application requires a full understanding of all the possible changes taking place within the melting system, as trace element behavior can be strongly influenced by the presence of single minerals or small changes in partitioning under certain conditions. Thus, constraining the inverse problem of identifying mantle source components from observed igneous rocks requires a detailed experimental understanding of the possible changes taking place in the melting region.

Manganese (Mn) contents of igneous rocks and minerals have recently assumed a key role in several geochemical debates. Modern electron microprobes and laser-ablation ICP-MS systems have allowed for analyses of Mn in igneous rocks and minerals at a level of precision that was not previously available. Thus, small changes in Mn contents that were previously difficult to measure have recently drawn attention as petrogenetic indicators.

Sobolev et al. (2007) noted that Mn contents and the Fe/Mn ratio of olivine grains from a variety of melting environments correlated with geochemical indices that suggest the absence of olivine in the melting source, such as nickel contents in magnesium-rich olivine phenocrysts. For example, high Ni-olivines also tended to be high-Fe/Mn olivines. They interpreted the changes in Mn contents and Fe/Mn ratios as related to the removal of olivine from the melting source region through the production of hybridized

pyroxenites, which changes the relative bulk partition coefficients for the oxides in question and produces liquids with elevated Fe/Mn ratios. Gurenko et al. (2009) expanded upon this concept to present an equation that allowed for the calculation of the fraction of pyroxenite in the mantle source based on Ni, Fe, and Mn contents, and a model for the partitioning of each of those elements.

Other possible mechanisms involving variation in Mn contents have been proposed. Qin and Humayun (2008) performed high-precision laser ablation ICP-MS measurements of Fe/Mn ratios in glasses and found variations in the Fe/Mn ratio between different hotspot systems that were larger than the within-volcano variations assigned to the influence of source-pyroxenite by Sobolev et al. (2007). Qin and Humayun (2008) concluded that the variation in Fe/Mn ratio could only be produced by independently varying the Fe and Mn contents in the source rock, and as they could give no obvious globally available reservoir for Mn, they suspected interaction with an iron-rich source, such as the outer core.

These conclusions regarding source components can only be made with experimental knowledge of the partitioning of Fe and Mn between solid phases and liquids during melting under all potentially accessible conditions, including volatile-driven melting. While there is some MnO partitioning data at lower pressures, the best data for the higher pressures that may be reached in ocean island basalt (OIB) and some mid-ocean ridge basalt (MORB) systems comes from Walter (1998), who investigated melting at high temperatures from 3 to 7 GPa. Other studies, including Pertermann and Hirschmann (2003), have provided partitioning measurements during pyroxenite melting. These data have been widely applied, but they do not represent a complete sampling of the behavior

of peridotite melting, as they were all performed under volatile-free conditions and at higher temperatures than may be available through much of the present-day mantle. In addition, some phases that should be stable throughout portions of the melting region only appear in certain experiments, and thus it may be difficult to fully characterize their effect on chemistry throughout the melting column.

We have produced a series of melting experiments on hydrous peridotite from 3 GPa, that will allow us to better constrain the melting relations under different pressure (*P*) and temperature (*T*) conditions than those examined by Walter (1998). From these experiments, we present high-precision analyses of MnO partitioning between peridotite and basaltic liquids that suggest that volatile-driven melting of garnet-bearing lithologies is an additional mechanism for creating variability in MnO contents and Fe/Mn ratio in basalts worldwide.

2. ANALYTICAL TECHNIQUES

Major element compositions and volatile compositions for solids and liquids from experiments at 1375 °C are given in Chapter 2. Additional analyses were undertaken for this study to better constrain the MnO content of the phases. All analyses were conducted using the Caltech JEOL JXA-8200 electron microprobe in wavelength dispersive mode. As high-precision analyses of low-concentration elements were necessary in this study, we used several different sets of analytical conditions. All analyses were performed with an accelerating voltage of 15kV. Initial survey measurements of the solid phases were conducted with count times of 20 s on-peak and 10 s off-peak, with a spot size of <1 μm and beam current of 30 nA. Initial survey measurements of the liquids were conducted with identical count times, a current of 10 nA, and a spot size of 15 μm.

Higher-precision measurements of MnO contents were conducted using higher currents and longer count times. For the solid phases, the current was increased to 100 nA, and the count time for MnO was increased to 100 s on-peak and 50 s off-peak. For the liquids, the same long count times were used for MnO, but the current could not be increased as much without excessive damage to the sample. By shortening the counting time for sodium and potassium by a factor of two, we were able to maintain reasonable analyses of the major elements up to a current of 30 nA while simultaneously producing higher-precision analyses of MnO. Analyses using higher currents up to 60 nA were also done, but these produced significant loss of sodium. No difference in the accuracy or precision of MnO analyses were found between the analyses at 30 nA and 60 nA, and thus the data for MnO under both conditions was used, but only the data at lower currents was used for other oxides. The increased counting time and current typically produced a decrease in the variation in MnO by a factor of two compared to the survey analyses. The highest 1σ absolute deviation observed within the measurements of any single experiment was 0.008%, and values below 0.005% were typical.

3. RESULTS

3.1. 1375 °C Experiments

Each experiment produced a volatile-rich basaltic liquid in contact with a garnet peridotite. Some crystallization of olivine, clinopyroxene (cpx), and garnet always occurred in the outer capsule, giving each experimental charge up to two analyzable sets of liquid-crystal pairs for each solid phase. Differences in the liquid composition between the outer and inner capsules were small (less than 10% for all elements) except for volatile elements, although the inner capsules often suffered more alteration on quench.

Substantial modification of the runs did occur upon quench. Interstitial liquid often rapidly crystallized on the edges of preexisting grains, and pargasitic amphibole often crystallized against the capsule walls. However, in each reported experiment, large pools of unaltered silicate glass and piles of solid crystals were found and analyzed. Compositional results for the elements in question for these experiments are given in Table 1.

A number of techniques suggest that these pairs represent equilibrium assemblages from which representative partition coefficients could be calculated. First, measurements of the olivine/liquid K_D parameter give similar values from experiment to experiment. These values are also close to those seen in other hydrous experiments (e.g, Gaetani and Grove, 1998) and those calculated using calibrations for the variation of this parameter (e.g., Toplis, 2005). The olivines were slightly more iron-rich than those reported by Walter (1998). A few experiments showed K_D values that differed from the average, possibly suggesting disequilibrium or alteration on quench did occur in those experiments. However, the measured partition coefficients for FeO and MnO did not substantially diverge from the values measured in the other experiments.

Second, the solid grains produced during these runs were typically in the range of 5 to 30 microns. Olivine grains were generally the largest. Limited evidence of zoning was found in the solids, including in clinopyroxene, in which Fe/Mg exchange is expected to be the slowest out of the available solids (e.g., Brady and McCallister, 1983; Cherniak, 2001). For garnets in the shortest run, the Mg# (= 100 * molar MgO/(MgO + FeO*)) was found to be 80.9 ± 1.0, a level of heterogeneity on the order of the errors on the probe analyses for those elements and similar to that found in experiments up to three

times as long. Clinopyroxenes and olivines typically showed a similar level of heterogeneity. Zoning that could indicate disequilibrium was minimal and did not increase or decrease with increasing run time, which could happen if there was substantial disequilibrium or loss of components from the capsules at a rate faster than the rate of equilibration between the solids and liquids. Both the lack of zoning and the lack of any correlation between run times and variation in electron probe analyses argue that the experiments represent equilibrated assemblages.

The partition coefficients D_{MnO} (= concentration of species in a solid phase/concentration in liquid) are plotted against D_{FeO} for each of the solid phases present in Figures 1-3. The data of Walter (1998) from a variety of pressures collapse to well-defined lines when the partition coefficients are plotted against *T*, but show at most weak correlations with *P* even when considered at a constant *T*. However, the olivine/melt partition coefficients of these two oxides are strongly correlated with each other and with experimental *T* in both our experiments and in those of Walter (1998), suggesting that this plot is a natural way to visualize our results. In the range from 3 to 7 GPa, therefore, it appears *P* has a much smaller impact on these partition coefficients than *T*, and as such we will not explicitly consider changes in partition coefficients with *P*. When plotted against *T* or against each other, our olivine/melt partition coefficients lie along the same linear trend defined by the other olivine/melt partition coefficients. Both $D_{MnO}^{olivine/melt}$ and $D_{FeO}^{olivine/melt}$ increase with decreasing *T* such that our data for hydrous experiments, although they lie on the same line as those of Walter (1998), occupy a distinct field in Figure 1. The clinopyroxene/melt partition coefficients for both MnO and FeO plot in a small field overlapping the values from Walter (1998); the range of values measured

during peridotite melting is very small and it is difficult to recognize any systematic relationship among $D_{MnO}^{cpx/melt}$, $D_{FeO}^{cpx/melt}$, and *T* (Figure 2).

Surprisingly, in all our experiments, MnO was observed to be compatible in garnet, with an average solid/liquid partition coefficient for garnet measured to be ~1.5. The partitioning of MnO was measured in every experiment to be $D_{MnO}^{garnet/melt} > D_{MnO}^{olivine/melt} > D_{MnO}^{cpx/melt}$, with garnet being the only phase showing a MnO partition coefficient greater than unity. This is surprising, insofar as MnO is slightly incompatible in garnet in all the experiments of Walter (1998). Furthermore, the new data clearly lie well above the extrapolation of the correlation line between $D_{MnO}^{garnet/melt}$ and *T* among the Walter (1998) data (Figure 3).

3.2. 1250 °C Experiments

These experiments produced a dacitic liquid with ~6% H_2O in the inner capsules (based on the calibration of Ohlhorst et al., 2001) sitting in contact with solid garnet, orthopyroxene, clinopyroxene, and olivine. The outer capsules were typically completely liquid. Quench features were limited to thin layers occasionally occurring on the outside of solid grains. Unlike the basaltic liquids, the higher silica liquids did not wet all grain boundaries, which may have reduced the ability of the solids to fully equilibrate with the liquids. Because of a combination of this effect and the lower *T*, these experiments did not attain chemical equilibrium during the run duration and may have required substantially longer times (run durations were limited by the diffusion of carbon through the capsules, which became measurable after 24 hours). This is most easily seen in the preservation of Fe-Mg zonation in garnets, which averaged Mg# of 86.7 ± 2.0, a larger range than seen in the higher-*T* experiments.

MnO contents also did not attain equilibrium between the solid phases and the liquids during the duration of the experiments, and garnets in particular showed a very large range in composition across a full order of magnitude. The garnets that were loaded into the experiment initially had 0.19% MnO in them. In the final results, a range in MnO contents in garnet was found from values similar to the initial content (0.20%) up to 2.5% MnO, with an average MnO content of 0.93%. The zoning prevents the calculation of an equilibrium partition coefficient at this *T*. However, the results are still instructive. At this *T*, the compatibility of MnO in garnet appears to be further enhanced. Compared to the experiments at 1375 °C, the liquid formed at 1250 °C is depleted in MnO by a factor of four. This large depletion and the large range in MnO contents suggest that the garnets that came into contact with the liquid incorporated virtually all of the available MnO into their structures, leaving little MnO for the other garnets that did not initially contact the liquid. The low cation diffusivity at this *T* preserves the variable MnO contents for the duration of the run. Although the calculation of an exact partition coefficient is impossible, our measurements show partition coefficients for garnet between 10 and 50 at these conditions. These values are similar to the measured values for $D_{MnO}^{garnet/melt}$ from Patino-Douce (1995) from melting experiments involving tonalitic sources at temperatures from 1000 °C to 1150 °C. Measuring higher values of D_{MnO} using standard electron probes could be difficult because the MnO content of the liquid has decreased to nearly the analytical precision.

$D_{MnO}^{cpx/melt}$ is similar to that measured at 1375 °C and cannot be distinguished given the low concentrations in the low-*T* runs. The olivine appears to have lower MnO contents than those recorded at 1375 °C by a factor of about 1.5, suggesting that the

garnet may have taken up MnO from the olivines as well. $D_{MnO}^{olivine/melt}$ however increased compared to lower *T* runs due to the drop in MnO contents in the liquid. Partition coefficients in the range measured in this experiment also diverge significantly from the linear trend of partition coefficients versus *T* defined by the experiments of Walter (1998), again suggesting that D_{MnO} for all phases likely increases substantially in higher-silica liquids generated at lower *T*.

4. DISCUSSION

The experiments of Walter (1998) have formed the basis of a number of analyses of peridotite melting from *P* of 3GPa and higher. There are many advantages to that data set due to the quality of experiments and coverage of *P* and *T* conditions reached by few other experiments. However, the volatile-free nature of those experiments limited them to higher-*T* conditions than are expected in the upper mantle away from all but the highest *T* locations such as, potentially, Hawaii or Iceland (Putirka, 2005). Our experiments show that rich behavior in manganese partitioning can occur during lower-*T* hydrous melting.

4.1 MnO partitioning in olivine

Wang and Gaetani (2008) performed experiments at lower temperatures (1200-1350 °C), equilibrating melts of variable composition with large olivine grains to measure partitioning during crystallization. The authors argue that during crystallization of olivine, the main control on the olivine/liquid partition coefficient for MnO is the degree of polymerization of the silicate liquid, parameterized by the ratio of non-bridging oxygens to tetrahedrally-coordinated cations, NBO/T. In their analysis, $D_{MnO}^{olivine/melt}$ is expected to decrease as the NBO/T parameter increases or as the temperature increases.

Hydrous melts present an interesting puzzle for this analysis. Typically, melts from higher *T* are expected to show higher NBO/T, as shown by the experiments of Walter (1998), where the highest-*T* experiments showed the highest fraction of network modifying cations, such as MgO, FeO, and CaO. In those experiments, MnO is most compatible in olivine at the lowest *T* and thus also at the lowest values of NBO/T, consistent with the relation suggested by Wang and Gaetani (2008). Hydrous melts are produced at lower *T*, and thus can have lower concentrations of the network-modifying cations, but water itself is a very strong network modifier due to its ability to react with bridging oxygen to give separate OH^- species as seen in infrared spectra (e.g., Mysen et al., 1980; Dixon and Stolper, 1995). Furthermore, the low mass of hydrogen compared with other typical major elements suggests that per unit mass, water should be particularly effective at increasing NBO/T. Thus, while the lower temperatures are expected to decrease NBO/T, the increased water contents would act to counteract that effect. The precise effect of water on NBO/T is difficult to compute because water is also present in silicate melts as molecular H_2O (which does not consume bridging oxygens) and the details of this speciation are not fully known as functions of *P*, *T*, water content, and major-element composition of the melt.

In our experiments, MnO is measurably more compatible in olivine than in any of the experiments by Walter (1998), but the measured partition coefficients sit on linear trends against *T*, $D_{FeO}^{olivine/melt}$, or $D_{MgO}^{olivine/melt}$ (Figure 1). If the hydrogen is acting to significantly increase NBO/T, then this behavior is surprising and difficult to predict based solely on consideration of NBO/T. In this case, although melt composition may

have some separate effect, it appears that the decreased *T* is a more straightforward and reliable variable for the prediction of $D_{MnO}^{olivine/melt}$.

While we currently know of no adequate calibration for the variation of NBO/T with the addition of water in the compositional range reflected by our basalts, we propose that taking advantage of empirical calibrations for the interaction of olivine and melt may allow for an adequate predictive model of $D_{MnO}^{olivine/melt}$. Toplis (2005) produced an empirical calibration for the variation in the olivine/liquid Fe/Mg K_D that includes the effects of *T*, *P*, and a number of liquid compositional variables, including the water content. Wang and Gaetani (2008)'s model for MnO partitioning included an expression where the effects of NBO/T and the other variables is eliminated algebraically such that $D_{MnO}^{olivine/melt}$ is solely a function of the partition coefficient $D_{MgO}^{olivine/melt}$. Combining our data, the data of Walter (1998), and the basaltic data from Wang and Gaetani (2008), we can calculate a fit that allows for a predictive calculation of the partition coefficient under the full range of conditions considered here, and potentially across the range of conditions for which the Toplis (2005) calibration is accurate. From a least-squares regression to the full data set, the best fit is:

$$Ln\,(DMnO) = 0.82 \times Ln\,(DMgO) - 1.20, \quad (1)$$

which yields fit parameters close to those calculated by Wang and Gaetani (2008) over a more narrow range of *T* and *P*. This calculation shows that MnO is in general more compatible in olivine during melting at lower *T* and suggests that variation in the NBO/T parameter due to hydrous melting produces a limited impact in these basaltic liquids, as shown in our experiments.

4.2 MnO partitioning in pyroxene

Pertermann and Hirschmann (2003) performed partial melting experiments on cpx-rich lithologies which provide an additional data set from 3 GPa pressure and temperatures from 1275 °C to 1500 °C that can be compared with our data and that of Walter (1998). Although the trend is not linear, there is a fairly smooth trend with *T* through both the experiments of Pertermann and Hirschmann and the experiments of Walter (1998). While the data from Walter (1998) on their own only define a weak trend against *T*, the experiments of Pertermann and Hirschmann show significant increases in the partition coefficients for FeO, MnO, and MgO with decreasing *T*. Our experiments show partition coefficients significantly below these values, close to the values predicted by a linear extension of the data from Walter (1998).

Overall, the increased partition coefficients seen in the pyroxenite melting experiments should not be unexpected. Melting of a pyroxenite at gradually lower *T* produces liquids that are enriched in silica and deficient in FeO and MgO relative to melting of peridotite (Pertermann and Hirschmann, 2003). Because FeO, MgO, and MnO decrease with increasing silica in the liquid, the partition coefficients increase accordingly. At *T* above 1525°C, the pyroxenites examined by Pertermann and Hirschmann (2003) are above their liquidus. While our experiments show a slight enrichment in SiO_2 due to their hydrous nature (Chapter 2), the enrichment is much less than that seen during pyroxenite melting. In peridotite melting, the presence of olivine buffers the MgO, FeO, MnO, and SiO_2 contents of the liquid within a much narrower range. Our experiments therefore show a lower partition coefficient for each element. Notably, the partition coefficients for each element change at different rates; D_{MgO} increases more with decreasing *T* than D_{MnO}, and D_{MnO} increases slightly more with

decreasing T than D_{FeO}, suggesting that pyroxenite melting near the solidus may be able to fractionate FeO and MnO.

Very few measurements of the partitioning of these elements between liquids and orthopyroxenes exist in this T range. Some experiments of Walter (1998) do include orthopyroxene as a phase and possibly define trends of variation with T as seen for other solids. Where they are reported by Walter (1998), the partition coefficients D_{FeO} and D_{MnO} for orthopyroxene are not significantly different from those measured in clinopyroxene. While it is possible that the behavior of the two pyroxenes could differ strongly at lower T during hydrous melting, there is no suggestion of that in the experiments of Walter (1998).

4.3 MnO partitioning in garnet

Prior to this work, measurements of the partitioning of MnO between garnet and liquid at 3 GPa were limited, and partitioning measurements involving hydrous melts at this P were non-existent. The work of Walter (1998) reported measurements of MnO partitioning from pressures greater than 3 GPa, but no single experiment at 3 GPa gives compositional measurements for both garnet and liquid. At higher P, measurements of both phases are given and thus partition coefficients can be calculated, but those partition coefficients differ significantly from the ones reported here. In contrast to the olivines and the pyroxenes, T dependence is not able to explain the difference in garnet/melt partitioning between the current experiments and those of Walter (1998) despite a well-defined relationship between $D_{MnO}^{garnet/melt}$ and T among Walter (1998)'s data (Figure 3). Our samples show both FeO and particularly MnO to be noticeably more compatible in garnet at this T than predicted by the trends defined by the experiments of Walter (1998).

Garnet is therefore the only phase for which D_{MnO} and D_{FeO} could not be approximated by linear extrapolation in *T* from the experiments of Walter (1998).

There are several causes of the stark differences in measured partition coefficients at a constant *T*. One obvious explanation would be that there was a major difference in the composition of the garnets between our samples in equilibrium with hydrous liquids and the experiments in equilibrium with anhydrous melts, as is discussed for cpx in Chapter 2. However, the differences in composition between the garnets from the two sets of experiments appear minor at best. Table 2 shows an analysis for a 3 GPa garnet given by Walter (1998) and a representative garnet composition from one of our experiments, and in general the compositions are similar. Cr_2O_3 and TiO_2 are measurably higher in the garnets from Walter (1998), but it seems unlikely that these minor components, whose cations substitute in garnet on a different crystallographic site than MnO, should strongly influence the $D_{MnO}^{garnet/melt}$. The major difference appears to be that the garnets in these experiments have a higher Mg#. This could relate to a number of factors. In the experiments of Walter (1998), the Mg# in garnet decreases with decreasing *T* at each constant *P*, and therefore the lower Mg# in our garnets is not unexpected. However, this temperature-trend is not nearly sufficient to fully explain the difference in measured (Figure 3).

A second possible explanation for the variation in partition coefficients is changes in oxygen fugacity. If our experiments were performed under considerably more oxidizing conditions and Mn^{3+} were more compatible in garnet, then fO_2 could provide an explanation for the variation in apparent $D_{MnO}^{garnet/melt}$. The MnO-Mn_3O_4 buffer should sit at an oxygen fugacity 4 log units above the QFM buffer at this *T* (Berndt et al., 2004).

This fact suggests that very oxidizing conditions must be imposed for Mn_3O_4 to become a factor. The experiments of Walter (1998), Longhi (2002), and Pertermann and Hirschmann (2003) were all performed in graphite capsules, which would be expected to fix the oxygen fugacity of the sample at the C-CO buffer. Our experiments were designed to stay close to two log units below the QFM buffer, which should be a realistic value for the current mantle. While they are not buffered by the presence of a specific phase, a strong buffer may be maintained by the pre-saturation of the capsules. As shown in Chapter 4 of this thesis and by Kessel et al. (2001), the Fe contents of Au/Pd and Pt capsules in equilibrium with silicate liquids are strong functions of fO_2. Thus, a large change in fO_2 would require a large change in the Fe content of the capsules and of the experiments themselves, which is not seen (although some variation in the Fe content does occur). Furthermore, the olivine-liquid exchange parameter K_D provides an additional check on our oxygen fugacity constraints; conditions that were too oxidizing would be expected to produce liquids with a higher total iron content than predicted by the calibrated K_D parameter due to the uptake of iron from the capsules. Our experiments best fit the predicted K_D parameter under reducing conditions, approximately 2 log units below the QFM buffer, close to where the liquids were originally set. Higher oxygen fugacities would result in more Mg-rich olivines than we measure at this iron content. The C-CO buffer is approximately 4 log units below the QFM buffer at this *T* and *P* (e.g., Frost and Wood, 1995), suggesting that our experiments likely show only slight increases in oxidized Fe and even less in Mn compared with the other experiments considered here, a conclusion consistent with the K_D relations. The consistent trend in partition

coefficients for olivine described above also argues that there is no major change in the oxidation state of Mn between the different sets of experiments.

As the experiments of Walter (1998) do not include a measurement of both garnet and liquid compositions from a single experiment at 3GPa, but only from a higher *P*, it seems plausible that there may be a significant *P* effect on the partitioning of these elements beginning between 3 and 4 GPa, although that would be unexpected. One way of confirming this could be investigation of MnO partitioning from other melting experiments from similar *P*. Longhi (2002) reported measurements of garnet and liquid compositions in anhydrous melting experiments from 2.8 GPa, and the partitioning of FeO is similar to the experiments of Walter (1998). In these same experiments, however, MnO is observed to be more compatible in garnet than in the experiments of Walter (1998), with reported partition coefficients varying between 1.2 and 1.7. A more precise calculation of MnO partitioning from the data reported by Longhi (2002) is difficult because of the high standard deviation on analyses for MnO in that study. Johnson (1986) also conducted melting experiments in a similar *P* and *T* range on basalts with high Al_2O_3 contents and measured elevated partition coefficients for MnO in garnets as well. While no obvious *T* or *P* correlation could be observed from that data, $D_{MnO}^{garnet/melt}$ at 1500 °C and 3GPa was measured to be ~1.6 and values up to 5.85 were measured at 1400 °C and 3 GPa. Finally, the experiments of Pertermann and Hirschmann (2003) at *P* from 2 to 3 GPa and temperatures from 1250 °C to 1375 °C showed $D_{MnO}^{garnet/melt}$ values from 3.1 to 4.9, with values at 3 GPa forming a trend versus *T* that does not form a consistent relationship with either our experiments or those from Walter (1998) (Figure 3). From the available experiments, no clear *P* dependence can be determined, although every experiment at 3

GPa and below, other than those of Walter (1998), shows $D_{MnO}^{garnet/melt}$>1.0. This does suggest that pressure-sensitivity may increase with decreasing *P*. When $D_{MnO}^{garnet/melt}$ is plotted against $D_{FeO}^{garnet/melt}$ or $D_{MgO}^{garnet/melt}$, which presumably have similar interactions with the liquid, straight lines are found (Figure 3). The slopes of these lines differ from unity, such that the ratios of partition coefficients do change with changing *T* and liquid compositions. Hence, changes in relative partitioning are possible under differing melting conditions. Overall, the general trend in all of the experiments, including those at lower *T*, is for $D_{MnO}^{garnet/melt}$ to increase faster than $D_{FeO}^{garnet/melt}$ as *T* decreases, leading to stronger fractionation at lower *T*.

While none of these explanations appear satisfactory on their own, each potentially plays at least a small role in the variation of $D_{MnO}^{garnet/melt}$ at constant *T* seen in our experiments. Based on the increase in $D_{MnO}^{garnet/melt}$ at still lower *T*, it appears that the effect of low *T* on the $D_{MnO}^{garnet/melt}$ may be particularly important. While it remains surprising that the experiments of Walter (1998), which cover a range of several hundred degrees in *T*, do not show variation of the magnitude observed here, it is possible that the variation in $D_{MnO}^{garnet/melt}$ becomes much more extreme and non-linear at lower temperatures or in different liquid compositions. The unexpected $D_{MnO}^{garnet/melt}$ in this work argues that experimental calibration across a much wider range of *T*, *P*, fO_2, and liquid composition is a prerequisite for understanding the global variation in Fe/Mn ratios in natural liquids. However, the pressures and compositions examined in the studies cited here do give us the ability to evaluate the plausible range of liquid compositions that could be produced

by natural melting from peridotites, pyroxenites, and hydrous peridotites, and therefore to make inferences about the production of natural melts.

4.3.1 Lattice strain partitioning model

Based on lattice strain calculations, Van Westrenen et al. (2001) produced a model for the partitioning of cations into garnet that allowed for predictive calculation of the solid/liquid partition coefficient for a number of elements, including Fe, Mg, and Mn. We performed a similar calculation using their model to try to fit the series of partition coefficients measured here, and the results suggest that, in this case, the liquid appears to exert an important control on the partitioning for all 3 elements.

In the lattice strain model of Van Westrenen et al. (2001), the elements with the greatest *D* will be those that fit into the available site with the least distortion of the lattice based on their ionic radii, and a plot of the ionic radius of each element versus the partition coefficient should be approximately parabolic. The ionic radius (*r*) of the divalent cations in the appropriate coordination for the X-site of garnet is $r_{Mn} > r_{Fe} > r_{Mg}$, such that either $D_{FeO}^{garnet/melt}$ should be greater than both $D_{MnO}^{garnet/melt}$ and $D_{MgO}^{garnet/melt}$ if Fe fits best into the garnet structure, or there should be a consistent pattern where the partition coefficients either decrease or increase in the same order as the ionic radius. Our results and the results of Walter (1998) both show a trend that is not predicted by this lattice-strain model as both sets of experiments show $D_{MnO}^{garnet/melt}$ and $D_{MgO}^{garnet/melt}$ greater than $D_{FeO}^{garnet/melt}$.

Using the lattice-strain formalism of Van Westrenen et al. (2001), we derived a fit to predict $D_{MnO}^{garnet/melt}$ based on a measured value of $D_{MgO}^{garnet/melt}$ (Figure 4) and calibrated by

varying r_0, the size of the lattice site on which these elements sit, to fit both $D_{MgO}^{garnet/melt}$ and $D_{MnO}^{garnet/melt}$. We performed a similar fit for experiment 40.06 at 4 GPa and 1590 °C from Walter (1998). In both cases, the value for r_0 of 2+ cations is smaller than that expected from the expressions in Van Westrenen et al. (2001) but probably this difference is within the uncertainty in both calibrations. However, in both our own experiments and those of Walter (1998), we are unable to fit the value of $D_{FeO}^{garnet/melt}$ and $D_{MnO}^{garnet/melt}$ simultaneously as functions of $D_{MgO}^{garnet/melt}$ (Figure 4). We can produce a fit to $D_{FeO}^{garnet/melt}$ based on the same model (Figure 4b) but it requires more extreme values of r_0 outside the range fit by Van Westrenen et al. (2001) and fails to fit the MnO data from the same experiments. We conclude that FeO, a major component of both garnet and melt, is probably not behaving like a trace element in a simple Henrian manner and fuller consideration of garnet and melt thermodynamics are required to explain the observations for this oxide.

4.4. Bulk partitioning calculations

Our measurements of mineral/melt partitioning of MnO and FeO allow the calculation of bulk partition coefficients and therefore we can estimate liquid compositions in equilibrium with a given solid assemblage. This particular set of partition coefficients produces a rich variety of melting behavior when small changes in the mineralogy of the melting source are considered. The MnO content of liquids are a strong function of the modal abundance of garnet. Conversely, the FeO content of a liquid is a strong function of the modal olivine/pyroxene ratio, because of iron's compatibility in olivine and incompatibility in either pyroxene. The FeO/MnO ratio of any liquid

produced, therefore, is a very strong function of the ratio of olivine to garnet in the source.

Qin and Humayun (2008) produced a large quantity of whole-rock Fe/Mn measurements that likely span much of the global variation in this parameter (for convenience, we plot FeO*/MnO here; the difference between these two parameters should be 0.3%). The Fe/Mn ratio for their available terrestrial database varied from ~53 to ~70, with depleted Atlantic Ocean MORB at the low end and Hawaii and Tahiti at the high end. If these represent the end-members for typical terrestrial basalts, this range can be understood from the partition coefficients given here and reasonable variations of the source material.

Our melting experiments were performed using a starting material recrystallized from fertile peridotite KLB-1 as discussed in Chapter 2. The composition of KLB-1 was measured by Davis et al. (2009) to have 8.2% FeO and 0.12% MnO. This gives an FeO/MnO ratio of 68 in the starting peridotite. The expected mode of KLB-1 in the garnet stability field is about 60% olivine, 30% cpx, and 10% garnet (Chapter 2). Melting of this starting material with its high olivine content will produce a liquid with a lower FeO/MnO ratio than the source because of the high $D_{FeO}^{olivine/melt}$. Our final liquid composition gives an FeO/MnO ratio of 59. This value is very internally consistent with the calculated composition of a low-degree melt of this source (also ~59).

Figure 5 shows ternary diagrams giving the estimated FeO/MnO ratio in a liquid generated by batch melting of a source with an assigned initial FeO/MnO ratio and assigned partition coefficients based on this work. As discussed above, the orthopyroxene and clinopyroxene appear to have similar FeO and MnO partitioning under the melting

conditions considered here. Neither FeO nor MnO is strongly compatible in either phase, and so their capacity to fractionate these oxides is limited and they will be considered together in this analysis. We estimate that variations in orthopyroxene and cpx ratio yield less than 2 units in FeO/MnO ratio, except in lithologies that are almost pure pyroxene, where it can be up to 5 units between the pure orthopyroxene and cpx end-members. We calculate the liquid FeO/MnO ratio solely using the batch melting equation and as such we do not explicitly consider large shifts in mineralogy due to non-modal melting reactions, although some insights may still be gained into that process by considering the change in the modal mineralogy of the residue during melting.

Using the recommended FeO/MnO ratio of KLB-1 (i.e. 68) as a starting point, melting of a fertile, olivine-rich peridotite similar to KLB-1 gives FeO/MnO ratios ~55-60. These values are consistent with the measurements of Qin and Humayun (2008) for MORB. Melting of a more depleted, olivine-rich source with the same initial FeO/MnO ratio produces basalts with lower FeO/MnO ratios. Production of Atlantic-type MORB by melting of a source with the same FeO/MnO ratio as KLB-1 requires a higher olivine fraction in the source, ~70% modal olivine. Using a constant value of the modal abundance of pyroxene of 20%, an FeO/MnO ratio of 53 in the equilibrium basalt occurs with a modal abundance of 75% olivine and 5% garnet. This high olivine content would be consistent with a low-aluminum, depleted source. Variation in the amount of pyroxene has only a limited effect on the calculated FeO/MnO – an 80% olivine, 10% pyroxene, 10% garnet source produces the same FeO/MnO ratio.

Low-degree melting of a more fertile source, with lower olivine content, produces liquids with a higher FeO/MnO ratio at these temperatures. Melting of this peridotite

under these conditions is expected to produce liquids with FeO/MnO close to 60 and ~0.14% total MnO. These values are, unsurprisingly, very close to the values produced in our experiments, and are more typical of the melting that produces Pacific-type MORB (Qin and Humayun, 2008).

Continued enrichment of the melting source is expected to continue to decrease the olivine modal abundance relative to garnet and pyroxenes. Thus, melting of a more enriched source material with the same initial FeO/MnO ratio at these temperatures would be expected to produce melts with increased FeO/MnO ratios. Considering only the variation in the garnet to olivine ratio under these conditions, a liquid with FeO/MnO of 70 would be produced when the garnet to olivine ratio is ~0.75. This theoretical high-garnet peridotite composed of minerals with our measured compositions would have a high-aluminum content compared to KLB-1, about 7.5% compared with 3.51% in the natural version (Davis et al., 2009). While this composition is rare, it is similar to some peridotites that have been sampled, such as in the Red Sea rift (e.g., Bonatti et al., 1986). Compared to typical mantle, this type of peridotite would be more enriched and may represent a metasomatic product or the product of the addition of a highly aluminous material, such as subducted sediment, to normal mantle. Increasing the modal abundance of pyroxene in the calculation allows us to produce a melt with a FeO/MnO ratio of ~70 with a lower alumina content, because it takes less garnet to alter that ratio. Thus, increasing the CaO, Al_2O_3, or SiO_2 content of a peridotite by addition of enriched or recycled material has the ability to produce high FeO/MnO ratios through the melting process without significant involvement of either an iron-rich or a manganese-rich component. Because we can now postulate a new mechanism for the variation of

FeO/MnO occurring solely within the melting column that could produce variations much larger than those seen in terrestrial basalts, we conclude that on its own, changes in FeO/MnO within or between suites of basalts cannot on its own be taken as evidence for core-mantle interaction. The complex melting process may obscure any signals of core-derived material unless the modal mineralogy of the source is very well known.

An important additional consideration must be the initial FeO/MnO ratio of any material added to normal peridotite. However, the available measurements and our data provide constraints on this as well. As noted by Qin and Humayun (2008), most of the common MORB have bulk FeO/MnO ratios between 50 and 60. These numbers are consistent with our calculations of the FeO/MnO ratios that would be produced by low-degree melting of a typical peridotite. If the FeO/MnO ratio is not disturbed by subduction-related processing, then eclogitic sources formed from subducted oceanic crust and gabbroic lower crust could be expected to start with FeO/MnO ratios in this range. Notably, most pyroxenitic or eclogitic materials used by other authors fall in this range as well. The pyroxenite compositions of Pertermann and Hirschmann (2003) are 49 (G2) and 57 (G2K). Johnson (1986) used high-alumina natural basalts with ratios of 48 and 36 and MORB samples with ratios of 58, 61, and 93 (with some possible analytical error on the low MnO concentration). Yaxley and Green (1998) used starting material with a ratio of 58. Takahashi and Nakajima (2002) used an Archean MORB with a ratio of 56, a normal MORB at 56, a sample from Iceland at 59, and a Columbia River basalt at 68. All of these experimental pyroxenite compositions, together with the global basalt survey of Qin and Humayun (2008), suggest that an FeO/MnO ratio of 55 is an adequate

estimate for pyroxenitic source components, although more extreme values may be possible.

Direct melting of a rock with an initial FeO/MnO ratio of 55 and our partition coefficients gives the triangle in Figure 5b. As long as the modal mineralogy remains composed of a mixture of pyroxene and garnet, the FeO/MnO ratio of the liquid produced is significantly greater than that of the source. The calculation in 5b assumes a high degree of melting (50%); a lower degree of melting produces even higher final ratios. We can also repeat this calculation using the partition coefficients for garnet and pyroxene from the pyroxenite melting experiments of Pertermann and Hirschmann (2003). Since the ratio D_{FeO}/D_{MnO} is lower in those experiments than in the experiments of Walter (1998), using their partition coefficients increases the FeO/MnO ratio in the calculated liquid (Figure 5c). In fact, every liquid composition reported in that work gives an FeO/MnO ratio over 90 except for the samples from the highest *T*, where the partition coefficients approach the values of Walter (1998) and very little garnet or clinopyroxene remain in the source.

Sobolev et al. (2007) and Gurenko et al. (2009) presented a model for the calculation of the source of melting based in part on the measured FeO/MnO ratio of olivines crystallized from liquids. In their model, elevated FeO/MnO ratios are produced by the melting of an olivine-free source created by interaction of peridotite with a high-silica melt derived by high-degree melting of upwelling recycled oceanic crust. Our derived mineral-melt partition coefficients provide a possible test of that hypothesis and the conditions under which it could be applicable. As shown above, high-degree melting of a recycled eclogite or pyroxenite source will produce liquids that have high FeO/MnO

ratios, higher than low-degree melts of peridotite even though the eclogite or pyroxenite source may have a lower FeO/MnO ratio than a typical peridotite source. If typical upper mantle can be adequately represented by KLB-1 (an assumption supported by the global range in FeO/MnO ratios in MORB seen by Qin and Humayun, 2008), then adding a high-degree melt of an eclogitic or pyroxenitic source will not decrease the FeO/MnO ratio of the starting peridotite. Therefore, the FeO/MnO ratio of the "reaction pyroxenite" produced can only be increased by the process of refertilization. This source would be olivine-free and would therefore contain a mixture of pyroxenes and garnet. Partial melting of this lithology would then be expected to produce basalts with very high FeO/MnO contents, even if melted to high degree (Figure 5d). Using estimates of the degree of melting similar to those in Sobolev et al. (2007), the FeO/MnO ratio of the melt of the reaction pyroxenite would be ~80. While this is higher than the average Hawaiian value of ~68-70, mixing of this liquid with a peridotite-derived liquid could bring the erupted final FeO/MnO ratio down. Sobolev et al. (2007) proposed that some Hawaiian volcanoes show 60-70% melts of pyroxenite in their sources, and those values are consistent with the mixing relations calculated here. In cases of nearly complete melts of pyroxenite, as proposed for Siberia (Sobolev et al., 2009) or the Canary Islands (Gurenko et al., 2009), this model predicts very elevated whole rock FeO/MnO contents. As above, utilizing the partition coefficients from Pertermann and Hirschmann (2003), even from their highest *T* measurement, only increases the FeO/MnO of the estimated pyroxenite melt and thus would require a reduction in the pyroxenite component in the source. In this case, the partition coefficients measured on peridotites in the study of Walter (1998) appear to better fit the Sobolev et al. (2007) model than the partition coefficients

measured on pyroxenites by Pertermann and Hirschmann (2003), suggesting that this model can only produce the measured FeO/MnO ratios during melting at *T* higher than expected in normal mantle.

The Sobolev et al. (2007) model also incorporated a number of additional elements on which we have more limited constraints. In particular, their model also incorporates nickel abundances in olivine; an element about which our experiments give no information because nickel is strongly compatible in our capsule material and is at or below the detection limit of our analyses. Furthermore, we note that our partitioning data only has limited applicability to Hawaii and Iceland, because of the estimated higher *T* at the site of melting. However, based on Figure 5(c) we can note that production of the elevated FeO/MnO signature in Hawaii or Tahiti by melting of a pyroxene and garnet rich source at low temperature will produce liquids with much greater FeO/MnO than are observed in the global synthesis of Qin and Humayun (2008), and mixing of these melts with low degree melts of peridotite would be unable to dilute this signal. While this calculation is idealized, it reinforces our statement that a full accounting of the partitioning of MnO must be completed before using MnO as a method of determining source abundances, as MnO compatibility in garnet can produce large shifts in the calculated source makeup.

4.6. Other implications

The effects on D_{MnO} observed here, in particular the increased $D_{MnO}^{garnet/melt}$ during hydrous melting may have other implications for global magmatism. During melting of peridotite under a mid-ocean ridge, much of the volume of melt is produced in the spinel peridotite field regardless of the water content. Thus, the melt produced by low-degree,

hydrous melting in the garnet field may be a component that is overprinted by later high-degree melting or by shallow-level fractional crystallization, which has also been shown to alter the FeO/MnO ratio (Qin and Humayun, 2008). One mechanism for possibly isolating the presence of hydrous melts from the garnet facies may be to look for correlations between FeO/MnO and other indices that suggest the presence of garnet during melting, such as high-precision measurement of Dy/Yb (e.g., Salters and Longhi, 1999). In Figure 5 we show a selection of data from Hildenbrand et al. (2008) from the Azores. These samples are whole rock measurements from a selection of their data filtered for effects of extensive fractional crystallization using La abundances, including high-precision MnO analyses. In these samples, whole rock Dy/Yb does appear to be correlated with whole rock FeO/MnO. Unfortunately, very few other data sets currently can be evaluated in this way, because very few give precise data on MnO concentrations at the level where small changes in FeO/MnO ratio could be treated as significant. This result suggests that interpreting the FeO/MnO variation during melting may require both high-precision analyses of MnO and simultaneous analyses of the trace element compositions, as both may give information on the presence and behavior of garnet during melting.

5. CONCLUSION

During hydrous melting in the garnet field, MnO is more compatible in garnet than would be predicted by previous experiments. FeO is compatible in olivine, and thus, varying amounts of olivine and garnet in a melting source are able to fractionate MnO from FeO during melting. Hydrous melting experiments on a peridotite close in composition to KLB-1 produces melts with a FeO/MnO ratio similar to that measured in

normal mid-ocean ridge basalt. Melting of a source with lower olivine content and higher garnet content can produce fractionations that are larger than the globally observed variation in this ratio. Hydrous melting in the presence of garnet may produce correlations between the FeO/MnO ratio and other indices indicative of the presence of garnet in the melting source.

6. ACKNOWLEDGEMENTS

The authors would like to thank Andrew Matzen and Mike Baker for illuminating discussions regarding the behavior and analysis of MnO in experiments. This work was supported by the NSF Ocean Sciences Marine Geology and Geophysics program, grant numbers OCE-0241716 and OCE-0550216.

References

Berndt, J., Koepke, J., and Holtz, F. (2005) An experimental investigation of the influence of water and oxygen fugacity on differentiation of MORB at 200 MPa. *J. Petrol.* **46**, 135-167.

Brady, J. B. and McCallister, R. H. (1983) Diffusion data for clinopyroxenes from homogenization and self-diffusion experiments. *Am. Mineral.* **68**, 95-105.

Bonatti, E., Ottonello, G., and Hamlyn, P. R., (1986) Peridotites from the island of Zabargad (St. John), Red Sea: petrology and geochemistry. *J. Geophys. Res.* **91**, 599-632.

Cherniak, D. J. (2001) Pb diffusion in Cr diopside, augite, and enstatite, and consideration of the dependence of cation diffusion in pyroxene on oxygen fugacity. *Chem. Geol.* **177**, 381-397.

Davis, F. A., Tangeman, J. A., Tenner, T. J., and Hirschmann, M. M. (2009) The composition of KLB-1 peridotite. *Am. Mineral.* **94**, 176-180.

Dixon, J. E., Stolper, E. M., and Holloway, J. R. (1995) An experimental study of water and carbon dioxide solubilities in mid ocean ridge basaltic liquids.1. Calibration and solubility models. *J. Petrol.* **36**, 1607-1631.

Frost, D. and Wood, B. (1995) Experimental measurements of the graphite C−O equilibrium and CO_2 fugacities at high temperature and pressure. *Contrib. Mineral.Petr.* **121**, 303-308.

Gaetani, G. A. and Grove, T. L. (1998) The influence of water on melting of mantle peridotite. *Contrib. Mineral. Petr.* **131**, 323-346.

Gurenko, A. A., Sobolev, A. V., Hoernle, K. A., Hauff, F., and Schmincke, H.-U. (2009) Enriched, HIMU-type peridotite and depleted recycled pyroxenite in the Canary plume: A mixed-up mantle. *Earth Planet Sc. Lett.* **277**, 514-524.

Hildenbrand, A., Madureira, P., Marques, F. O., Cruz, I., Henry, B., and Silva, P. (2008) Multi-stage evolution of a sub-aerial volcanic ridge over the last 1.3 Myr: S. Jorge Island, Azores Triple Junction. *Earth Planet Sc. Lett.* **273**, 289-298.

Johnson, A. D. (1986) Anhydrous P-T phase relations of near-primary high-alumina basalt from the South Sandwich Islands. Implications for the origin of island arcs and tonalite-trondjemite series rocks. *Contrib. Mineral. Petr.* **92**, 368-382.

Kessel, R., Beckett, J. R., and Stolper, E. M. (2001) Thermodynamic properties of the Pt-Fe system. *Am. Mineral.* **86**, 1003-1014.

Longhi, J. (2002) Some phase equilibrium systematics of lherzolite melting: I. *Geochem. Geophys. Geosyst.* **3**, 1020.

Mysen, B. O., Virgo, D., Harrison, W. J., and Scarfe, C. M. (1980) Solubility mechanism of H_2O in silicate melts at high pressures and temperatures: a Raman spectroscopic study. *Am. Mineral.* **65**, 900-914.

Qin, L. and Humayun, M. (2008. The Fe/Mn ratio in MORB and OIB determined by ICP-MS. *Geochim Cosmochim Ac.* **72**, 1660-1677.

Ohlhorst, S., Behrens, H., and Holtz, F. (2001) Compositional dependence of molar absorptivities of near-infrared OH^- and H_2O bands in rhyolitic to basaltic glasses. *Chem. Geol.* **174**, 5-20.

Patino-Douce, A. E. (2005) Vapor-Absent Melting of Tonalite at 15-32 kbar. *J. Petrol.* **46**, 275-290.

Pertermann, M. and Hirschmann, M. M. (2003) Anhydrous partial melting experiments on MORB-like eclogite: phase relations, phase compositions and mineral-melt partitioning of major elements at 2-3 GPa. *J. Petrol.* **44**, 2173-2201.

Putirka, K. D. (2005) Mantle potential temperatures at Hawaii, Iceland, and the mid-ocean ridge system, as inferred from olivine phenocrysts: evidence for thermally driven mantle plumes. *Geochem. Geophys. Geosyst.* **6**, Q05L08.

Salters, V. J. M. and Longhi, J. (1999) Trace element partitioning during the initial stages of melting beneath mid-ocean ridges. *Earth Planet Sc. Lett.* **166**, 15-30.

Sobolev, A. V., Hofmann, A. W., Kuzmin, D. V., Yaxley, G. M., Arndt, N. T., Chung, S.-L., Danyushevsky, L. V., Elliott, T., Frey, F. A., Garcia, M. O., Gurenko, A. A., Kamenetsky, V. S., Kerr, A. C., Krivolutskaya, N. A., Matvienkov, V. V., Nikogosian, I. K., Rocholl, A., Sigurdsson, I. A., Sushchevskaya, N. M., and Teklay, M. (2007) The amount of recycled crust in sources of mantle-derived melts. *Science* **316**, 412-417.

Sobolev, A., Krivolutskaya, N., and Kuzmin, D. (2009) Petrology of the parental melts and mantle sources of Siberian trap magmatism. *Petrology* **17**, 253-286.

Takahashi, E. and Nakajima, K. (2002) Melting processes in the Hawaiian plume: an experimental study. In: Lipman, P. W., Garcia, M. O., Naka, J., and Aramake, S. Eds.) *Hawaiian Volcanoes: Deep Underwater Perspectives. Geophys. Mono.* American Geophysical Union, **128**, 403-418.

Toplis, M. J. (2005) The thermodynamics of iron and magnesium partitioning between olivine and liquid: criteria for assessing and predicting equilibrium in natural and experimental systems. *Contrib. Mineral. Petr.* **149**, 22-39.

Walter, M. J. (1998) Melting of garnet peridotite and the origin of komatiite and depleted lithosphere. *J. Petrol.* **39**, 29-60.

Wang, Z. and Gaetani, G. A. (2008) Partitioning of Ni between olivine and siliceous eclogite partial melt: experimental constraints on the mantle source of Hawaiian basalts. *Contrib. Mineral. Petr.* **156**, 661-678.

Van Westrenen, W., Allan, N. L., Blundy, J. D., Purton, J. A., and Wood, B. J. (2000) Atomistic simulation of trace element incorporation into garnets-comparison with experimental garnet-melt partitioning data. *Geochim. Cosmochim. Ac.* **64**, 1629-1639.

Yaxley, G. and Green, D. (1998) Reactions between eclogite and peridotite: Mantle refertilisation by subduction of oceanic crust. *Schweizerische mineralogische und petrographische Mitteilungen* **78**, 243-255.

TABLES

Table 1

	D_{MnO}	D_{FeO*}	D_{MgO}	K_D
Clinopyroxenes				
R385	0.67	0.47	1.29	
R389	0.71	0.56	1.30	
R390	0.66	0.43	1.31	
R393	0.73	0.49	1.36	
R395	0.71	0.56	1.32	
R396	0.73	0.53	1.30	
R398	0.73	0.50	1.27	
Garnets				
R385	1.55	1.00	1.45	
R389	1.48	1.12	1.39	
R390	1.53	1.04	1.28	
R393	1.55	0.92	1.44	
R395	1.48	1.12	1.36	
R396	1.56	0.94	1.46	
R398	1.43	0.96	1.39	
Olivines				
R385	0.85	1.22	3.56	0.350
R389	0.83	1.32	3.44	0.399
R390	0.85	1.19	3.50	0.339
R393	0.81	1.20	3.54	0.362
R395	0.83	1.32	3.40	0.383
R396	0.85	1.24	3.46	0.360
R398	0.76	1.11	3.39	0.328
Liquid FeO/MnO				
R385	60.3			
R389	51.8			
R390	62.7			
R393	59.4			
R395	49.6			
R396	59.0			
R398	54.4			

Table 1: Experimental data used in this study from samples where MnO contents were measured using high-precision techniques. Remaining oxides are presented in Chapter 2.

Table 2

	Walter, 1998	This work
Run:	30.05	R396
SiO_2	42.42	41.91
TiO_2	0.53	0.18
Cr_2O_3	1.53	0.80
Al_2O_3	22.2	23.01
FeO	6.22	8.14
MgO	21.81	20.43
CaO	5.43	6.26
MnO	0.2	0.23
Na_2O	0.03	0.02
Total	100.37	100.99
Mg#	86.2	81.73

Table 2: Measured 3 GPa garnet compositions from Walter (1998) and from this work. Experiment 30.05 was conducted at 1500°C, but no liquid composition was reported so a full partition coefficient could not be explicitly calculated.

FIGURE CAPTIONS

Figure 1. Measured values of mineral-melt partition coefficients for olivine from this work (triangles), Walter (1998) (squares), and basalts from Wang and Gaetani (2008) (circles). The trend in Figure 1c is linear, and the lack of linearity in the other figures can be understood using the relationships between liquid composition, *T*, and K_D calibrated by Toplis (2005).

Figure 2. Measured values of the mineral/melt partition coefficients for clinopyroxene from this work (triangles), Walter (1998) (squares), and Pertermann and Hirschmann (2003) (blue diamonds). Cpx from our experiments overlap the partition coefficients from Walter (1998) despite much lower *T*. The values from Pertermann and Hirschmann (2003) diverge substantially, and imply increasing compatibility of the oxides with decreasing *T*. The highest T experiment of Pertermann and Hirschmann (2003) is approaching its liquidus at 3GPa and also approaches the partition coefficients measured by Walter (1998) at similar *T*.

Figure 3. Measured partition coefficients for garnet. Symbols as in Figure 2. Arrow in Figure 3a points towards remaining experiments from Pertermann and Hirschmann (2003); we adjusted our scale in this image to best illustrate the relationship between our measured partition coefficients and the trend of Walter (1998) (black line). Our values for $D_{MnO}^{garnet/melt}$ are significantly above the trend predicted based on extrapolation in *T* from Walter (1998). They are also substantially below the values measured during pyroxenite melting by Pertermann and Hirschmann (2003) at the same *T*.

Figure 4. Garnet/melt partition coefficients fit to a lattice-strain model of the form of Van Westrenen et al. (2001). Filled circles are average partition coefficients from this work, open circles are measured partition coefficients from experiment 40.06 from Walter (1998). Solid lines represent calculated partition coefficients based on the measurement of $D_{MgO}^{garnet/melt}$ and dashed lines represent calculated partition coefficients based on the same experiment from Walter (1998), both fit to a model of the form of Van Westrenen et al. (2001). In Figure 4a, a value of 0.9225Å for the parameter r_0 is used for the solid line and a value of 0.929Å for the parameter r_0 is used for the dashed line. In Figure 4b a value of 0.88Å for the parameter r_0 is used for the solid line and a value of 0.87Å for the parameter r_0 is used for the dashed line. In both cases we are unable to produce a curve that fits both the values of $D_{MnO}^{garnet/melt}$ and $D_{FeO}^{garnet/melt}$ simultaneously based on a measured value of $D_{MgO}^{garnet/melt}$.

Figure 5. Calculated melt FeO/MnO ratios as discussed in the text, plotted for a fixed FeO/MnO ratio in the source and variable mineralogies. 5(a) 1% melt of peridotite with the FeO/MnO ratio of KLB-1 given by Davis et al. (2009) gives similar results to the liquids measured in our experiments. 5(b) The melts that would be produced by 50% melting of a source with an initial FeO/MnO = 55, simulating melting of recycled material. 5(c) The same melt scenario in 5(b), but using the partition coefficients measured at 1375 °C by Pertermann and Hirschmann (2003), giving much higher values of FeO/MnO for any pyroxene-rich source. 5(d) The liquids that would be produced by

melting of an approximate “reaction pyroxenite” as hypothesized by Sobolev et al. (2007) using the measured partition coefficients from this work.

Figure 6. Whole rock Dy/Yb versus FeO/MnO for selected samples from Hildenbrand et al. (2008), from the Azores. Samples displayed here were selected based on the criteria used by these authors to distinguish increasing amounts of differentiation from processes occurring in the melting source region. Curve represents a mixing hyperbola calculated using end-members just outside of the data range. Error bars are estimated based on the reported precision in that work.

FIGURES

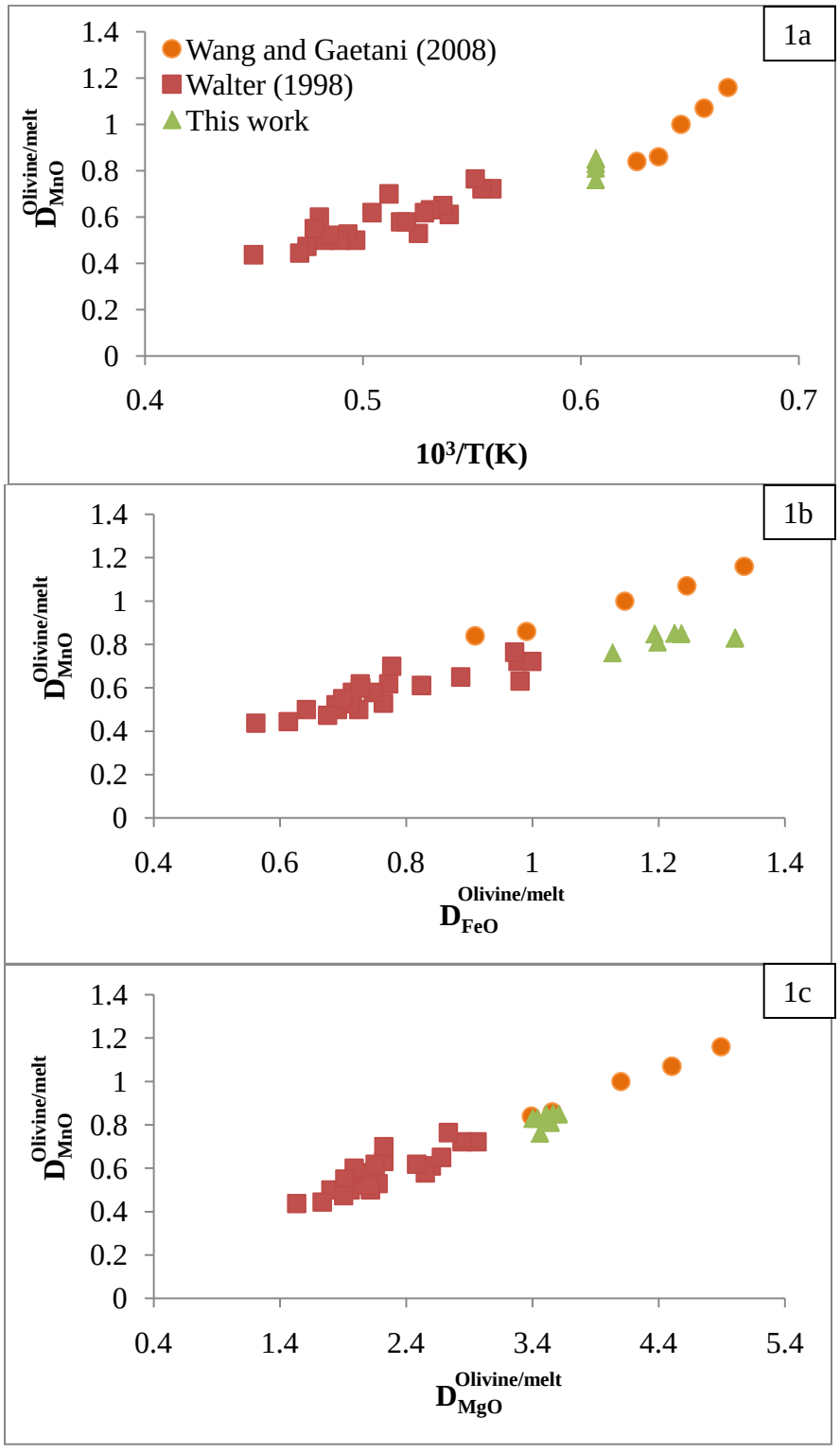

Figure 1

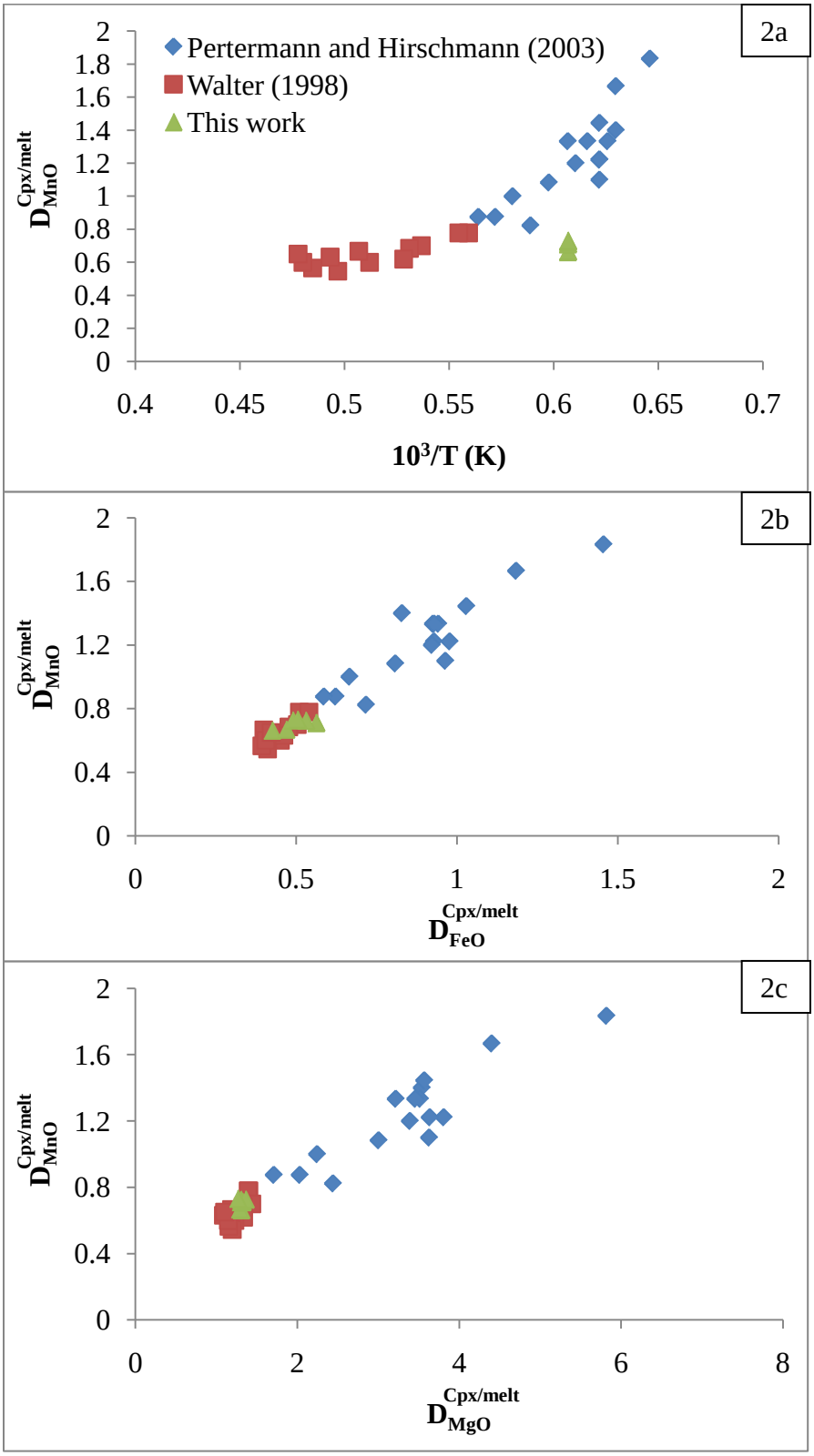
2a
Pertermann and Hirschmann (2003)
Walter (1998)
This work
$D^{Cpx/melt}_{MnO}$
$10^3/T$ (K)
2b
$D^{Cpx/melt}_{MnO}$
$D^{Cpx/melt}_{FeO}$
2c
$D^{Cpx/melt}_{MnO}$
$D^{Cpx/melt}_{MgO}$

Figure 2

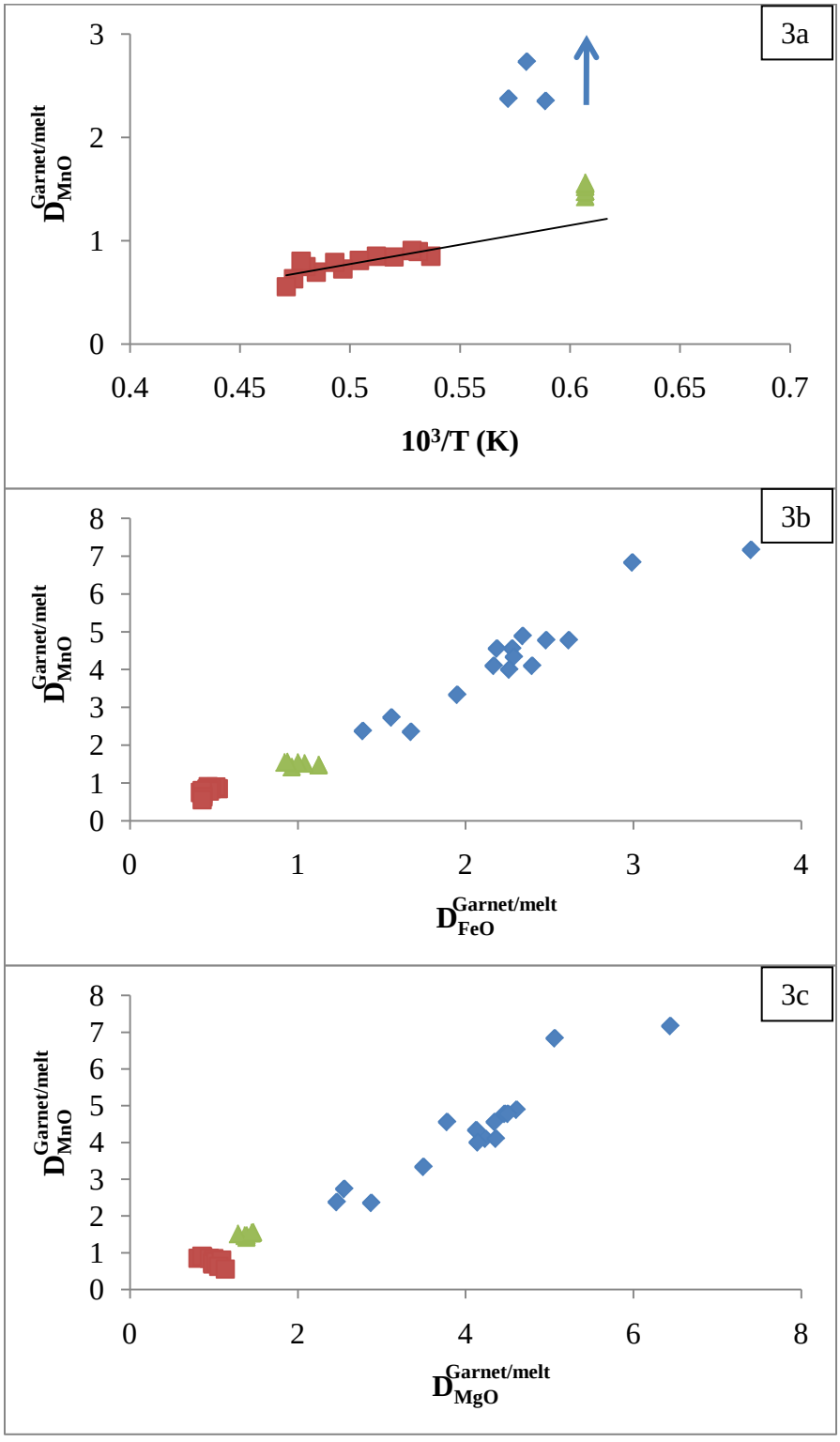
3a
$D^{Garnet/melt}_{MnO}$
10^3/T (K)
3b
$D^{Garnet/melt}_{MnO}$
$D^{Garnet/melt}_{FeO}$
3c
$D^{Garnet/melt}_{MnO}$
$D^{Garnet/melt}_{MgO}$

Figure 3

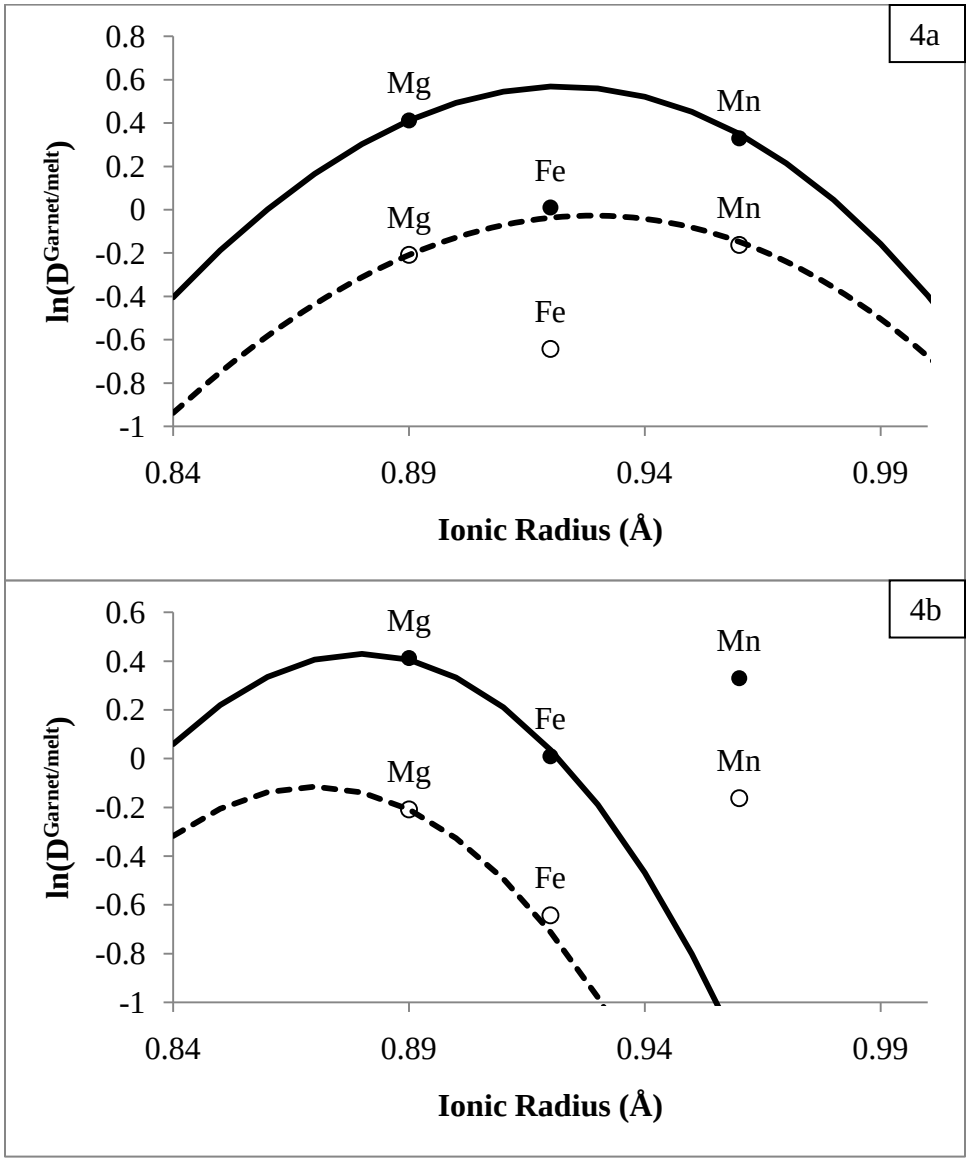
4a
0.8
0.6
0.4
0.2
0
-0.2
-0.4
-0.6
-0.8
-1
Mg
Mn
Fe
Mg
Mn
Fe
0.84
0.89
0.94
0.99
ln(D Garnet/melt)
Ionic Radius (Å)
4b
0.6
0.4
0.2
0
-0.2
-0.4
-0.6
-0.8
-1
Mg
Mn
Fe
Mg
Mn
Fe
0.84
0.89
0.94
0.99
ln(D Garnet/melt)
Ionic Radius (Å)

Figure 4

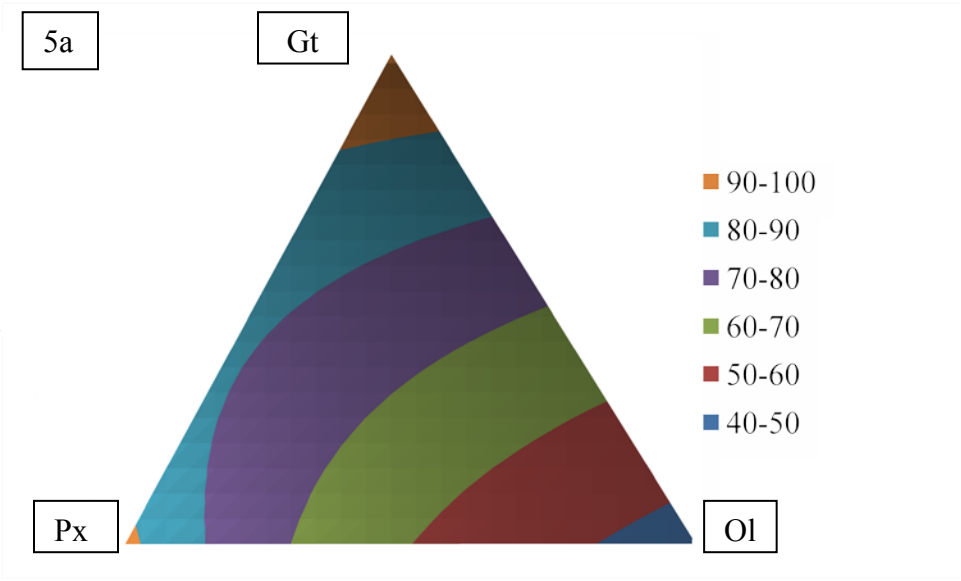
5a
Gt
90-100
80-90
70-80
60-70
50-60
40-50
Px
Ol

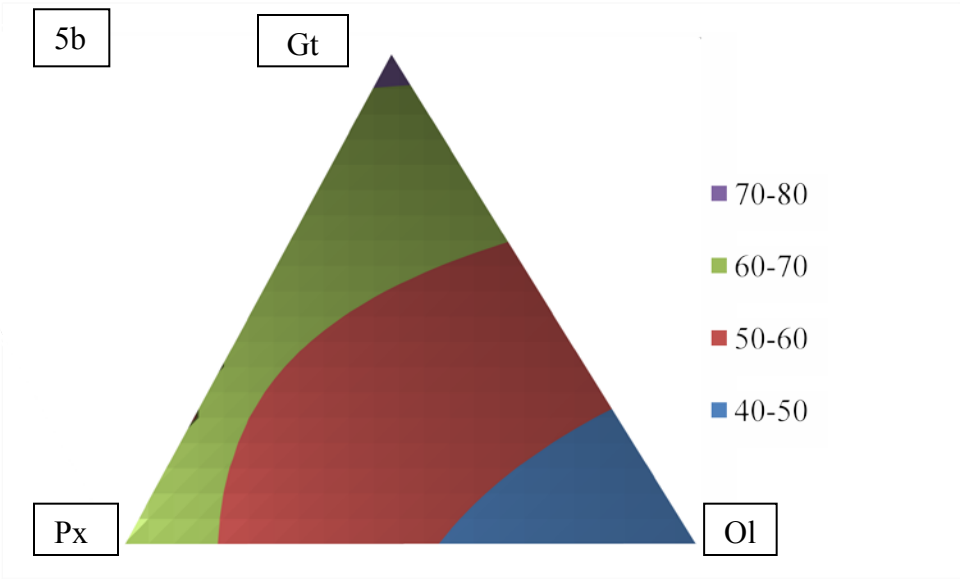
5b
Gt
70-80
60-70
50-60
40-50
Px
Ol

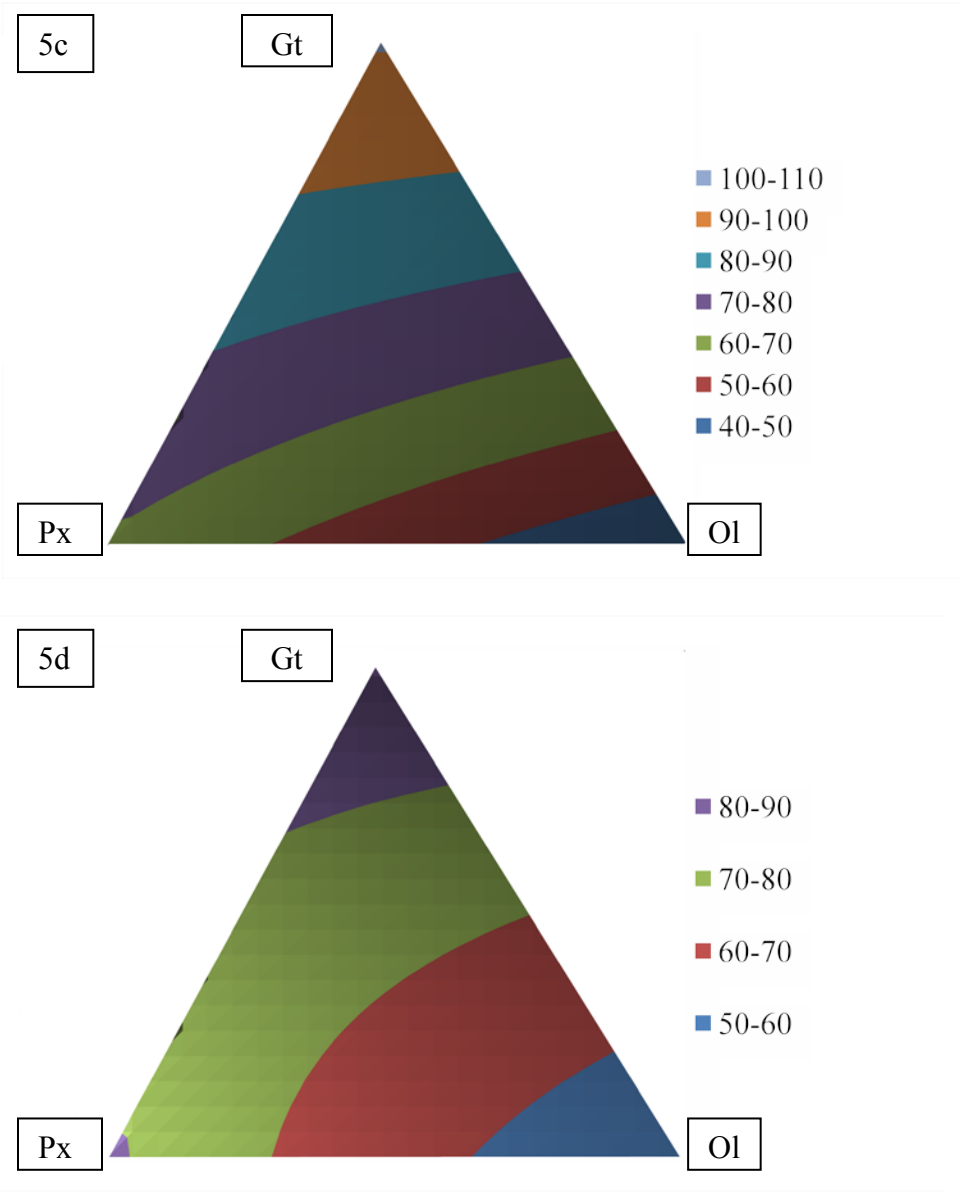
5c
Gt
100-110
90-100
80-90
70-80
60-70
50-60
40-50
Px
Ol
5d
Gt
80-90
70-80
60-70
50-60
Px
Ol

Figure 5

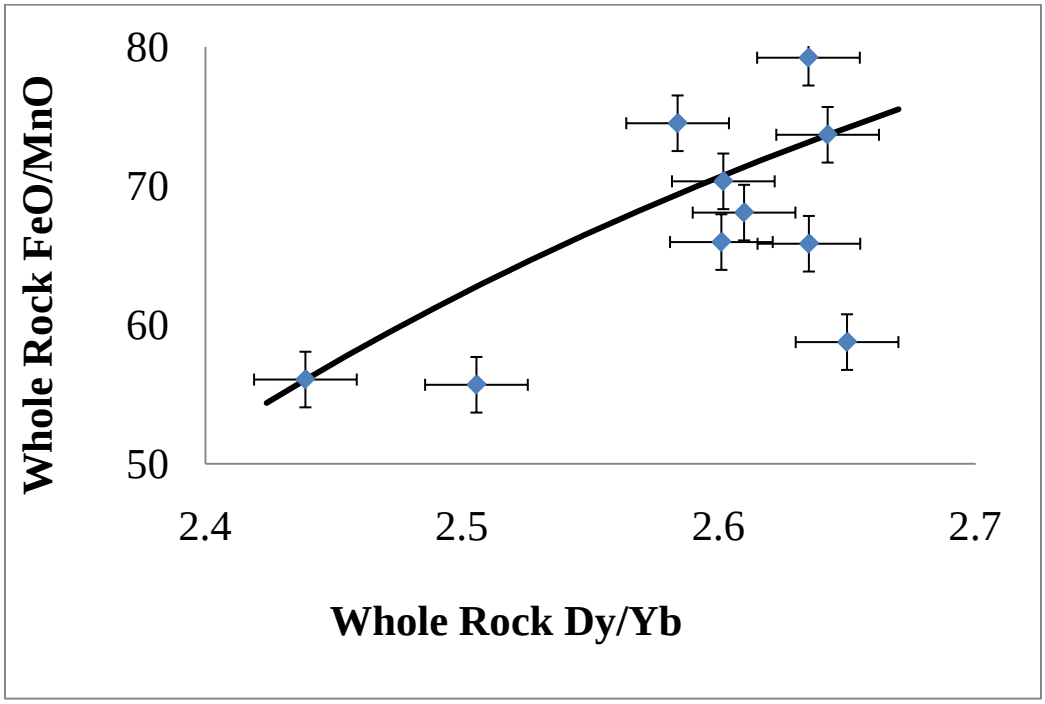

Figure 6

THERMODYNAMIC PROPERTIES OF MIXED ALLOYS OF GOLD-75/PALLADIUM-25 AND IRON

By

J. Brian Balta

John R. Beckett

Paul D. Asimow

ABSTRACT

Alloys of gold and palladium are commonly used during petrology experiments as a method of minimizing the loss or gain of hydrogen from samples being held at high temperature and high pressure. The presence of palladium causes the alloy to react with any iron present in the sample and will cause loss of iron during the experiment if appropriate steps are not taken to minimize this problem. We have produced a thermodynamic calibration for the mixing of $Au_{75}Pd_{25}$ with iron across the range of oxygen fugacities and iron activities of interest for petrological and metallurgical applications. This calibration can be used for preparation of capsules to maintain samples with little to no iron loss, and also provides a method for buffering the oxygen fugacity of samples when other oxygen buffers are not present. We have also observed internal oxidation of iron through this alloy during experiments, suggesting that oxygen can in fact be transferred across capsule boundaries during high-temperature experiments.

1. INTRODUCTION

The application of experimental petrology, a science rooted in classical thermodynamics, to understanding rock-forming processes in the present and past on Earth and other worlds requires production of equilibrated samples covering a considerable range of temperatures, pressures, and compositions. Studying high-temperature and high-pressure metamorphism and melting of rocks involves special challenges because it can be difficult to keep a sample effectively isolated from its surroundings for durations sufficient to approach equilibrium. Encasing the experimental charge in a capsule of a precious metal with a high melting point is the preferred method of performing these experiments. Capsules of Pt, Au, and Ag are among the most common materials used in capsule construction (e.g., Chou, 1986; Kawamoto and Hirose, 1994). However, at the temperatures of geologic interest, interaction between the capsules and the sample and diffusion of elements through the capsules appears to be commonplace. Thus, a wide variety of techniques have been developed to attempt to better isolate experimental charges from their surroundings under extreme conditions.

For simple melting experiments, platinum appears to be a good candidate as a capsule material due to its high melting point and lack of oxidation (which is generally thought to be prerequisite for solution into silicate and oxide liquids or minerals) at high temperature. However, Pt capsules have a number of disadvantages, including a high diffusivity of volatile elements and a tendency to alloy with iron (Kawamoto and Hirose, 1994). For volatile-bearing experiments, gold capsules are often used, as gold appears to show the slowest diffusion of hydrogen at high temperature among the commonly used metals (Chou, 1986; Truckenbrodt and Johannes, 1999). The main disadvantage of Au is

that its melting point is low compared with the temperatures that are required for typical silicate melting on Earth (Okamoto and Massalski, 1985). Thus, an alloy of Au doped with palladium is commonly used in an effort to obtain the benefits of slow diffusion of hydrogen at temperatures where pure Au is not suitable.

Pd-doped metal capsules have a notable disadvantage: like capsules made of Pt, Pd-doped capsules will react with Fe-bearing samples and can absorb a significant amount of Fe from the experiment, causing a number of problems by significantly changing the equilibrium chemistry (Hall et al. 2004).

A number of techniques have been applied to avoid Fe loss to Pt-or Pd-bearing capsules. These include graphite capsule linings (e.g., Medard et al., 2008), oxidizing conditions (Hall et al., 2004), and doping of capsules with Fe before use in experiments (e.g., Aubaud et al. 2008). Fe-doping is, in principle, the most flexible of these methods, since graphite linings or highly oxidizing conditions are limited to particular oxygen fugacity conditions. Experimentation with typical Fe-bearing geologic samples at the conditions of interest in the mantle requires work under a variety of oxygen fugacity conditions, with variable amounts of Fe and not necessarily at graphite saturation.

Fe-doping a capsule such that it will not exchange significant quantities of Fe with a particular experimental charge requires pre-saturating the capsule with the right amount of Fe in advance. That implies both knowing the correct Fe concentration and knowing what pre-saturation conditions and protocol will yield that concentration. Previously, for AuPd alloys, only ad-hoc methods were available, such as presaturation of capsules at ambient pressure and elevated temperature in a controlled oxygen fugacity gas mixture using liquids similar to the ones expected in the high-pressure experiments

(e.g., Aubaud et al. 2008; Botcharnikov et al. 2008). Shifting of pressure, temperature, and liquid or mineral composition from the presaturation conditions to the run conditions, however, can change the oxygen fugacity that is required to produce the Fe^{3+}/Fe^{2+} ratio in the liquid and, in turn, the Fe content of the capsule in equilibrium with that liquid.

Kessel et al. (2001) presented a detailed calibration for the dissolution of Fe into Pt capsules, which can be used as a method for preparation of capsules that will minimize Fe exchange with geologic samples under very general conditions. Because AuPd alloys are superior for volatile-bearing experiments, a similar calibration for that system is needed for work with H_2O and Fe-bearing charges. This requires a calibration defining the Fe content of AuPd capsules as a function of the activity of Fe and a method for determining the activity of Fe in the desired experimental charge as a function of liquid composition, pressure, temperature, and oxygen fugacity. Since thermodynamic calculators are available to calculate the Fe activity in silicate liquids, the essential need is for an activity-composition model for Fe-Au-Pd alloys. Here we present a calibration along a binary subsystem of this ternary, along the join from Fe to 75% Au, 25% Pd (weight units). The method and the thermodynamic basis of this work parallels closely the approach of Kessel et al. (2001) for the Fe-Pt system.

2. METHODS

Experiments were conducted following the techniques outlined by Chamberlin et al., (1993) and Kessel et al. (2001) in a 1 atm. Deltech DT-31 furnace using a mixture of H_2 and CO_2 gases to control the fO_2. Gas mixtures were set using an yttria-doped zirconia solid electrolyte oxygen sensor calibrated at fixed points against air and the iron-wüstite buffer. The oxygen sensor readings were maintained to within ± 3 mV, which

should maintain the fO_2 to within ± 0.1 $\log_{10}$ bars (1σ). Temperatures were measured using a type S (Pt-$Pt_{90}Rh_{10}$) thermocouple, and are expected to be accurate and constant to ± 1°C (1σ).

For each experiment, the sample was prepared by cutting a thin strip of laboratory grade $Au_{75}Pd_{25}$ (confirmed accurate to within 1% by repeated electron microprobe analysis). The strip was packed in laboratory grade Fe_2O_3 and compressed into a pellet. The pellet was placed into an alumina crucible and suspended in the hot spot of the vertical tube furnace (Chamberlin et al., 1993). The experiments were run at temperatures of 1125 °C, 1190 °C, and 1240 °C. The upper limit was set by the solidus temperature of this alloy, ~1250 °C. Most experiments were conducted at 1190 °C, which is above the liquidus of common basaltic liquids often used for pre-saturation. Other experiments were conducted at 1125 °C and 1240 °C to evaluate the effect of temperature changes on the composition. All experiments were conducted at fO_2 and temperature conditions such that the stable oxide phase should be either magnetite or wüstite. Experiments were run for a minimum of 48 hours for the two higher temperatures and 72 hours at the lowest temperature. While diffusion of metals in AuPd capsules is not as well calibrated as diffusion of Fe in Pt (Berger and Schwartz, 1978), in all cases these times were sufficient to fully convert the oxide pellet to either FeO or Fe_3O_4 and to homogenize the metal strip to better than the standard error of the electron microprobe measurement. To confirm equilibrium, a reversal experiment was conducted by placing two strips in iron oxide simultaneously under reducing conditions, retaining the second strip after the experiment, and repeating the experiment by placing the extra strip back into iron oxide under oxidizing conditions with a fresh strip of metal for comparison. Experiments were

quenched by removing the crucible from the furnace and cooling it in air; cooling times were on the order of 10's of seconds. This time was rapid enough that no obvious conversion of FeO or Fe_3O_4 to Fe_2O_3 was observed, and no significant changes in alloy composition were expected.

Completed samples were removed from their pellets manually while wearing gloves to avoid contamination. Strips were cut into multiple pieces, with at least 1/3 of the original strip stored for reference. Other strips were mounted in epoxy and polished using alumina pads and diamond pastes. The strips were oriented at angles relative to the polishing surface, to expose a full transect across the metal strip. Samples were carbon coated and analyzed using the JEOL JXA-8200 electron microprobe at the California Institute of Technology in wavelength dispersive mode. Samples were analyzed using focused beams with an accelerating voltage of 15 kV and currents of 30-40 nA. Between 10 and 25 spots were analyzed for each sample, typically covering 2 different cuttings from the same experiment. No obvious variation was observed either on transects or on different cuttings from the same experiment, strongly suggesting that the samples reached equilibrium. Fe oxides were also analyzed by electron probe with Fe standardized on Fe metal, allowing calculation of the oxidation state of the Fe by assuming that the mass deficit is entirely due to oxygen.

3. RESULTS

$Au_{75}Pd_{25}$ alloys reacted with the oxides at temperature and produced final equilibrated alloys of Fe mixed with AuPd. Compositions of the experimental alloys are given in Table 1 and displayed as a function of fO_2 in Figure 1. Smooth trends in Fe content versus fO_2 are observed at each temperature.

Calculation of an equilibrium composition between a silicate liquid and a capsule alloy requires conversion of oxygen fugacity information to an activity of Fe. The stable Fe oxide phase in each experiment was either wüstite or magnetite. The thermodynamic properties of both phases have been well calibrated previously and allow conversion to Fe metal activities. Neither phase is expected to be fully stoichiometric under these conditions. However, as pointed out by Kessel et al. (2001), magnetite approaches nominal stoichiometry as the temperature decreases. The difference between stoichiometric magnetite and the likely actual composition at these temperatures should be minimal, and thus magnetite was assumed to be stoichiometric. We expect that the activity of Fe_3O_4 in the spinel phase component differs from unity by no more than 1%. The activity of Fe in magnetite can then be calculated using the reaction

$$3\ \mathrm{Fe(alloy)} + 2\ \mathrm{O_2(g)} = \mathrm{Fe_3O_4(spinel)},$$

whose equilibrium constant is given by:

$$K_{Mt} = \frac{a_{spinel}^{Fe_3O_4}}{\left(a_{alloy}^{Fe}\right)^3 \left(fO_2\right)^2}\ . \qquad (1)$$

The equilibrium constant K_{Mt} was calculated from the values of the free energy of formation given by Kessel et al. (2001) using linear interpolation between the temperatures at which ΔG^0 is reported in that work. The values of this parameter are well fit by a linear function of temperature and the error in this interpolation should be minimal.

Wüstite is expected to vary significantly in its stoichiometry across these oxygen fugacities. The activity of FeO is therefore significantly different from unity under the conditions of these experiments and the activity of Fe will be a function of the

composition of this mineral. To calculate an activity of FeO, we repeated the Gibbs-Duhem integration of Darken and Gurry (1945) at the temperatures and oxygen fugacities of interest. Specific details of the integration are given in Kessel et al. (2001). After calculation of the variation in activity of FeO across the range sampled in our experiments, the activity of Fe was calculated using the reaction

$$\text{Fe(alloy)} + 1/2\ O_{2(\text{gas})} = \text{FeO(wüstite)},$$

whose equilibrium constant is

$$K_{Wü} = \frac{a_{wüstite}^{FeO}}{\left(a_{alloy}^{Fe}\right)\left(fO_2\right)^{1/2}}. \quad (2)$$

The equilibrium constant $K_{Wü}$ was calculated via linear interpolation from the equilibrium constants given in Darken and Gurry (1945) at various temperatures. Calculated activities of Fe give a smooth trend versus measured alloy composition, as shown in Figure 2.

In addition to deviation of the oxide phases from nominal oxygen stoichiometry, solution of any other components, including Au or Pd, would lead to errors by decreasing the activity of Fe in that oxide. A simple check can be performed from our data to verify that this effect is negligible. There is no reason to expect that the solubility of Au and Pd in Fe oxides will be identical; therefore, a change in the ratio of Pd to Au in the samples would potentially reflect loss of one of these species to the oxide. Only 1 sample showed a measurable difference: run 12, which was the most reducing experiment conducted at 1240 °C (Table 1). However, this sample still plots on the trend in Fe activity versus composition defined by the remaining samples, so we suggest the effect here is likely limited. Future experiments conducted at conditions more reducing than this experiment

may find this effect to be a greater concern. Interestingly, the Pd/Au ratio in the analyzed metal increased in this experiment, suggesting preferential incorporation of Au into wüstite. Since the Au-Fe miscibility gap is larger than that in the Pd-Fe system (Okamoto et al., 1986), one might have expected the opposite behavior, with preferred solution of Pd into the Fe-oxide phase. The analysis of the Au/Pd ratio of our final alloys is also an important check for the application of our results to mixing along the pseudo-binary join between Fe and $Au_{75}Pd_{25}$.

We conducted a reversal experiment from reducing conditions to very oxidizing conditions to verify that the samples were able to achieve equilibrium on the timescales of the experiment. Beginning with pure $Au_{75}Pd_{25}$, the reducing step should create an alloy with a high concentration of Fe, which must then diffuse out during the oxidizing step. Reaching the same composition as achieved by diffusing a small concentration into initially pure $Au_{75}Pd_{25}$ under oxidizing conditions documents a reversed equilibrium. Sample 8R reflects the final analysis of the reversed sample, which achieved an identical composition to Sample 8, run at the same time. The reversal experiment produced an unexpected result, however. It was expected that the added iron would diffuse out of the metal and move back into the large pool of Fe oxide. However, instead of leaving the metal, the extra Fe nucleated crystals of Fe oxide within the solid metal layer (Figure 3). Examination of the orientation of the polished surface and polishing to different levels within the sample verified that the Fe oxide grains were isolated within the metal. This Fe oxide was verified by electron probe totals to be magnetite, which was the stable phase under those conditions. Previously, the species capable of diffusing through capsules was questionable, as the analysis of specific diffusing species is complicated by the difficulty

in preparing experiments with known amounts of oxygen and other volatiles (Truckenbrodt and Johannes, 1999). This experiment verifies that oxygen itself is able to be transferred across capsule boundaries in high-temperature experiments, although it remains possible that the diffusing species is not atomic oxygen but could instead be an oxide species such as CO_2 or H_2O. The diffusion of oxygen-containing species should be considered a method of changing the oxygen fugacity of samples during unbuffered experiments even when volatiles or high metal concentrations are not present.

4. ACTIVITY-COMPOSITION MODEL

The Au-Pd-Fe system shows negative deviations from ideal solution of Fe (that is, the activity of Fe is less than the mole fraction of Fe) over the full compositional range examined here; the deviation from ideality decreases with increasing Fe content. The deviation from ideality is smaller than that seen in the Pt-Fe system (Kessel et al. 2001). To model this system in full would require construction of a ternary solution model, which would require more data covering other Pd/Au ratios. However, in the more limited case of this single Pd/Au ratio, we can produce a simplified (pseudobinary) model where the Au and Pd are treated as a single end member into which Fe is dissolving. We caution that application of this solution model is only applicable for $Au_{75}Pd_{25}$ alloys reacting with Fe, but this is a common choice of capsule material and so this preliminary calibration should prove useful on its own.

We modeled our data by fitting it to an asymmetric regular solution model of the form:

$$RT \ln \gamma_{Fe} = [W_{G1} + 2(W_{G2} - W_{G1})X_{Fe}](X_{AuPd})^2 \quad (3)$$

$$RT \ln \gamma_{AuPd} = [W_{G1} + 2(W_{G2} - W_{G1})X_{Fe}](X_{Fe})^2 \quad (4)$$

$$X_{Fe} = 1 - X_{AuPd,} \quad (5)$$

where γ is the activity coefficient for the component in the solution, X is the measured mole fraction of the component, and W_{G1} and W_{G2} are temperature-and-composition-independent Margules parameters. We attempted to fit our data to a symmetric regular solution, where $W_{G2} = W_{G1}$, but the quality of the fit was poor compared to that in the asymmetric case including both parameters. Fit values of these parameters are -45.0 ± 1.79 kJ/mol and +19.5 ± 7.70 kJ/mol, respectively (the errors are obtained by Monte Carlo simulation, varying all independent and dependent data parameters over Gaussian distributions). These Margules parameters have lower absolute values than those for the Pt-Fe system, again consistent with a less negative deviation from ideality and lower solubility of Fe in these AuPd alloys. The fit is compared to our measured data in figure 4, and appears to be reasonable within the margin of error across the full compositional range.

5. APPLICATION OF SOLUTION MODEL TO PREPARATION OF CAPSULES FOR FE-BEARING EXPERIMENTS

Prevention of Fe-loss to the capsule in melting experiments requires conversion from an activity-composition relationship measured in a metal alloy to one calculated in the silicate liquid in question. The thermodynamics-based MELTS algorithm (Ghiorso and Sack, 1995) can be used as a method of calculating activities of oxide-components within any silicate liquid for which it is calibrated. A full explanation of this procedure is given in Kessel et al. (2001) and is summarized here. The MELTS algorithm returns values of ΔG^0 and activity for the liquid components Fe_2SiO_4 and SiO_2 that can be used to calculate the activity of Fe using the reaction

$$2\ Fe(alloy) + O_2(gas) + SiO_2(liq) = Fe_2SiO_4(liq)$$

for which the law of mass action states, at equilibrium,

$$\Delta G = 0 = \Delta G^0 + RT \ln\left(\frac{a^{liq}_{Fe_2SiO_4}}{a^{liq}_{SiO_2}\,(a^{alloy}_{Fe})^2\, f_{O_2}}\right) \quad (6)$$

.

However, the values of ΔG^0 returned by MELTS are apparent values relative to the elements at 298.15K and 1 bar. The standard state must therefore be corrected to the temperature of interest, using values for the thermodynamic properties of Si, Fe, and O from Robie et al. (1978) and the expression shown in Kessel et al. (2001).

Figure 5 shows an example calculation of the capsule alloy composition that would be in equilibrium with Kilauea 1919 basalt across a range of oxygen fugacities at 1 bar pressure and 1190 °C (all fO_2 values are relative to the QFM buffer). A single experimental value is presented based on actual capsule pre-saturation work using this basalt as a starting material (X_{Fe} = .114 at QFM–1.6). Table 2 gives the values extracted from MELTS that are necessary for this calculation from Kilauea 1919 basalt. This calculation shows how large the shifts in alloy composition can be if capsule material is not pre-saturated at the correct level. Under oxidizing conditions, a change of 1 log unit in oxygen fugacity can correlate with a change in the alloy composition by a factor of 2. Under more reducing conditions, a change in 1 log unit in fO_2 can still change the equilibrium alloy composition by a factor of 1.5. Thus, pre-saturation of a capsule with an inappropriate Fe content can still lead to large shifts in oxygen fugacity and Fe content during experiments, even under oxidizing conditions or in experiments with lower Fe contents. Conversely, the presence of an appropriately pre-saturated AuPd capsule can provide a strong compositional buffer across a large range of oxygen fugacities, as a

significant and measureable change in alloy composition would be required for a sample to move to a different oxygen fugacity (Figure 5). While the buffering capacity of a capsule in any experiment depends on the ratio of the capsule mass to the sample mass, under all but the most oxidizing conditions or in very low-Fe samples, a variation of a single log unit in fO_2 should produce significant changes in the composition of the equilibrium alloy and likely also significant shifts in the Fe content of the sample.

Continued refinements and improvements of the MELTS algorithm will also improve the reliability of this calculation. The pMELTS algorithm (Ghiorso et al., 2001) can be used for more accurate calculation of the thermodynamic properties of liquids at pressures up to 3 GPa. Water in particular can be expected to have a significant impact on the activities of silica and possibly iron in the liquid phase (e.g., Chapter 2) and thus must be considered in any calculation. The adiabat_1ph front-end for the various MELTS algorithms (Smith and Asimow, 2005) can be used to return the thermodynamic parameters in question for liquids calculated by any of the algorithms, and instructions for this process can be obtained from the authors.

6. ACKNOWLEDGEMENTS

The authors would like to thank June Wicks and Andrew Matzen for their help with the 1-atmosphere furnace experiments. This work was supported by the NSF Ocean Sciences Marine Geology and Geophysics program, grant numbers OCE-0241716 and OCE-0550216.

REFERENCES

Aubaud, C., Hirschmann, M. M., Withers, A. C., and Hervig, R. L. (2008) Hydrogen partitioning between melt, clinopyroxene, and garnet at 3 GPa in a hydrous MORB with 6 wt.% H_2O. *Contrib. Mineral. Petr.* **156**, 607-625.

Berger, D. and K. Schwartz (1978) Zur Fremddiffusion in Platin. Neue Huette **23**, 210-212.

Botcharnikov, R. E., Almeev, R. R., Koepke, J., and Holtz, F. (2008) Phase relations and liquid lines of descent in hydrous ferrobasalt - implications for the Skaergaard intrusion and Columbia River flood basalts. *J. Petrol.* **49**, 1687-1727.

Chamberlin, L., Beckett, J. R., and Stolper, E. M. (1994) Pd-oxide equilibration: a new experimental method for the direct determination of oxide activities in melts and minerals. *Contrib. Mineral. Petr.* **116**, 169-181.

Chou, I.-M. (1986) Permeability of precious metals to hydrogen at 2 kb total pressure and elevated temperatures. *Am. J. Sci.* **286**, 638-658.

Darken, L. S. and R. W. Gurry (1945) The system iron-oxygen. I. The wüstite field and related equilibria. *J. Amer. Chem. Soc.* **67**, 1398-1412.

Garcia, M. O., Pietruszka, A., and Rhodes, J. M. (2003) A petrologic perspective of Kilauea volcano's summit magma reservoir. *J. Petrol.* **44**, 2313-2339.

Ghiorso, M. S. and R. O. Sack (1995) Chemical mass-transfer in magmatic processes IV. A revised and internally consistent thermodynamic model for the interpolation and extrapolation of liquid-solid equilibria in magmatic systems at elevated temperatures and pressures. *Contrib. Mineral. Petr.* **119**, 197-212.

Ghiorso, M. S., Hirschmann, M. M., Reiners, P. W., and Kress, V. C. (2001) The pMELTS: a revision of MELTS for improved calculation of phase relations and major element partitioning related to partial melting of the mantle to 3 GPa. *Geochem. Geophys. Geosyst.* **3**, 1030.

Hall, L. J., Brodie, J., Wood, B. J., and Carroll, M. R. (2004) Iron and water losses from hydrous basalts contained in $Au_{80}Pd_{20}$ capsules at high pressure and temperature. *Mineral. Mag.* **68**, 75-81.

Medard, E., McCammon, C. A., Barr, J. A., and Grove, T. L. (2008) Oxygen fugacity, temperature reproducibility, and H_2O contents of nominally anhydrous piston-cylinder experiments using graphite capsules. *Am. Mineral.* **93**, 1838-1844.

Kawamoto, T. and K. Hirose (1994) Au-Pd sample containers for melting experiments on iron and water bearing systems. *Eur. J. Mineral.* **6**, 381-385.

Kessel, R., Beckett, J. R., and Stolper, E. M. (2001) Thermodynamic properties of the Pt-Fe system. *Am. Mineral.* **86**, 1003-1014.

Okamoto, H. and T. Massalski (1985) The Au−Pd (Gold-Palladium) system. *J. Phase Equilib.* **6**, 229-235.

Okamoto, H., Massalski, T., Swartzendruber, L., and Beck, P. (1986) The Au−Fe system. *J. Phase Equilib.* **7**, 522-522.

Robie, R. A. and B. S. Hemingway (1978) Thermodynamic properties of minerals and related substances at 298.15 K and 1 bar (105 Pascals) pressure and at higher temperatures. *Geological Survey Bulletin* **1452,** 456 p.

Smith, P. M. and P. D. Asimow (2005) Adiabat_1ph: A new front end to the MELTS, pMELTS, and pHMELTS models. *Geochem. Geophys. Geosyst.* **6**, Q02004.

Truckenbrodt, J. and W. Johannes (1999) H_2O loss during piston-cylinder experiments. *Am. Mineral.* **84**, 1333-1335.

TABLES

Table 1

Run Number	T (°C)	Log (fO_2), bars	Fe Oxide Phase	X_{Fe}	1σ	a_{Fe}	Pd/Au	γ_{Fe}
1	1190	-6.5	Magnetite	0.014	0.002	0.0004	0.658	0.029
2	1190	-6.75	Magnetite	0.017	0.001	0.0006	0.658	0.035
3	1190	-8.85	Magnetite	0.099	0.003	0.015	0.657	0.151
4	1190	-9.75	Wüstite	0.178	0.002	0.049	0.660	0.273
5	1190	-10.5	Wüstite	0.244	0.002	0.129	0.667	0.531
6	1190	-5	Magnetite	0.0021	0.0006	0.00004	0.663	0.020
7	1190	-11	Wüstite	0.300	0.003	0.245	0.655	0.817
8	1190	-3.9	Magnetite	0.0003	0.0003	0.000008	0.653	0.029
8R	1190	-3.9	Magnetite	0.0004	0.0007	0.000008	0.659	0.021
9	1190	-7.5	Magnetite	0.039	0.001	0.0019	0.661	0.049
10	1125	-10.5	Magnetite	0.188	0.002	0.047	0.661	0.252
11	1240	-8.75	Wüstite	0.130	0.002	0.029	0.667	0.220
12	1240	-9.5	Wüstite	0.217	0.002	0.075	0.690	0.346
13	1125	-11.1	Wüstite	0.227	0.002	0.102	0.650	0.450
14	1190	-8.25	Magnetite	0.066	0.001	0.0060	0.651	0.091
15	1240	-7.5	Magnetite	0.063	0.002	0.0051	0.658	0.080
16	1125	-9	Magnetite	0.069	0.001	0.0047	0.656	0.069

Table 1: Experimental results. Fe Oxide phase is calculated based on established phase diagrams for Fe and confirmed via electron microprobe analysis. 1σ errors are values taken from repeat electron microprobe analysis. Pd/Au ratio is mole fractions of Pd and Au from electron microprobe analysis, with standard deviations of similar magnitude to those seen for Fe. Only run 12 shows a Pd/Au ratio significantly different from other samples. Gamma term is activity coefficient based on calculated activities of Fe at that temperature and oxygen fugacity and measured Fe content in the alloy.

Table 2

Oxide	Wt %	Component	Mole fraction	ΔG^0	Activity
SiO_2	50.34	SiO_2	0.427457	1040.63	0.461304
TiO_2	2.78	TiO_2	0.02933		
Al_2O_3	13.78	Al2O3	0.128616		
Fe_2O_3	1.01	Fe_2O_3	0.00628		
Cr_2O_3	0.1	$MgCr_2O_4$	0.000653		
FeO	10.08	Fe_2SiO_4	0.069658	1888.07	0.094583
MnO	0.17	$MnSi_{0.5}O_2$	0.00238		
MgO	7.08	Mg_2SiO_4	0.086889		
NiO	0	$NiSi_{0.5}O_2$	0.00004		
CaO	11.5	$CaSiO_3$	0.197753		
Na_2O	2.36	Na_2SiO_3	0.037811		
K_2O	0.53	$KAlSiO_4$	0.011173		
P_2O_5	0.28	$Ca_3(PO_4)_2$	0.001959		

Table 2: Composition of Kilauea 1919 basalt (Garcia et al., 2003) used here and values produced by calculation using the MELTS algorithm. Normative components are calculated by MELTS at 1190°C and QFM-1.6. Values for ΔG^0 (in kJ/mol) are apparent values relative to the standard state at 298.15K and 1 bar, and must be corrected to the appropriate temperature for use in equation 6 using the data of Robie et al (1978). After this correction, using these values for the activity allowed for calculation of a_{Fe} via equation 6 and conversion into X_{Fe} using equations 4 and 5.

FIGURE CAPTIONS

Figure 1. Mole fractions of Fe measured in Au-Pd alloys after each experiment. Lines represent approximate boundary between wüstite (low fO_2) and magnetite at each temperature. Errors here are expected to be smaller than the size of the symbol (maximum 2σ values ~0.2 in fO_2 and ~0.01 in Fe content).

Figure 2. Plot of activity-composition relationship based on calculated activities of Fe in wüstite or magnetite and measured alloy compositions.

Figure 3. Backscattered electron images of Samples 4 and 8R. Sample 4 (a) is a typical sample; lines are polishing features and black spots are dust or specks accumulated on surface. Sample 8R (b) shows the presence of an additional phase. The large dark spots are iron oxide crystals that formed during the reversal experiment. Electron probe measurements establish the phase to be magnetite.

Figure 4. Calculated RTln γ_{Fe} versus measured Fe content. Blue curve is the fit to the regular solution model presented in the text. All samples in this range show negative deviations from ideal solution, such that the value of ln γ_{Fe} is negative. The solution model, however, predicts that at higher values of X_{Fe}, beyond those examined in this study, the value of ln γ_{Fe} will become positive.

Figure 5(a). Composition of AuPd alloy calculated in equilibrium with Kilauea 1919 basalt at various values of oxygen fugacity. Data point is measured value of alloy

composition equilibrated with Kilauea 1919 basalt at QFM-1.6 (measured X_{Fe} = .114).

5(b). Buffering capacity of a capsule in equilibrium with Kilauea 1919 basalt. Buffering capacity is defined here as the change in the mole fraction of Fe in the capsule per log unit change in oxygen fugacity. Under all but the most oxidizing conditions, a variation of a full log unit in oxygen fugacity should produce measurable changes in both alloy composition and measurable Fe loss or gain in the experiment itself.

FIGURES

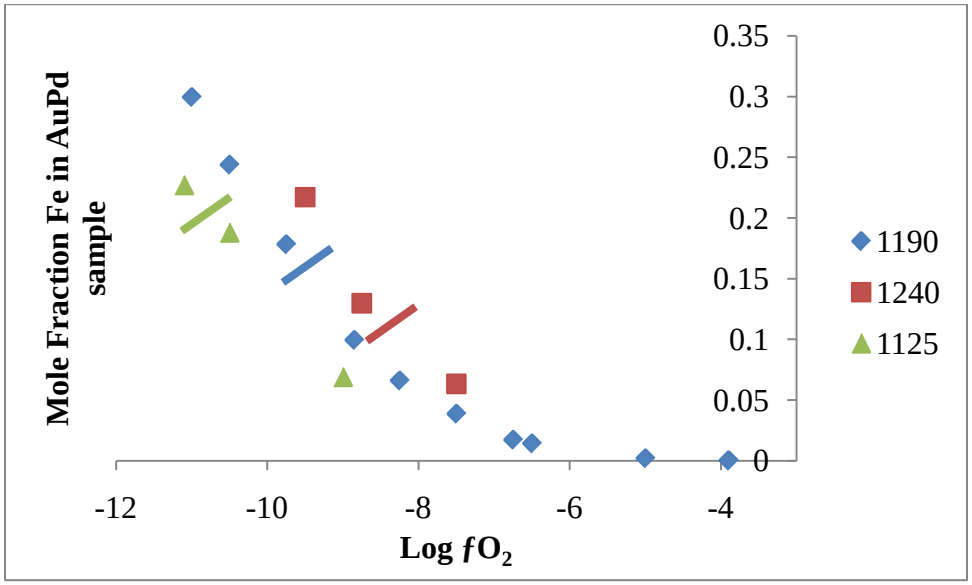

Figure 1

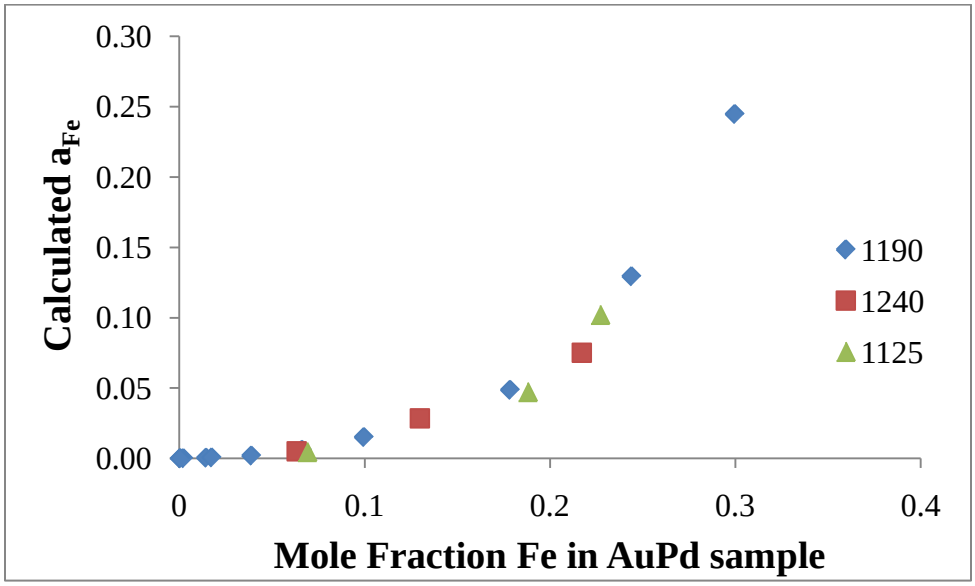
0.30
0.25
0.20
0.15
0.10
0.05
0.00
Calculated a_{Fe}
0
0.1
0.2
0.3
0.4
Mole Fraction Fe in AuPd sample
1190
1240
1125

Figure 2

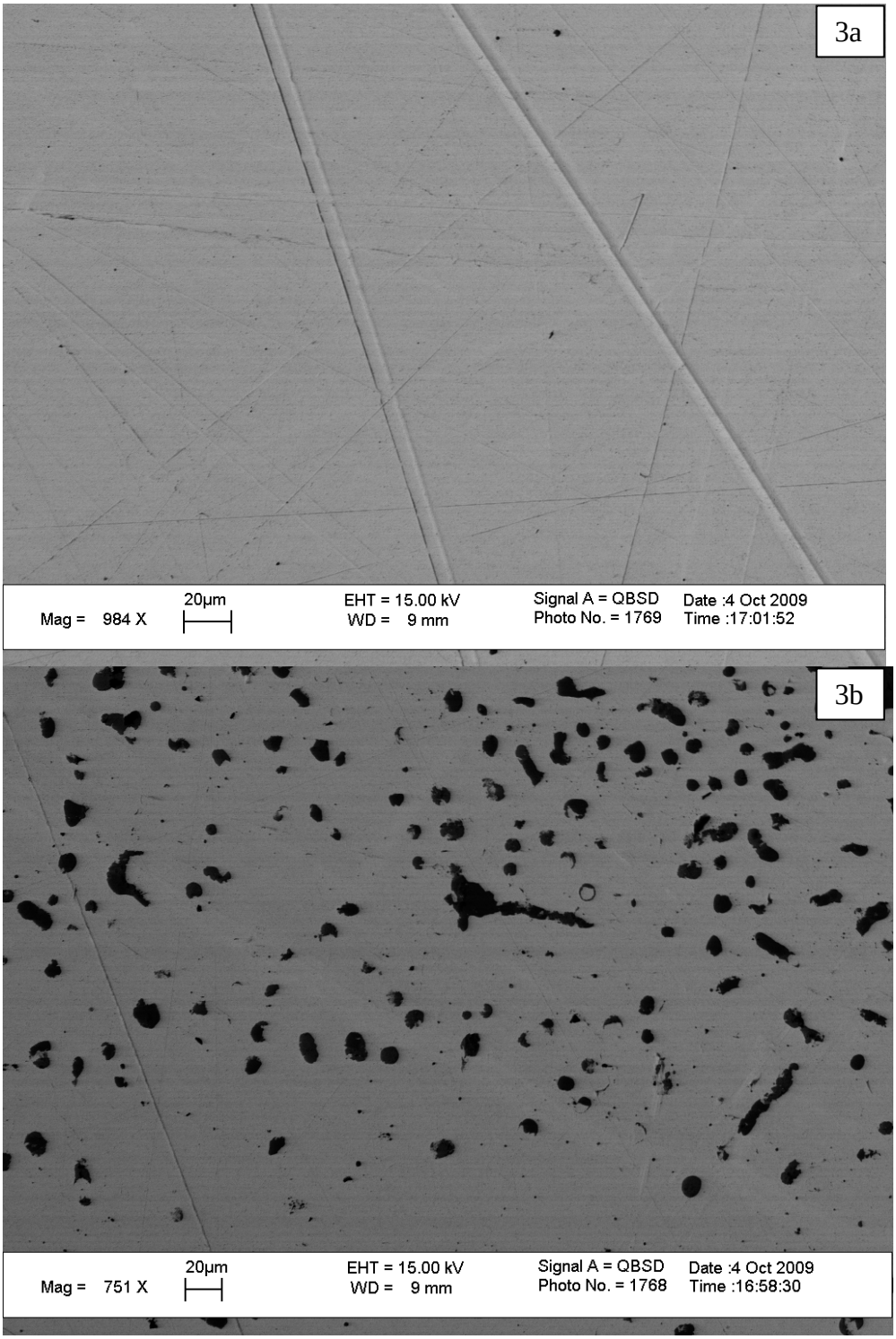
3a
Mag = 984 X
20µm
EHT = 15.00 kV
WD = 9 mm
Signal A = QBSD
Photo No. = 1769
Date :4 Oct 2009
Time :17:01:52
3b
Mag = 751 X
20µm
EHT = 15.00 kV
WD = 9 mm
Signal A = QBSD
Photo No. = 1768
Date :4 Oct 2009
Time :16:58:30

Figure 3

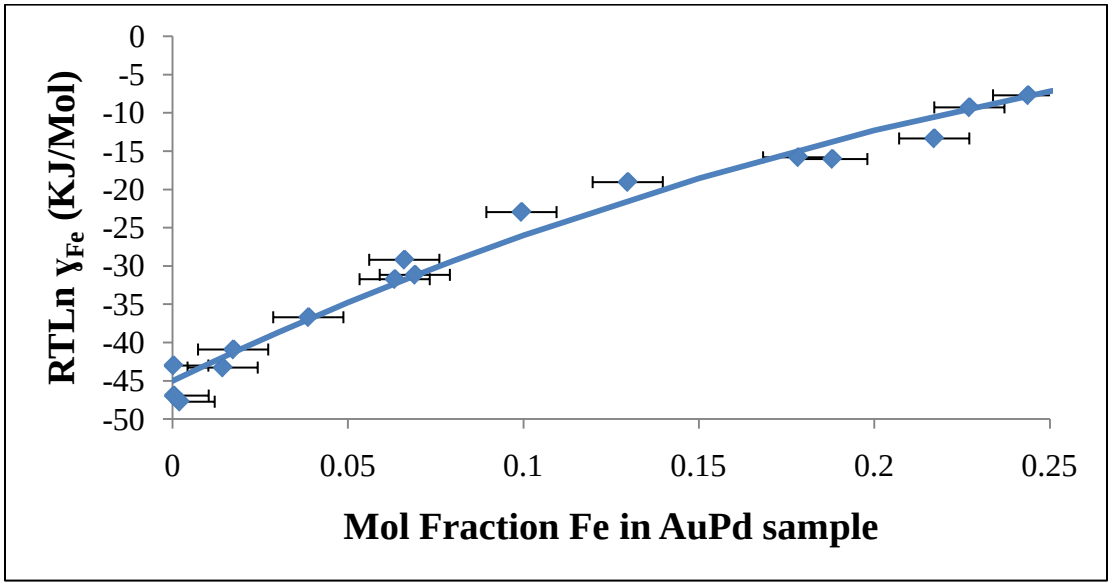
RTLn y_{Fe} (KJ/Mol)
0
-5
-10
-15
-20
-25
-30
-35
-40
-45
-50
0
0.05
0.1
0.15
0.2
0.25
Mol Fraction Fe in AuPd sample

Figure 4

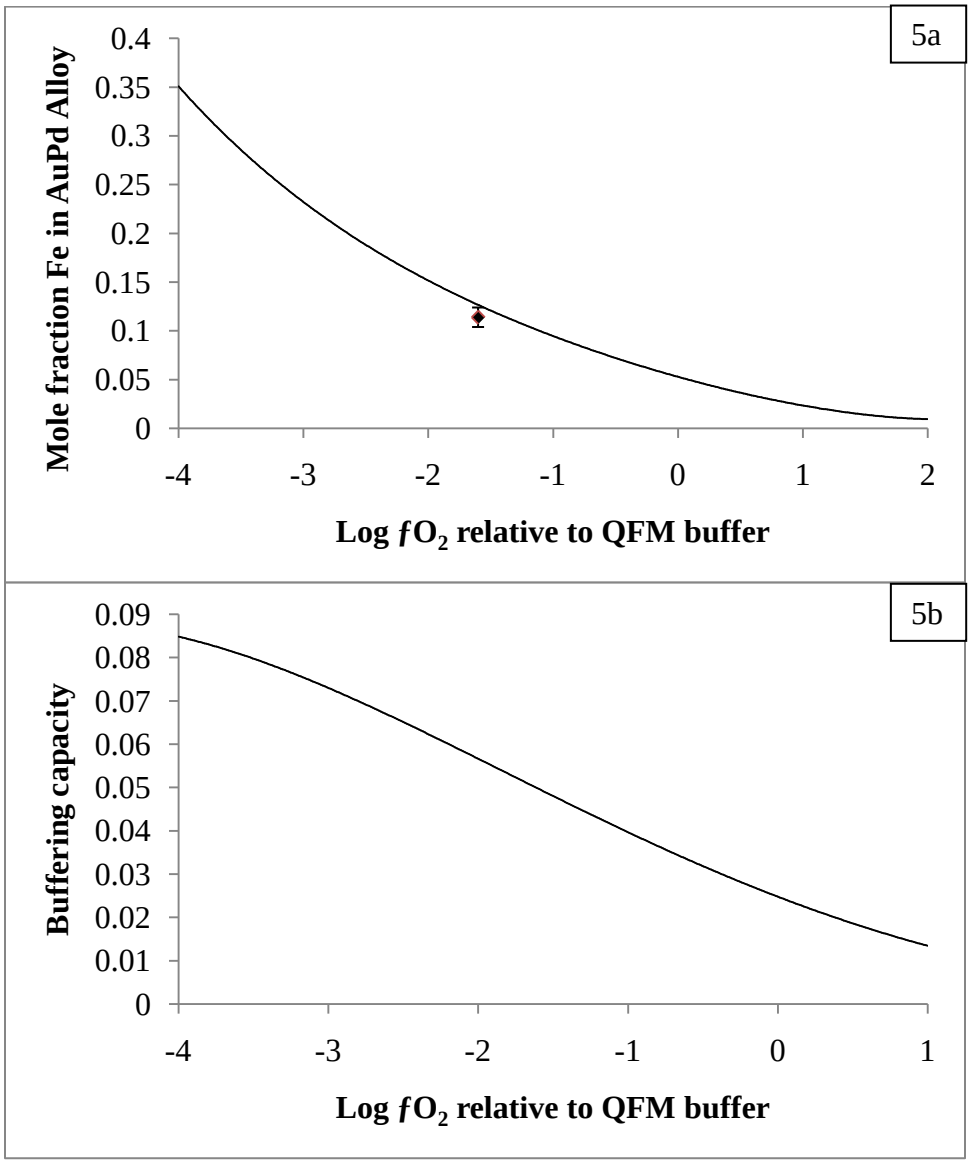
5a
Mole fraction Fe in AuPd Alloy
0.4
0.35
0.3
0.25
0.2
0.15
0.1
0.05
0
-4
-3
-2
-1
0
1
2
Log fO_2 relative to QFM buffer
5b
Buffering capacity
0.09
0.08
0.07
0.06
0.05
0.04
0.03
0.02
0.01
0
-4
-3
-2
-1
0
1
Log fO_2 relative to QFM buffer

Figure 5.

OLIVINE ABUNDANCES AND COMPOSITIONS IN HAWAIIAN LAVAS

By

J. Brian Balta

Michael B. Baker

Edward M. Stolper

ABSTRACT

Crystallization of olivine phenocrysts is the dominant differentiation mechanism of Hawaiian lavas. Some fraction of these olivine crystals are entrained within liquids as they erupt and produce the typical whole rock compositions of Hawaiian lavas that lie on mixing trends between basaltic liquids and olivines. Understanding the relationship between the olivines and the liquids that host them is key to interpreting data obtained on whole rocks, glasses, and mineral separates. The continually increasing supply of whole rock and olivine compositional analyses from Hawaiian volcanoes and the new availability of large, stratigraphically-controlled data sets from the Hawaii Scientific Drilling Project (HSDP) has allowed us to undertake a detailed analysis of the mixing process between Hawaiian basalts and crystallized olivines. The HSDP drill cores suggest that there is significant variability in the quantity of olivine carried by liquids through time, possibly related to changes that occur during volcanic evolution. We use these data sets to calculate estimated equilibrium parental liquid compositions for the best-sampled Hawaiian volcanoes and to test whether the olivine addition calculations are consistent with the bulk rock sample analyses.

1. INTRODUCTION

Over the past few years, sampling and analysis of the compositions of whole rocks and minerals making up the Hawaiian Islands has produced a wealth of new data that allows for the application of statistical techniques and chronological analysis of the growth and evolution of Hawaii at scales that were previously not practical. The Hawaii Scientific Drilling Project pilot hole (hereafter HSDP1) produced 1056 meters of core sampling 27 distinct lithologic units from Mauna Loa and 184 units from Mauna Kea (DePaolo et al., 1996). The second HSDP core (hereafter HSDP2) produced 3098 meters of core, sampling 32 units from Mauna Loa and over 300 units from Mauna Kea, including 2019 meters of submarine material and covering nearly 650 k.y. of time (Garcia et al., 2007). While the HSDP cores provide the most complete stratigraphic and chronological data set available for any Hawaiian volcano, other coring and sampling efforts have provided data covering many other Hawaiian volcanoes. The Ko'olau Scientific Drilling project (hereafter KSDP) produced 679 meters of core from Ko'olau volcano on the island of Oahu, sampling 103 units from that volcano (Haskins and Garcia, 2004). The SOH-1 drill core produced ~1700 meters of core from Kilauea's East Rift Zone, sampling 368 units (Quane et al., 2000). Drill cores are also not the only sampling technique that has produced a large quantity of data from Hawaiian volcanoes. The long-lived Pu'u O'o eruption of Kilauea has been monitored and sampled in great detail (e.g., Thornber et al., 2003). Offshore sampling efforts have produced representative data from many of the volcanoes in the Hawaiian chain, and many of these samples have been dateable due to associated biological activity (e.g., Clague et al.,

1995). The work of Sobolev et al., (2007) produced a large number of analyses of olivine compositions from several Hawaiian volcanoes, in addition to other studies of the same mineral (e.g., Helz, 1987; Garcia, 1996). Finally, onshore sampling of exposures and eruptions continues to improve the data available covering many of the Hawaiian shields (e.g., Rhodes, 1988; Marske et al., 2007).

Changing conditions during the growth of a volcano, such as changes in magma supply or average liquid composition, can affect the composition of the eruption products. Measurements of the compositions of erupted liquids and solids can give information on these changes and on the conditions under which they formed. Highly forsteritic olivines, with Mg #'s (= $100*X_{Mg}/(X_{Mg} + X_{Fe})$ on a molar basis) of 90 or above are found in Hawaiian lavas, and olivines with slightly lower Mg # are common, indicating that Hawaiian basalts must begin their fractionation process as highly magnesian liquids (e.g., Clague et al., 1991; Clague et al., 1995; and Garcia et al., 1996). However, analyses of the lavas being erupted from Hawaiian volcanoes indicate that very few lavas and no glasses have high enough MgO contents and MgO/FeO ratios to be in equilibrium with such primitive olivines. These facts suggest that some fraction of the olivine that crystallizes from the parental liquid is never erupted and is deposited within the volcanic plumbing system. (e.g., Clague and Delinger, 1994; Rhodes and Vollinger, 2004).

It has long been established that olivine-control lines define the main compositional variations amongst Hawaiian shield-stage lavas (e.g., Wright, 1971). The process generating this variation in Hawaiian lavas is now fairly well understood; highly

magnesian parental magmas rise through the crust, stall at a level of neutral buoyancy, and begin to crystallize olivine as they cool (e.g., Ryan, 1988; Garcia and Wolfe, 1988). Variable amounts of the crystallized olivine are entrained by erupting liquids as they move upwards, while other crystals are left behind within the volcano and form a dense, olivine-rich cumulate pile within the volcano (e.g., Clague and Denlinger, 1994; Kauahikaua et al., 2000). This description is a simplification as it is complicated by the effect of volatiles, which can decrease the overall density and therefore drive eruptions (e.g., Anderson, 1995), and entry of new magma into the system, which can displace earlier liquids from the magma chamber (e.g., Garcia, 1989). The mixing behavior that generates olivine abundance variations in a magma was demonstrated on a smaller scale by the 1959 Kilauea Iki eruption, which was originally erupted as a moderately olivine-phyric lava in a fire-fountaining event driven by volatile degassing (e.g., Gerlach and Graeber 1985; Decker 1987) but also formed a lava lake that slowly crystallized and mixed. This combination of crystallization and mixing created whole rocks that vary from highly olivine phyric to nearly aphyric due to addition and subtraction of olivine (Richter and Moore, 1966). A similar process likely works to generate heterogeneity in bulk rock olivine contents on a magma-chamber scale. As this process is evidently common in Hawaiian volcanoes, a more thorough examination of the processes leading to variable amounts of olivine within and between the Hawaiian shields should provide insight into the development of those volcanoes.

Clague and Denlinger (1994) calculated that based on their estimated parental magma for Kilauea, between 10 and 22% of the original mass of magma entering the

volcano remains within the volcanic edifice as olivine cumulates. The common occurrence of dunite xenoliths (e.g., Jackson, 1968), along with the evidence for a high-density anomaly near the core of each volcano (Kauahikaua et al. 2000), suggests that the missing olivine is deposited inside the volcano as the magma stalls and crystallizes. Conversely, the common occurrence of strained olivine grains within Hawaiian lavas suggests that olivines can be re-entrained in magmas as they move through the system (e.g., Helz, 1987), as those olivines must have resided for a time in a partially solid pile that is able to transmit shear stresses. Based on the HSDP1 drill core, Baker et al. (1996) estimated that only 4% of the mass of magma entering Mauna Kea is deposited as olivine within that volcano. Understanding the processes by which olivine grains are processed prior to eruption is particularly important for geochemical analyses, as mineral separates are often used to analyze isotopic compositions of Hawaiian rocks, and a close relationship between olivine grains and their host melt is a standard assumption in those analyses.

This paper will use the newly available databases covering a number of Hawaiian volcanoes including Mauna Kea, Mauna Loa, Kilauea, Hualalai, Loihi, and Ko'olau, to examine in detail the relationship between olivines and the melts that host them. We estimate the amount of olivine being stored within each volcano, and the bulk compositions of olivine that fractionate as the parental liquids evolve to liquids that represent the groundmass of erupted lavas, and calculate the parental magma compositions feeding the Hawaiian system.

2. METHODS

2. 1. Data compilation

Over 6700 whole rock analyses of Hawaiian basalts, 1700 glass compositions, and 8200 olivine analyses (including the data from Sobolev et al., 2007) were compiled from the literature and the GEOROC database (http://georoc.mpch-mainz.gwdg.de) (Sarbas and Nohl, 2008); data. Sources for this database are listed in Supplementary Table 1.

Whole rock analyses were processed as follows. Iron analyses were recalculated with all iron taken as FeO*. Data were sorted first by volcano and then filtered to produce data sets for each volcano where the variation is dominated by mixing of tholeiitic basalt (with 7-8% MgO) with olivine. First, all samples with less than 7 wt % MgO were eliminated to avoid samples that had crystallized significant amounts of phases other than olivine, which typically reach saturation at ~7% MgO (e.g., Richter and Moore, 1968; Wright and Peck, 1978). However, it is also possible that a liquid could fractionate to below this MgO content and then re-entrain enough olivine to produce a whole rock composition that meets this standard. For volcanoes such as Kilauea, Mauna Loa, or Mauna Kea, where there is a large amount of data available, making this filter more selective by limiting the dataset to samples above 7.5% MgO does not significantly change any of our conclusions and typically only removes a small number of samples, suggesting that the effects of plagioclase and clinopyroxene fractionation on rocks not removed by this filter is limited. The second filter applied to the data sets used the K_2O/P_2O_5 ratio to screen for samples that were highly altered. We removed all samples with K_2O/P_2O_5 ratios greater than 2.0 (Huang et al., 2007) or less than 1.0 (Huang and Frey, 2003). Again, a more stringent filter, removing all samples with K_2O/P_2O_5 less than

1.4 was tested and found to have no significant change on our conclusions. Finally, we filtered out all points that were from alkaline rocks, using the definition of alkali index from Rhodes and Vollinger, (2004). These filtering steps excluded over 50% of the whole rock analyses available for Hawaii, although some volcanoes were more heavily filtered than others (Table 1). Data sets built from the analyses passing these successive filters form the basis of the regression analysis presented here.

2. 2. Conversion between mineralogy and geochemical analyses

For samples from the four major drill cores examined by this study, along with various other data sets, published point counting results are available for modal olivine abundances. To supplement the existing data in Garcia et al. (2007), we conducted a series of 43 point counts on slides from the Caltech Reference Suite of samples from the HSDP2 drill core (Table 2). Between 500 and 800 points were counted and identified as olivine, vesicles, plagioclase, or matrix. Phases <0.5 mm were considered part of the groundmass, similar to the standard used by Baker et al. (1996). The typical step size was 1 mm. One sample was counted on four separate occasions to yield an estimate of the uncertainties on the mode, which were found to be ± 2% absolute olivine abundance. The abundance of olivine, which has MgO content near 50 wt. %, should be strongly correlated with the whole rock wt. % MgO. There is expected to be some scatter, as the sample used to make the thin section may not always be fully representative of the larger sample used for bulk rock analysis. In general, each volcano shows a linear relationship between modal olivine and whole rock wt. % MgO (Figure 1). We derived a regression line for each volcano, as was done by Baker et al. (1996). Essentially all of the slopes of

the different regression lines overlap at the 1σ level. There is some scatter around each line, although this is typically less than 10 % absolute olivine modal abundance (1σ). Each of the data sets from the different volcanoes overlaps at the 1σ level, suggesting that modal olivine abundance can be estimated with good precision for any Hawaiian sample from the whole rock MgO content. In this database and in Fig. 1, this variation in modal olivine at a constant MgO content provides an estimate of the variation inherent in analyzing samples of variable size from different portions of units with possible variations in liquid compositions superimposed. This comparison suggests the variation seen here is the magnitude that should be expected in any work based on point counting from similar rock types.

A key issue for the data presented in Figure 1 is the handling of vesicle contents. As whole rock analyses use crushed or fused rock powders, the vesicle content in a sample will have no effect on the whole rock composition. However, volume percentages measured via point count can be sensitive to the percentage of vesicle space in a given thin section. In Figure 1, the olivine volume percentages were normalized to total vesicle-free volume in the point count. This correction can potentially be a source of significant error (and hence a source of scatter in Figure 1) as the variation in vesicle contents can be large even within individual flows (Self et al. 1998). To minimize this issue, we adopt for all unknown samples the linear relationship between whole rock wt. % MgO and olivine contents defined by regression of the point counts from HSDP2 normalized to vesicle-free volume for any sample with a whole rock analysis but no available point counts. We

will generally present data as whole rock weight % MgO, but conversion to olivine abundance can be done simply with the expression from Figure 1.

2. 3. Chronology

Determining approximate ages for units in the available drill cores is a necessary step in understanding the evolution of these magmatic systems over time. For HSDP1 and HSDP2, we adopt the age versus depth relationships of Sharp and Renne, (2005), based on ^{40}Ar-^{39}Ar dating performed on the HSDP2 drill core.

Ages in the other drill cores are less well constrained. The SOH-1 drill core, and its companion hole SOH-4, have been dated by ^{40}Ar-^{39}Ar and produced ages ranging up to 350 ka for the oldest rocks (Quane et al., 2000). However, other dating has suggested that the Kilauea pre-shield stage may not have ended until 130 ka (Lipman et al., 2000). Teanby et al. (2002) performed a detailed paleomagnetic survey of the subaerial portion of the SOH-1 drill core and could not reconcile the radiometric ages with paleomagnetic age estimates. They calculated an age progression that dated the bottom of the subaerial portion of this drill core at 45 ka, giving an accumulation rate of just over 15 m/k.y. for that section of the core. This rate is consistent within a factor of two with the accumulation rates estimated by Sharp and Renne (2005) for Mauna Kea and is well-fit by the growth model for Hawaiian volcanoes of Depaolo and Stolper (1996). Assuming that this average accumulation rate persisted over the submarine section of the SOH-1 drill core gives an age of 107 ka for the bottom of the core. We therefore used the age model of Teanby et al. (2002) for the subaerial section and this constant accumulation rate for the submarine section of this core.

Applying an appropriate age model to the KSDP drill core also is difficult. Several ^{40}Ar-^{39}Ar dates were reported by Haskins and Garcia (2004), but given the age of the rocks and the uncertainty in the measurements the ages of the top and bottom of the drill core were indistinguishable. Based on the data from the other drill cores, however, a reasonable chronology for the KSDP sequence can be constructed. The reported errors in ages from Haskins and Garcia (2004) were ± 200 k.y. An average accumulation rate at the KSDP site of 3 m/k.y. or less would mean that the KSDP core would represent more than 200 k.y. of time and should have yielded ages that were measurably distinct, placing a lower bound on the accumulation rate. Placing an upper bound on the accumulation rate at this site is more difficult, but the KSDP core samples material from the latter stages of activity of Ko'olau when the volcanic activity was presumably waning. An average accumulation rate of 5 m/k.y. at the site gives a total age of just over 100 k.y. for the flows reflected in the core and a resurfacing interval of 1000 years for the site, similar to that reported for Mauna Kea (Garcia et al., 2007), so this is the accumulation rate we have chosen as an average for this core. However, we have no ability to recognize changes in accumulation rate and may be missing events such as a change in accumulation rate with time like that seen in Mauna Kea.

3. RESULTS

3.1 Olivine regression analysis

There are sufficient bulk rock analyses for eight Hawaiian volcanoes to construct statistically meaningful olivine control lines in the sense that when extrapolated to the olivine composition line, the olivine composition is constrained within ± 1.2 Mg#. These

include: Kilauea, Ko'olau, Haleakala, Mauna Loa, Mauna Kea, Loihi, Waianae, and Hualalai. The full set of bulk rock analyses and olivine control lines are shown in Figure 2. Each volcano is well fit by an olivine control line calculated via unweighted least squares linear regression. The differences in slopes reflect differences in the liquid compositions at each volcano that entrains olivine and differences in the average composition of the entrained olivine.

Projecting the linear regression lines in these analyses from the available data set towards the composition line representing an olivine end member (including minor and trace components as calculated in the olivine addition analysis below) allows for determination of the average olivine composition mixing in each volcano's magma series, as was done with a more limited data set from HSDP1 in Baker et al. (1996). With these data sets, several differences become apparent. Most notably, there appear to be some volcanoes which have different average olivines at the end of their olivine control line trend. Mauna Kea, Hualalai, and Mauna Loa appear to contain on average more forsteritic olivines, with Mauna Kea averaging Mg# 87.9, Hualalai averaging Mg# 87.4, and Mauna Loa averaging Mg# 87.3. Conversely, Ko'olau, Waianae, and to a lesser extent Kilauea sample olivines that are slightly more fayalitic than olivines from other volcanoes, with Ko'olau averaging Mg #86.2 and Kilauea averaging Mg# 86.6. Loihi, and Haleakala sit in-between these volcanoes and are indistinguishable from each other.

The differences in these data sets can be visualized from Figure 2 by noticing the differences in slope and absolute FeO* content of the regression lines at 7 wt% MgO between the volcanoes. Mauna Kea has a noticeably flatter slope to its olivine control line

compared to the other volcanoes, which reflects the higher Mg # of the olivine in its whole rocks, while Ko'olau and Waianae show slopes that are somewhat steeper than those of the other volcanoes. The differences in FeO* between volcanoes are small and most of the volcanoes are statistically indistinguishable (Figure 3). Ko'olau and Mauna Kea appear to be the only two volcanoes with FeO* contents that can be distinguished. At 7% MgO, Mauna Kea averages FeO*=11.3 ± 0.4, while Ko'olau averages FeO*= 10.4±0.3. The other volcanoes all fall within the range of FeO* 10.5-11.0, except for Loihi, which averages 12.0%±0.5 but is less well sampled than the others. In Figure 3 we plot histograms of olivine abundance for Mauna Kea and Ko'olau to illustrate the different average FeO* contents. Notably, Ko'olau shows a larger range in FeO*, and many of its higher FeO* content samples are also more olivine-phyric, suggesting that the small difference in FeO* may be entirely due to the different average olivine composition being crystallized from the volcano. Loihi may actually show higher FeO* contents across its full range of samples, but more sampling is required to better constrain the variability at the low-olivine end.

We also applied a similar regression analysis to the available drill cores. All of the drill core data are included in Figure 2, but only for Mauna Kea do they constitute 50% or more of the available whole rock analyses. The SOH-1 core through Kilauea was not useful for olivine control regression analysis as there were not enough olivine-rich points to generate a significant trend. The HSDP cores through Mauna Kea and Mauna Loa and the KSDP core through Ko'olau all produce trends that cannot be distinguished within error from the trends seen in the full data sets from the same volcano, suggesting that the

full data sets are representative of the behavior of the volcanoes over time. Mauna Kea's average olivine composition as predicted by the bulk rock HSDP2 FeO*-MgO regression is indistinguishable from that reported by Baker et al. (1996) for the HSDP1 core, which sampled only subaerial Mauna Kea flows. Stolper et al. (2004) identified two different magma series in the HSDP2 glasses from Mauna Kea defined by high and low silica compositions. Using their definition for high and low silica glasses and taking whole rock analyses from the same units, we have sufficient data to define olivine control line trends for both magma series. Both high and low SiO_2 units mix towards olivines with Mg # of 87.9, again indistinguishable from the full core (Figure 4).

For volcanoes where >100 olivine composition measurements are available, the measured olivine compositions provide an alternate way to infer the composition of the average added olivine. Six volcanoes have a sufficient number of reported olivine compositions to allow for an analysis of their populations (Figure 5). We plotted histograms of individual analyses from these volcanoes, most of which sample the composition of the core of a single grain. The distributions for several volcanoes show sharp peaks around Mg# 88, while Hualalai and Ko'lau show more broad patterns. Mauna Loa shows on average the most magnesian olivine, with a median value of Mg# 88.9, followed by Mauna Kea at Mg# 87.9, which is the exact value calculated from the olivine control line. The mean absolute deviation for these two volcanoes is 2.0 units. Mauna Loa shows a median value with a slightly higher Mg# than its average composition seen in the regression analyses, but the values overlap within error. This slight difference could occur if the olivines selected for analyses were slightly biased

towards higher Mg# olivines, such that the distribution of analyses is not fully representative of the mass distribution of olivine compositions. Ko'olau and Loihi both have a median average olivine measured at Mg# 86.6, again similar to the olivine control line trend. The mean absolute deviation for both is also constrained to better than 2 units. Hualalai and Ko'olau each show evidence of two separate abundance peaks, one close to Mg# 88 and another close to Mg# 84. Several authors (e.g., Clague, 1988; Shamberger and Hammer, 2006) have argued that the dunites from Ko'olau and Hualalai represented the products of crystallization from post-shield, alkali magmas. This lower peak at Mg# =83-84 appears in Ko'olau, Mauna Kea, and Hualalai, and according to our data set most of these samples represent olivines from post-shield magmatism or dunites. The peak in Mauna Kea is small compared to the other volcanoes because many of its measured olivines come from the HSDP drill cores, which sample much of its shield-building stage. Kilauea also shows a large peak at Mg# 88, but also has significant quantities of olivine with Mg#'s below those measured from any other volcano. The large spread of olivine compositions for Kilauea also increases the mean absolute deviation to 4.1 units in Mg#. These low-Mg# olivines from Kilauea typically represent the products of crystallization of magmas that evolve in the magma chamber (e.g., Garcia et al., 1989) or the product of re-equilibration inside lava lakes (Moore and Evans, 1967). While these processes likely occur at all Hawaiian volcanoes, these low Mg# olivines may be found most commonly in Kilauea because of the detailed sampling done during the full duration of eruptions, whereas other volcanoes are sampled more commonly as individual events long after deposition. In these cases, the earliest or latest olivines in an eruption may be less likely

to be sampled and thus are only seen in substantial quantities in Kilauea. Except for Kilauea and Hualalai as noted, the average and median compositions for all the volcanoes calculated in this analysis overlap within error of the average olivine composition calculated by the olivine control line regression analysis.

3.2. Olivine abundance chronology

The chronologic series of units in HSDP2 and the other drill cores was analyzed for olivine abundances over time, as represented by the bulk MgO content of the rocks (Figure 6). Using the bulk rock analyses, the thicknesses of the measured units, and point count data including the average vesicle content of the units where available, we have calculated a bulk average composition of the volcanoes sampled by the HSDP1, HSDP2, KSDP, and SOH-1 drill cores. These bulk average compositions are given in Table 4d. To perform this calculation, we averaged the bulk composition analyses for each drill core weighted by the thickness of each unit on a vesicle-free basis. This exercise was hampered by the fact that not all of the units in each drill core were sampled by both point counts and bulk rock analyses. In addition, we could not correct the KSDP drill core thicknesses for vesicle count as the vesicle abundances were not explicitly recorded, so the raw thicknesses were used (Haskins and Garcia, 2004). Both Mauna Loa and Mauna Kea in the HSDP sections are highly olivine-phyric compared to the KSDP and SOH-1 drill cores. On average, the HSDP2 Mauna Loa section contains 13.6% MgO, Mauna Kea's HSDP2 section contains 14.1% MgO, the KSDP section contains 8.5% MgO, and the SOH-1 section contains 7.6% MgO. Based on the calibration given in Figure 1, these equal 16.4 volume % olivine for Mauna Loa, 15.6 volume % olivine for

Mauna Kea, 3.3 volume % olivine for Ko'olau, and 1.4 volume % olivine for Kilauea. This value for Mauna Kea is similar to the integrated MgO abundance of 13.2% calculated by Baker et al. (1996) for the Mauna Kea section of the HSDP1 drill core. However, the value for the SOH-1 drill core is less than the average MgO abundance for either bulk Kilauea (10 wt.%) or for only subaerial Kilauea flows (9 wt.%) estimated by Clague and Denlinger (1994). Clague and Denlinger (1994) based their estimate in part on individual samples collected from specific eruptions, without correction for the volume of erupted material or long-term sampling, which may explain the difference in estimated bulk Kilauea composition.

There is a difference in sampling density between the cores that could provide a substantial margin of error to this examination if units are not sampled at random. The geochemical analyses of the KSDP drill core samples represent over 90% of the total thickness of units, the HSDP2 drill core samples represent approximately 75% of the total thickness of units (depending on how individual intrusive units are counted), while the SOH-1 analyses only sample approximately 33% of the total thickness of units.

The HSDP2 core through Mauna Kea produces a detailed record of the variations in olivine deposition at the drill site through much of the growth of the volcano, while the other drill cores provide samples of specific intervals of the lifetimes of those volcanoes. Several differences can be seen by comparison of these cores (Figure 6). First, the SOH-1 core through Kilauea has lower olivine content than any of the other Hawaiian volcanoes sampled. Secondly, the latter stages of each volcano's lifetime, represented by the flows through Mauna Loa in HSDP2 (e.g., Moore and Clague, 1992; DePaolo and Stolper,

1996),the KSDP core through Ko'olau (Haskins and Garcia, 2004), and the latter part of Mauna Kea's lifetime in HSDP2 (Sharp and Renne, 2005), is marked by high-frequency variation in the olivine content being deposited at these drill sites, with swings from low to high average olivine contents on about a 20 k.y. timescale. This behavior can be seen in the sequences for Mauna Loa, Ko'olau, and in the portion of Mauna Kea younger than 420 ka, and is well expressed in the changes in the calculated moving averages with depth (Figure 6). Younger than 330 k.y., Mauna Kea again shows limited variation but also shows more sparse sampling, mostly within its postshield lavas. Conversely, the SOH-1 core and the majority of the submarine section of the HSDP2 core show fairly stable trends in olivine abundance with time; the average olivine contents only change on timescales of 100 k.y. The lowest portion of the HSDP2 core, however, again shows more rapid changes in olivine content.

Although not plotted here, the HSDP1 section through Mauna Loa and Mauna Kea shows similar behavior to the upper portion of HSDP2 in both the high-frequency variation in olivine abundances and in the olivine-controlled bulk composition, measured to be 13.2% MgO (12.5% olivine) on average in Mauna Kea in HSDP1 (Baker et al., 1996) and 13.9% MgO (14% olivine) for the subaerial section of Mauna Kea in HSDP2. Conversely, the deeper portion of Mauna Kea and the section through Kilauea shows a different style of behavior, with longer periods of steady olivine contents.

The pattern of MgO abundances in Mauna Kea changes immediately below the submarine to subaerial transition at a calculated age of 413 ka. The upper submarine deposits are highly olivine-phyric, and the abundance of olivine gradually decreases with

increasing depth. The moving average of whole rock MgO shown in Figure 6 reaches a local maximum of 20.07% MgO (26.8% olivine) at 444 ka and decreases steadily deeper in the section to a local minimum of 10.25% MgO (6.4% olivine) at 584 ka. The 67 k.y. section just below the subaerial/submarine transition averages 17.42% whole rock MgO (21.3% olivine). The lower portion of this trend, covering a period of nearly 80 k.y. from 530 k.a. to 610 k.a., averages only 11.45% MgO (8.9% olivine). This is a much lower olivine content than has been measured for any extended portion of Mauna Kea in this area prior to sampling in HSDP2. This trend continues across different flow unit types and across both the low and high SiO_2 magma series. The bottom section of the core seems to resume more high-frequency variation, but this appears to be due to the presence of a series of high-olivine pillow basalts. Aside from these deep pillows, the trend of decreasing olivine abundance includes both hyaloclastite and massive units and even some pillow lavas (Figure 6).

3.3. Historic flows

The modern magmatic activity provides a final set of data to allow for comparison between the olivine abundances in the drill cores and the full magmatic history. Analyses of the available, well-dated historic flows for Mauna Loa and Kilauea are plotted in Figure 7. Both volcanoes show significant variation in olivine content between and within successive flows, some of which can be related to crystallization and accumulation within a particular unit. The modern Kilauea flows prior to 1983 average 8.30 wt. % MgO, with no weighting by unit thickness, volume, or number of samples per unit; a number similar to the low whole rock MgO value seen in the SOH-1 drill core.

The modern Mauna Loa flows, similarly unweighted, average 9.11 wt. % MgO, greater than seen in modern Kilauea flows but significantly less than the average seen for Mauna Loa flows in the HSDP drill cores. For future flows, including the current Pu'u O'o eruption at Kilauea, accurate estimates of the volume of extruded material will make these analyses far more complete.

The modern eruption of Pu'u O'o currently consists of 3.38 cubic kilometers of material, up to 35 meters thick, according to data published by the Hawaiian Volcano Observatory (see http://hvo.wr.usgs.gov/kilauea/summary/Current_table.html). This thickness is comparable to some of the larger units sampled in the HSDP cores, which are tens of meters to roughly one hundred meters in thickness. The Pu'u O'o eruption has been sampled in great detail, and therefore provides an example for the evolution of olivine abundances during a single eruption (Figure 8). The average whole rock MgO in the Pu'u O'o eruption is 8.19 wt. % (2.1% olivine), similar to the long-term average composition for Kilauea and to the bulk average seen in the SOH-1 drill core. Samples from the Pu'u O'o eruption do show some variation in olivine abundance, reflected by the whole rock wt. % MgO analyses in Figure 8. The variation in olivine abundance in the Pu'u O'o eruption is less in magnitude than the variation seen in Figure 1 (~3% olivine abundance), suggesting that intra-unit variation can make up a small part of the scatter seen in that figure.

3.4. Olivine addition calculations

The average basaltic liquid erupted by Hawaiian volcanoes contains 6-8 wt. % MgO (e.g., Wright and Fiske, 1971; Thornber et al., 2003; Stolper et al., 2004). A

significant amount of olivine must crystallize to move a melt from equilibrium with olivines with Mg # of 90-91 to those typical liquid MgO contents (e.g., Basaltic Volcanism Study Project 1981; Clague et al., 1995; Baker et al., 1996). Starting from typical glass compositions for the best-studied Hawaiian volcanoes, we have mathematically reversed this process to calculate the liquids that would be in equilibrium with the most highly magnesian olivine sampled in each volcano. Average glass compositions were obtained for the best-sampled volcanoes in Hawaii: Mauna Kea, Mauna Loa, Kilauea, Ko'olau, and Hualalai (Table 4) to use as starting points. The initial starting glasses for the calculation were calculated by averaging glass measurements with >7% MgO to ensure that the starting liquids were only saturated with olivine and spinel. The calculations were performed by adding 0.1 % of equilibrium olivine to the glass or whole rock composition at each step. For completeness, at every step we also added 0.001% of a chromian spinel, based on the ratio given in Roeder et al. (2006). The spinel added was an average spinel composition from Pu'u O'o as measured by Roeder et al. (2003).

The olivine-melt Fe-Mg exchange parameter K_D is the key variable in these calculations. Calculations were performed first with the olivine K_D parameterized following the method of Toplis (2005). For that parameterization, we chose values of H_2O content to be 0.7 wt % (similar to average H_2O content of undegassed samples from Seaman et al. (2004)), a pressure of 1 bar, and a temperature at each step calculated using the olivine-liquid thermometer of Beattie (1993). This leads to some variation in calculated K_D values between the volcanoes due to the differing initial compositions; the

lowest average K_D was .305 in the Mauna Kea low SiO_2 series, and the highest was .318 at Haleakala. An oxygen fugacity of 1 unit below the quartz-fayalite-magnetite buffer was assumed based on recent analyses of olivine-melt equilibria (e.g., McCann and Barton, 2005), and Fe^{2+}/Fe^{3+} ratios were calculated at this oxygen fugacity using the calibration of Kilinic et al. (1983). Nickel and manganese were considered in the olivine and calculated based on the experimentally calibrated expressions of Wang and Gaetani (2008). Nickel contents were typically not measured in glasses, and so a value of 0.008% was used as the initial glass starting composition; this produced high-Mg# olivines containing ~0.5% NiO, similar to values measured by Sobolev et al. (2007). Calcium, chromium, and aluminum were included in olivine in small proportions based on average olivine compositions from Hawaii from the GEOROC database and assuming charge-balancing for the +3 oxidation state cations by putting ½ the Cr and Al in the tetrahedral site and ½ in the octahedral site.

The olivine addition calculations continued until the calculated olivine was equal to the most magnesian olivine reported in the GEOROC database for each volcano. Mauna Loa and Hualalai show olivines up to Mg# 91.2, Mauna Kea shows one sample in the Sobolev et al. (2007) database with Mg# 91, but the remainder of its olivines are 90.5 and below and this analysis appears uniquely high. The highest recorded Mg# olivine for Kilauea is 90.7. For Ko'olau, most of the existing analyses come from xenoliths or from post-erosional flows. A few samples have Mg # greater than 91, but the highest Mg # in a lava flow was 90.5 recorded in a basanite (Sobolev and Nikogosian, 1994), and this olivine was used as the stopping point for the olivine addition in that volcano. For

Haleakala there are available glass compositions but not extensive analyses of olivine compositions, and so we assumed its olivines were similar to Ko'olau and Mauna Kea. A few very highly forsteritic olivines (up to Mg#=97) have been found in Hawaii, but Garcia et al. (2000) noted that these are likely alteration products created by high-temperature alteration producing magnetite and hypersthene by replacing the original olivine, and thus they will not be considered here.

The variety of data sets available in this analysis gives us a new ability to assess the utility of these calculations. Because we know the mass of olivine added in each step and its composition, it is trivial to calculate the average olivine composition added. This number can then be compared with the average olivine compositions seen in the previous analyses. For most of the volcanoes considered here, the match between the average added olivine and the olivine composition inferred from the olivine control line in FeO*-MgO space is quite good (Table 4). The olivine addition calculation predicts that the average olivine in Mauna Loa (Mg# = 87.7) and Hualalai (Mg# = 87.5) is more magnesian than that found in Ko'olau (Mg#= 86.5), Kilauea (Mg# = 86.7), and Haleakala (Mg# = 86.7), and all of these calculated average olivine compositions lie within the errors of the mean values seen in the regression analysis or the mean absolute deviation of the histogram populations. Because the olivine compositions added to Ko'olau are calculated to be slightly different than the olivine compositions added to the other volcanoes, the difference in whole rock FeO* contents from Ko'olau shown in Figure 3 disappears as the calculation proceeds, suggesting that the slightly low FeO* contents in Ko'olau are a consequence of the composition of olivine being crystallized.

Mauna Kea, notably, shows a mismatch between the average added olivine composition and the olivine control line and histogram trends; the average added olivine is less forsteritic than seen in the other analyses. Mauna Kea's olivine addition trends produce average olivines of Mg# 86.4 and 86.7 for the high and low SiO_2 series, respectively, compared to Mg#= 87.9 in the regression analysis. There are a number of possible explanations for this result, which we consider below. It is possible we are underestimating the final olivine Mg# at which we should end the calculation by stopping at Mg# 90.5. If we extend the calculation to Mg# 91 to match the single olivine from Sobolev et al. (2007), it improves the match but does not entirely resolve the discrepancy (average added Mg# = 87.2 and 86.9), and also increases the MgO content of the calculated liquid substantially. An alternate possibility is that Mauna Kea is actually producing less low-Mg# olivine. One method by which this could be achieved is a rapid flushing of new magma through its system sustained by a very high magma flux; in this case, the average liquid in the magma chamber would remain above 7% MgO and olivines with lower Mg#'s would not be involved in the mixing process in the magma chamber. By rapidly flushing the magma through Mauna Kea, the low-Mg# olivines we assume in our calculation would only have crystallized after eruption, if at all. A similar suggestion was offered by Rhodes and Vollinger (2004) as an explanation for the lack of low-MgO content whole rocks over a substantial portion of the HSDP2 drill core. We tested this suggestion in the olivine addition calculation by using starting glass compositions created by averaging only glasses from Stolper et al. (2004) with >8% MgO. In this case, we were able to produce a much better fit to the expected average

olivine composition (Mg# = 88.0 and 87.7). If we start the olivine addition calculation with a liquid at ~9% MgO, we can produce an adequate fit to the average olivine composition with a parental liquid consisting of the liquids given in Table 4b with 17% MgO and with a maximum olivine Mg# of 90.5, suggesting that 9% MgO is the highest MgO content of the erupting liquid that would be consistent with the olivine addition trends.

3.5 Olivine CaO contents and re-equilibration

To better understand the applicability of these olivine control lines and olivine addition calculations to the evolution of natural Hawaiian magmas, we also examined the CaO compositions of olivines for the sampled volcanoes (Figure 9). CaO was ideal for this analysis, since we have both high-precision analyses of olivine CaO contents and a calibration for the variation of CaO in olivine during crystallization (e.g., Libourel, 1999). In addition, the diffusion rates for CaO in olivine are slower than for MgO or FeO (Jurewicz and Watson, 1998b) and thus CaO can preserve information that other oxides do not. For this analysis, we focused on the olivine composition measurements from Sobolev et al. (2007) because in this single data set we know that all analyses were obtained under the same analytical conditions and with appropriate settings to analyze low-concentration elements with minimal errors. This limited us to the five volcanoes sampled in that study; Loihi, Mauna Kea, Mauna Loa, Ko'olau, and the Kilauea Iki eruption from Kilauea.

Libourel (1999) developed an empirical model for CaO partitioning between olivine and melt that allowed for estimation of the CaO content of olivine in equilibrium

with silicate melts. That model predicted that as a Hawaiian magma evolves from crystallizing olivines with Mg# 90 to Mg# 80, there should be a substantial increase in the CaO content of the olivine (the red line shown in the panel for Mauna Kea in Figure 9) from ~0.2% to ~0.4% due to increasing CaO contents in the melt and increasing D_{CaO} (=CaO concentration in olivine/CaO concentration in liquid). After the liquid reaches ~7% MgO and begins to crystallize olivine with Mg# ~ 81, the liquid reaches plagioclase saturation and the CaO content of the olivine should then begin to decrease because of decreasing liquid CaO contents (e.g., Wright and Peck, 1978; Libourel, 1999). The available Hawaiian olivine analyses show a more complicated pattern (Figure 9). Every volcano shows low CaO contents of ~ 0.2% in their highly magnesian olivines, consistent with the prediction of Libourel (1999). However, as crystallization proceeds, the patterns diverge. Ko'olau and the olivines from Kilauea Iki show fairly flat trends, with less increase in olivine CaO content than predicted by the model of Libourel (1999). Mauna Kea and Loihi show some olivines that increase in CaO content with decreasing Mg# as predicted by Libourel (1999), but also have an additional population that varies between this trend and the nearly-flat trend similar to Kilauea and Ko'olau. Finally, Mauna Loa shows most of its olivines along a flat trend, similar to Kilauea and Ko'olau, but has a small group of olivines that show elevated CaO contents, similar to the high CaO olivines from Mauna Kea and Loihi but fewer in number.

The increasing CaO content in olivine predicted by Libourel (1999) occurs because the CaO content of the liquid increases when olivine is the sole crystallizing silicate phase and because the D_{CaO} increases as the olivine Mg# decreases. Lower olivine

CaO contents than predicted by the crystallization trend should only be produced if the olivine equilibrates with either a liquid that has begun to fractionate plagioclase or if the olivine remains in equilibrium with a highly magnesian liquid that is lower in CaO than the melt from which it initially crystallized. A number of lines of evidence suggest that the low CaO contents of these olivines represent re-equilibration of the olivine with a highly magnesian liquid during residence inside the volcano. First, the crystallization of significant amounts of plagioclase would likely produce olivines with even lower olivine contents than seen in the horizontal trends in Figure 9. Examples of this behavior can potentially be seen in some samples from Loihi (Figure 9) and from post-shield dunites from Hualalai (Chen et al., 1992; Clague and Denlinger, 1994) which show lower CaO contents than most of the olivines discussed here. In both cases, these olivines likely equilibrated with liquids that had crystallized significant amounts of plagioclase and were therefore low in total CaO. These liquids are likely not common during the main shield-building stage because of the higher magma flux. Second, we have additional evidence for the MgO content of the liquid that cumulate olivines equilibrated with provided by the histograms of olivine compositions (Figure 5). A smooth fractional crystallization trend in a Hawaiian basalt produces more high Mg# olivine than low Mg# olivine, but the change in weight fraction is small (Figure 10) and the large single peak close to the average composition would not be produced by simple crystallization. The large peak in olivine modal abundances likely reflects re-equilibration between the olivines and their host liquid. In a cumulate pile, the fraction of olivine would be large relative to the fraction of liquid, and due to diffusive exchange of FeO and MgO the olivines in the pile

would approach the average composition across the full pile, creating the large peak in olivine Mg# close to the average olivine composition. Diffusion of FeO and MgO in olivine is expected to be fast relative to CaO diffusion (Jurewicz and Watson, 1988b; Coogan et al., 2005), thus if the CaO contents of the olivines are able to diffusively equilibrate with their host liquid, FeO and MgO should as well.

Mauna Kea and Loihi each show significant quantities of olivine with higher CaO content, and Mauna Loa shows a small quantity as well. These olivines could potentially represent olivines that have not fully re-equilibrated by diffusion. For Mauna Kea and Mauna Loa, the existence of these olivines may suggest that they were formed and erupted during periods of high magma flux, as discussed previously, such that they did not have a long enough residence time for their CaO contents to re-equilibrate. For Loihi, conversely, these olivines may suggest that there currently is not yet a single, integrated magma chamber through which every liquid passes, and as such there may be no large cumulate pile in which the majority of the olivines can re-equilibrate.

This model makes a number of predictions for the CaO contents of Hawaiian olivines, some of which can be tested. In particular, it predicts that the maximum CaO content in an olivine should be found in crystals that form from lavas just before they reach plagioclase saturation. Microphenocrysts and core to rim transects across single grains could be expected to show high CaO contents without time for equilibration, but only if they formed before the onset of plagioclase crystallization (which could obscure this trend). Some microphenocrysts from the Pu’u O’o eruption do in fact show elevated CaO contents up to 0.48% CaO in a microphenocryst with Mg#=81.2 (Garcia et al.,

2000). Based on the other available olivine analyses, this measured composition is unexpected other than through a crystallization path as suggested by Libourel (1999). Yang et al. (1994) also examined CaO contents in some olivines from Mauna Kea, and found them to be consistent with the model of Jurewicz and Watson (1988a), which predicts a similar evolution to the model of Libourel (1999). Currently, the literature contains very few analyses of CaO contents in olivine microphenocrysts or of transects across single olivine grains that include CaO contents, and thus a full test of this model is currently difficult, although it does appear consistent with the available data.

4. DISCUSSION

4.1. Olivine accumulation within Hawaiian volcanoes

In virtually every Hawaiian volcano considered here, the average erupted liquid has significantly lower wt. % MgO than the calculated parental liquid. This result requires that some portion of the original mass of liquid entering the volcano remains deposited within the volcano as crystallized olivine, consistent with the geophysical evidence for olivine cumulates (Kauahikaua et al., 2000). Based on more limited previously available data sets, estimates of the average weight fraction of the total mass entering the volcano that has been deposited within Mauna Kea and Kilauea as olivine cumulates have been calculated (Clague and Denlinger, 1994; Baker et al., 1996). Using the larger data sets available here, we have repeated this calculation based on our olivine addition trends. While this number can only be considered an estimate, as the exact ratio depends on the exact composition of liquid entering and of olivine deposited within the volcano, it still appears to provide insight into volcanic development.

The results of our calculations are given in Table 5, along with the previous estimates of Clague and Denlinger (1994) and Baker et al. (1996). For both Kilauea and Mauna Kea, our estimate of the deposited mass is consistent with the numbers calculated in the earlier estimates. This analysis confirms several of the details discussed previously; both the Mauna Loa and Mauna Kea samples from the HSDP2 drill core have lost less olivine than typical samples from Kilauea or the KSDP core. The historic samples from Mauna Loa contain less olivine on average than those at the drill site, having lost an additional 7.8% of their mass on average. The historic flows from Kilauea, the Pu'u O'o eruption of Kilauea, and the SOH-1 drill core set have lost similar amounts of their mass as olivine; on average roughly 20% of the mass currently entering Kilauea is deposited within the volcano as accumulated olivine. The samples from the KSDP drill core have also lost a similarly large amount of olivine.

The alternate calculations and stratigraphic variation from Mauna Kea produce some interesting results in this calculation. As noted previously, we performed several different olivine addition calculations on Mauna Kea to try to fit the accumulated olivine composition. Using a higher MgO parental liquid (with ~19% MgO) requires up to 9% of the initial liquid mass to be deposited within the volcano to produce the drill core. In addition, the stratigraphic details in the HSDP2 core revealed sections with low and high wt % MgO over long durations. The upper submarine section of Mauna Kea, covering 67 k.y., has on average lost virtually zero olivine (based on the liquids from Table 4b). The lower portion of the submarine section, covering 80 k.y., has on average lost up to 12.7% of its mass as accumulated olivine.

4.2. Chronological trends in olivine abundance

The chronological variations in olivine abundance expressed in the drill cores provide a previously unavailable view into the development of Hawaiian volcanoes. Mauna Kea, Mauna Loa, and Ko'olau all show fairly high-frequency variations in olivine abundance at their drill sites later in their life. Successive flows likely reach each site on the order of a thousand years apart, based on the calibrated timescales, and as the volcanic activity wanes, an olivine-poor flow will be followed by a highly olivine-rich flow with seemingly no consistent pattern. The older, submarine section of Mauna Kea shows a different pattern with less variation between successive flows. The upper portion of the core is highly olivine-rich, and there is a long-term trend towards less olivine deeper in the core.

Garcia et al. (2007) noted that the HSDP drill cores through Mauna Loa and Mauna Kea were much more olivine-rich than the SOH-1 drill core through Kilauea, which they related to the locations of the drill cores. The SOH-1 core was drilled far down the East Rift zone of Kilauea where eruptions are less frequent, and the low olivine abundances were interpreted to be caused by longer periods of magma storage prior to eruption at those distances from the summit, giving crystals more time to settle out. If that were the main mechanism driving the increasing olivine abundance with time in Mauna Kea, it would imply that the residence time for magmas in the lower section of the core is greater than that found in the upper submarine section of the core and that the eruptive rate peaks just before the submarine to subaerial transition. This timetable differs from the growth model for Mauna Kea of Sharp and Renne (2005), which used a linear

fit to describe accumulation at the drill site through the submarine section and a decreasing accumulation rate thereafter.

Rhodes and Vollinger (2004) noted the increasing whole rock MgO content in the upper portion of the submarine Mauna Kea section and proposed that the increasing MgO content reflected a period of high magma flux. During times of high magma flux, the parental liquids entering the volcano may not have sufficient time to crystallize to the point where they reach saturation with additional phases. However, a higher MgO content in the erupted liquids does not explain the change in whole-rock MgO content without the entrainment of additional olivine, for several reasons. As noted previously, one method of fitting the average olivine composition sampled by Mauna Kea is to interrupt olivine phenocryst crystallization with ~9% MgO in the liquid, rather than at ~7% MgO where other phases become saturated (e.g., Rhodes and Vollinger, 2004). This increased liquid MgO content would be consistent with the observation of Rhodes and Vollinger (2004) that there are very few whole rock analyses with <8% MgO throughout much of the submarine section. However, the upper portion of the submarine section shows a much larger increase in whole rock MgO content than the change from 7 to 9% MgO we calculate for the liquid compositions, and there are very few glasses measured from the HSDP2 section with >9% MgO (Stolper et al., 2004). Eruption of liquids containing MgO contents greater than this amount would produce elevated whole rock MgO values without growing significant amounts of olivine phenocrysts, and as such would disturb the relationship between whole rock MgO content and olivine abundance seen in Figure 1. This pattern could possibly be masked by the growth of rims on previously crystallized

phenocrysts during eruption, but this type of growth may be observable by chemical analyses of other oxides (such as CaO and NiO). Therefore, while the liquids may be higher in MgO, significant additional olivine is still required to explain the whole rock measurements. This additional olivine may however still be related to elevated magma fluxes; increased magma flux could decrease the time available for olivine grains to settle out into a cumulate and could therefore produce more olivine-rich eruptions. A high magma flux through Mauna Kea during the period sampled in the upper submarine section at the HSDP2 drill site appears to be one explanation for the variation in olivine abundance with time seen in this drill core.

4.3. Olivine addition and equilibration

Rhodes and Vollinger (2004) argued that the olivine-addition calculations presented here may not be representative of the actual mixing process occurring within a Hawaiian volcano. Specifically, they noted that olivine addition trends involving oxides other than MgO and FeO* often projected towards compositions that could not represent a realistic olivine composition. They explained this by suggesting that the linear trends examined here were in fact mixing lines between olivine rich, high MgO liquids and low MgO liquids that had begun to crystallize plagioclase and clinopyroxene. The olivine compositions considered here suggest a possible alternative explanation.

Calculating the olivine composition being added along an olivine-control line involves projecting over a large range in composition space, such that small but consistent changes in the measured compositions could be magnified by the mathematical projection. In Figure 11 we consider the oxides CaO and Al_2O_3, as was done by Rhodes

and Vollinger (2004). In a similar plot, they noted that when projected back to zero Al_2O_3 (and hence, the average olivine composition), the olivine control lines projected to >0.4% CaO, which is an implausible olivine composition for Hawaii, as discussed earlier. However, this extrapolation presupposes that there is no re-equilibration between the olivine and the liquid hosting it. In Figure 11, we also show an olivine control line that would be generated by an increase from 10.2% CaO to 10.4% CaO in the high MgO parental liquid if it was not accompanied by an increase in the CaO content of the fractionated liquid. This small increase in the CaO content of the high MgO liquids in the volcano produces a similar increase in the estimated CaO content of the olivine to that discussed by Rhodes and Vollinger (2004).

The olivine compositions examined in Figure 9 provide a possible mechanism for producing this exact type of enrichment. As noted previously, based on the work of Libourel (1999), a typical fractional crystallization trend in a Hawaiian liquid would be expected to produce olivines with >0.4% CaO when their Mg# approached 80, but olivines of this CaO content are typically not seen in Hawaii and there is a strong suggestion that the olivine CaO contents have undergone diffusive re-equilibration. CaO is relatively incompatible in olivine, and thus diffusive equilibration between olivine and liquid will increase the CaO content of the liquid slightly as the CaO content of the olivine decreases. This effect will be small, but it would be expected to be most prominent in a setting where the mass ratio of olivine to liquid is high, such as a cumulate pile of the sort envisioned here. The effect noted by Rhodes and Vollinger (2004) was

found to be more intense in Mauna Loa than Mauna Kea, which is also consistent with the greater intensity of olivine CaO depletion observed in olivines from Mauna Loa.

The proposed re-equilibration mechanism would work similarly for a number of other oxides. NiO, for example, is compatible in olivine, and crystallization of a liquid should produce a decrease in olivine NiO content as crystallization proceeds. Like MgO, the olivine addition calculation predicts a smooth decrease in the NiO content of olivines as crystallization proceeds. Like MgO however, a histogram of the measured NiO contents shows a large population of olivines around ~0.4% NiO, and few olivines at the tails of the distribution (Figure 12), suggesting that re-equilibration of NiO contents is plausible as well.

If this mechanism is an appropriate explanation for the variable projected olivine compositions from Rhodes and Vollinger (2004), it removes one of the concerns expressed over this type of calculation; that the variability seen in projected olivine composition could reflect mixing between high MgO liquids and liquids that had begun to crystallize other minerals. It does, however, suggest that care must be taken to understand the changes in each oxide in olivine during the olivine addition calculations. For example, assuming an increasing CaO content in olivine with increasing Mg# may be appropriate in some settings, but here, many of the olivines have re-equilibrated to a lower CaO content independent of Mg#, and therefore assuming that olivine CaO content was changing significantly during crystallization would produce a slightly erroneous parental liquid CaO content.

If this proposed mechanism is the correct way to explain the olivine compositions discussed above, it also potentially gives insight into the question of the exact relationship between olivines and their host liquid. As discussed previously, a number of lines of evidence suggest that some fraction of the olivines in any given Hawaiian lava have likely spent some time residing in a cumulate pile at the base of a magma chamber. Many studies have based their conclusions on compositional analyses of olivine grains or on bulk analyses of olivine separates (e.g., Sobolev et al., 2007; Eiler et al., 1996; Wang et al., 2003). A close relationship between olivines and their host melts is a common assumption of these studies, and is supported by the fact that there are correlations between measurements from whole rocks and measurements made on olivine separates (e.g., Blitchert-Toft et al., 2003; Kurz et al., 2004). As the olivine CaO content measurements appear to reflect varying degrees of diffusive re-equilibration, CaO content measurements in olivine provide a potential method for discriminating olivines that moved rapidly through the magma chamber from those that resided for long periods in a magma chamber. Jurewicz and Watson (1988b) measured MgO diffusion in olivine that was a factor of ~10 faster than CaO diffusion in olivine, and suggested that typical phenocrysts may take only a few years to fully re-equilibrate in Fe-Mg. Therefore, while Fe-Mg zonation in olivines would be difficult to preserve even in olivine phenocrysts that moved rapidly through the magmatic system, the preservation of high CaO contents in olivines such as those from Mauna Kea suggests that the high CaO fraction of olivines is able to move through the magma chamber more rapidly than other grains from the same flows. Based on the expected evolution of olivine CaO contents from Libourel (1999), it

appears possible to separate olivines that show substantial re-equilibration from those that do not. Therefore, the CaO content of olivines could be used as a potential discriminant to separate olivines that spent significant time residing in a cumulate pile from those that are more directly related to the lavas that host them; olivines that sit closest to the trend predicted by Libourel (1999) would likely have spent the least time residing in a magma chamber.

5. ACKNOWLEDGEMENTS

This work was supported by the NSF Ocean Sciences Marine Geology and Geophysics program, grant numbers OCE-0241716 and OCE-0550216.

References

Althaus, T., Niedermann, S., and Erzinger, J. (2003) Noble gases in olivine phenocrysts from drill core samples of the Hawaii Scientific Drilling Project (HSDP) pilot and main holes (Mauna Loa and Mauna Kea, Hawaii). *Geochem. Geophys. Geosyst.* **4**, 8701.

Anderson, A. T. (1995) CO_2 and the eruptibility of picrite and komatiite. *Lithos* **34**, 19-25.

Arevalo, R. and McDonough, W. F. (2008) Tungsten geochemistry and implications for understanding the Earth's interior. *Earth Planet Sc. Lett.* **272**, 656-665.

Baker, M. B., Alves, S., and Stolper, E. M. (1996) Petrography and petrology of the Hawaii Scientific Drilling Project lavas: inferences from olivine phenocryst abundances and compositions. *J. Geophys. Res.* **101**, 11715-11727.

Basaltic Volcanism Study Project. (1980) *Basaltic volcanism on the terrestrial planets*. Pergamon Press, New York.

Beattie, P. (1993) Olivine-melt and orthopyroxene-melt equilibria. *Contrib. Mineral. Petr*. **115**, 103-111.

Beeson, M. H. (1976) Petrology, mineralogy, and geochemistry of the East Molokai volcanic series, Hawaii, U.S. *U.S. Geological Survey Professional Paper* **961**, 1-53.

Bergmanis, E. C., Sinton, J. M., and Trusdell, F. A. (2000) Rejuvenated volcanism along the southwest rift zone, East Maui, Hawai'i. *B. Vulcanol.* **62**, 239-255.

Blichert-Toft, J., Weis, D., Maerschalk, C., Agranier, A., and Albarède, F. (2003) Hawaiian hot spot dynamics as inferred from the Hf and Pb isotope evolution of Mauna Kea volcano. *Geochem. Geophys. Geosyst.* **4**, 8704.

Bohrson, W. A. and Clague, D. A. (1988) Origin of ultramafic xenoliths containing exsolved pyroxenes from Hualalai Volcano, Hawaii *Contrib. Mineral. Petr.* **100**, 139-155.

Budahn, J. R. and Schmitt, R. A., 1985. Petrogenetic modeling of Hawai'ian tholeiitic basalts: a geochemical approach. *Geochim Cosmochim Ac.* **49**, 67-87.

Burkhard, D. J. M. (2001) Crystallization and oxidation of Kilauea Basalt glass: processes during reheating experiments. *J. Petrol.* **42**, 507-527.

Casadevall, T. J. and Dzurisin, D. (1987) Stratigraphy and petrology of the Uwekahuna bluff section, Kilauea Caldera. *U.S. Geological Survey Professional Paper* **1350**, 351-375.

Casadevall, T. J. and Dzurisin, D. (1987) Intrusive rocks of Kilauea Caldera. *U.S. Geological Survey Professional Paper* **1350**, 377-394.

Chen, C. Y., Frey, F. A., and Garcia, M. O. (1990) Evolution of alkalic lavas at Haleakala volcano, East Maui, Hawai'i: major, trace element, and isotopic constraints. *Contrib. Mineral. Petr.* **105**, 197-218.

Chen, C. Y., Frey, F. A., Garcia, M. O., Dalrymple, G. B., and Hart, S. R. (1991) The tholeiite to alkalic basalt transition at Haleakala volcano, Maui, Hawai'i. *Contrib. Mineral. Petr.* **106**, 183-200.

Chen, C. H., Presnall, D. C., and Stern, R. J. (1992) Petrogenesis of ultramafic xenoliths from the 1800 Kaupulehu Flow, Hualalai Volcano, Hawaii. *J. Petrology* **33**, 163-202.

Chen, C. Y. (1993) High-magnesium primary magmas from Haleakala Volcano, East Maui, Hawai'i: petrography, nickel, and major element constraints. *J. Volcanol. Geoth. Res.* **55**, 143-153.

Chen, C. Y., Frey, F. A., Rhodes, J. M., and Easton, R. M. (1996) Temporal geochemical evolution of Kilauea Volcano: comparison of Hilina and Puna basalt. In: *Earth Processes: Reading the Isotopic Code*. (eds. Basu, A. and Hart, S. R.), American Geophysical Union, Washington D.C. pp. 161-181.

Clague, D. A. and Beeson, M. H. (1980) Trace element geochemistry on the East Molokai Volcanic Series, Hawaii. *Am. J. Sci.* **280-A**, 820-844.

Clague, D. A., Chen, D.-G., Murnane, R., Beeson, M. H., Lanphere, M. A., Dalrymple, G. B., Friesen, W. B., and Holcomb, R. T., 1982. Age and petrology of the Kalaupapa Basalt, Molokai, Hawaii. *Pac. Sci.* **36**, 411-420.

Clague, D. A. and Frey, F. A. (1982) Petrology and trace element geochemistry of the Honolulu volcanic series, Oahu: implications of the oceanic mantle beneath Hawai'i. *J. Petrol.* **23**, 447-504.

Clague, D. A. (1988) Petrology of ultramafic xenoliths from Loihi seamount, Hawai'i. *J. Petrol.* **29**, 1161-1186.

Clague, D. A. and Moore, J. G. (1991) Geology and petrology of Mahukona Volcano, Hawai'i. *B. Vulcanol.* **53**, 159-172.

Clague, D. A. and Bohrson, W. A. (1991) Origin of xenoliths in the trachyte at Puu Waawaa, Hualalai Volcano, Hawaii. *Contrib. Mineral. Petr.* **108**, 439-452.

Clague, D. A., Weber, W. S., and Dixon, J. E. (1991) Picritic glasses from Hawaii. N*ature* **353**, 553-556.

Clague, D. A. and Denlinger, R. P. (1994) Role of olivine cumulates in destabilizing the flanks of Hawaiian volcanoes. *B. Vulcanol.* **56**, 425-434.

Clague, D. A., Moore, J. G., Dixon, J. E., and Friesen, W. B. (1995) Petrology of submarine lavas from Kilauea's Puna Ridge, Hawai'i. *J. Petrol.* **36**, 299-349.

Clague, D. A. and Moore, J. G. (2002) The proximal part of the giant submarine Wailau Landslide, Molokai, Hawai'i. *J. Volcanol. Geoth. Res.* **113**, 259-287.

Clague, D. A. P., J.B., McIntosh, W. C., Cousens, B. L., Davis, A. S., and Reynolds, J. R. (2006) A submarine perspective of the Honolulu volcanics, Oahu. *J. Volcanol. Geoth. Res.* **151**, 279-307.

Coogan, L. A., Hain, A., Stahl, S., and Chakraborty, S. (2005) Experimental determination of the diffusion coefficient for calcium in olivine between 900°C and 1500°C. *Geochim Cosmochim Ac.* **69**, 3683-3694.

Coombs, M. L., Clague, D. A., Moore, G. F., and Cousens, B. (2004) Growth and collapse of Waianae volcano, Hawai'i, as revealed by exploration of its submarine flanks *Geochemistry, Geophysics, Geosystems*, Q8006.

Crocket, J. H. (2002) Platinum-group elements in basalts from Maui, Hawai'i: low abundances in alkali basalts. *Can. Mineral.* **40**, 595-609.

Davis, M. G., Garcia, M. O., and Wallace, P. J. (2003) Volatiles in glasses from Mauna Loa Volcano, Hawai'i: implications for magma degassing and contamination, and growth of Hawai'ian volcanoes. *Contrib. Mineral. Petr.* **144**, 570-591.

Decker, R. W. (1987) Dynamics of Hawaiian volcanoes: an overview. *U.S. Geological Survey Professional Paper 1350*, 997-1018.

DePaolo, D. J., Stolper, E. M., and Thomas, D. (1996) The Hawaii Scientific Drilling Project: Summary of preliminary results. *GSA today* **6**, 1-8.

DePaolo, D. J. and Stolper, E. M. (1996) Models of Hawaiian volcano growth and plume structure: Implications of results from the Hawaii Scientific Drilling Project. *J. Geophys. Res.* **101**, 11643-11654.

Desilets, D. and Zreda, M. G. (2006) Elevation dependence of cosmogenic ^{36}Cl production in Hawai'ian lava flows. *Earth Planet Sc. Lett.* **246**, 277-287.

Dixon, J. E. and Clague, D. A. (2001) Volatiles in basaltic glasses from Loihi seamount, Hawai'i: evidence for a relatively dry plume component. *J. Petrol.* **42**, 627-654.

Dixon, J., Clague, D. A., Cousens, B., Monsalve, M. L., and Uhl, J. (2008) Carbonatite and silicate melt metasomatism of the mantle surrounding the Hawaiian plume: Evidence from volatiles, trace elements, and radiogenic isotopes in rejuvenated-stage lavas from Niihau, Hawaii. *Geochem. Geophys. Geosyst.* **9**, Q09005.

Dzurisin, D., Lockwood, J. P., Casadevall, T. J., and Rubin, M. (1995) The Uwekahuna Ash Member of the Puna Basalt: product of violent phreatomagmatic eruptions at Kilauea Volcano Hawai'i between 2800 and 2100 years ago. *J. Volcanol. Geoth. Res.* **66**, 163-184.

Eason, R. M. and Garcia, M. O. (1980) Petrology of the Hilina formation, Kilauea volcano, Hawai'i. *B. Vulcanol.* **43**, 657-673.

Eiler, J. M., Valley, J. W., and Stolper, E. M. (1996) Oxygen isotope ratios in olivine from the Hawaii Scientific Drilling Project. *J. Geophys. Res.* **101**, 11807-11813.

Feigenson, M. D. and Spera, F. J., 1983. Case studies on the origin of basalt II: the transition from tholeiitic to alkalic volcanism on Kohala volcano, Hawai'i. *Contrib. Mineral. Petr.* **84**, 390-405

Fekiacova, Z., Abouchami, W., Galer, S. J. G., Garcia, M. O., and Hofmann, A. W. (2007) Origin and temporal evolution of Ko'olau volcano: Hawai'i: inferences from isotope data on the Ko'olau Scientific Drilling Project (KSDP), the Honolulu volcanics and ODP site 843. *Earth Planet Sc. Lett.* **261**, 65-83.

Fiske, R. S. and Koyanagi, R. Y. (1968) The December, 1965 eruption of Kilauea Volcano, Hawai'i. *U.S. Geological Survey Professional Paper* **607**, 1-21.

Fleet, M. E. and Stone, W. E. (1990) Nickeliferous sulfides in xenoliths, olivine megacrysts and basaltic glass. *Contrib. Mineral. Petr.* **105**, 629-636.

Fodor, R. V. and Vandermeyden, H. J. (1988) Petrology of Gabbroic Xenoliths From Mauna Kea Volcano, Hawaii. *J. Geophys. Res.* **93**, 4425-4452.

Fodor, R. and Moore, R. (1994) Petrology of gabbroic xenoliths in 1960 Kilauea basalt: crystalline remnants of prior (1955) magmatism. *B. Vulcanol.* **56**, 62-74.

Fodor, R. V. and Galar, P. (1997) A view into the subsurface of Mauna Kea volcano, Hawai'i: crystallization processes interpreted through the petrology and petrography of gabbroic and ultramafic xenoliths. *J. Petrol.* **38**, 581-624.

Frey, F. A. and Clague, D. A. (1983) Geochemistry of diverse basalt types from Loihi Seamount, Hawai'i, petrogenic implications. *Earth Planet Sc. Lett.* **66**, 337-355.

Frey, F. A., Wise, W. S., Garcia, M. O., Kwon, S.-T., and Kennedy, A. K. (1990) Evolution of Mauna Kea volcano, Hawai'i: petrologic and geochemical constraints on postshield volcanism. *J. Geophys. Res.* **B95**, 1271-1300.

Frey, F. A., Garcia, M. O., Wise, W. S., Kennedy, A. K., Gurriet, P., and Albarède, F. (1991) The evolution of Mauna Kea volcano, Hawai'i: Petrogenesis of tholeiitic and alkalic basalts. *J. Geophys. Res.* **B96**, 14347-14375.

Frey, F. A., Garcia, M. O., and Roden, M. F. (1994) Geochemical characteristics of Ko'olau volcano: implications of intershield geochemical differences among Hawai'ian volcanoes. *Geochim Cosmochim Ac.* **58**, 1441-1462.

Gaffney, A. M. (2002) Environments of crystallization and compositional diversity of Mauna Loa xenoliths. *J. Petrol.* **43**, 963-980.

Gaffney, A. M., Nelson, B. K., and Blichert-Toft, J. (2004) Geochemical constraints on the role of oceanic lithosphere in intra-volcano heterogeneity at West Maui, Hawai'i. *J. Petrol.* **45**, 1663-1687.

Garcia, M. O. and Wolfe, E. W. (1988) Petrology of the erupted lava. *U.S. Geological Survey Professional Paper* **1463**, 127-143.

Garcia, M. O., Ho, R. A., Rhodes, J. M., and Wolfe, E. W. (1989) Petrologic constraints on rift-zone processes - results from episode-1 of the Pu'u O'o eruption of Kilauea volcano, Hawai'i. *B. Vulcanol.* **52**, 81-96.

Garcia, M. O., Muenow, D. W., Aggrey, K. E., and O'Neil, J. R. (1989) Major element, volatile, and stable isotope geochemistry of Hawaiian submarine tholeiitic glasses. *J. Geophys. Res.* **94**, 10525-10538.

Garcia, M. O., Rhodes, J. M., Wolfe, E. W., Ulrich, G. E., and Ho, R. A. (1992) Petrology of lavas from episodes 2-47 of the Pu'u O'o eruption of Kilauea volcano, Hawai'i: evaluation of magmatic processes. *B. Vulcanol.* **55**, 1-16.

Garcia, M. O., Foss, D. J. P., West, H. B., and Mahoney, J. J. (1995) Geochemical and isotopic evolution of Loihi Volcano, Hawaii. *J. Petrol.* **36**, 1647-1674.

Garcia, M. O., Hulsebosch, T. P., and Rhodes, J. M. (1995) Olivine-rich submarine basalts from the southwest rift zone of Mauna Loa volcano: implications for magmatic processes and geochemical evolution. In: *Mauna Loa Revealed: Structure, Composition, History, and Hazards* (eds. Rhodes, J. M. and Lockwood, J. P.) *Geophys. Monogr. Ser., vol.92*. AGU, Washington D.C. pp. 219-239.

Garcia, M. O. (1996) Petrography and olivine and glass chemistry of lavas from the Hawaii Scientific Drilling Project. *J. Geophys. Res.* **101**, 11701-11713.

Garcia, M. O., Rhodes, J. M., Trusdell, F. A., and Pietruska, A. J. (1996) Petrology of lavas from the Pu'u'O'o eruption of Kilauea volcano - 3 - the Kupaianaha episode (1986-1992). *B. Vulcanol.* **58**, 359-379.

Garcia, M. O., Ito, E., Eiler, J. M., and Pietruska, A. J. (1998) Crustal contamination of Kilauea Volcano magma revealed by oxygen isotope analyses of glass and olivine from Pu'u O'o eruption lavas,. *J. Petrol.* **39**, 803-817.

Garcia, M. O., Rubin, K. H., Norman, M. D., Rhodes, J. M., Graham, D. W., Muenow, D. W., and Spencer, K. (1998) Petrology and geochronology of basalt breccia from the 1996 earthquake swarm of Loihi seamount, Hawaii: magmatic history of its 1996 eruption. *B. Vulcanol.* **59**, 577-592.

Garcia, M. O., Pietruska, A. J., Rhodes, J. M., and Swanson, K. (2000) Magmatic Processes during the prolongued Pu'u 'O'o eruption of Kilauea Volcano, Hawai'i. *J. Petrol.* **41**, 967-990.

Garcia, M. O. and Pietruska, A. J. R., J.M. (2003) A petrologic perspective of Kilauea volcano's summit magma reservoir. *J. Petrol.* **44**, 2313-2339.

Garcia, M. O., Haskins, E. H., Stolper, E. M., and Baker**,** M. (2007) Stratigraphy of the Hawai'i Scientific Drilling Project core (HSDP2): anatomy of a Hawaiian shield volcano. *Geochem. Geophys. Geosyst.* **8**, Q02G20.

Garcia, M. O., Ito, E., and Eiler, J. M. (2008) Oxygen isotope evidence for chemical interaction of Kilauea historical magmas with basement rocks. *J. Petrol.* **49**, 757-769.

Gerlach, T. M. and Graeber, E. J. (1985) Volatile budget of Kilauea volcano. *Nature* **313**, 273-277.

Guillou, H., Garcia, M. O., and Turpin, L. (1997) Unspiked K-Ar dating of young volcanic rocks from Loihi and Pitcairn hot spot seamounts. *J. Volcanol. Geoth. Res.* **78**, 239-249.

Guillou, H., Sinton, J. M., Laj, C., Kissel, C., and Szeremeta, N. (2000) New K-Ar ages of shield lavas from Waianae volcano, Oahu, Hawaiian archipelago. *J. Volcanol. Geoth. Res.* **96**, 229-242.

Gunn, B. M. (1971) Trace element partitioning during olivine fractionation of Hawai'ian basalts. *Chemical Geology* **8**, 1-13.

Hammer, J. E., Coombs, M. L., Shamberger, P. J., and Kimura, J.-I. (2006) Submarine sliver in North Kona: a window into the early magmatic and growth history of Hualalai Volcano, Hawai'i. *J. Volcanol. Geoth. Res.* **151**, 157-188.

Haskins, E. H. and Garcia, M. O. (2004) Scientific drilling reveals geochemical heterogeneity within the Ko'olau shield, Hawai'i. *Contrib. Mineral. Petr.* **147**, 162-188.

Hauri, E. H. and Kurz, M. D. (1997) Melt migration and mantle chromatography, 2: a time-series Os isotope study of Mauna Loa Volcano, Hawai'i. *Earth Planet Sc. Lett.* **153**, 21-36.

Hawkins, J. and Melchoir, J. (1983) Petrology of Basalts from Loihi Seamount, Hawai'i. *Earth Planet Sc. Lett.* **66**, 356-368.

Hay, R. L. and Iijima, A. (1968) Nature and origin of palagonite tuffs of the Honolulu group on Oahu, Hawai'i. *Memoirs of the Geological Society of America* **116**, 331-376.

Helz, R. T. (1987) Diverse olivine types in lava of the 1959 eruption of Kilauea volcano and their bearing in eruption dynamics. *U.S. Geological Survey Professional Paper* **1350**, 691-721.

Helz, R. T. and Wright, T. L. (1992) Differentiation and magma mixing on Kilauea's east rift zone: A further look at the eruptions of 1955 and 1960. I: The late 1955 lavas. *B. Vulcanol.* **54**, 361-384.

Ho, R. A. and Garcia, M. O. (1988) Origin of differentiated lavas at Kilauea Volcano, Hawaii: Implications from the 1955 eruption. *B. Vulcanol.* **50**, 35-46.

Huang, S. and Frey, F. A. (2003) Trace element abundances of Mauna Kea basalt from phase 2 of the Hawaii Scientific Drilling Project: Petrogenetic implications of correlations with major element content and isotopic ratios. *Geochem. Geophys. Geosyst.* **4**, 8711.

Huang, S., Frey, F. A., Blichert-Toft, J., Fodor, R. V., Bauer, G. R., and Xu, G. (2005) Enriched components in the Hawaiian plume: evidence from Kahoolawe Volcano, Hawaii. *Geochem. Geophys. Geosyst.* **6**, Q11006

Huang, S. C., Humayun, M., and Frey, F. A. (2007) Iron/manganese ratio and manganese content in shield lavas from Ko'olau Volcano, Hawai'i. *Geochim Cosmochim Ac.* **71**, 4557-4569.

Jackson, E. D. and Wright, T. L. (1970) Xenoliths in the Honolulu volcanic series, Hawai'i. *J. Petrol.* **11**, 405-430.

Jackson, M. C., Frey, F. A., Garcia, M. O., and Wilmoth, R. A. (1999) Geology and geochemistry of basaltic lava flows and dikes from the Trans-Koolau tunnel, Oahu, Hawai'i. *B. Vulcanol.* **60**, 381-401.

Jurewicz, A. J. G. and Watson, E. B. (1988a) Cations in olivine, Part 1: calcium partitioning and calcium-magnesium distribution between olivines and coexisting melts, with petrologic applications. *Contrib. Mineral. Petr.* **99**, 176-185.

Jurewicz, A. J. G. and Watson, E. B. (1988b) Cations in olivine, Part 2: diffusion in olivine xenocrysts, with applications to petrology and mineral physics. *Contrib. Mineral. Petr.* **99**, 186-201.

Kauahikaua, J., Hildenbrand, T., and Webring, M. (2000) Deep magmatic structures of Hawaiian volcanoes, imaged by three-dimensional gravity models. *Geology* **28**, 883-886.

Kilinc, A., Carmichael, I. S. E., Rivers, M. L., and Sack, R. O. (1983) The ferric-ferrous ratio of natural silicate liquids equilibrated in air. *Contrib. Mineral. Petr.* **83**, 136-140.

Kimura, J.-I., Sisson, T. W. N., Nakano, Coombs, M. L., and Lipman, P. W. (2006) Isotope geochemistry of early Kilauea magmas from the submarine Hilina bench: the nature of the Hilina mantle component. *J. Volcanol. Geoth. Re*s. **151**, 51-72.

Kostera, A. Z. (1997) Mineralogy and petrology of xenoliths in the Huehue flows of Hualalai volcano, Hawaii. *Proceedings of the 10th Keck Research Symposium. Geol., Wooster, OH*, 215-218.

Kuno, H., Yamasaki, K., Iida, C., and Nagashima, K. (1957) Differentiation of Hawai'ian Magmas. *Japanese Journal of Geology and Geography* **28**, 179-218.

Kurz, M. D., Curtice, J., Lott, D. E., III, and Solow, A. (2004) Rapid helium isotopic variability in Mauna Kea shield lavas from the Hawaiian Scientific Drilling Project. *Geochem. Geophys. Geosyst.* **5**, Q04G14.

Kyser, T. K., O'Neil, J. R., and Carmichael, I. S. E. (1981) Oxygen isotope thermometry of basic lavas and mantle nodules. *Contrib. Mineral. Petr.* **77**, 11-23.

Kyser, T. K., O'Neil, J. R., and Carmichael, I. S. E. (1982) Genetic relations among basic lavas and ultramafic nodules: Evidence from oxygen isotope compositions. *Contrib. Mineral. Petr.* **81**, 88-102.

Lanphere, M. A. and Frey, F. A. (1987) Geochemical evolution of Kohala volcano, Hawai'i. *Contrib. Mineral. Petr.* **95**, 100-113.

Leeman, W. P. and Scheidegger, K. F. (1977) Olivine/liquid distribution coefficients and a test for crystal-liquid equilibrium. *Earth Planet Sc. Lett.* **35**, 247-257.

Libourel, G. (1999) Systematics of calcium partitioning between olivine and silicate melt: implications for melt structure and calcium content of magmatic olivines. *Contrib. Mineral. Petr.* **136**, 63-80.

Lipman, P. W., Banks, N. G., and Rhodes, J. M. (1985) Degassing-induced crystallization of basaltic magma and effects on lava rheology. *Nature* **317**, 604-607.

Lipman, P. W., Rhodes, J. M., and Dalrymple, G. B. (1990) The Ninole basalt: implications for the structural evolution of Mauna Loa volcano, Hawai'i. *B. Vulcanol.* **53**, 1-19.

Lipman, P. W., Sisson, T. W., Ui, T., and Naka, J. (2000) In search of ancestral Kilauea volcano. *Geology* **28**, 1079-1082.

Lipman, P. W., Sisson, T. W., Coombs, M. L., Calvert, A., and Kimura, J. (2006) Piggyback tectonics: Long-term growth of Kilauea on the south flank of Mauna Loa. *J. Volcanol. Geoth. Res.* **151**, 73-108.

Lockwood, J. P., Dvorak, J. J., English, T. T., Koyangi, R. Y., Okamura, A. T., Summers, M. L., and Tanigawa, W. R. (1987) Mauna Loa 1974-1984: a decade of intrusive and extrusive activity. *U.S. Geological Survey Professional Paper* **1350**, 537-570.

Macdonald, G. A. (1942) Potash-oligoclase in Hawaiian Lavas. *Am. Mineral.* **27**, 793-800.

Macdonald, G. A. and Powers, H. A. (1946) Contribution to the petrography of Haleakala volcano, Hawai'i. *Bull. Geol. Soc. Am.* **57**, 115-123.

Macdonald, G. A. (1949) Petrography of the island of Hawaii. *U.S. Geological Survey Professional Paper 214-D*, 51-96.

Macdonald, G. A. and Eaton, J. P. (1955) Hawai'ian volcanoes during 1953. *U.S. Geological Survey Bulletin* **1021-D**, 127-166.

Macdonald, G. A. and Katsura, T. (1961) Variations in the lava of the 1959 eruption of Kilauea Iki. *Pac. Sci.* **15**, 358-369.

Macdonald, G. A. and Eaton, J. P. (1964) Hawai'ian volcanoes during 1955. *U.S. Geological Survey Bulletin* **1171**, 1-170.

Macdonald, G. A. and Katusra, T. (1964) Chemical composition of Hawai'ian lavas. *J. Petrol.* **5**, 82-133.

Macdonald, G. A. (1968) Composition and origin of Hawai'ian Lavas. *Memoirs of the Geological Society of America* **116**, 477-522.

Macdonald, G. A. (1968) A further contribution to the petrology of Haleakala Volcano, Hawai'i. *Bull. Geol. Soc. Am.* **79**, 877-887.

Mangan, M. T., Heliker, C. C., Mattox, T. N., Kauahikaua, J. P., and Helz, R. T. (1995) Episode 49 of the Pu'u'O'o-Kupaianahana eruption of Kilauea Volcano - breakdown of a steady-state eruptive era. *B. Vulcanol.* **55**, 127-135.

Marske, J. P., Pietruska, A. J., Weis, D., Garcia, M. O., and Rhodes, J. M. (2007) Rapid passage of a small-scale mantle heterogeneity through the melting regions of Kilauea and Mauna Loa volcanoes. *Earth Planet Sc. Lett.* **259**, 34-50.

Marske, J. P., Garcia, M. O., Pietruska, A. J., Rhodes, J. M., and Norman, M. D. (2008) Geochemical variations during Kilauea's Pu'u 'O'o-eruption reveal a fine-scale mixture of mantle heterogeneities within the Hawai'ian plume. *J. Petrol.* **49**, 1297-1318.

Martin, C. E. (1991) Osmium isotopic characteristics of mantle-derived rocks. *Geochim Cosmochim Ac.* **55**, 1421-1434.

Matvenkov, V. V. and Sorokhtin, O. G. (1998) Petrological characteristics of the initial stages of interplate volcanism, Loihi (Hawai'i, Pacific Ocean). *Okeanologiya* **38**, 742-749.

McCann, V. E. and Barton, M. (2005) Olivine-melt equilibrium and the oxygen fugacities of lavas from Hawai'i, EOS Transactions AGU. #V31B-0615 (abstr.).

Moore, J. G. (1965) Petrology of deep sea basalt near Hawai'i. *Am. J. Sci.* **263**, 40-52.

Moore, J. G. and Evans, B. W. (1967) The role of olivine in the crystallization of the prehistoric Makaopuhi tholeiitic lava lake, Hawaii. *Contrib. Mineral. Petr.* **15**, 202-223.

Moore, J. G. and Koyanagi, R. Y. (1969) The October 1963 eruption of Kilauea Volcano, Hawai'i. *U.S. Geological Survey Professional Paper* **614-C**, 1-13.

Moore, R. B., Helz, R. T., Dzurisin, D., Eaton, G. P., Koyanagi, R. Y., Lipman, P. W., Lockwood, J. P., and Puniwai, G. S. (1980) The 1977 eruption of Kilauea Volcano, Hawai'i. *J. Volcanol. Geoth. Res.* **7**, 189-210.

Moore, R. B. (1983) Distribution of the differentiated tholeiite basalts on the lower East Rift Zone of Kilauea Volcano, Hawai'i: a possible guide to geothermal exploration. *Geology* **11**, 136-140.

Moore, J. G. and Clague, D. A. (1987) Coastal lava flows from Mauna Loa and Hualalai volcanoes, Kona, Hawaii. *B. Vulcanol.* **49**, 752-764.

Moore, J. G., Clague, D. A., Ludwig, K. R., and Mark, R. K. (1990) Subsidence and volcanism of the Haleakala Ridge, Hawaii. *J. Volcanol. Geoth. Res.* **42**, 273-284.

Moore, J. G. and Clague, D. A. (1992) Volcano growth and evolution of the island of Hawaii. *Geol. Soc. Am. Bull.* **104**, 1471-1484.

Moore, J. G., Bryan, W. B., Beeson, M. H., and Normark, W. R. (1995) Giant blocks in the South Kona landslide, Hawaii. *Geology* **23**, 125-128.

Morgan, J. K., Moore, G. F., and Clague, D. A. (2003) Slope failure and volcanic spreading along the submarine south flank of Kilauea volcano, Hawai'i. *J. Geophys. Res.* **108**, 2415.

Morgan, J. K., Clague, D. A., Borchers, D. C., Davis, A. S., and Milliken, K. L. (2007) Mauna Loa's submarine western flank: landsliding, deep volcanic spreading, and hydrothermal alteration. *Geochem. Geophys. Geosyst.* **8**, Q05002.

Muir, I. D., Tilley, C. E., and Scoon, J. H. (1957) Contributions to the petrology of Hawaiian Basalts 1. The picrite-basalts of Kilauea. *Am. J. Sci.* **255**, 241-253.

Muir, I. D. and Tilley, C. E. (1961) Mugearites and their place in alkali igneous rock series. *Journal of Geology* **69**, 186-203.

Muir, I. D., Tilley, C. E., and Scoon, J. H. (1963) Contributions to the petrology of Hawai'ian basalts II: the tholeiitic basalts of Mauna Loa and Kilauea. *Am. J. Sci.* **261**, 111-128.

Mukhopadhyay, S., Lassiter, J. C., Farley, K. A., and Bogue, S. W. (2003) Geochemistry of Kauai shield-stage lavas: Implications for the chemical evolution of the Hawaiian plume. *Geochem. Geophys. Geosyst.* **4**, 1009.

Murata, K. J. and Richter, D. H. (1961) Magmatic differentiation in the Uwekahuna Laccolith, Kilauea Caldera, Hawai'i. *J. Petrol.* **2**, 424-437.

Murata, K. J., Bastron, H., and Brannock, W. W. (1965) X-Ray determinative curve for Hawaiian olivines of composition Fo76-88. *U.S. Geological Survey Professional Paper 525-C*, C35-C37.

Murata, K. J. and Richter, D. H. (1966) Chemistry of the lavas of the 1959-60 eruption of Kilauea Volcano, Hawai'i. *U.S. Geological Survey Professional Paper* **537-A**, 1-26.

Neal, C. A., Duggan, T. J., Wolfe, E. W., and Brandt, E. L. (1988) Lava samples, temperatures, and compositions. *U.S. Geological Survey Professional Paper* **1463**, 99-126.

Nicholls, J. and Stout, M. Z. (1988) Picritic Melts in Kilauea--Evidence from the 1967-1968 Halemaumau and Hiiaka Eruptions. *J. Petrology* **29**, 1031-1057.

Norman, M. D. and Garcia, M. O. (1999) Primitive magmas and source characteristics of the Hawai'ian plume: petrology and geochemistry of shield picrites. *Earth Planet Sc. Lett.* **168**, 27-44.

Oze, C. and Winter, J. D. (2005) The occurrence, vesiculation, and solidification of dense blue glassy pahoehoe. *J. Volcanol. Geoth. Res.* **142**, 285-301.

Powers, H. A. (1931) Chemical analyses of Kilauea Lavas. *Volcano Letters* **362**, 1-2.

Quane, S. L., Garcia, M. O., Guillou, H., and Hulsebosch, T. P. (2000) Magmatic history of the east rift zone of Kilauea Volcano, Hawai'i, based on drill core SOH-1. *J. Volcanol. Geoth. Res.* **102**, 319-388.

Ren, Z.-Y., Takahashi, E., Orihashi, Y., and Johnson, K. T. M. (2004) Petrogenesis of tholeiitic lavas from the submarine Hana Ridge. *J. Petrol.* **45**, 2067 - 2099.

Rhoden, M. F., Frey, F. A., and Clague, D. A. (1984) Geochemistry of tholeiitic and alkalic lavas from the Ko'olau range, Oahu, Hawai'i: implications for Hawai'ian volcanism. *Earth Planet Sc. Lett.* **69**, 141-158.

Rhodes, J. M. (1983) Homogeneity of lava flows: chemical data for historic Mauna Loan eruptions. *Proceedings fo the 13th Lunar and Planetary Sciences Conference, Part 2, J. Geophys. Res.* **Supplemental A 88**, 869-879.

Rhodes, J. M. (1988) Geochemistry of the 1984 Mauna Loa eruption: implications for magma storage and supply. *J. Geophys. Res.* **93**, 4453-4466.

Rhodes, J. M. (1995) The 1852 and 1868 Mauna Loa picrite eruptions: clues to parental magma compositions and the magmatic plumbing system In: Rhodes, J. M. and Lockwood, J. P. (Eds.), *Mauna Loa Revealed.* American Geophysical Union, Washington D.C. pp. 241-262.

Rhodes, J. M. and Hart, S. R. (1995) Episodic trace element and isotopic variations in historical Mauna Loa lavas: implications for magma and plume dynamics. In: Rhodes, J. M. and Lockwood, J. P. (Eds.), *Mauna Loa Revealed.* American Geophysical Union, Washington D.C. pp. 263-288.

Rhodes, J. M. (1996) Geochemical stratigraphy of lava flows sampled by the Hawai'i Scientific Drilling Project. *J. Geophys. Res.* **101**, 11729-11746.

Rhodes, J. M. and Vollinger, M. J. (2004) Composition of basaltic lavas sampled by phase-2 of the Hawai'i Scientific Drilling Project: geochemical stratigraphy and magma types. *Geochemistry, Geophysics, Geosystems* **5**, Q03G13.

Rhodes, J. M. and Vollinger, M. J. (2005) Ferric/ferrous ratios in 1984 Mauna Loa lavas: a contribution to understanding the oxidation state of Hawai'ian magmas. *Contrib. Mineral. Petr.* **149**, 666-674.

Richter, D. H., Ault, W. U., Eaton, J. P., and Moore, J. G. (1965) The 1961 eruption of Kilauea Volcano, Hawai'i'. *U.S. Geological Survey Professional Paper* **474-D**, 1-34

Richter, D. H. and Moore, J. G. (1966) Petrology of the Kilauea Iki lava lake, Hawai'i. *U.S. Geological Survey Professional Paper* **537-B**, 1-26.

Roeder, P. L., Thornber, C., Poustovetov, A., and Grant, A. (2003) Morphology and composition of spinel in Pu'u 'O'o lava (1996-1998), Kilauea volcano, Hawaii. *J. Volcanol. Geoth. Res.* **123**, 245-265.

Roeder, P., Gofton, E., and Thornber, C. (2006) Cotectic proportions of olivine and spinel in olivine-tholeiitic basalt and evaluation of pre-eruptive processes. *J. Petrol.* **47**, 883-900.

Ryan, M. P. (1988) The mechanics and three-dimensional internal structure of active magmatic systems; Kilauea volcano, Hawaii. *J. Geophys. Res.* **93**, 4213-4248.

Sarbas, B. and Nohl, U. (2008) The GEOROC database as part of a growing geoinformatics network. In: Brady, S. R., Sinha, A. K., and Gunderson, L. C. Eds.), *Geoinformatics 2008 - Data to Knowledge, Proceedings: U.S. Geological Survey Scientific Investigations Report 2008 - 5172*.

Seaman, C., Sherman, S. B., Garcia, M. O., Baker, M. B., Balta, B., and Stolper, E. (2004) Volatiles in glasses from the HSDP2 drill core. *Geochem. Geophys. Geosyst.* **5**, Q09G16.

Scowen, P. A. H., Roeder, P. L., and Helz, R. T. (1991) Reequilibration of chromite within Kilauea Iki lava lake, Hawaii. *Contrib. Mineral. Petr.* **107**, 8-20.

Self, S., Keszthelyi, L., and Thordarson, T. (1998) The importance of pahoehoe. *Annu. Rev. Earth Planet. Sci.* **26**, 81-110.

Shamberger, P. J. and Hammer, J. E. (2006) Leucocratic and Gabbroic Xenoliths from Hualalai Volcano, Hawai'i. *J. Petrology* **47**, 1785-1808.

Sharp, W. D. and Renne, P. R. (2005) The Ar-40/Ar-39 dating of core recovered by the Hawaii Scientific Drilling Project (phase 2), Hilo, Hawaii. *Geochem. Geophys. Geosyst.* **6**, Q04G17.

Shepherd, E. S. (1938) The gases in rocks and some related problems. *Am. J. Sci.* **35A**, 311-351.

Sherrod, D. A., Nishimitsu, Y., and Takahiro, T. (2003) New K-Ar ages and the geologic evidence against rejuvenated-stage volcanism at Haleakala, East Maui, a postshield-stage volcano of the Hawaiian chain. *Bull. Geol. Soc. Am.* **115**, 683-694.

Sherrod, D. R., Murai, T., and Tagami, T. (2007) New K-Ar ages for calculating end-of-shield extrusion rates at West Maui volcano, Hawaiian island chain. *B. Vulcanol.*, 627-642.

Sims, K. W. W., DePaolo, D. J., Murrell, M. T., Baldridge, W. S., Goldstein, S. J., Clague, D. A., and Jull, M. (1999) Porosity of the melting zone and variations in the solid mantle upwelling rate beneath Hawai'i: inferences from 238-U-230Th-226Ra and 235U-231PA disequilibria. *Geochim Cosmochim Ac.* **63**, 4119-4138.

Sobolev, A. V. and Nikogosian, I. K. (1994) Petrology of long-lived mantle plume magmatism: Hawai'i, Pacific, and Reunion Island, Indian Ocean. *Petrology* **2**, 111-144.

Sobolev, A. V., Hofmann, A. W., Kuzmin, D. V., Yaxley, G. M., Arndt, N. T., Chung, S. L., Danyushevsky, L. V., Elliott, T., Frey, F. A., Garcia, M. O., Gurenko, A. A., Kamenetsky, V. S., Kerr, A. C., Krivolutskaya, N. A., Matvienkov, V. V., Nikogosian, I. K., Rocholl, A., Sigurdsson, I. A., Sushchevskaya, N. M., and Teklay, M. (2007) The amount of recycled crust in sources of mantle-derived melts. *Science* **316**, 412-417.

Spengler, S. and Garcia, M. O. (1988) Geochemistry of the Hawi Lavas, Kohala Volcano, Hawai'i. *Contrib. Mineral. Petr.* **99**, 90-104.

Stoll, B., Jochum, K. P., Herwig, K., Amini, M., Flanz, M., Kreuzburg, B., Kuzmin, D., Willbold, M., and Enzweiler, J. (2008) An automated iridium-strip heater for LA-ICP-MS bulk analysis of geological samples. *Geostand. Geoanal. Res.* **32**, 5-26.

Stolper, E., Sherman, S., Garcia, M., Baker, M., and Seaman, C. (2004) Glass in the submarine section of the HSDP2 drill core, Hilo, Hawaii. *Geochem. Geophys. Geosyst.* **5**, Q07G15.

Takahiro, T., Nishimitsu, Y., and Sherrod, D. A. (2003) Rejuvenated-stage volcanism after 0.6 M.Y. quiescence at West Maui volcano, Hawai'i: new evidence from K-Ar ages and chemistry of Lahaina volcanics. *J. Volcanol. Geoth. Res.* **120**, 207-214.

Tanaka, R. N., E. and Takahashi, E. (2002) Geochemical evolution of Ko'olau volcano, Hawai'i, *Hawai'ian volcanoes, Deep Underwater Perspectives (Geophysical Monograph).* American Geophysical Union.

Tanaka, R. and Eizo, N. (2005) Boron isotopic constraints on the source of Hawai'ian shield lavas. *Geochim Cosmochim Ac.* **69**, 3385-3399.

Teanby, N., Laj, C., Gubbins, D., and Pringle, M. (2002) A detailed palaeointensity and inclination record from drill core SOH1 on Hawaii. *Physics of The Earth and Planetary Interiors* **131**, 101-140.

Thornber, C. R., Sherrod, D. R., Siems, D. F., Heliker, C. C., Meeker, G. P., Oscarson, R. L., and Kauahikaua, J. P. (2002) Whole-rock and glass major-element geochemistry of Kilauea Volcano, Hawaii, near-vent eruptive products: September 1994 through September, 2001. *U.S. Geological Survey Open File Report* **02-17**, 1-9.

Thornber, C. R., Heliker, C., Sherrod, D. R., Kauahikaua, J. P., Miklius, A., Okubo, P. G., Trusdell, F. A., Budahn, J. R., Ridley, W. I., and Meeker, G. P. (2003) Kilauea east rift zone magmatism: an episode 54 perspective. *J. Petrol.* **44**, 1525-1559.

Thornber, C. R., Hon, K., Heliker, C. C., and Sherrod, D. A. (2003) A compilation of whole-rock and glass major-element geochemistry of Kilauea Volcano, Hawai'i, near-vent eruptive products: January 1983 through September 2001 *U.S. Geological Survey Open File Report* **03-477**.

Tilley, C. E. (1960) Kilauea Magma. *Geological Magazine* **97**, 494-497.

Tilley, C. E. and Scoon, J. H. (1960) Differentiation of Hawai'ian basalts - some variants in lava suites of dated Kilauean eruptions. *J. Petrol.* **1**, 47-55.

Tilley, C. E. and Scoon, J. H. (1961) Differentiation of Hawai'ian basalts; trends of Mauna Loa and Kilauea historic magma. *Am. J. Sci.* **259**, 60-68.

Toplis, M. J. (2005) The thermodynamics of iron and magnesium partitioning between olivine and liquid: criteria for assessing and predicting equilibrium in natural and experimental systems. *Contrib. Mineral. Petr.* **149**, 22-39.

Wang, Z. G., Kitchen, N. E., and Eiler, J. M. (2003) Oxygen isotope geochemistry of the second HSDP core. *Geochem. Geophys. Geosyst.* **4**, 29.

Wang, Z. and Gaetani, G. A. (2008) Partitioning of Ni between olivine and siliceous eclogite partial melt: experimental constraints on the mantle source of Hawaiian basalts. *Contrib. Mineral. Petr.* **156**, 661-678.

Wanless, V. D., Garcia, M. O., Rhodes, J. M., Weis, D., and Norman, M. D. (2006) Shield-stage alkalic volcanism on Mauna Loa volcano, Hawai'i. *J. Volcanol. Geoth. Res.* **151**.

Wanless, V. D., Garcia, M. O., Trusdell, F. A., Rhodes, J. M., Norman, M. D., Weis, D. F., D.J., Kurz, M. D., and Guillou, H. (2006) Submarine radial vents on Mauna Loa volcano, Hawai'i. *Geochemistry, Geophysics, Geosystems* **7**, Q05001.

Washington, H. S. (1923) Petrology of the Hawai'ian Islands I: Kohala and Mauna Kea. *Am. J. Sci.* **5**, 465-502.

Washington, H. S. (1923) Petrology of the Hawai'ian Islands III: Kilauea and general petrology of Hawai'i. *Am. J. Sci.* **6**, 338-367.

Weinstein, J. P., Fodor, R. V., and Bauer, G. R. (2004) Ko'olau shield basalt as xenoliths entrained during rejuvenated-stage eruptions: perspectives on magma mixing. *B. Vulcanol.* **66**, 182-199.

Wentworth, C. K. and Winchell, H. (1947) Ko'olau basalt series, Oahu, Hawai'i. *Bull. Geol. Soc. Am.* **58**, 49-77.

West, H. B., Garcia, M. O., Frey, F. A., and Kennedy, A. K. (1988) Nature and cause of compositional variation among the alkalic cap lavas of Mauna Kea volcano, Hawai'i. *Contrib. Mineral. Petr.* **100**, 383-397.

West, H. B., Garcia, M. O., Gerlach, D. C., and Romano, J. (1992) Geochemistry of tholeiites from Lanai, Hawai'i. *Contrib. Mineral. Petr.* **112**, 520-542.

White, R. W. (1966) Ultramafic inclusions in basaltic rocks from Hawaii. *Contrib. Mineral. Petr.* **12**, 245-314.

Wilkinson, J. F. G. and Hensel, H. D. (1988) The petrology of some picrites from Mauna Loa and Kilauea volcanoes, Hawai'i. *Contrib. Mineral. Petr.* **98**, 326-345.

Winchell, H. (1947) Honolulu Series, Oahu, Hawai'i. *Bull. Geol. Soc. Am.* **58**, 1-48.

Wolfe, E. W., Wise, W. S., and Dalrymple, G. B. (1997) The geology and petrology of Mauna Kea volcano, Hawai'i - a study of postshield volcanism. *U.S. Geological Survey Professional Paper* **1557**, 1-129.

Wright, T. L., Kinoshita, W. T., and Peck, D. L. (1968) March 1965 eruption of Kilauea Volcano and the formation of Makaopuhi Lava Lake. *J. Geophys. Res.* **73**, 3181.

Wright, T. L. (1971) Chemistry of Kilauea and Mauna Loa lava in space and time. *U.S. Geological Survey Professional Paper* **735**, 1-40.

Wright, T. L. and Fiske, R. S. (1971) Origin of the differentiated and hybrid lavas of Kilauea Volcano, Hawai'i. *J. Petrol.* **12**, 1-65.

Wright, T. L. and Okamura, R. T. (1977) Cooling and crystallization of tholeiitic basalt, 1965 Makaopuhi Lava Lake, Hawai'i. *U.S. Geological Survey Professional Paper* **1004**, 78p.

Wright, T. L. and Peck, D. L. (1978) Crystallization and differentiation of the Alae Magma, Alae Lava Lake, Hawai'i. *U.S. Geological Survey Bulletin* **935-C**, 1-20.

Wright, T. L. (1984) Origin of Hawai'ian tholeiite: a metasomatic model. *J. Geophys. Res.* **89**, 3233-3252.

Wright, T. L. and Helz, R. (1996) Differentiation and magma mixing on Kilauea's east rift zone: A further look at the eruptions of 1955 and 1960. 2. The 1960 lavas. *B. Vulcanol.* **57**, 602-630.

Xu, G. P., Frey, F. A., Clague, D. A., Weis, D., and Beeson, M. H. (2005) East Molokai and other Kea-trend volcanoes: Magmatic processes and sources as they migrate away from the Hawaiian hot spot. *Geochem. Geophys. Geosyst.* **6**, 28.

Yang, H. J., Frey, F. A., Garcia, M. O., and Clague, D. A. (1994) Submarine lavas from Mauna Kea Volcano, Hawai'i: implications for Hawai'ian shield stage processes. *J. Geophys. Res.* **99**, 15577-15594.

Yoder, H. S. J. and Tilley, C. E. (1962) Origin of basalt magmas: an experimental study of natural and synthetic rock systems. *J. Petrol.* **3**, 342-532.

Yokose, H. and Lipman, P. W. (2004) Emplacement mechanisms of the South Kona slide complex, Hawai'i Island: sampling and observations by remotely operated vehicle Kaiko. *B. Vulcanol.* **66**, 569-584.

Yokose, H., Lipman, P. W., and Kanamatsu, T. (2005) Physical and chemical properties of submarine basaltic rocks from the submarine flanks of the Hawai'ian islands. *Mar. Geol.* **219**, 173-193.

Zreda, M. G., Phillips, F. M., Elmore, D., Kubik, P. W., Sharma, P., and Dorn, R. I. (1991) Cosmogenic chlorine-36 production rates in terrestrial rocks. *Earth Planet Sc. Lett.* **105**, 94-109.

TABLES

Table 1: Available whole rock analyses

	Total points	Points after filtering
East Molokai	171	9
Haleakala	286	82
Hualalai	268	122
Kahoolawe	24	4
Kauai	27	10
Kilauea	3171	1959
Kohala	137	4
Ko'olau	436	128
Lanai	22	6
Loihi	84	15
Mahukona	19	16
Mauna Kea	1059	325
Mauna Loa	676	303
Niihau	44	11
Waianae	128	49
West Maui	94	35
West Molokai	104	0
Total	6750	3078

Table 1:Total available whole rock analyses for Hawaiian volcanoes and remaining data after filtering for alteration, alkalinity, and fractionation of mineral phases other than olivine. References in Supplementary Table 1, filtering process as described in text.

Table 2: Point count results from the HSDP2 Caltech Reference Suite

Sample #	Unit	Wt. % MgO	Matrix (Vol %)	Oliv. (Vol %)	Plag. (Vol %)	Pyr. (Vol %)	Ves. (Vol %)
SR238-0.0	96	18.38	63.4	30.1	0.9	0.0	5.5
	96	18.38	63.1	30.3	1.4	0.0	5.2
	96	18.38	66.5	26.5	1.1	0.0	5.9
	96	18.38	66.1	27.6	0.9	0.0	5.5
SR125-6.48	45	10.26	68.1	2.1	0.0	0.0	29.8
SR127-5.7	46	6.64	87.8	7.1	2.9	1.5	0.7
SR170-0.7	71	17.71	70.9	23.6	0.0	0.0	5.5
SR175-1.4	73	23.96	51.1	37.9	0.0	0.0	11.0
SR186-5.3	77	16.76	54.5	20.2	0.6	0.0	24.7
SR258-3.6	104	7.12	96.4	0.7	0.1	0.0	1.3
SR262-.6	105	15.32	61.2	14.4	0.0	0.0	24.4
SR267-6.85	107	23.16	61.7	33.4	0.0	0.0	4.9
SR279-4.7	113	11.94	80.9	2.8	0.1	0.0	16.1
SR306-9.7	120	13.47	68.8	10.2	0.0	0.1	20.8
SR310-5.7	123	14.98	77.4	11.7	0.3	0.0	10.6
SR331-9.7	128	20.65	67.3	30.6	0.0	0.0	2.1
SR344-3.1	134	8.53	86.3	3.0	0.0	0.0	10.7
SR363-7.4	141	18.2	62.2	21.3	0.0	0.0	16.5
SR392-5.35	148	21.62	70.2	22.1	0.0	0.0	7.7
SR399-2.4	150	28.68	40.2	39.5	0.0	0.0	20.3
SR407-3.2	154	18.74	68.0	24.9	0.0	0.0	7.1
SR425-6.0	158	7.49	68.4	7.0	2.4	0.0	22.2
SR433-5.7	161	9.59	78.8	7.1	0.1	0.0	13.9
SR447-7.0	168	7.99	80.1	1.3	0.0	0.0	18.6
SR455-7.4	179	26.01	45.2	42.7	3.2	0.3	8.6
SR462-2.0	181	8.54	93.0	3.5	0.7	0.0	2.7
SR502-5.1	191	26.46	55.0	40.4	0.9	0.0	3.6
SR548-9.9	199	19.52	73.4	26.6	0.0	0.0	0.0
SR560-7.6	202	19.09	70.1	29.6	0.0	0.0	0.3
SR582-10.4	207	19.62	71.4	28.4	0.0	0.0	0.1
SR604-2.9	217	11.63	95.8	4.2	0.0	0.0	0.0
SR630-6.4	224	18.32	76.5	23.3	0.0	0.0	0.3
SR649-5.9	234	13.76	87.5	12.5	0.0	0.0	0.0
SR650-7.9	236	13.83	83.4	15.9	0.1	0.0	0.6
SR691-8.8	251	11.31	88.4	11.6	0.0	0.0	0.0
SR743-14.00	280	16.66	79.7	20.1	0.0	0.0	0.2
SR756-14.1	284	18.91	77.8	21.0	1.2	0.0	0.0
SR846-18.8	304	12.19	95.6	2.0	0.0	0.0	2.4
SR855-.1	305	8.92	89.2	6.6	4.2	0.0	0.0
SR891-17.4	316	22.04	72.9	27.0	0.0	0.0	0.1

SR915-4.8	328	13.31	80.1	15.3	0.3	0.0	4.1
SR930-16.6	333	22.11	67.2	28.1	0.2	0.0	4.5
SR949-11.5	336h	9.32	99.6	0.4	0.0	0.0	0.0

Table 2: Mineral proportions and vesicle abundances based on 500-800 points per thin section. All phases <0.5 mm were counted as part of the groundmass. Whole-rock MgO content for each flow from Rhodes and Vollinger (2004). Abbreviations are Oliv, Olivine; Plag, plagioclase; Aug, augite; Ves, vesicles. Groundmass (vol %) = 100 – reported mineral and vesicle abundances.

Table 3: Olivine compositions from this study and the literature

	Average olivine	Highest Mg #	Reference for highest Mg# olivine
Mauna Loa	87.5(3)	91.2	Garcia and Hulsebosch, 1995
Hualalai	87.4(5)	91.2	Kuno, 1969
Kilauea	86.6(5)	90.7	Clague et al., 1991
Mauna Kea	87.9(6)	90.5	Frey et al., 1991, Sobolev et al., 2007
Ko'olau	86.2(3)	90.5	Sobolev and Nikogosian, 1994
Waianae	85.0(7)		
Haleakala	86.6(4)		
Loihi	87.2(12)		

Table 3: The average olivine composition was calculated via linear regression on the compiled data shown in Figure 2, projected back to its intercept with a curve representing the composition of the olivine end-member with some trace-constituents as described in the text and shown in Figure 3. The upper and lower limits were calculated by extending the curves calculated as the 95% confidence limits on the regression analysis to their intersection point with the olivine composition curve. The highest Mg # olivines are specified here for volcanoes that are involved in the olivine addition calculations, where analyses of glass are available and data coverage is best. Other volcanoes were examined, but were not included because of a lack of data points to define the olivine control line.

Table 4

4a	SiO_2	TiO_2	Al_2O_3	Cr_2O_3	FeO	MnO	NiO	MgO	CaO	Na_2O	K_2O	P_2O_5
Mauna Kea Low SiO_2	48.96	2.64	13.93	0.10	11.48	0.17	0.008	7.73	11.43	2.40	0.42	0.22
Mauna Kea High SiO_2	51.20	2.48	13.55	0.10	11.32	0.17	0.008	7.42	10.61	2.22	0.38	0.20
Mauna Loa	51.96	2.10	13.83	0.10	10.21	0.17	0.008	7.58	10.89	2.21	0.32	0.19
Ko'olau	51.70	2.36	14.22	0.10	10.88	0.17	0.008	7.13	10.44	2.18	0.39	0.21
Kilauea	51.01	2.47	13.52	0.10	10.97	0.17	0.008	7.22	11.15	2.40	0.44	0.23
Hualalai	51.49	2.28	14.09	0.10	10.49	0.16	0.008	7.53	11.39	2.30	0.37	0.22
Haleakala	51.76	2.38	13.47	0.10	10.87	0.17	0.008	7.84	11.11	1.96	0.36	0.26

4b.	SiO_2	TiO_2	Al_2O_3	Cr_2O_3	FeO	MnO	NiO	MgO	CaO	Na_2O	K_2O	P_2O_5	Final olivine	Average olivine
Mauna Kea Low SiO_2	46.76	1.97	10.47	0.21	11.78	0.17	0.080	17.71	8.59	1.79	0.31	0.16	90.5	86.7
Mauna Kea High SiO_2	48.25	1.83	10.06	0.21	11.72	0.17	0.090	17.72	7.88	1.64	0.28	0.15	90.5	86.4
Mauna Loa	49.13	1.59	10.52	0.20	10.60	0.16	0.080	17.37	8.29	1.67	0.24	0.14	91.2	87.7
Ko'olau	48.70	1.76	10.67	0.21	11.34	0.17	0.091	17.14	7.85	1.63	0.29	0.16	90.5	86.5
Kilauea	48.13	1.83	10.05	0.21	11.38	0.17	0.095	17.58	8.29	1.77	0.32	0.17	90.7	86.7
Hualalai	48.31	1.69	10.48	0.21	10.78	0.16	0.087	17.68	8.47	1.70	0.27	0.16	91.2	87.5
Haleakala	48.45	1.78	10.08	0.21	11.22	0.17	0.075	17.48	8.64	1.46	0.27	0.19	90.5	86.7

4c.	SiO_2	TiO_2	Al_2O_3	Cr_2O_3	FeO	MnO	NiO	MgO	CaO	Na_2O	K_2O	P_2O_5	Final olivine	Average olivine
Mauna Kea Low SiO_2 glass	48.46	2.55	13.63	0.10	11.74	0.17	0.008	8.76	11.06	2.37	0.37	0.20		
Mauna Kea High SiO_2 glass	51.19	2.32	13.01	0.10	10.48	0.17	0.008	8.47	11.09	2.11	0.36	0.19		
Mauna Kea Low SiO_2	46.31	1.87	10.04	0.22	11.75	0.16	0.072	19.27	8.15	1.73	0.27	0.15	91.2	88.0
Mauna Kea High SiO_2	48.69	1.78	10.02	0.20	10.75	0.17	0.062	17.75	8.55	1.61	0.27	0.15	91.2	87.7

4d.	SiO_2	TiO_2	Al_2O_3	Fe_2O_3*	MnO	MgO	CaO	Na_2O	K_2O	P_2O_5
KSDP	47.17	1.96	12.23	10.95	0.16	8.47	9.25	2.13	0.29	0.20
Mauna Kea - HSDP2	47.95	2.19	11.14	12.67	0.18	14.06	9.35	1.77	0.26	0.22
SOH-1	49.99	2.58	13.31	12.54	0.16	7.62	10.36	2.19	0.43	0.27
Mauna Loa -HSDP2	49.21	1.80	11.72	12.35	0.17	13.56	9.06	1.65	0.22	0.18

Table 4: Results of glass composition compilation, olivine addition, and compositional averaging calculations presented in this study. Table 4a shows the starting liquid compositions calculated by averaging measured glass compositions from sources as described in the text. NiO and Cr_2O_3 contents are typically not measured in glasses and so were assumed here. Table 4b gives the calculated liquid composition at the end of the olivine addition calculations. The final olivine composition gives the Mg # composition of the final olivine added to the liquid, and the average olivine composition is the mass-weighted average Mg# of olivine added during the analysis. Table 4c shows the alternate calculations referred to in the text; the lava series from Mauna Kea were fit using a more magnesian liquid and ended at a more forsteritic olivine composition to try to better fit the olivine composition seen in the regression and histogram analyses. Table 4d gives the average weighted composition for the KSDP drill core through Ko'olau, the HSDP2 sections for Mauna Kea and Mauna Loa, and the SOH-1 drill core through Kilauea.

Table 5

Volcano/section	Percent of mass left behind	Source
Kilauea	10-22%	Clague & Denlinger, 1994
Mauna Kea	4-7%	Baker et al., 1996
Mauna Loa	7.8%	HSDP2
Mauna Loa	16.7%	Historic
Kilauea	18.9%	Historic and Pu'u O'o
Kilauea	20.5%	SOH-1
Mauna Kea	6.7%	HSDP2
Ko'olau	17.8%	KSDP
Mauna Kea high MgO section	0.5%	HSDP2
Mauna Kea Low MgO section	12.7%	HSDP2
Mauna Kea high MgO liquid	9.0%	HSDP2

Table 5: The percent of mass of the liquid entering each volcano that is deposited within the volcano as accumulated olivine based on the data sets examined here. The high and low MgO sections for Mauna Kea in the HSDP2 drill core are as defined in the text.The high MgO liquid value is the value for the full core using the high MgO liquid for Mauna Kea from Table 4c.

FIGURE CAPTIONS

Fig 1. Compilation of point count data for available drill cores and other selected data sets. Line is best fit line for counts from HSDP2 – this work. All data is plotted as whole rock wt% MgO versus olivine modal abundance measured by point counts on the same unit. All olivine modal abundances are normalized to a vesicle-free basis in this case.

Figure 2. Whole rock FeO* versus MgO (wt. %) for tholeiites from the eight best-sampled Hawaiian volcanoes. All iron is taken as FeO*, as in the text. Solid lines represent linear regression best fit lines for the data and represent the average olivine control line for each volcano. Dashed curves reflect 95% confidence limits for the olivine control regression lines. Numbers of points plotted for each volcano are as listed in Table 1 and sources are given in Supplementary Table 1.

Figure 3. Histogram of whole rock wt. % FeO* contents from Mauna Kea and Ko'olau. The median value for Ko'olau is 10.6, while Mauna Kea is 11.3.

Figure 4. Whole rock analyses from the HSDP2 drill core, divided into low and high SiO_2 series based on the measurements of Stolper et al. (2004).

Figure 5. Histograms of olivine populations from the best-sampled Hawaiian volcanoes.

Figure 6. Whole rock wt. % MgO variations from the four volcanoes sampled by the major drill cores analyzed in this project. Ages are calculated as described in the text.

Solid lines are five point unweighted moving averages calculated for each volcano. Decreasing or increasing the number of points included in the moving average typically only increases or decreases, respectively, the magnitude of the shifts but does not change the overall structure. For each core, units that were sampled more than one time were averaged to produce a single result for each sampled unit, and that result is plotted here. Data for Mauna Kea cover a number of different flow types and therefore were separated by flow type here, although the moving average is calculated across each flow type.

Figure 7. Whole rock wt. % MgO variations measured from historically dated eruptions from Mauna Loa and Kilauea. No samples are included in this plot from the long-lived Pu'u O'o eruption phase from Kilauea. Several points along a horizontal line are typically measurements of different samples from a single eruption. The 1959 eruption of Kilauea produced a lava lake that was sampled over a number of years as it cooled and crystallized, and thus samples from it represent variable amounts of olivine accumulation, loss, and crystallization of other phases. Data sources are given in Supplemental Table 1.

Figure 8. Dated whole rock sample measurements from the long-lived Pu'u O'o eruption phase at Kilauea. Data sources are given in Supplemental Table 1.

Figure 9. CaO contents in olivines measured by Sobolev et al. (2007). Only analyses from this study were considered so that the analytical conditions in each measurement would remain constant. Red line in panel Mauna Kea shows the estimated increase in olivine CaO content predicted during olivine crystallization by the model of Libourel

(1999). Samples move to lower CaO contents by re-equilibration with a high MgO, low CaO liquid, likely while residing in a cumulate pile. A few samples from Loihi show noticeably lower values, likely reflecting equilibration with a low CaO liquid that has previously crystallized plagioclase.

Figure 10. weight fraction of olivine crystallized by Mg # during the olivine addition calculations. Totals were calculated by summing the weight crystallized during every 0.5 Mg# units and normalizing by the total amount of olivine crystallized between the primary liquid and the end of the calculation at 7.4% MgO. This calculation was done specifically for the high SiO_2 series from Mauna Kea, but a similar trend could be calculated for any volcano. The large peaks in Mg# seen in the histograms (Figure 5) and the Mg# at which this peak occurs are not predicted by this calculation without re-equilibration.

Figure 11. Whole rock Al_2O_3 and CaO contents as calculated in the olivine addition analyses. The blue line segment shows the actual whole rock compositions calculated by olivine addition. The solid line at lower CaO content is the extension of this addition trend back to zero Al_2O_3 content. The higher line shows the increase in projected CaO content if 0.2% CaO is added to the high Mg, low CaO and Al_2O_3 liquid, proposed here to be sourced from the decreasing CaO content in re-equilibrating olivines.

Figure 12. Histogram of measured NiO concentrations in olivines from Mauna Kea, as measured by Sobolev et al., (2007). The median measured NiO concentration is .379. As

in Figure 10 with MgO, the olivine addition calculations predict a fairly uniform distribution of NiO contents as crystallization proceeds. The large peak in number of olivines measured close to the average NiO content suggests many of these olivines have re-equilibrated towards the average composition while inside the volcano.

FIGURES

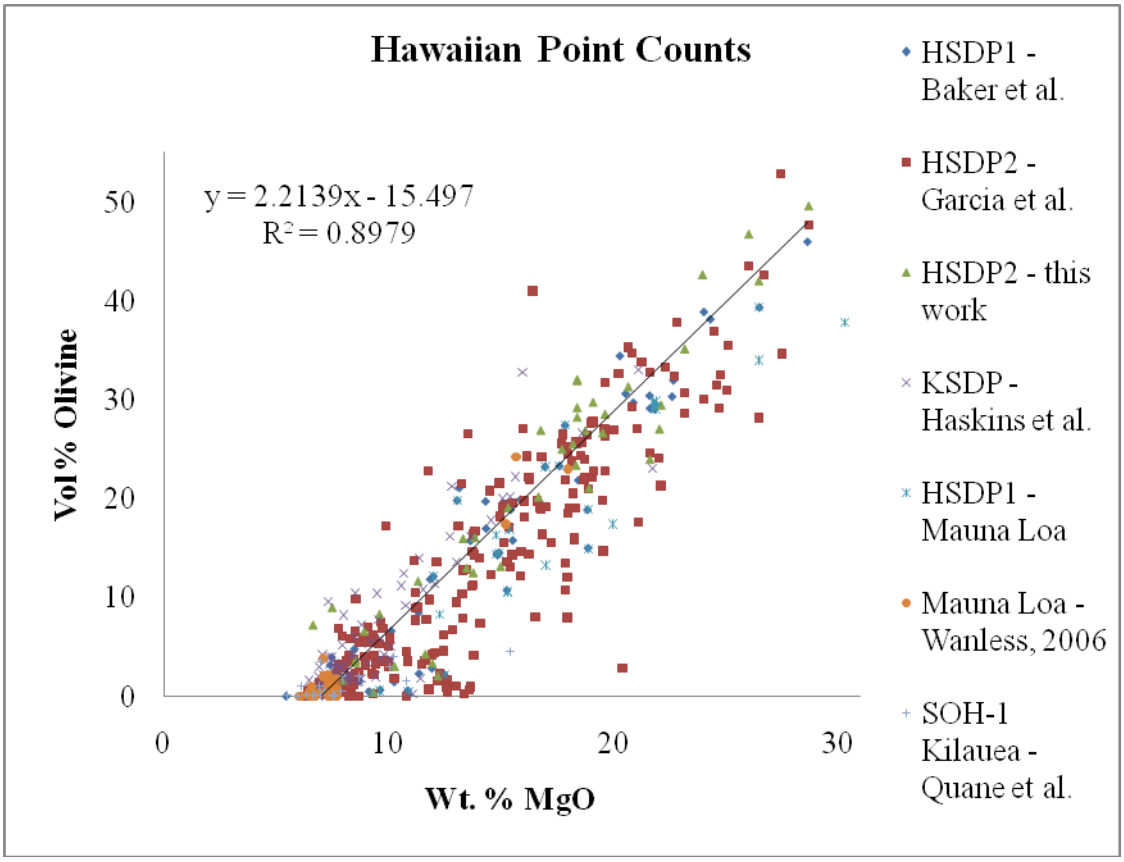

Figure 1

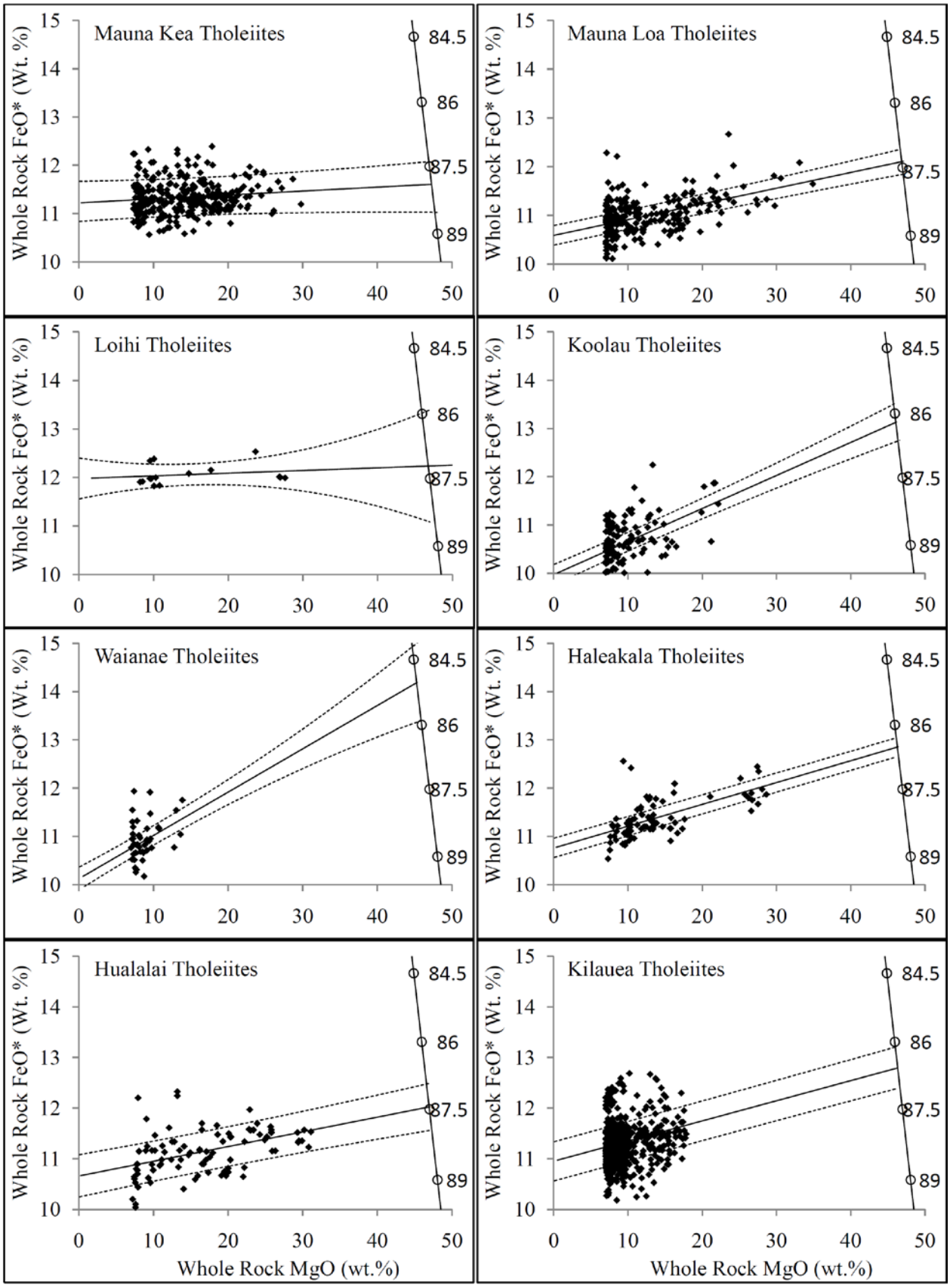
Mauna Kea Tholeiites
Mauna Loa Tholeiites
Loihi Tholeiites
Koolau Tholeiites
Waianae Tholeiites
Haleakala Tholeiites
Hualalai Tholeiites
Kilauea Tholeiites
Whole Rock FeO* (Wt. %)
Whole Rock MgO (wt.%)
84.5
86
87.5
89
0
10
20
30
40
50
10
11
12
13
14
15

Figure 2

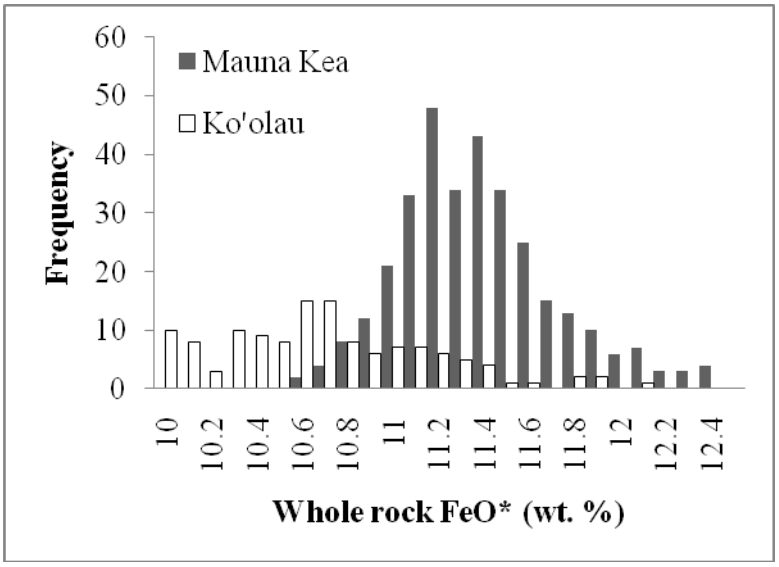
60
50
40
30
20
10
0
Frequency
Mauna Kea
Ko'olau
10
10.2
10.4
10.6
10.8
11
11.2
11.4
11.6
11.8
12
12.2
12.4
Whole rock FeO* (wt. %)

Figure 3

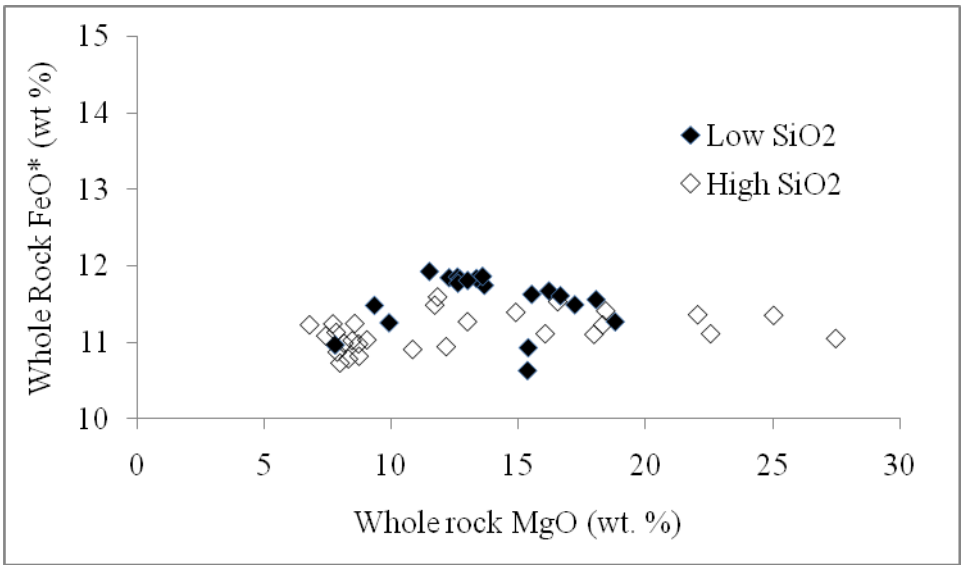
15
14
13
12
11
10
Whole Rock FeO* (wt %)
0
5
10
15
20
25
30
Whole rock MgO (wt. %)
Low SiO2
High SiO2

Figure 4

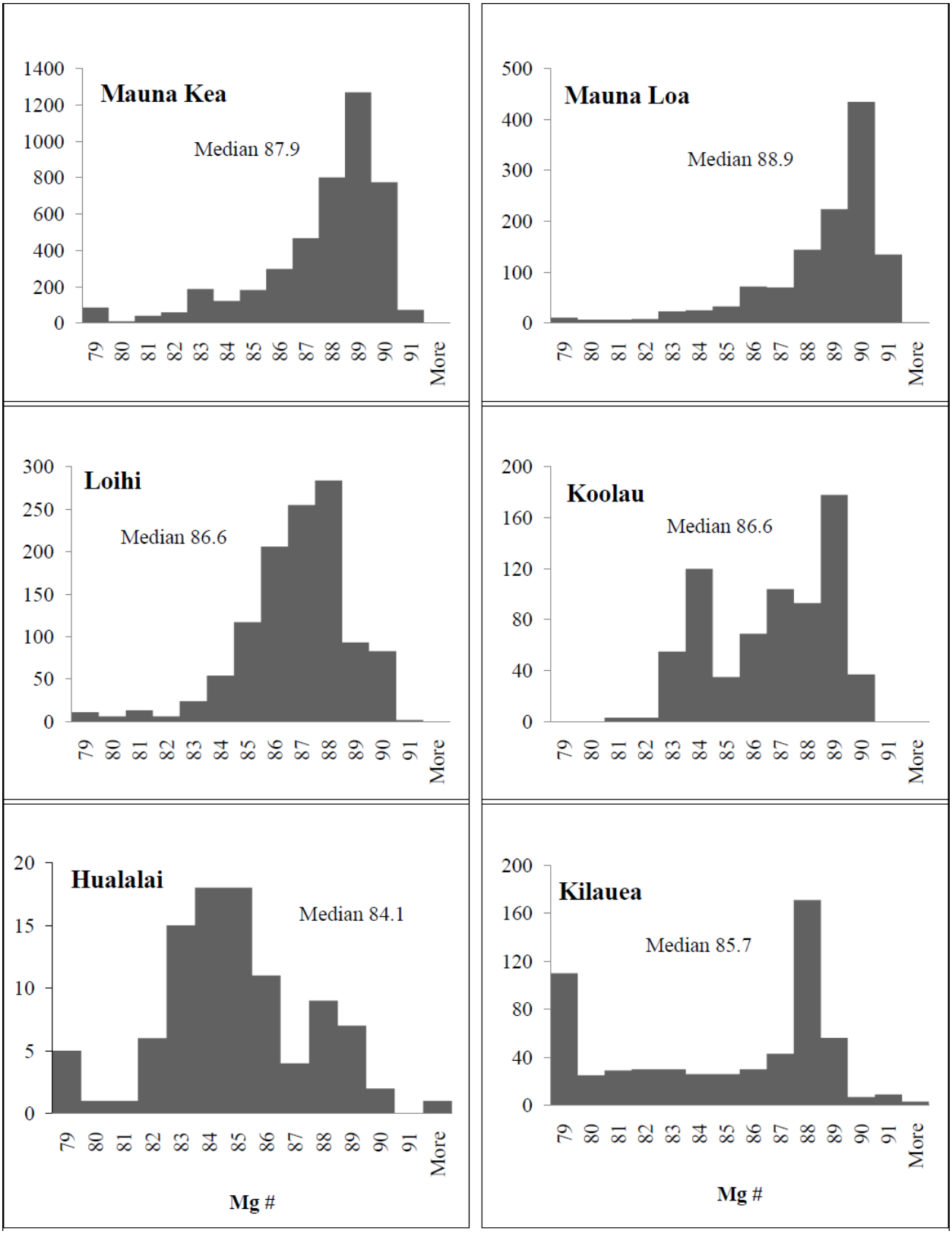
Mauna Kea
Median 87.9
Mauna Loa
Median 88.9
Loihi
Median 86.6
Koolau
Median 86.6
Hualalai
Median 84.1
Kilauea
Median 85.7
79 80 81 82 83 84 85 86 87 88 89 90 91 More
Mg #

Figure 5

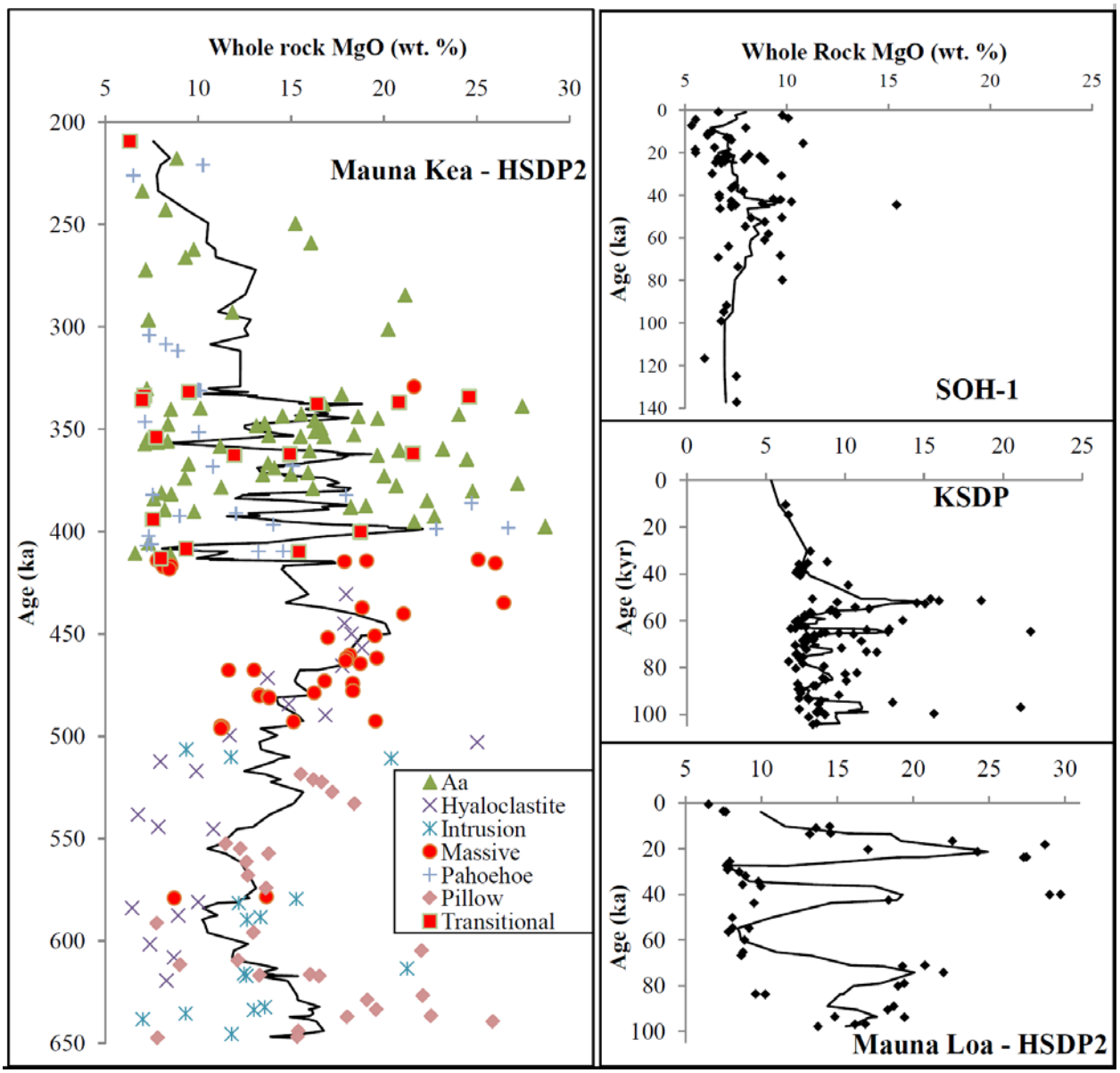
Whole rock MgO (wt. %)
Mauna Kea - HSDP2
Age (ka)
Aa
Hyaloclastite
Intrusion
Massive
Pahoehoe
Pillow
Transitional
Whole Rock MgO (wt. %)
SOH-1
Age (ka)
KSDP
Age (kyr)
Mauna Loa - HSDP2
Age (ka)

Figure 6

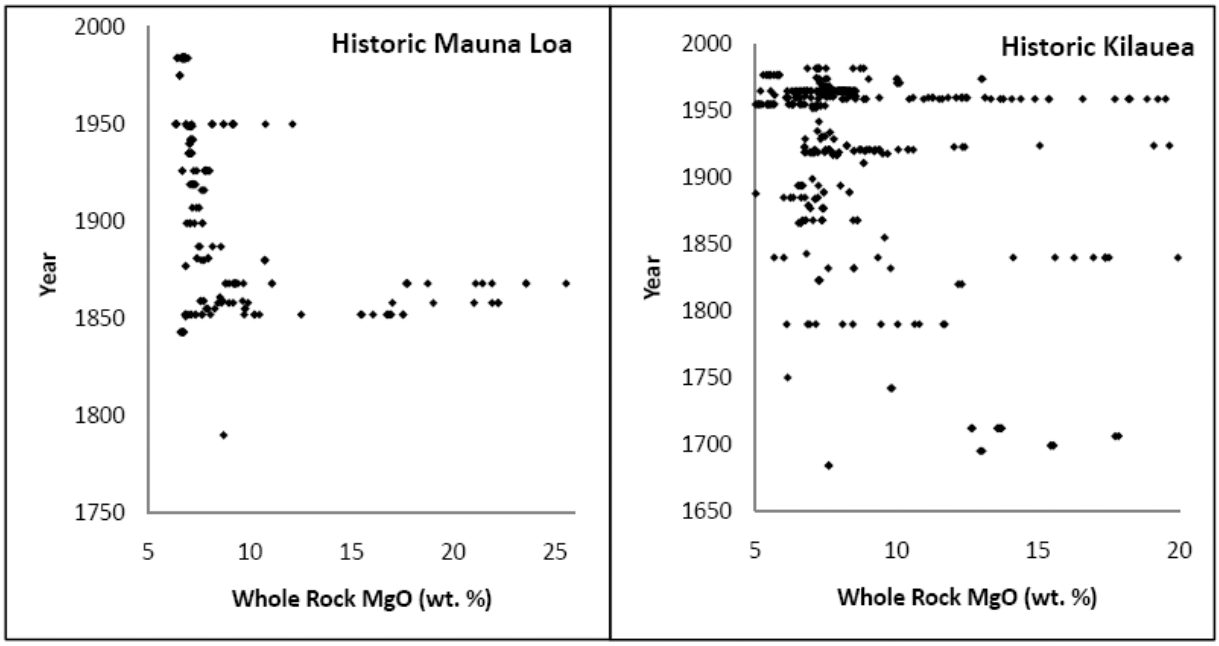
Historic Mauna Loa
Year
2000
1950
1900
1850
1800
1750
5
10
15
20
25
Whole Rock MgO (wt. %)
Historic Kilauea
Year
2000
1950
1900
1850
1800
1750
1700
1650
5
10
15
20
Whole Rock MgO (wt. %)

Figure 7

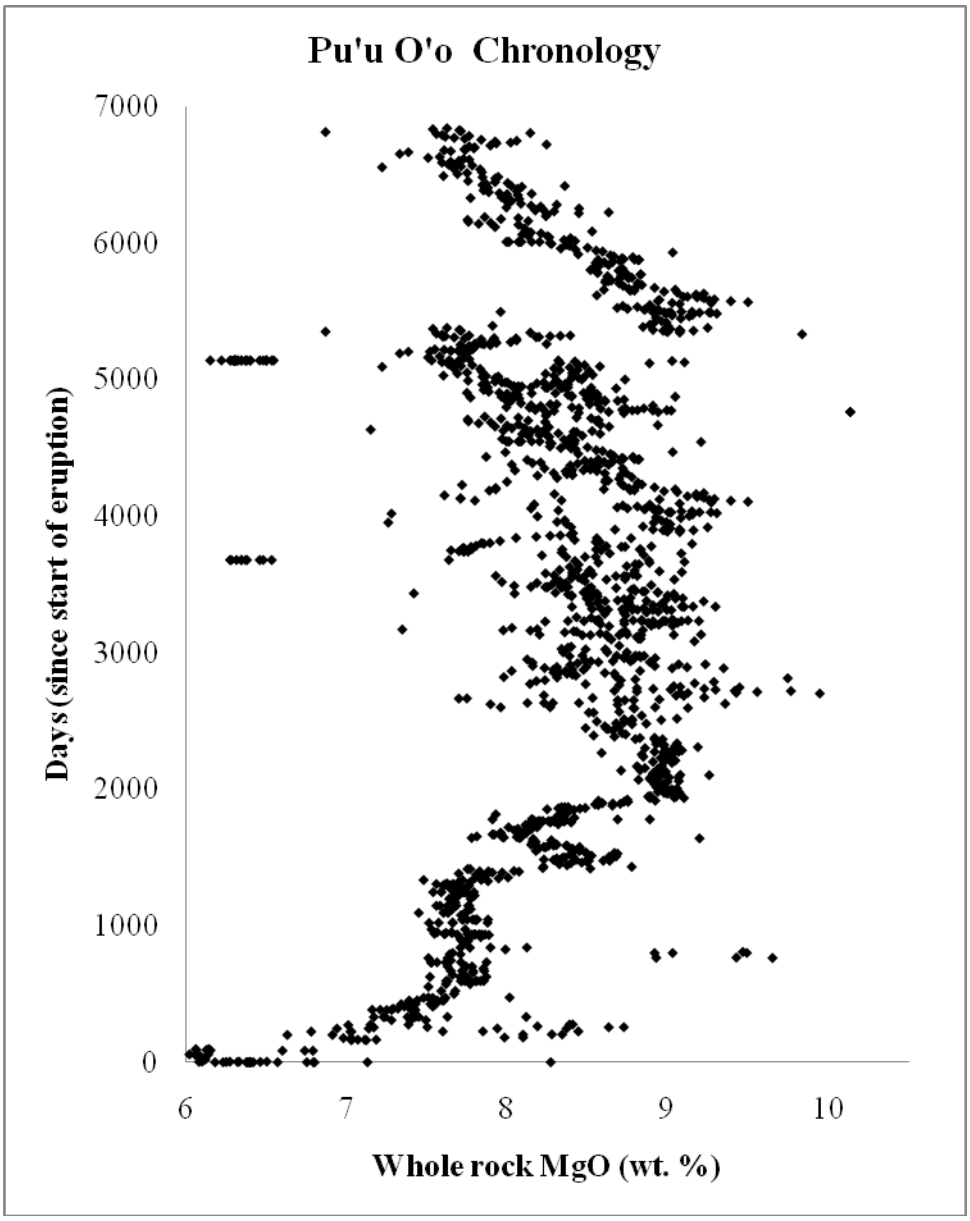
Pu'u O'o Chronology
Days (since start of eruption)
7000
6000
5000
4000
3000
2000
1000
0
6
7
8
9
10
Whole rock MgO (wt. %)

Figure 8

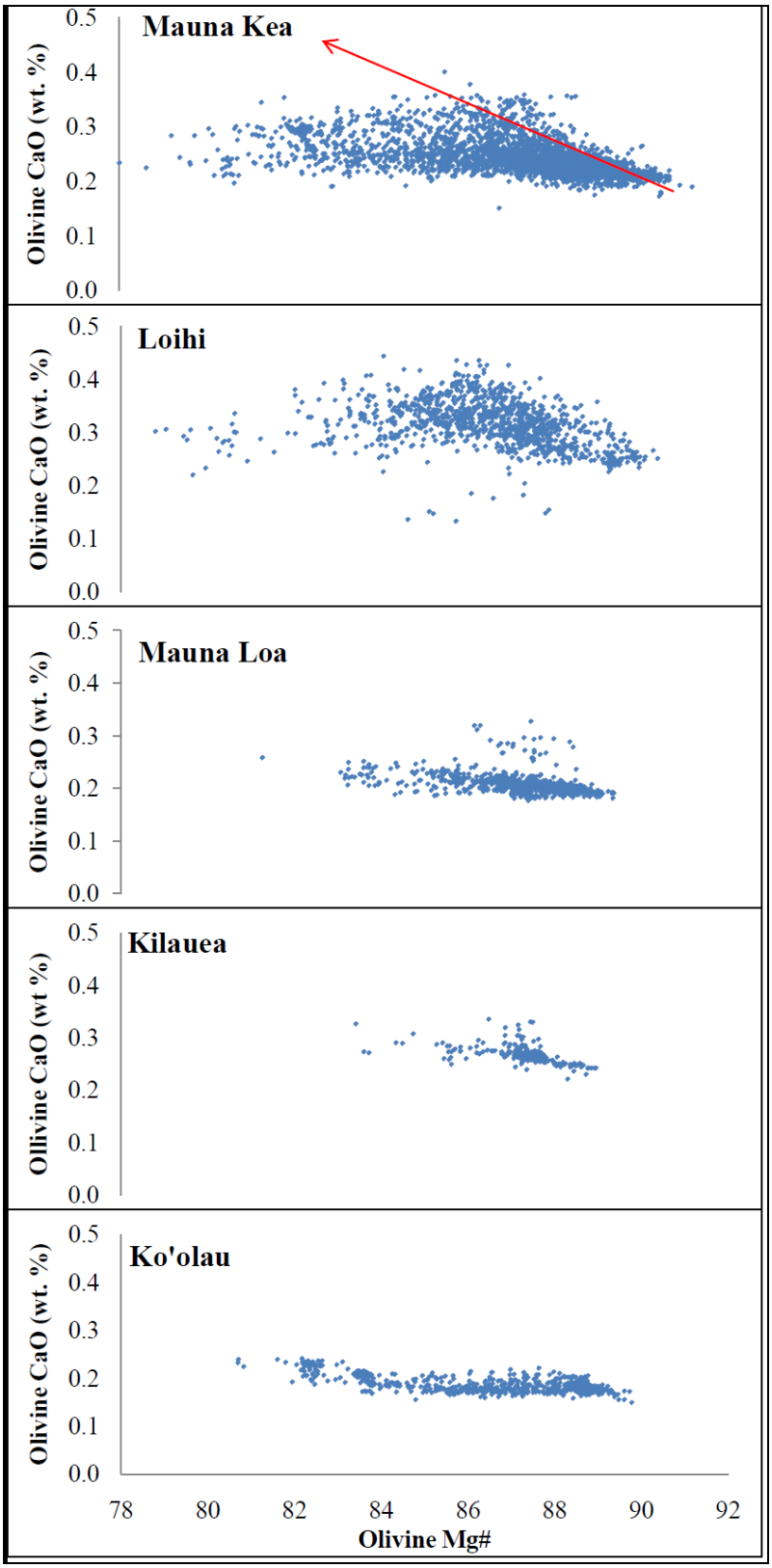
Mauna Kea
Loihi
Mauna Loa
Kilauea
Ko'olau
Olivine CaO (wt. %)
Ollivine CaO (wt %)
0.0
0.1
0.2
0.3
0.4
0.5
78
80
82
84
86
88
90
92
Olivine Mg#

Figure 9

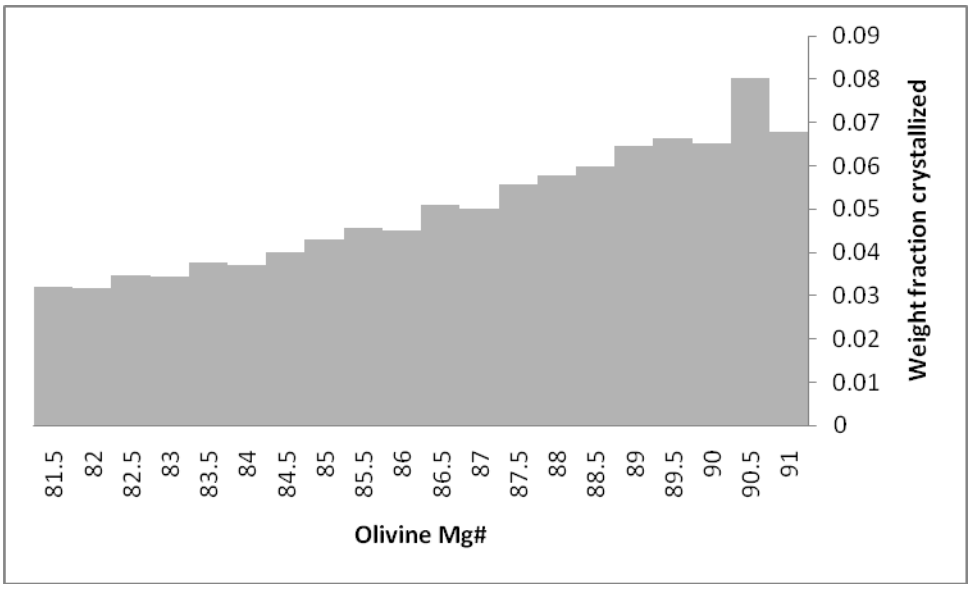
0.09
0.08
0.07
0.06
0.05
0.04
0.03
0.02
0.01
0
Weight fraction crystallized
81.5
82
82.5
83
83.5
84
84.5
85
85.5
86
86.5
87
87.5
88
88.5
89
89.5
90
90.5
91
Olivine Mg#

Figure 10

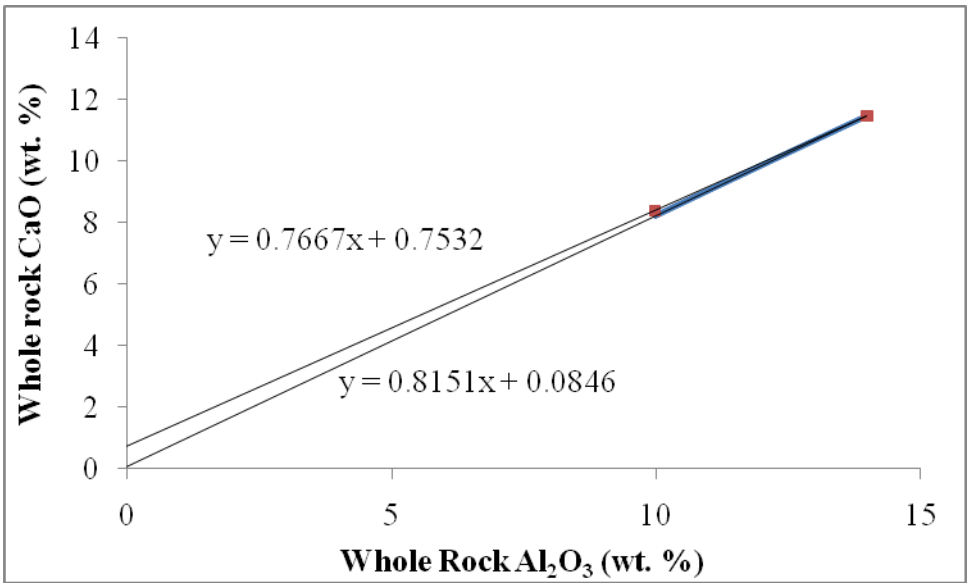
14
12
10
8
6
4
2
0
0
5
10
15
Whole rock CaO (wt. %)
Whole Rock Al2O3 (wt. %)
y = 0.7667x + 0.7532
y = 0.8151x + 0.0846

Figure 11

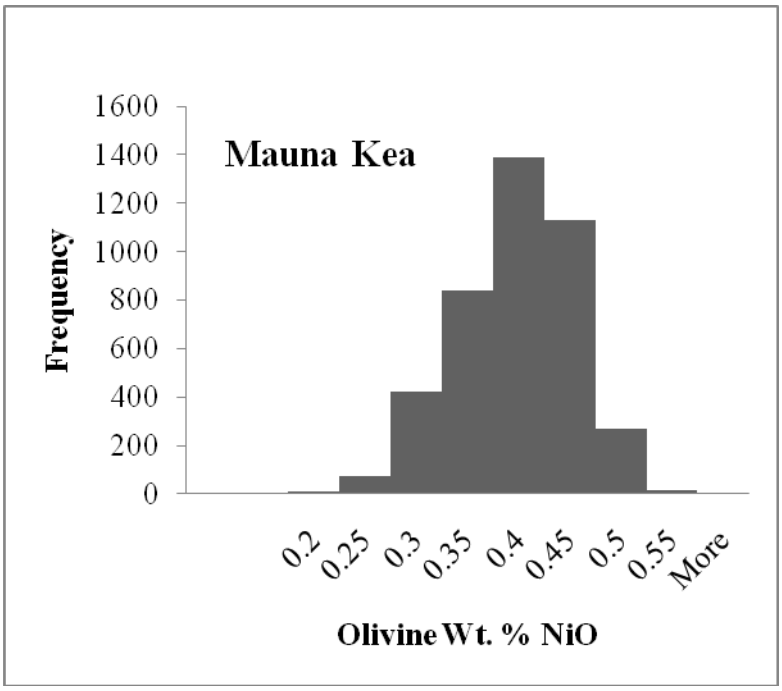
Mauna Kea
Frequency
1600
1400
1200
1000
800
600
400
200
0
0.2
0.25
0.3
0.35
0.4
0.45
0.5
0.55
More
Olivine Wt. % NiO

Figure 12: